MECHANICAL PROPERTIES AND GALVANIZING OF MEDIUM-MN STEEL

MECHANICAL PROPERTY DEVELOPMENT, SELECTIVE OXIDATION, AND GALVANIZING OF MEDIUM-MN THIRD GENERATION ADVANCED HIGH STRENGTH STEEL

BY KAZI MAHMUDUL HAQUE BHADHON, B.Sc., M.A.Sc.

A Thesis

Submitted to the School of Graduate Studies

in Partial Fulfilment of the Requirements

for the Degree

Doctor of Philosophy

McMaster University

Doctor of Philosophy (2022) McMaster University

(Materials Science & Engineering) Hamilton, Ontario, Canada

TITLE:	Mechanical Property Development, Selective Oxidation, and Galvanizing of Medium-Mn Third Generation Advanced High Strength Steel
AUTHOR:	Kazi Mahmudul Haque Bhadhon, B.Sc. (Bangladesh University of Engineering and Technology), M.A.Sc. (McMaster University)
SUPERVISOR:	Professor. Joseph Robert McDermid
NUMBER OF PAGES:	xxvi, 240

Lay Abstract

One of the largest challenges associated with incorporating the next generation of advanced high strength steels into the automotive industry lies in processing these steels in existing industrial production lines. In that regard, a two-stage heat treatment with an intermediate flash pickling stage and process atmosphere compatible with existing industrial continuous galvanizing line technology was developed for a prototype medium-Mn steel. The heat-treated prototype steel met the target mechanical properties outlined for the next generation of advanced high strength steels. Furthermore, the heat treatment and process atmosphere utilised in this research produced a surface that facilitated the successful galvanizing of the prototype medium-Mn steel. This adherent and high-quality galvanized coating will provide robust corrosion protection if the candidate medium-Mn steel is used in future automotive structural applications.

Abstract

Medium Mn (med-Mn) third generation advanced high strength steels (3G AHSSs) are promising candidates for meeting automotive weight reduction requirements without compromising passenger safety. However, the thermal processing of these steels should be compatible with continuous galvanizing line (CGL) processing capabilities as it provides cost effective, robust corrosion protection for autobody parts. Hence, the main objective of this Ph.D. research is to develop a CGL-compatible thermal processing route for a prototype 0.2C-6Mn-1.5Si-0.5Al-0.5Cr-xSn (wt%) (x = 0 and 0.05 wt%) med-Mn steel that will result in the 3G AHSS target mechanical properties (24,000 MPa% ≤ UTS × TE ≤ 40,000 MPa%) and high-quality galvanized coatings *via* enhanced reactive wetting.

It was found that the starting microstructure, intercritical annealing (IA) time/temperature, and Sn micro-alloying had a significant effect on the retained austenite volume fraction and stability and, thereby, the mechanical properties of the prototype med-Mn steel. For the as-received cold-rolled (CR) starting microstructure, the intercritical austenite nucleated and grew on dissolving carbide particles and resulted in blocky retained austenite. However, Sn micro-alloying significantly effected the intercritical austenite chemical stability by segregating to the carbide/matrix interface and retarding C partitioning to the intercritical austenite. This resulted in lower volume fractions of low stability retained austenite which transformed to martensite (*via* the TRIP effect) at low strains, thereby quickly exhausting the TRIP effect and resulting in a failure to sustain high work hardening rates and delay the onset of necking. Consequently, the Sn micro-alloyed CR starting microstructure was unsuccessful in achieving 3G AHSS target mechanical properties regardless of the IA parameters employed. Contrastingly, the CR starting microstructure without Sn micro-alloying was able to meet target 3G mechanical properties *via* intercritical

annealing at 675 °C × 60 s and 120 s, and at 690 °C × 60 s owing to sufficiently rapid carbide dissolution and C/Mn partitioning into the intercritical austenite such that it had sufficient mechanical and chemical stability to sustain a gradual deformation-induced transformation to martensite and maintain high work hardening rates.

On the other hand, the martensitic (M) starting microstructure produced higher volume fractions of chemically and mechanically stable lamellar retained austenite regardless of Sn micro-alloying. Intercritical annealing at 650 °C × 60 s and 675 °C × 60 s and 120 s produced 3G AHSS target mechanical properties. It was shown that the stable lamellar retained austenite transformed gradually during deformation. Furthermore, deformation-induced nano-twin formation in the retained austenite was observed, suggesting the TWIP effect being operational alongside the TRIP effect. As a result, a continuous supply of obstacle to dislocation motion was maintained during deformation, which aided in sustaining a high work hardening rate and resulted in a high strength/ductility balance, meeting 3G AHSS target properties. Based on these results, the martensitic starting microstructure without Sn micro-alloying and the M-675 °C × 120 s IA condition were chosen for the selective oxidation and reactive wetting studies.

The selective oxidation study determined the effect of a N_2-5H_2-$x$$H_2O$ (vol%) process atmosphere pO_2 (–30, –10, and +5 °C dew point (T_{dp})) on the composition, morphology, and spatial distribution of the external and internal oxides formed during the austenitizing and subsequent intercritical annealing cycles. The objective of this study was to identify the process atmosphere for the promising M-675 °C × 120 s heat treatment that would result in a pre-immersion surface that could be successfully galvanized in a conventional galvanizing (GI) bath. The austenitizing heat treatment (775 °C × 600 s) used to produce the martensitic starting microstructure resulted in thick (~ 200 nm) external oxides comprising MnO, $MnAl_2O_4$, $MnSiO_3$/Mn_2SiO_4, and $MnCr_2O_4$,

regardless of the process atmosphere pO_2. However, intermediate flash pickling was successful in dissolving the external oxides to a thickness of approximately 30 nm along with exposing metallic Fe in areas which contained relatively thin external oxides. Furthermore, extruded Fe nodules that were trapped under the external oxides were revealed during the flash pickling process. Overall, flash pickling resulted in a surface consisting of dispersed external oxide particles with exposed metallic substrate and extruded Fe nodules. This external surface remained unchanged during IA owing to the multi-micron (~ 2–8 μm) solute-depleted layer that formed during the austenitizing heat treatment.

Subsequent galvanizing in a 0.2 wt% (dissolved) Al GI bath with an immersion time of 4 s at 460 °C was successful in achieving high-quality, adherent galvanized coatings through multiple reactive wetting mechanisms. The dispersed nodule-type external oxides along with exposed substrate and extruded Fe nodules on the pre-immersion surface facilitated direct wetting of the steel substrate and promoted the formation of a robust and continuous $Fe_2Al_5Zn_x$ interfacial layer at the steel/coating interface. Additionally, oxide lift-off, oxide wetting, bath metal ingress, and aluminothermic reduction were operational during galvanizing. The galvanized med-Mn steels met 3G AHSS target mechanical properties. Overall, this Ph.D. research showed that it is possible to employ a CGL-compatible thermal processing route for med-Mn steels to successfully produce 3G AHSS target mechanical properties as well as robust galvanized coatings.

Acknowledgements

First and foremost, I am thankful for all the blessings that Allah has bestowed upon me. He always plans what's best for you. Alhamdulillah for everything.

I would like to thank my supervisor, Dr. Joseph R. McDermid, for giving me an opportunity to be a part of one of the best research groups in the world. His valuable mentorship and continuous guidance helped me throughout this Ph.D. research. With his support, I was able to present my research at various international conferences and meet prominent minds in the field of my research. His detailed and constructive critiques helped me improve the quality of my work as well as my writing skills. I also like to sincerely thank my supervisory committee members Dr. Joey Kish and Dr. David Wilkinson for their insightful comments and fruitful discussions during the course of my study.

I would also like to thank the following people for their technical assistance: John Thomson and Raymond Fullerton (McMaster Galvanizing Simulator) from the McMaster Steel Research Centre (SRC); Dr. Xiaogang Li, Doug Culley, and Ed McCaffery for their help in the MSE labs; Chris Butcher, Jhoynner Martinez (SEM), Travis Casagrande (FIB and SAM-AES), Dr. Carmen Andrei, Dr. Natalie Hamada, and Dr. Xiang Wang (TEM) from the Canadian Centre for Electron Microscopy (CCEM); Dr. James Britten, Victoria Jarvis, and Maureen Fitzpatrick (XRD) from the McMaster Analytical X-Ray Facility (MAX); Dr. Moisei Bruhis and Dr. Elizabeth McNally from the Centre for Automotive Materials and Corrosion (CAMC); Dr. Zeynel Bayindir (XPS) form the BioInterfaces Institute; my fellow CAMC group members, especially Dr. Maedeh Pourmajidian and Jonas Wagner for their help with APT analysis.

I want to extend my gratitude to the International Zinc Association Galvanized Autobody Partnership (IZA-GAP) program and the Natural Sciences and Engineering Research Council of

Canada (NSERC, grant CRDPJ 522309 – 17) for funding this Ph.D. research. U.S. Steel Research is also greatly acknowledged for the provision of the sheet steels used in this study.

Last, but not least, I am grateful to my friends and family for their unconditional support. I want to express my warmest gratitude to my parents and kid brother who have always believed in me to do something good. I hope I can keep making them proud. Finally, I appreciate all the sacrifices that my wife, Fatema Tuj Zohra, had to make in order to support me. Thank you for your immense patience.

Table of Contents

List of Figures

List of Tables

Abbreviations and Symbols

List of Abbreviations

A	Retained Austenite
A.F.	Area Fraction
AHSS	Advanced High Strength Steel
APT	Atom Probe Tomography
ART	Austenite Reversion Transformation
BF	Bright Field
BIW	Body-in-White
C	Carbides
CGL	Continuous Galvanizing Line
CR	Cold-Rolled
dp	Dew Point
DF	Dark Field
DP	Dual Phase
EDM	Electric Discharge Machining
EDS	Energy Dispersive X-Ray Spectroscopy
EELS	Electron Energy Loss Spectroscopy
F	Ferrite
FE-SEM	Field Emission Scanning Electron Microscope
FIB	Focussed-Ion Beam
GI	Galvanizing
GND	Geometrically Necessary Dislocation

HAADF	High Angle Annular Dark Field
HR-STEM	High-Resolution Scanning Transmission Electron Microscopy
IA	Intercritical Annealing
IAT	Intercritical Annealing Temperature
ICP	Inductively Coupled Plasma
K-S	Kurdjumov-Sachs Crystallographic Orientation Relationship
M	Martensite
MART	Martensitic
M-F	Martensite-Ferrite
Med-Mn	Medium-Mn
MGS	McMaster Galvanizing Simulator
ND	Normal Direction
N-W	Nishiyama-Wassermann Crystallographic Orientation Relationship
OT	Overaging Temperature
PDF	Powder Diffraction File
PHS	Press-Hardened Steel
Q&P	Quench and Partitioning Steel
RD	Rolling Direction
RSW	Resistance Spot Welding
SAD	Selected Area Diffraction
SEI	Secondary Electron Image/Imaging
SEM	Scanning Electron Microscope/Microscopy

SFE	Stacking Fault Energy
STEM	Scanning Transmission Electron Microscope/Microscopy
TD	Transverse Direction
TE	Total Elongation
TEM	Transmission Electron Microscopy
TMP	Thermo-mechanical Processing
TRIP	Transformation-Induced Plasticity
TT	Through-Thickness Direction
TWIP	Twinning-Induced Plasticity
UE	Uniform Elongation
U.S. DOE	United States Department of Energy
UTS	Ultimate Tensile Strength
XPS	X-Ray Photoelectron Spectroscopy
XRD	X-Ray Diffraction
YS	Yield Strength
YPE	Yield Point Elongation
1D	One Dimensional
2D	Two Dimensional
3D	Three Dimensional
1G	First Generation
2G	Second Generation
3G	Third Generation

List of Symbols

a_i	Activity of species i

A_O	Original sample cross-sectional area
A_f	Cross-sectional area of the fracture surface
at%	Atomic percent
D_i	Diffusivity of species *i*
D_i'	Pre-exponential term to calculate diffusivity of species *i*
g^*	Critical volume fraction of insoluble oxide resulting in blocked inward diffusion of oxygen
$\Delta G°$	Standard Gibbs free energy change
L_f	Load prior to fracture
M_S	Martensite start temperature
M_S^σ	Deformation-induced martensite start temperature
$N_{B,crit}^{(O)}$	Critical mole fraction of alloying element *B* for the transition from internal to external oxidation
$N_O^{(S)}$	Mole fraction of adsorbed oxygen at the surface
n	Stoichiometric ratio between oxygen and metal atoms in oxide BO_n
pH_2	Partial pressure of hydrogen
pH_2O	Partial pressure of water
pO_2	Partial pressure of oxygen
Q_i	Activation energy for diffusion of species *i*
R	Universal Gas Constant

T_{atm}	Process atmosphere temperature
T_{dp}	Dew point temperature
V	Molar volume of the alloy
V_{BO_n}	Molar volume of oxide BO_n
vol%	Volume percent
wt%	Weight percent
α	Ferrite
α'	Martensite
β_A^S	Degree of grain boundary or surface segregation of solute atom A in solvent atom B
γ	Austenite
γ_{ret}	Retained austenite
γ_{sl}	Interfacial tension between solid and liquid phases
γ_{sv}	Interfacial tension between solid and vapor phases
γ_{lv}	Interfacial tension between liquid and vapor phases
ε	True strain
ε_f	True strain at fracture
θ	Contact angle
σ	True stress
σ_f	True stress at fracture
Ω	Mixing enthalpy of A and B for calculating β_A^S

Declaration of Academic Achievement

This dissertation was prepared for partial fulfilment of the *Doctor of Philosophy* degree requirements at McMaster University. The research for the dissertation was conducted from September 2017 to February 2022. The author studied the mechanical property development, selective oxidation, and reactive wetting of a prototype medium-Mn third generation advanced high strength steel during continuous galvanizing line compatible heat treatments.

The author performed the experiments, analysed the results, and prepared all manuscripts under the supervision of Professor Joseph R. McDermid. Additionally, Dr. Xiang Wang, the second author of the published peer-review journal paper (reproduced in Chapter 3), performed transmission electron microscopy (TEM) analysis for that journal paper. The major results of this research have been published in one peer-review journal publication, one submitted manuscript to a peer-review journal that is under review at the time this thesis was submitted, and one draft manuscript for submission to a peer-review journal, as listed below. It should be noted that *Elsevier Ltd.*, the publisher of record for paper 1 in *Materials Science and Engineering A,* permits authors to reuse their published articles in their theses/dissertations.

1. K.M.H. Bhadhon, X. Wang, J.R. McDermid, Effects of CGL-Compatible Thermal Processing, Starting Microstructure, and Sn Micro-alloying on the Mechanical Properties of a Medium-Mn Third Generation Advanced High Strength Steel, Mater. Sci. Eng. A. 833 (2022) 142563. doi: https://doi.org/10.1016/j.msea.2021.142563.
2. K.M.H. Bhadhon, J.R. McDermid, Selective Oxidation of a Medium-Mn Third Generation Advanced High Strength Steel during Austenitizing and Intercritical Annealing, J. Electrochem. Soc., Under Review (2022).
3. K.M.H. Bhadhon, J.R. McDermid, On Continuous Hot-Dip Galvanizing of a Prototype Medium-Mn Third Generation Advanced High Strength Steel, Draft Manuscript.

1 Introduction

1.1 Overall Context

The research and development of advanced high strength steels (AHSSs) started during the 1970s to meet the weight reduction and fuel efficiency demands of the automotive market [1]. The high strength and ductility balance of AHSSs allows the design of thinner cross-sections for automotive body parts, which results in higher fuel efficiency and reduced greenhouse gas emissions without compromising passenger safety. Although aluminum and magnesium alloys have replaced some steel components in modern automotive designs, issues regarding cost and formability for aluminum alloys and the relatively poor mechanical properties and poor corrosion performance for magnesium alloys have limited their application [2]. As a result, first generation AHSSs (1G AHSSs) are being extensively used in designing the vehicle body-in-white (BIW), as shown in Figure 1.1.

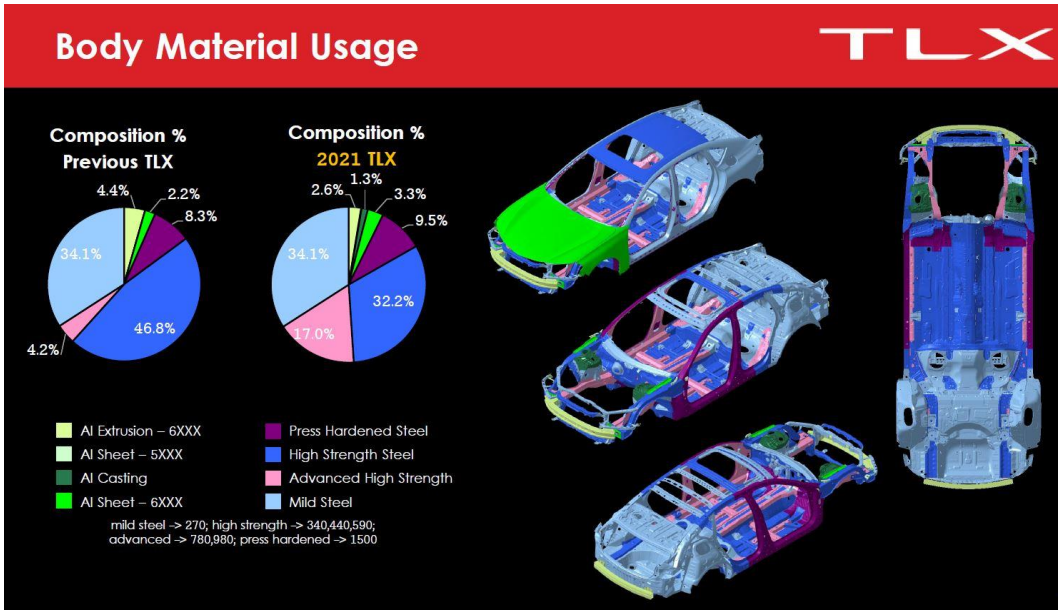

Figure 1.1: Schematic of different materials used in the construction of different generations of the Acura TLX body-in-white [3].

The constant drive to improve the mechanical properties of AHSSs has resulted in the development of three generations of AHSSs over the years. Dual phase (DP) steels, transformation induced plasticity (TRIP) steels, martensitic (MART) steels, and press-hardened steels (PHS), shown in Figure 1.2, are some of the widely used first generation advanced high strength steels (1G AHSSs) in modern automotive designs. These steels have a typical ultimate tensile strength × total elongation (UTS × TE) product of ≤ 20,000 MPa% [4,5]. In particular, low alloy TRIP-assisted steels –which typically contain approximately 2 wt% Mn with varying levels of Si and Al– show an exceptional combination of strength and ductility owing to the deformation-induced transformation of metastable retained austenite to martensite [6,7]. In comparison, the second generation advanced high strength steels (2G AHSSs) have superior combinations of strength and ductility (UTS × TE ≥ 60,000 MPa%) owing to their austenitic microstructure combined with both twinning and transformation induced plasticity effects [8]. Twinning induced plasticity (TWIP) steels are amongst the most widely researched 2G AHSSs. These steels generally have 22–30 wt% Mn along with significant C contents (0.4–0.6 wt%) and relatively high concentrations of Al, Si, and other alloying elements [9,10]. However, due to the high alloying content, these steels are relatively expensive and are difficult to galvanize due to the formation of external oxides of the major alloying elements, i.e., Mn and Si [10].

Hence, current research is focused on developing third generation advanced high strength steels (3G AHSS) which would have superior mechanical properties compared to the 1G AHSSs with less alloying elements and lower alloying costs compared to the 2G AHSSs. Target mechanical properties for the 3G AHSSs were outlined by Matlock and Speer [5], where 24,000 ≤ UTS × TE ≤ 40,000 MPa% was targeted. Additionally, specific UTS and TE targets were proposed by the U.S. Department of Energy (i.e., 1200 MPa UTS × 30% TE and 1500 MPa UTS

× 25% TE) and the AutoSteel Partnership (i.e., 1500 MPa UTS × 20% TE) [11,12]. Figure 1.2 shows the different generations of advanced high strength steels with their respective mechanical property ranges.

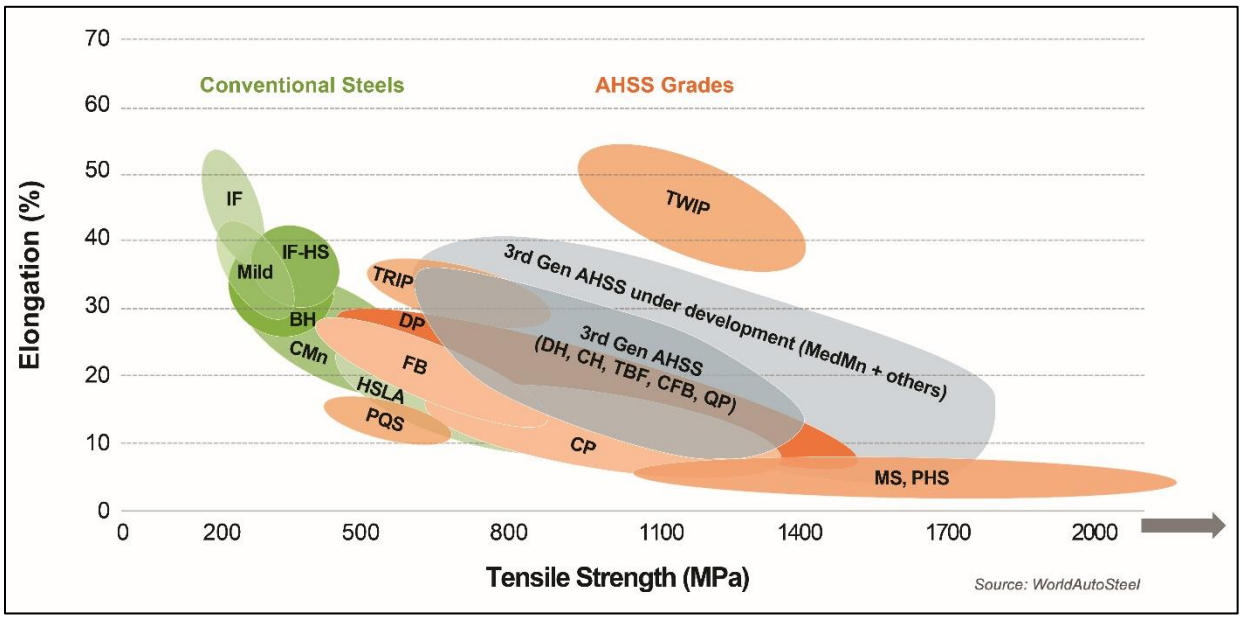

Figure 1.2: The global formability diagram (2021) comparing strength and elongation of different generation of AHSS [13].

Medium-Mn (med-Mn) steels are promising candidates for meeting 3G AHSS target mechanical properties. These steels usually contain 5–10 wt% Mn along with significant concentrations of alloying elements such as C, Si, Al, Cr, and microalloying elements such as Ti, Nb, V, etc. Recent research [14-19] has shown that med-Mn steels can meet 3G AHSS target mechanical properties through optimal thermal processing and starting microstructures. The unique strength and ductility combination is obtained due to plasticity enhancing mechanisms operating during deformation that maintain a high work hardening rate. However, the thermal processing times used in those studies were quite long, often in the order of hours, which far exceeds the typical heating and soaking times used in the continuous galvanizing line (CGL), i.e.,

3-5 minutes depending on the line speed [20]. This adds complexity to the integration of the annealing process to the subsequent galvanizing step, which is essential for the corrosion protection of thinner gauge AHSSs. Therefore, the annealing parameters should conform to these time limits in order to maintain the desired productivity of the CGL, while targeting the desired microstructures and mechanical property balance.

Furthermore, selective oxidation of the alloying elements during the pre-galvanizing heat treatment can significantly affect the galvanizibility of AHSSs. In particular, commonly used alloying elements, such as Mn, Si, Al, and Cr, are known to selectively oxidize in the dew point controlled process atmosphere used in CGL and, depending on the oxide chemistry, morphology, and distribution, these external oxides can lead to poor reactive wetting during continuous galvanizing [21-34]. Hence, it is important to determine the effect of process atmosphere oxygen partial pressure (pO_2) of the annealing furnace on the selective oxidation and reactive wetting of med-Mn 3G AHSSs. Micro-alloying of surface active elements, such as Sn, Sb, and Bi, to modify the oxide morphology and use of a high process atmosphere pO_2 during the pre-galvanizing heat treatment to suppress external oxidation have been successful in improving galvanized coating quality in med-Mn steels [33,35]. However, the effects of annealing parameters and micro-alloying of Sn on the mechanical properties of these steel substrates were not determined.

1.2 Research Objectives

Recent research has shown that the intercritical annealing parameters, starting microstructure, steel chemistry, and the annealing process atmosphere pO_2 can significantly influence the mechanical properties, selective oxidation, and reactive wetting of med-Mn steels [14-19,32-35]. While a certain number of intercritical annealing treatments designed for med-Mn steels have been successful in obtaining 3G AHSS target mechanical properties, they were incompatible with CGL

processing parameters [14-16,18,19]. Furthermore, there are only few studies on the mechanical properties, selective oxidation, and reactive wetting of med-Mn steels with CGL-compatible processing parameters.

Hence, the main objective of this Ph.D. research is to determine the effects of intercritical annealing parameters, starting microstructure, and surface active element (Sn) micro-addition on the mechanical properties, selective oxidation, and reactive wetting of a prototype 0.2C-6Mn-1.5Si-0.5Al-0.5Cr-xSn (wt%) (x = 0 and 0.05 wt%) med-Mn steel in order to develop a CGL-compatible thermal processing route that will result in 3G AHSS target mechanical properties and high-quality galvanized coatings via enhanced reactive wetting. In that regard, the research objectives of this Ph.D. can be divided into:

1) Determining the effects of intercritical annealing parameters, starting microstructure, and surface active element (Sn) micro-alloying on the microstructural evolution and mechanical properties of the prototype med-Mn steels within the context of developing CGL-compatible heat treatment parameters that would result in 3G AHSS target mechanical properties.
2) Determining the effect of process atmosphere pO_2 on the selective oxidation of the prototype med-Mn steel during the most promising starting microstructure/thermal processing route from the mechanical property development investigation.
3) Determining the effect of process atmosphere pO_2 on the reactive wetting of the prototype med-Mn steel during galvanizing in a conventional GI bath containing 0.2 wt% dissolved Al.

1.3 Thesis Layout

This sandwich-style thesis comprises the following chapters:

- Chapter 1 – Introduction: This chapter presents a brief background on different generation of AHSSs along with the motivation that is driving the development of med-Mn 3G AHSS. Furthermore, the research objectives of this Ph.D. are also outlined in this chapter.
- Chapter 2 – Literature Review: This chapter comprises a concise and critical review of the literature on the microstructural and mechanical property evolution of the med-Mn steels along with works related to the selective oxidation and reactive wetting of AHSSs.
- Chapter 3 – Microstructure and Mechanical Properties Development: This chapter is a reproduction of the manuscript entitled "Effects of CGL-Compatible Thermal Processing, Starting Microstructure, and Sn Micro-alloying on the Mechanical Properties of a Medium-Mn Third Generation Advanced High Strength Steel", published in *Materials Science and Engineering A* [36]. The effects of starting microstructure, annealing parameters, and micro-alloying of Sn on the microstructural evolution and mechanical properties were determined in this manuscript within the context of developing a CGL-compatible thermal processing route which would result in 3G AHSS target mechanical properties in the prototype med-Mn steels.
- Chapter 4 – Selective Oxidation: This chapter is a reproduction of the submitted manuscript entitled "Selective Oxidation of a Medium-Mn Third Generation Advanced High Strength Steel during Austenitizing and Intercritical Annealing". The effect of process atmosphere pO_2 on the selective oxidation during austenitizing and promising intercritical annealing heat treatment that resulted in 3G AHSS target mechanical properties was determined in this study. The goal was to produce a pre-immersion surface on the prototype med-Mn steel which can be successfully galvanized after intercritical annealing in a conventional CGL. The manuscript has been submitted to *Journal of The Electrochemical Society*.

- Chapter 5 – Reactive Wetting: This chapter is a reproduction of the draft manuscript entitled "On Continuous Hot-Dip Galvanizing of a Prototype Medium-Mn Third Generation Advanced High Strength Steel". The effect of intercritical annealing process atmosphere pO_2 on reactive wetting of the martensitic prototype med-Mn steel was determined in this investigation. The objective was to determine a process atmosphere for the promising intercritical annealing heat treatment which can produce high quality galvanized coating in a conventional GI bath. This manuscript will be submitted to *Surface and Coatings Technology*.
- Chapter 6 – Global Discussion: This chapter links the major findings of the mechanical property development, selective oxidation, and reactive wetting investigation and discusses their relationship within the context of developing a CGL-compatible thermal processing route that can produce 3G AHSS target mechanical properties and high quality galvanized coating.
- Chapter 7 – Conclusions and Future Directions: The primary findings of this research will be summarised in this chapter. Moreover, this chapter also recommends some future research projects regarding the physical metallurgy, selective oxidation, and reactive wetting of med-Mn 3G AHSSs.

1.4 References

[1] D.K. Matlock, J.G. Speer, E.D. Moor, P.J. Gibbs, Recent developments in advanced high strength sheet steels for automotive applications: an overview, JESTECH 15(1) (2012) 1–12.

[2] E. Ghassemieh, Materials in automotive application, state of the art and prospects, new trends and developments in automotive industry, Prof. Marcello Chiaberge (Ed.) (2011), ISBN: 978-953-307-999-8, InTech.

[3] J. Lucas, 2021 Acura TLX, Great Designs in Steel 2021, Novi, Michigan, USA (2021).

[4] E. De Moor, P.J. Gibbs, J.G. Speer, D.K. Matlock, Strategies for third-generation advanced high strength steel development, AIST Trans. 7(3) (2010) 133–144.

[5] D.K. Matlock, J.G. Speer, Design Considerations for the Next Generation of Advanced High Strength Sheet Steels, in: H.C. Lee (Ed.), Proc. 3rd Int. Conf. Struct. Steels, Seoul, Korea (2006) 774–781.

[6] J.R. McDermid, H.S. Zurob, Y. Bian, Stability of retained austenite in high-Al, low-Si TRIP-assisted steels processed via continuous galvanizing heat treatments, Metall. Mater. Trans. A. 42A (2011) 3627–3637.

[7] P.J. Jacques, Transformation-induced plasticity for high strength formable steels, Curr. Opin. Solid State Mater. Sci. 8 (2004) 259–265.

[8] O. Bouaziz, S. Allain, C. Scott, Effect of grain and twin boundaries on the hardening mechanisms of twinning-induced plasticity steels, Scr. Mater. 58 (2008) 484–487.

[9] M. Ghasri-Khouzani, J.R. McDermid, Effect of carbon content on the mechanical properties and microstructural evolution of Fe–22Mn–C steels, Mater. Sci. Eng. A. 621 (2015) 118–127.

[10] M. Blumenau, M. Norden, F. Friedel, K. Peters, Use of pre-oxidation to improve reactive wetting of high manganese alloyed steel during hot-dip galvanizing, Surf. Coat. Technol. 206 (2011) 559–567.

[11] C. Schutte, DOE Focuses on Developing Materials to Improve Vehicle Efficiency, SAE Technical Paper 2015-01-0405 (2015), https://doi.org/10.4271/2015-01-0405.

[12] L.G. Hector Jr., The Next Generation of Advanced High Strength Steels – Computation, Product Design and Performance, 12th Annual Great Designs in Steel Seminar, Livonia, MI (2013).

[13] The Global Formability Diagram (2021), Courtesy of WorldAutoSteel.

[14] P.J. Gibbs, E. De Moor, M.J. Merwin, B. Clausen, J.G. Speer, D.K. Matlock, Austenite stability effects on tensile behavior of manganese-enriched-austenite transformation induced plasticity steel, Metall. Mater. Trans. A. 42A (2011) 3691–3702.

[15] W.Q. Cao, C. Wang, J. Shi, M.Q. Wang, W.J. Hui, H. Dong, Microstructure and mechanical properties of Fe–0.2C–5Mn steel processed by ART-annealing, Mater. Sci. Eng. A. 528 (2011) 6661–6666.

[16] S. Lee, B.C. De Cooman, On the selection of the optimal intercritical annealing temperature for medium Mn TRIP steel, Metall. Mater. Trans. A. 44A (2013) 5018–5024.

[17] S. Lee, K. Lee, B.C. De Cooman, Observation of the TWIP + TRIP plasticity-enhancement mechanism in Al-added 6 wt pct medium Mn steel, Metall. Mater. Trans. A. 46A (2015) 2356–2363.

[18] A. Arlazarov, M. Gouné, O. Bouaziz, A. Hazotte, G. Petitgand, P. Barges, Evolution of microstructure and mechanical properties of medium Mn steels during double annealing, Mater. Sci. Eng. A. 542 (2012) 31–39.

[19] J. Shi, X. Sun, M. Wang, W. Hui, H. Dong, W. Cao, Enhanced work-hardening behavior and mechanical properties in ultrafine-grained steels with large-fractioned metastable austenite, Scr. Mater. 63 (2010) 815–818.

[20] J.R. McDermid, A. Chakraborty, Identification of steel chemistries and galvanizing process design, ZCO-53-1 Project Report, (2012), Hamilton, Canada.

[21] R. Sagl, A. Jarosik, D. Stifter, G. Angeli, The role of surface oxides on annealed high strength steels in hot-dip galvanizing, Corros. Sci. 70 (2013) 268–275.

[22] J. Mahieu, S. Claessens, B.C. De Cooman, Galvanizability of high-strength steels for automotive applications, Metall. Mater. Trans. A. 32A (2001) 2905–2908.

[23] J. Maki, J. Mahieu, B.C. De Cooman, S. Claessens, Galvanisability of silicon free CMnAl TRIP steels, Mater. Sci. Technol. 19 (2003) 125–131.

[24] M. Blumenau, M. Norden, F. Friedel, K. Peters, Use of pre-oxidation to improve reactive wetting of high manganese alloyed steel during hot-dip galvanizing, Surf. Coat. Technol. 206 (2011) 559–567.

[25] E.M. Bellhouse, J.R. McDermid, Selective Oxidation and Reactive Wetting of 1.0 Pct Si-0.5 Pct Al and 1.5 Pct Si TRIP-Assisted Steels, Metall. Mater. Trans. A. 41A (2010) 1539–1553.

[26] E.M. Bellhouse, J.R. McDermid, Selective Oxidation and Reactive Wetting during Galvanizing of a CMnAl TRIP-Assisted Steel, Metall. Mater. Trans. A. 42 (2011) 2753–2768.

[27] R. Khondker, A. Mertens, J.R. McDermid, Development of the surface structure of TRIP steels prior to hot-dip galvanizing, Mater. Sci. Eng. A. 463 (2007) 157–165.

[28] G.S. Mousavi, J.R. McDermid, Selective oxidation of a C-2Mn-1.3 Si (Wt Pct) advanced high-strength steel during continuous galvanizing heat treatments, Metall. Mater. Trans. A. 49 (2018) 5546–5560.

[29] G.S. Mousavi, J.R. McDermid, Effect of dew point on the reactive wetting of a C-2Mn-1.3Si (wt%) advanced high strength steel during continuous galvanizing, Surf. Coat. Technol. 351 (2018) 11–20.

[30] L. Cho, G.S. Jung, B.C. De Cooman, On the Transition of Internal to External Selective Oxidation on CMnSi TRIP Steel, Metall. Mater. Trans. A. 45A (2014) 5158–5172.

[31] L. Cho, M.S. Kim, Y.H. Kim, B.C. De Cooman, Influence of Minor Alloying Elements on Selective Oxidation and Reactive Wetting of CMnSi TRIP Steel during Hot Dip Galvanizing, Metall. Mater. Trans. A. 45A (2014) 4484–4498.

[32] M. Pourmajidian, J.R. McDermid, Selective Oxidation of a 0.1C-6Mn-2Si Third Generation Advanced High-Strength Steel During Dew-Point Controlled Annealing, Metall. Mater. Trans. A. 49 (2018) 1795–1808.

[33] M. Pourmajidian, J.R. McDermid, Effect of Annealing Temperature on the Selective Oxidation and Reactive Wetting of a 0.1C-6Mn-2Si Advanced High Strength Steel During Continuous Galvanizing Heat Treatments, ISIJ Int. 58(9) (2018) 1635–1643.

[34] M. Pourmajidian, J.R. McDermid, On the reactive wetting of a medium-Mn advanced high-strength steel during continuous galvanizing, Surf. Coat. Technol. 357 (2019) 418–426.

[35] M. Pourmajidian, B. Langelier, J.R. McDermid, Effect of Process Atmosphere Dew Point and Tin Addition on Oxide Morphology and Growth for a Medium-Mn Third Generation Advanced Steel During Intercritical Annealing, Metall. Mater. Trans. A. 49 (2018) 5561–5573.

[36] K.M.H. Bhadhon, X. Wang, J.R. McDermid, Effects of CGL-compatible thermal processing, starting microstructure, and Sn micro-alloying on the mechanical properties of a medium-Mn third generation advanced high strength steel, Mater, Sci. Eng. A. 833 (2022) 142563.

2 Literature Review

This chapter summarises the research that has been conducted on medium-Mn steels, both to develop the desired microstructure and mechanical properties as well as successfully galvanize them via enhanced reactive wetting. However, there is limited literature on these emerging 3G AHSSs as their physical metallurgy, selective oxidation, and reactive wetting are currently being developed through extensive research. Hence, the relevant fundamental knowledge developed for 1G and 2G AHSSs are also discussed in this chapter. This would help elucidating design strategies, strengthening mechanisms, and microstructure-mechanical property relationship of medium-Mn steels. Furthermore, challenges encountered in continuous hot-dip galvanizing owing to selective oxidation and strategies to improve reactive wetting of these new generation of steels are also discussed in this chapter.

2.1 Approaches in Developing 3G AHSS

Different approaches have been considered in developing steels to meet the 3G AHSS target mechanical properties. These approaches are mainly based on enhancing the mechanical properties of 1G AHSSs via grain refinement, designing new thermal processing cycles, and alloy design. In that regard, various research was conducted on enhanced DP steel [1,2], modified low alloy TRIP-assisted steels [3,4], ultrafine bainitic steels [5–8], flash processing [9], delta ferrite TRIP steels [10,11], and quench and partitioning (Q&P) steels [12,13]. However, the thermal processing parameters used in most of these approaches were not compatible with CGL processing windows [14]. Moreover, although some of these steels were able to meet 3G AHSS target mechanical properties, the high C content in those steels would deteriorate weldability, which is a common assembly process in the automotive industry.

De Moor et al. [15] used a simplified composite model to calculate the mechanical properties of martensite/ferrite and martensite/austenite microstructures with varying phase fractions. The authors used the ultimate tensile strength (UTS) and uniform elongation (UE) of ferrite, austenite, and martensite as the input parameters for the model. The model predicted that the property band of the martensite/austenite mixtures corresponded with the 3G AHSS property regime. However, in these cases, the austenite was considered to be fully stable, i.e., austenite would not transform to martensite during deformation. In the next step of modeling, the authors considered four different austenite stabilities and found that austenite stability – as exemplified by varying deformation induced austenite to martensite transformation kinetics – had a significant effect on the predicted mechanical properties, as shown in Figure 2.1. Based on these model calculations, it was shown that 3G AHSS target mechanical properties could be achieved with approximately 40% volume fraction of austenite which would have a moderate deformation induced austenite to martensite transformation kinetics, similar to curve B in Figure 2.1a).

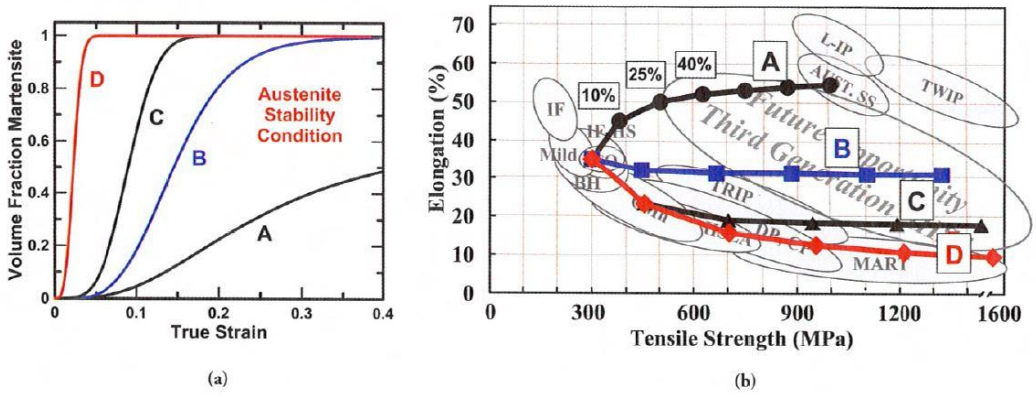

Figure 2.1: Effect of austenite stability on predicted mechanical property combinations: a) four different austenite stabilities and b) corresponding predicted mechanical property combinations where each data point corresponds to an initial austenite volume fraction [15].

Research has also been carried out on medium-Mn steels as promising candidates for 3G AHSSs by utilising plasticity enhancing mechanisms during deformation. Optimal selection of intercritical annealing parameters and starting microstructure can lead to high volume fraction of chemically and mechanically stable retained austenite with an appropriate (~20 mJ/m^2) stacking fault energy (SFE) which can result in gradual transformation of the retained austenite to martensite and formation of mechanical twins in the retained austenite during deformation [16,17]. As a result, high work hardening rates can be sustained during deformation by successful activation of both TWinning Induced Plasticity (TWIP) and TRansformation Induced Plasticity (TRIP) effects, both of which can contribute to delaying the onset of necking. Recent research [18,19] on medium-Mn steels with martensitic starting microstructures has shown that it is possible to achieve mechanical properties in the range of 3G AHSS with CGL-compatible thermal processing cycles. However, the effect of the proposed thermal processing on the selective oxidation and reactive wetting of the steels was not explored. On the other hand, successful reactive wetting has been previously reported by Alibeigi et al. [20] and Pourmajidian and McDermid [21,22] for medium-Mn steels annealed under CGL-compatible conditions. Nevertheless, the microstructure evolution and mechanical properties were not determined in those studies.

2.2 Medium-Mn 3G AHSS

2.2.1 Alloy Design

Medium-Mn steels were first studied by Grange and Hribal [23] and later by Miller [24]. Their studies revealed that a martensitic microstructure can be obtained for a 0.1C-6Mn (wt%) steel, even when cooled at a very slow rate (1.7 °C/min) after annealing. Moreover, a tempering heat treatment (640 °C for 1 hour) resulted in an excellent strength/ductility balance (1144 MPa UTS × 30.5% TE) owing to the presence of significant volume fractions of chemically stable retained

austenite in the microstructure and the resultant TRIP effect upon deformation [24]. The chemically stable retained austenite in these microstructures arose from the initial martensite via an Austenite Reversion Transformation (ART) reaction, where the intercritical austenite was chemically stabilised due to C and Mn partitioning during the tempering treatment and was retained in the final microstructure. Recent research [17,18] on medium-Mn steels has utilised this approach to achieve large volume fractions of chemically stable retained austenite which has a stacking fault energy compatible with the activation of deformation twins (i.e., the TWIP effect) and later gradually transform to martensite to activate the TRIP effect during deformation. A high work hardening rate was sustained during deformation resulting in a high strength and ductility combination in these steels. Hence, the alloy design of medium-Mn steels has tended to focus on retaining and stabilising large volume fractions of chemically stable retained austenite after intercritical annealing which can later undergo the $\gamma \rightarrow \alpha'$ transformation through mechanical activation.

Medium-Mn steels usually contain 5–10 wt% Mn along with 0.1–0.4 wt% C, 0.5–3 wt% Al, 0.5–2 wt% Si, 0–0.5 wt% Cr, and 0–0.22 wt% Mo. While C and Mn stabilise austenite [25], high alloy C contents can deteriorate weldability, which is used extensively for joining the automotive body parts [14]. Si is added as a solid solution strengthener [26] which also delays carbide precipitation [25], thereby assisting in the formation of retained austenite. However, the formation of film-type SiO_2 at the steel surface during annealing in standard N_2–(5-20)H_2-xH_2O (vol%) process atmospheres is detrimental to reactive wetting and coating adhesion [27]. To avoid this issue, Si can be partially replaced by Al in these steel grades as Al also delays carbide precipitation [27,28,29,30]. However, in terms of solid solution strengthening, Al is less potent compared to Si [26]. Cr and Mo are added to improve hardenability [31,32]. Furthermore, based on the beneficial

effect of surface active element (Sn, Sb, and Bi) micro-alloying on the selective oxidation and reactive wetting of low-alloy Si-containing TRIP steels [33-36], Sn micro-alloying has been investigated recently for a model medium-Mn steel [22,37].

It should be noted that the above alloying elements have a significant effect on the critical transformation temperatures (Ac_1, Ac_3, and M_s) of these steels [38], as shown in Figure 2.2. Higher Ac_1 and Ac_3 temperatures can lead to faster austenite reversion kinetics during intercritical annealing and make the annealing parameters compatible with CGL (i.e., shorter holding time at intercritical annealing temperature) [14]. Hence, alloying elements such as Si, Al, and P play a vital role in this regard along with other above-mentioned benefits. Furthermore, M_s temperature should be lowered in order to improve the stability of the retained austenite. In that regard, alloying elements such as C, Mn, Si, Cr, Mo, Ni, and Nb are considered during alloy design as they can lower the M_s temperature of medium-Mn steels (Figure 2.2) [38].

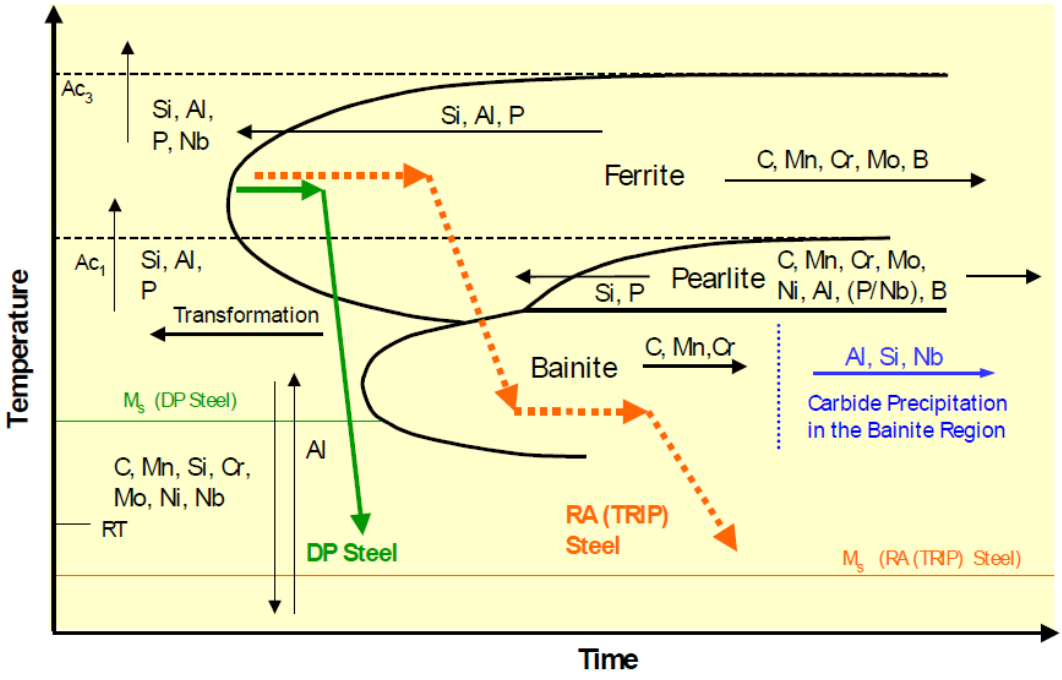

Figure 2.2: Influence of alloying elements on the TTT curve of ferrous alloys [38].

2.2.2 Strengthening Mechanisms

The high strength/ductility balance of medium-Mn steels is usually achieved through several strengthening mechanisms operating during deformation. Depending on the steel chemistry and annealing parameters, solid solution strengthening, grain refinement, precipitation strengthening, and plasticity enhancing mechanisms have been reported for medium-Mn steels [15,17-19,39]. In particular, plasticity enhancing mechanisms (TWIP and TRIP) are important in terms of achieving the target mechanical properties for 3G AHSS. Successful activation of the TRIP/TWIP effect can maintain high work hardening rates during deformation and delay the onset of necking, resulting in a superior combination of high strength and ductility. The following section will discuss these two plasticity enhancing mechanisms in detail.

2.2.2.1 Transformation Induced Plasticity (TRIP) Effect

Retained austenite with suitable chemical and mechanical stability will transform gradually to martensite during plastic deformation and result in a sustained high work hardening rate in 3G AHSSs via two mechanisms [40]: the first being the formation of harder martensite phase from the retained austenite which provides dynamic composite strengthening; the second is the formation of dislocations in the surrounding phases due to the volume expansion associated with martensite formation. These dislocations, known as "geometrically necessary dislocations" (GNDs), along with dislocations in the adjacent ferrite grains, improve the local strength of the ferrite grains. The presence of these newly formed GNDs was confirmed by the transmission electron microscopy work on a low alloy TRIP steel by Jacques [40].

Spenger et al. [41] summarised the dislocation density evolution in TRIP-assisted steels and compared it with mild and DP steels. As shown in Figure 2.3, the incremental work hardening rate ($\frac{\Delta\sigma}{\Delta\varepsilon}$) in conventional mild steels is equal to the change in stored dislocation density ($\Delta\rho_s$). In

other words, the work hardening rate would increase incrementally when the stored dislocation density increased. However, GNDs are produced alongside the stored dislocations in DP steels with hard martensite islands in a soft ferritic matrix. As a result, the $\frac{\Delta\sigma}{\Delta\varepsilon}$ in DP steels would be significantly higher compared to the conventional mild steels owing to the contribution from both the stored dislocation and the GND densities ($\Delta\rho_s + \Delta\rho_{Geom}$). In addition to these, more mobile dislocations are generated in TRIP-assisted steels during the deformation-induced austenite to martensite transformation due to the associated volume change, as shown in Figure 2.3. Consequently, high work hardening rates are maintained due to the high mobile dislocation densities (i.e., $\Delta\rho_s + \Delta\rho_{Geom} + \Delta\rho_{Mart}$) in TRIP-assisted steels. However, the work hardening rate also depends on the transformation kinetics of the retained austenite i.e., its stability during deformation. A gradual transformation of the retained austenite is required in order to sustain a high work hardening rate [42,43]. In that regard, the morphology of the retained austenite plays a key role as it has been concluded by several researchers [18,19,43,44] that lath or film-type retained austenite is more chemically and mechanically stable compared to blocky retained austenite owing to higher C content and increased hydrostatic pressure from the surrounding phases.

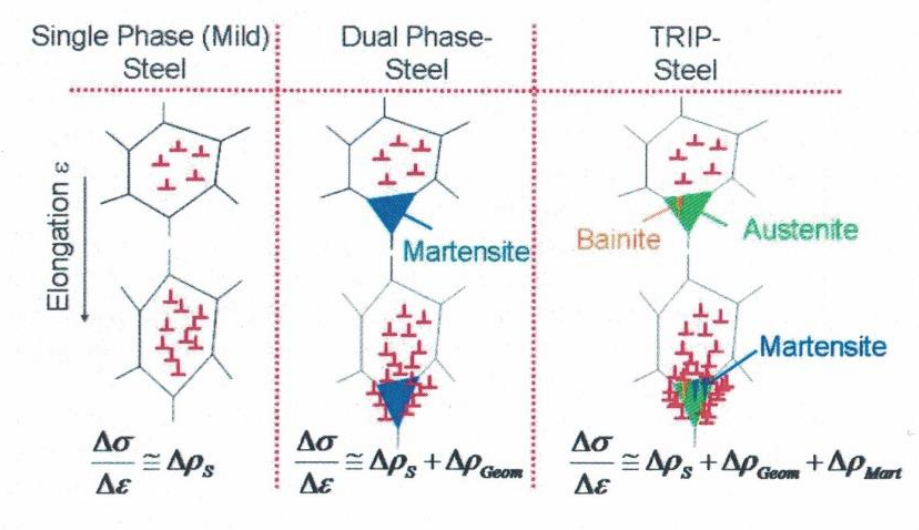

Figure 2.3: Schematic of the evolution of dislocation density in mild, DP, and TRIP steels where $\frac{\Delta\sigma}{\Delta\varepsilon}$ = incremental work hardening rate, $\Delta\rho_s$ = change in stored dislocation density, $\Delta\rho_{Geom}$ = change in geometrically necessary dislocation density, and $\Delta\rho_{Mart}$ = change in dislocation density from deformation-induced austenite to martensite transformation [41].

The transformation of austenite to martensite can be stress or strain activated depending on the temperature range where the transformation is occurring. Olson and Cohen [45] classified these transformation temperature ranges in a ferrous system, which can be explained by analysing the schematic diagram shown in Figure 2.4. Spontaneous transformation of austenite to martensite is observed when the temperature is below M_s, due to thermal activation. In the case where the temperature is between the M_s and M_s^σ (the stress-induced martensite start temperature), the austenite to martensite transformation takes place when the sum of the mechanical energy due to an externally applied stress and the chemical driving force exceeds a critical activation energy. This type of transformation is known to be "stress-activated" martensite transformation. On the other hand, within the M_s^σ and M_d (deformation induced martensite temperature) range, "strain-activated" martensite transformation occurs due to the applied stress exceeding the yield stress of

the parent austenite. And finally, above M_d, austenite deforms plastically instead of transforming to martensite.

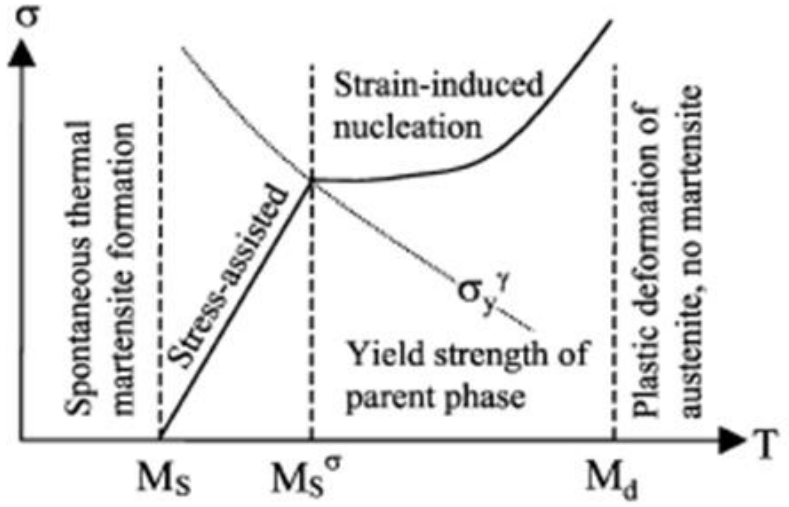

Figure 2.4: Schematic showing the temperature range for stress and strain activated austenite to martensite transformation [45].

However, McDermid et al. [43] showed that it is possible to model retained austenite to martensite transformation kinetics of conventional low alloyed TRIP-assisted steels as a function of the normalized flow stress. The authors compared their model with the strain-based model of Olsen and Cohen [45] and suggested that retained austenite to martensite transformation is stress-induced for temperatures above M_s^σ (the temperature at which the stress required to initiate martensite transformation equals the yield strength of parent austenite). The stress-induced model is less complex compared to the strain-induced models. Moreover, stress is a state function, i.e., it is path independent.

Bhadhon et al. [18] reported a high strength and ductility combination for a prototype medium-Mn steel (0.2C-6Mn-1.5Si-0.5Al-0.5Cr wt%) with a martensitic starting microstructure that were intercritically annealed with CGL-compatible parameters. The authors reported that plasticity enhancing mechanisms (both TRIP and TWIP) were operative during deformation, which assisted

in sustaining high work hardening rates and delayed the onset of necking. Interrupted tensile test results confirmed the gradual transformation of retained austenite to martensite and successful activation of the TRIP effect during deformation. It was concluded that sufficient TRIP and TWIP effect along with other strengthening mechanisms can result in superior strength/ductility combinations (UTS × TE ≥ 30,000 MPa%) which met 3G property targets for their prototype medium-Mn steel. Gradual transformation of chemically stable retained austenite to martensite also resulted in attaining 3G AHSS target mechanical properties in a medium-Mn steel (0.15C-6Mn-1.9Al-1Si wt%) investigated by Pallisco and McDermid [19]. The authors reported that high work hardening rate was sustained during deformation owing to successful activation of plasticity enhancing mechanism (marked by arrows in Figure 2.5b)) and gradual transformation of retained austenite to martensite (Figure 2.5c)).

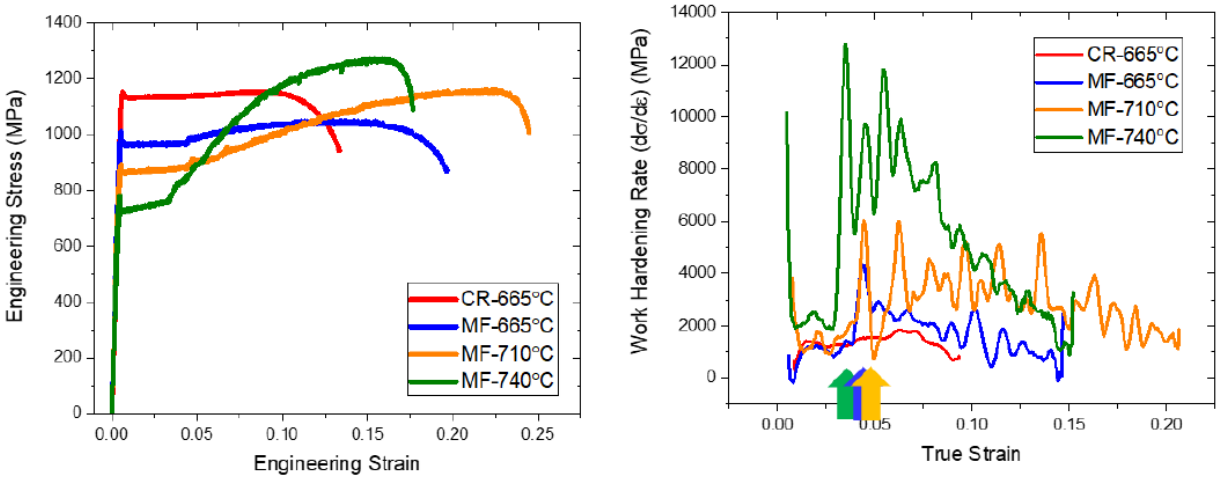

a) b)

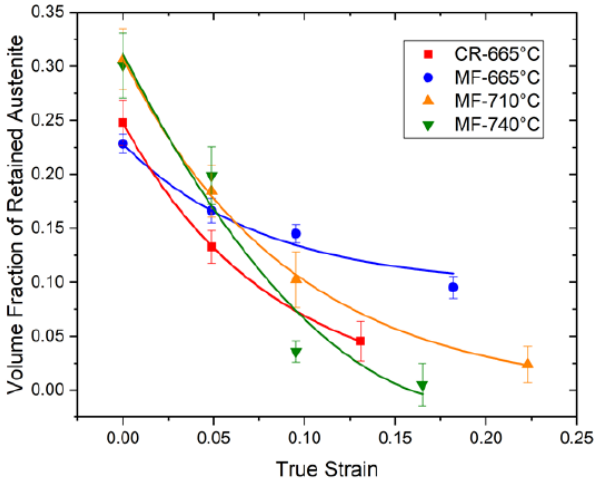

c)

Figure 2.5: a) Engineering stress *vs.* strain curves, b) corresponding work hardening rate *vs.* true strain, and c) retained austenite transformation kinetics of a medium-Mn steel (0.15C-6Mn-1.9Al-1Si wt%) with cold-rolled (CR) and martensite-ferrite (MF) starting microstructures intercritically annealed at different temperatures [19].

2.2.2.2 Twinning Induced Plasticity (TWIP) Effect

The second plasticity enhancing mechanism that can be operative alongside the TRIP effect in medium-Mn steels is the TWIP effect. When the room temperature stacking fault energy (SFE) of retained austenite was within a certain range ~15–45 mJ/m^2, the TWIP effect can be observed [46]. Pallisco and McDermid [19] reported the presence of deformation nano-twins alongside the TRIP effect by analysing the interrupted tensile test samples of a medium-Mn steel (0.15C-6Mn-1.9Al-1Si wt%) using TEM, as shown in Figure 2.6. The SAD patterns clearly revealed the presence of twin spots in the retained austenite, marked with the red arrows in the inset SAD patterns (Figure 2.6).

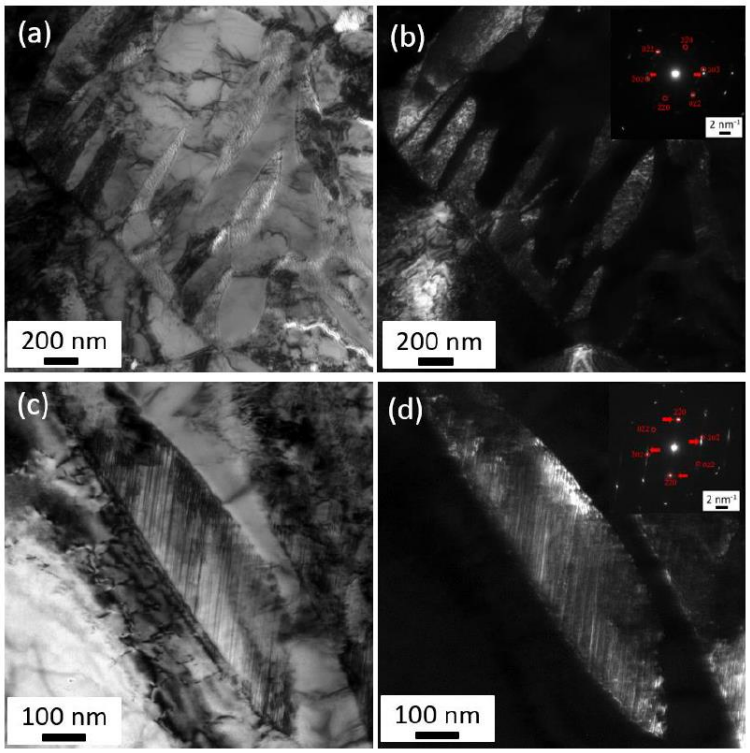

Figure 2.6: TEM images from the MF-710 °C condition after 0.05 true strain deformation: (a) BF; (b) DF corresponding to $< 02\bar{2} >\gamma$ with inset SAD pattern corresponding to $[111]\gamma$. For fracture: (c) BF; (d) DF corresponding to $< 002 >\gamma$ with inset SAD pattern corresponding to $[110]\gamma$ [19].

Strengthening due to the TWIP effect is related to the so-called “dynamic Hall-Petch effect” created by the deformation twins. Deformation or mechanical twins form due to the passage of Shockley partials along every successive {111} plane. These twin boundaries divide the grains into smaller parts, decreasing the dislocation mean free path, as shown in Figure 2.7 [47]. As a result, the strength of material increases in a similar manner as the grain size refinement.

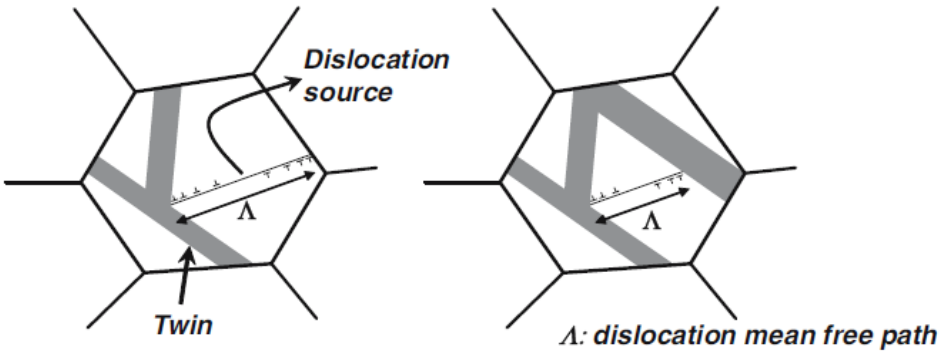

Figure 2.7: Schematic showing how twins decrease dislocation mean free path [47].

Lee and De Cooman [39] investigated a Fe-0.3C-10Mn-3Al-2Si (wt%) steel and found that 800 °C intercritical annealing temperature resulted in an excellent mechanical property balance (i.e., 1200 MPa UTS and 60% TE). High work hardening rates were sustained during deformation owing to both TWIP and TRIP effects working in succession. In another study by Lee et al. [17] on medium-Mn steels with 6Mn-1.5Si-3Al (wt%) and varying C content (0.15–0.3 wt%), high UTS × TE product (~65,000 MPa%) was obtained when both TRIP and TWIP effects were activated during deformation. The optimal intercritical annealing temperature was selected by considering the SFE of ultrafine grained austenite (~15–20 mJ/m^2). The work hardening rate analysis revealed two maxima suggesting more than one plasticity enhancing mechanisms at work, i.e., TWIP and TRIP effects. The first maximum was from the TWIP effect which was followed by the TRIP effect where α′ martensite nucleated at the twin-twin intersections.

Alloying elements significantly affect the retained austenite SFE and in turn the likelihood of the TWIP effect. Research on high Mn TWIP steels [48,49] has shown that the SFE increases significantly with increasing Mn content in high Mn (>20 wt%) austenitic TWIP steels. C also increases the SFE in austenitic TWIP steels. Dumay et al. [50] calculated the room temperature SFE of a Fe-22Mn-0.6C steel with other alloying additions, shown in Figure 2.8.

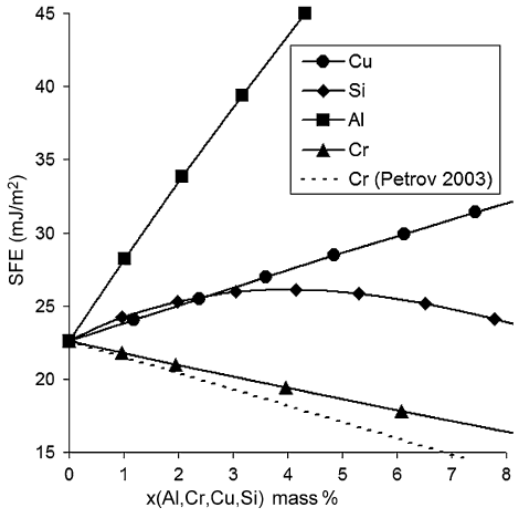

Figure 2.8: Influence of different alloying elements on the SFE of a Fe-22Mn-0.6C steel [50].

However, these SFE calculations are all based on high Mn (>20 wt%) TWIP steels. The effectiveness of these model equations needs to be validated for medium-Mn steels. A validated model would be able to accurately predict the SFE range for which the benefit of both TWIP and TRIP effect can be achieved in medium-Mn 3G AHSSs. One of the promising models is the one proposed by Saeed-Akbari et al. [51].

2.2.3 Effect of Intercritical Annealing Parameters on Mechanical Properties

Intercritical annealing temperature and holding time have significant effect on retained austenite stability and properties in medium-Mn steels. Proper selection of the intercritical annealing conditions can result in high volume fractions of chemically stable retained austenite. Lee and De Cooman [52] proposed a model for selecting intercritical annealing temperatures for a Fe-0.3C-6Mn (wt%) medium-Mn TRIP steel which would result in high volume fractions of chemically stable retained austenite. The model was based on the C and Mn content of the intercritical austenite as these elements are known to chemically stabilise intercritical austenite and prevent the transformation to martensite upon final cooling to room temperature [40]. The authors

verified the model with experimental data collected for various intercritical annealing temperatures (600–680 °C) and annealing times (0.5–2 hours). It was found that intercritical annealing at 650 °C resulted in highest volume fractions (~0.60) of retained austenite and for temperatures above this, the amount of retained austenite significantly decreased. The authors suggested that the intercritical austenite was no longer chemically stable and transformed to athermal martensite during final cooling to room temperature.

Gibbs et al. [53] investigated a Fe-7.1Mn-0.1C (wt%) steel that was annealed at different intercritical annealing temperatures (575–675 °C) for 168 hours (Figure 2.9). The authors reported a high UTS (1200 MPa) along with low total elongation (10%) for the steel samples annealed at 650 °C for 168 hours, as shown in Figure 2.9. It was concluded that yielding for this heat treatment was controlled by the stress-induced austenite to martensite transformation. Moreover, this transformation was rapid and resulted in a high initial work hardening rate. However, as most of the retained austenite transformed at low strain, before the plastic deformation of ferrite could begin, low work hardening rates at high strains were observed. This resulted in a high UTS with low total elongation. On the other hand, the samples annealed at 600 °C for 168 hours showed a significant increase in total elongation (~41.5%) with a significant decrease in UTS (~870 MPa) compared to samples annealed at 650 °C. In the 600 °C annealed samples, yielding was first controlled by localized plastic deformation of the strain aged recrystallized ferrite which resulted in significant yield point elongation. After that, both the austenite and ferrite deformed plastically and homogeneously. Moreover, a gradual transformation of austenite to martensite was also observed in these samples which resulted in sustaining a high work hardening rate at high strains. As a result, high strength, as well as high total elongation, was observed in the medium-Mn TRIP

steel annealed at 600 °C for 168 hours. Consequently, a high UTS × TE product (> 36,000 MPa%) was achieved – meeting 3G AHSS target mechanical properties – albeit at quite low strengths.

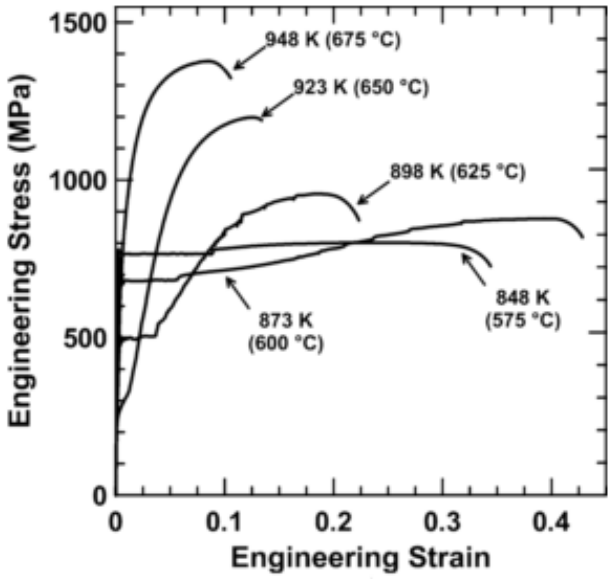

Figure 2.9: Engineering stress *vs*. strain curves for a Fe-7.1Mn-0.1C (wt%) steel annealed for 168 hours [53].

Suh et al. [54] studied three different grades of medium-Mn steels (Fe-0.11C-4.5Mn-0.45Si-2.2Al, Fe-0.075C-5.1Mn-0.49Si-2.1Al, and Fe-0.055C-5.6Mn-0.49Si-2.2Al wt%) which were annealed at 700–780 °C for 120 s. High Al contents (>2 wt%) were used to reduce the holding time at intercritical annealing temperature due to the fact that Al increases the Ac_1 and Ac_3 temperatures (i.e., expands the intercritical annealing temperature range), resulting in rapid solute diffusion compared to lower intercritical annealing temperatures. It was reported that the retained austenite volume fraction increased with increasing annealing temperature up to 760 °C, followed by a significant decrease in retained austenite volume fraction at 780 °C. It was suggested that the intercritical austenite transformed to martensite due to low chemical stability (dilution of C and Mn content owing to higher volume fraction of intercritical austenite formation at 780 °C) as well as mechanical stability (i.e., the larger grain size reduced the hydrostatic pressure from the

surrounding phases). However, the highest total elongation (~30%) was observed for samples annealed at 720 °C. This suggested that the chemical stability of the retained austenite – which can be quantified with the retained austenite C and Mn content – also played a vital role, along with retained austenite volume fraction, in determining the mechanical properties of these annealed medium-Mn steels. Moreover, significant yield point elongation was observed for all samples. It was suggested that high Al content resulted in significant volume fractions of recrystallized coarse ferrite which deformed plastically before the austenite to martensite transformation, resulting in significant yield point elongation.

2.2.4 Effect of Starting Microstructure on Mechanical Properties

The starting microstructure of medium-Mn steels has a significant effect on the volume fraction of retained austenite and the resultant mechanical properties. Luo and Dong [44] examined the martensitic starting microstructure and as-received cold-rolled microstructure of two different steel grades (0.11C-4.87Mn and 0.17C-4.72Mn wt%) which were heat treated over a range of intercritical annealing temperatures (635–710 °C) for 10 min followed by oil quenching. There was a distinct difference in the retained austenite volume fractions and the corresponding tensile properties of the steels as a function of starting microstructure. For each annealing temperature, the martensitic starting microstructure yielded higher volume fractions of retained austenite compared to the cold-rolled starting microstructure samples. The morphology of the retained austenite also depended on the starting microstructure. Lamellar retained austenite was observed for the martensitic starting microstructure whereas equiaxed retained austenite was found in the case of the cold-rolled starting microstructure samples. It was concluded that the lamellar shaped retained austenite was more stable owing to higher levels of C and Mn, resultant of short diffusion distance in lamellar austenite grains compared to their equiaxed or blocky counterparts.

Furthermore, the hydrostatic pressure from the surrounding martensitic matrix provided mechanical stability to the lamellar retained austenite. Overall, this resulted in higher amounts of chemically and mechanically stable retained austenite in the martensitic starting microstructure samples. Pallisco and McDermid [19] also reported similar lamellar retained austenite with higher chemical and mechanical stability in an intercritically annealed 0.15C-6Mn-1.9Al-1Si (wt%) medium-Mn steel with martensite-ferrite starting microstructure.

Arlazarov et al. [55] proposed austenite reversion transformation (ART) mechanisms for both cold-rolled (martensite + bainite) and martensitic starting microstructures by analysing a 0.1C-4.6Mn (wt%) alloy. A schematic diagram showing these mechanisms is presented in Figure 2.10. The authors reported that partial recrystallisation occurred followed by carbide precipitation at high angle grain boundaries, such as prior austenite grain boundaries, which acted as the austenite nucleation sites during intercritical annealing of the as-received tempered martensitic starting microstructure. This resulted in globular microstructure containing homogeneously distributed austenite (Figure 2.10b)). Contrastingly, carbides precipitated at low- and high-angle lath and grain boundaries for martensitic starting microstructure, resulting in a mixed microstructure with lamellar and globular constituents. However, as reported by Lai et al. [56], the growth of the intercritical austenite which nucleated on the intergranular cementite particles depends on the Mn content of cementite particle. Lai et al. [56] studied austenite growth kinetics for a Fe-0.1C-3.5Mn (wt%) steel with spheroidized microstructure. The authors reported that the austenite growth mode and kinetics changed from C partitioning controlled to Mn partitioning controlled when the cementite Mn content was high (~ 25 wt%). This resulted in significantly slower growth of the austenite. Mehrabi et al. [57] also reported similar slower austenite growth rate controlled by Mn partitioning in ferrite (martensite) during intercritical annealing (665 °C for

60 s) of a Fe-0.15C-5.56Mn-1.1Si-1.89Al (wt%) medium-Mn steel with cold-rolled starting microstructure comprising cementite with 10-15 wt% Mn. By comparison, significantly faster austenite growth was reported for martensite-ferrite starting microstructure which was controlled by C partitioning in ferrite (martensite).

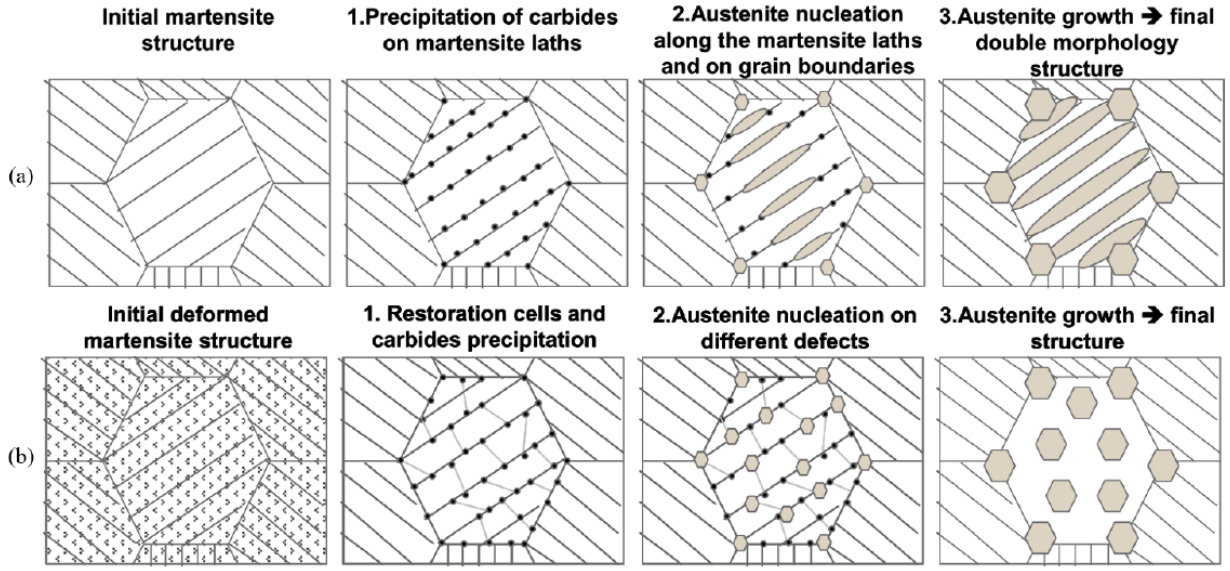

Figure 2.10: Schematic diagrams of the austenite reversion processes for initial microstructures comprising (a) fresh martensite and (b) cold-rolled martensite + bainite, as proposed by Arlazarov et al. [55].

Furthermore, Nakada et al. [58] reported that the martensite to austenite transformation is more rapid than that from tempered martensite, due to the fact that the martensite is highly strained and supersaturated with carbon as it is the product of a diffusionless transformation of intercritical austenite during quenching. Hence, less energy is required for the nucleation and growth of intercritical austenite at the martensite lath boundaries during intercritical annealing, resulting in the rapid reversion of the martensite to austenite. Additionally, Wei et al. [59] reported that thin films of retained austenite might have started to grow without a nucleation barrier at martensite lath boundaries owing to the pre-existing interlath retained austenite in the martensitic starting

microstructure. The authors studied the growth of austenite during intercritical annealing in an as-quenched martensitic Fe-0.1C-3Mn-1.5Si (wt%) alloy, with a higher Mn content (~3 wt% Mn) compared to conventional low-alloy TRIP-assisted steels. It was concluded that growth of austenite grains consisted of three distinct stages based on DICTRA simulation results. Initially, the growth was controlled by rapid C diffusion in ferrite followed by C diffusion in austenite. The intermediate slow growth stage, on the other hand, was controlled by diffusion of the substitutional elements (Mn and Si) in ferrite. The final stage was characterised by very slow growth which was controlled by the diffusion of the substitutional elements (Mn and Si) in austenite. Moreover, excess volume fractions of austenite were observed compared to the calculated equilibrium amounts which was linked to the slow diffusion of the substitutional elements in austenite relative to the grain boundary migration. This suggested that the retained austenite growth was controlled by solute drag which depended on the diffusivity ratio of the alloying elements in the parent and growing phases, intercritical annealing temperature, and steel composition.

Shi et al. [60] studied the mechanical properties and work hardening behaviour of four medium-Mn steels (0.2C-5Mn, 0.26C-5Mn, 0.4C-5Mn, and 0.2C-7Mn wt%) with martensitic starting microstructures which were batch annealed at 650 °C for 6 hours. High volume fractions (>30%) of retained austenite formed by ART was observed in all four annealed steel grades. Moreover, tensile tests revealed an excellent strength/ ductility balance (UTS × TE > 38,000 MPa%) in the annealed samples, with the highest UTS × TE product (44,000 MPa%) being reported for the annealed 0.2C-7Mn (wt%) medium-Mn steel. It was concluded that the presence of high volume fractions of mechanically stable ultrafine lath-shaped retained austenite was the main reason behind the excellent mechanical properties. The mechanically stable retained austenite transformed gradually to martensite during deformation, resulting in a sustained high

work hardening rate at high tensile strains. As a result, the onset of necking was delayed during deformation, which resulted in the high strength and ductility combination.

2.3 Continuous Hot-Dip Galvanizing

Steel substrates require some form of corrosion protection before they can be exposed to the external environment, particularly the high Cl^- environments typically experienced in automotive applications as a result of the use of de-icing salts. Continuous hot-dip galvanizing is amongst the most cost-effective methods used by the industry for this purpose. Hence, the continuous galvanizing/galvannealing line (CGL) has become an integral part of the automotive steel manufacturing industry. Figure 2.11 shows a schematic of a typical radiant tube heated CGL [61]. The steel stays a relatively short time, usually 3–5 minutes depending on the line speed, in the radiant tube heating and soaking sections of the CGL. In order to maintain the desired productivity of the CGL, the annealing parameters have to be within these time limits while producing the desired microstructures and mechanical property balance. However, many recent studies [16,39,44,52,53,55,60,62] on medium-Mn steels utilised heat treatment cycles that have been confined to long soaking times, often in terms of hours which are only suitable for batch annealing. As a result, although those heat treatments yielded 3G AHSS target strength/ductility balances, the long holding times render them incompatible with CGL processing windows. Therefore, it is highly desirable to develop alloy chemistries and thermal processing schemes compatible with the CGL thermal processing capabilities.

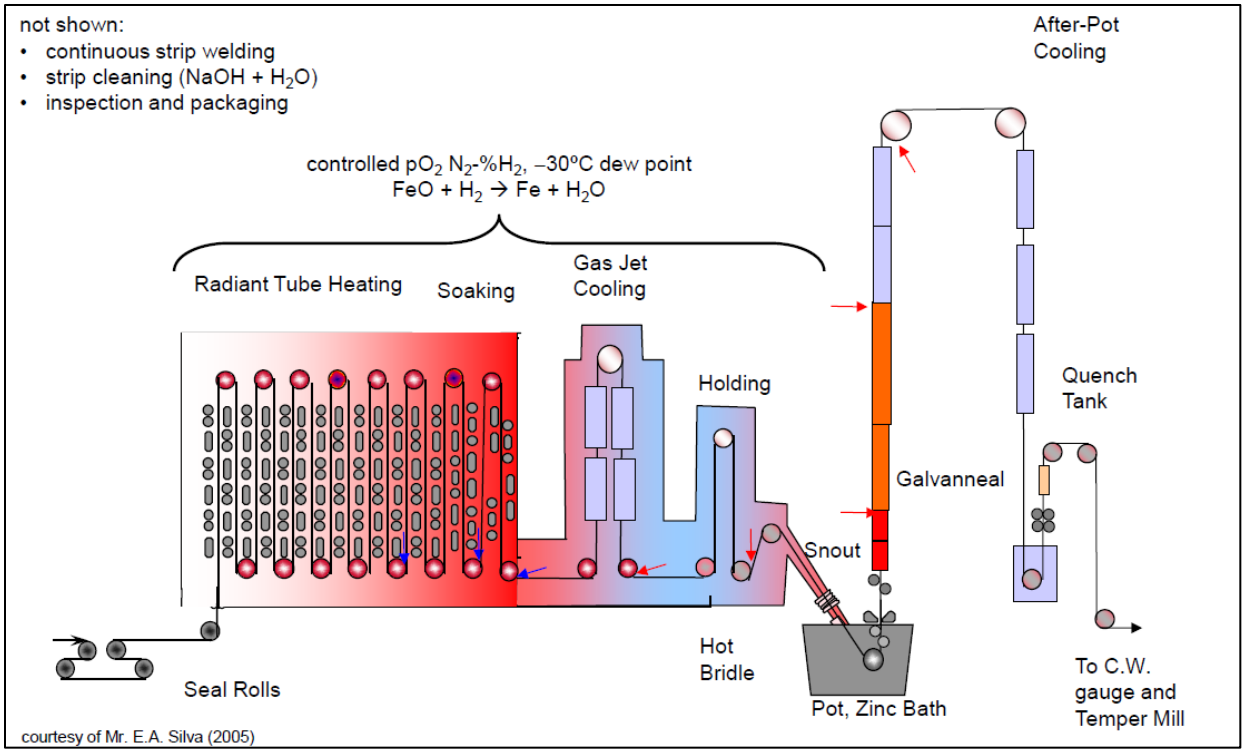

Figure 2.11: Schematic of a continuous galvanizing/galvannealing line [61].

2.4 Selective Oxidation

2.4.1 Gas-Metal Reactions in the CGL Furnace

The process atmosphere in the CGL furnace is typically composed of a N_2–(5-20 vol%) H_2 gas mixture which has a controlled dew point or water vapour partial pressure (pH_2O). The dew point controls the process atmosphere oxygen partial pressure as a function of temperature. Oxygen partial pressure (pO_2), in this case, is a measure of the relative oxidation power of the atmosphere that is linked to the water vapour partial pressure (pH_2O) in a process atmosphere with fixed H_2 content and temperature (T). At the dew point temperature (T_{dp}), liquid water and water vapour are at equilibrium (Equation (2.1)):

$$H_2O_{(l)} \Leftrightarrow H_2O_{(g)} \qquad (2.1)$$

The standard Gibbs free energy change for this reaction ($\Delta G^{\circ}_{2.1}$) can be calculated from Equation (2.2), which relates the dew point temperature and the water vapour partial pressure:

$$\Delta G^{\circ}_{2.1} = -RT_{dp} \ln \frac{pH_2O_{(g)}}{a_{H_2O(l)}} = -RT_{dp} \ln pH_2O_{(g)} \tag{2.2}$$

where R is the universal gas constant and $a_{H_2O(l)} = 1$ as liquid water is assumed to be a pure condensed species.

The process atmosphere pO_2 can be related to process atmosphere pH_2O and pH_2 at the process temperature (T_{atm}) according to Equations (2.3) – (2.5):

$$H_{2(g)} + \frac{1}{2} O_{2(g)} \Leftrightarrow H_2O_{(g)} \tag{2.3}$$

$$\Delta G^{0}_{2.3} = -RT_{atm} \ln \frac{pH_2O_{(g)}}{pH_{2(g)} pO_{2(g)}^{\frac{1}{2}}} \tag{2.4}$$

$$\Rightarrow pO_{2(g)} = \left(\frac{pH_2O_{(g)}}{pH_{2(g)} \exp\left[\frac{-\Delta G^{\circ}_{2.3}}{RT_{atm}} \right]} \right)^2 \tag{2.5}$$

The thermodynamic stability of a metal oxide at T_{atm} can be determined as a function of process atmosphere pO_2 from Equations (2.6) and (2.7):

$$\frac{x}{y} M_{(s)} + \frac{1}{2} O_{2(g)} \Leftrightarrow \frac{1}{y} M_x O_{y(s)} \tag{2.6}$$

$$\Delta G^{\circ}_{2.6} = -RT_{atm} \ln \left(\frac{a_{M_xO_{y(s)}}^{\frac{1}{y}}}{a_{M_{(s)}}^{\frac{x}{y}} pO_{2(g)}^{\frac{1}{2}}} \right) = -RT_{atm} \ln \left(\frac{1}{a_{M_{(s)}}^{\frac{x}{y}} pO_{2(g)}^{\frac{1}{2}}} \right) \tag{2.7}$$

where M and M_xO_y are a general metallic element and its oxide, respectively, where the oxide is assumed to be pure condensed species (i.e., $a_{M_xO_y}=1$).

From Equation (2.7), the equilibrium process atmosphere oxygen partial pressure above which the metal oxide is stable can be calculated as:

$$pO_{2(g)} = \left(\frac{1}{a_{M_{(s)}}^{\frac{x}{y}} \exp\left[\frac{-\Delta G_{2.6}^{\circ}}{RT_{atm}} \right]} \right)^2 \tag{2.8}$$

Using the data from Morris [63], Jung et al. [64], and Jung [65], the thermodynamic stability of different metal oxides as a function of annealing temperature and process atmosphere pO_2 in a N_2–5 vol% H_2 atmosphere was determined. The results are shown in Figure 2.12. It can be seen that, although the atmosphere with various dew point temperatures (–30, –10, and +5 °C) are reductive to Fe oxides, they will oxidize Al, Si, Mn, and Cr, all of which are common alloying elements in medium-Mn 3G AHSSs. However, it should be noted that the pO_2 has no physical meaning in terms of the number of O_2 molecules in the atmosphere, but it does have a physical meaning in that it delineates the stability of the equilibrium between a metal and its oxide as shown in Figure 2.12.

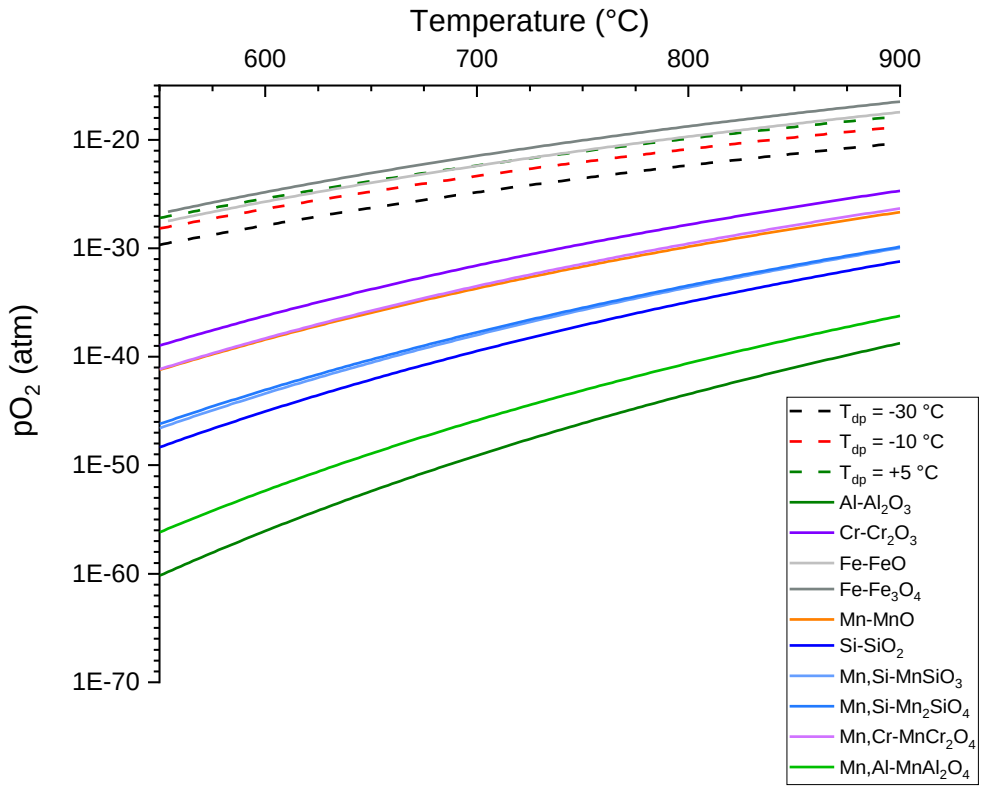

Figure 2.12: Thermodynamic stability of oxides with respect to annealing temperature and oxygen partial pressure in a N_2–5 vol% H_2 atmosphere.

2.4.2 Internal and External Oxidation – Wagner Model

Wagner [66] was amongst the first researchers to propose a model for predicting the transition from internal to external oxidation. The author developed the following equation for a single crystal metallic binary A-B alloy in which A is the noble matrix and B is the ignoble solute that is selectively oxidized to an insoluble stoichiometric oxide BO_n:

$$N_{B,crit}^{(O)} = \left[\frac{\pi g * V N_O^{(S)} D_O}{2 n V_{BO_n} D_B} \right]^{\frac{1}{2}} \tag{2.9}$$

where

$N_{B,crit}^{(O)}$ = the critical mole fraction of solute B for the transition from internal to external oxidation

$g*$ = the critical volume fraction of oxide that blocks the inward diffusion of oxygen (determined to be 0.3 by Rapp [67] for an Ag-In alloy and later determined experimentally to be 0.2 by Lashgari et al. [68] for austenitic Fe-Mn alloys forming MnO)

n = the stoichiometric ratio between the oxygen and metal atoms in the oxide BO_n

V = the molar volume of the alloy,

V_{BO_n} = the molar volume of the oxide BO_n

$N_O^{(S)}$ = the mole fraction of adsorbed oxygen at the surface

D_O = the diffusion coefficient of oxygen and,

D_B = the diffusion coefficient of solute B.

Internal oxidation occurs when $N_B < N_{B,crit}^{(O)}$ whereas external oxidation would occur for $N_B > N_{B,crit}^{(O)}$. Birks et al. [69] derived and explained the Wagner equation in English as the original paper was in German. The authors stated that the selective oxidation mode is determined based on the balance between the inward diffusion of adsorbed oxygen from the atmosphere/surface into the substrate and the outward diffusion of the ignoble solute B from the substrate. Internal oxidation is the result of a greater inward oxygen flux compared to the outward flux of the solute B. On the other hand, external oxidation will occur if the outward diffusion of the solute B to the surface is greater than the inward diffusion flux of oxygen.

Several modifications to the Wagner model have been proposed by various authors in order to overcome the limitations of the assumptions used in the classic model. Mataigne et al. [70]

proposed one modification by considering the fact that oxygen and alloying elements can diffuse much faster through short circuit diffusion paths, such as grain boundaries and dislocation pipes, than in the lattice. In their model, grain boundary oxidation was accounted for by halving the activation energy of bulk diffusion due to accelerated diffusion at the grain boundaries:

$$N_{B,crit,GB}^{O} = \left[\frac{\pi g^{*} V N_{O}^{S} D_{O}' \exp\left(\frac{-Q_{O}}{2RT}\right)}{2nV_{BO_n} D_{B}' \exp\left(\frac{-Q_{B}}{2RT}\right)} \right]^{\frac{1}{2}} \tag{2.10}$$

Mataigne et al. [70] further modified the model by considering an additive effect when multiple alloying elements are present and proposed the following criterion for the internal-external oxidation transition for a multi-solute alloy with N ignoble components:

$$\sum_{N} N_{B}^{O} \left(n D_{B} V_{BO_n} \right)^{\frac{1}{2}} \geq \left(\frac{0.3\pi V N_{O}^{S} D_{O}}{2} \right)^{\frac{1}{2}} \tag{2.11}$$

Therefore, external oxidation will occur if the combined flux of the ignoble solutes to the surface, given by the terms in the left-hand side of Equation (2.11), exceeds the inward flux of atomic O into the substrate given in the right-hand side. However, the case of complex oxides such as manganese silicates were not considered in this model.

Another limitation of the Wagner model is that the oxides are assumed to be insoluble in the matrix. However, that is not always the case, especially for the oxidation of AHSSs where MnO has a significant solubility in both ferrite and austenite [71]. In that regard, a modified value of g^{*} = 0.2 was experimentally determined for Mn oxides in high-Mn (1.7, 3.5, and 7.0 wt%) steels at 950 °C by Lashgari et al. [68].

Another modification to the Wagner model was proposed by Shastry et al. [72], who considered the additive effect of solutes proposed by Mataigne et al. [70] and included a rule of

mixture component to account for the presence of two phases (ferrite and austenite) in the substrate microstructure, as is commonly the situation seen in the intercritical annealing of AHSSs.

$$f\left[\sum_B N_B^{(O)}\left[nV_{BO_n}D_B\right]^{\frac{1}{2}}\right]_\gamma + (1-f)\left[\sum_B N_B^{(O)}\left[nV_{BO_n}D_B\right]^{\frac{1}{2}}\right]_\alpha \geq \left[\frac{0.3\pi V}{2}\right]^{\frac{1}{2}}\left\{\left[f\left[N_O^{(S)}D_O\right]^{\frac{1}{2}}\right]_\gamma + \left[(1-f)\left[N_O^{(S)}D_O\right]^{\frac{1}{2}}\right]_\alpha\right\} \quad (2.12)$$

where f is the volume fraction of austenite. According to this model, external oxidation will occur if the above inequality is satisfied.

Huin et al. [71] extended the Wagner model by using a one-dimensional finite difference model. The authors accounted for the non-zero solubility product of the oxides along with the oxidation of multiple solutes and the formation of complex oxides. However, it was necessary to use known precipitates as the first trial hypothesis in order to minimize the number of iterations needed to evaluate thermodynamic equilibrium. Leblond et al. [73] further extended the Huin et al. model by considering the formation of complex, non-stoichiometric precipitate phases and improved grain boundary conditions.

The shortcoming of Wagner criterion was highlighted by Mousavi and McDermid [74], who investigated the effect of process atmosphere pO_2 on the selective oxidation of a 0.1C-2Mn-1.3Si (wt%) AHSS during annealing. The authors compared experimental observations and Wagner model predictions regarding the selective oxidation mode of Mn and Si. Although the Wagner and the modified Wagner model of Mataigne et al. [70] were able to successfully predict the selective oxidation mode of Mn and Si for –50 °C and +5 °C dew point process atmosphere, the experimental results did not conform with the prediction regarding the mode of oxidation of Si for the –30 °C dew point N_2–5 vol% H_2 process atmosphere.

2.5 The Zn(Al, Fe) Bath and Reactive Wetting

The quality of the galvanized coating in AHSSs depends on the successful wetting of the steel substrate by the liquid Zn and type of reaction product that form at the steel/coating interface during galvanizing. Hence, it is important to discuss the fundamentals of wetting under different thermodynamic conditions. Aksay et al. [75] reported that the degree of wetting of a solid by a liquid phase, in a solid (*s*)-liquid (*l*)-vapor (*v*) system can be defined based on the conditions of thermodynamic equilibrium (i.e., minimisation of the free energy). Under chemical equilibrium condition and neglecting gravitational forces for a small enough liquid drop, the degree of wetting or non-wetting of a solid by liquid can be defined by Young's equation [76], equation (2.13), which shows the relationship between the horizontal components of the interfacial tensions (γ) of each two phases:

$$\gamma_{sv} - \gamma_{sl} = \gamma_{lv} \cos\theta \qquad (2.13)$$

where θ is the equilibrium contact angle, as shown in Figure 2.13.

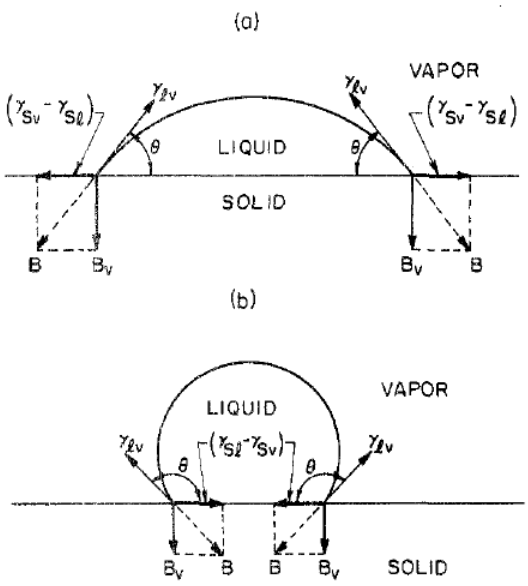

Figure 2.13: Components of forces present in a solid-liquid-vapor system with an (a) acute and (b) obtuse contact angle. B is the balancing force equal and of opposite direction to γ_{lv} [75].

Under chemical equilibrium conditions, the free energy changes in the system are directly related to the changes in the interfacial areas. For these conditions, the wetting of the solid occurs when the contact angle (θ) is acute, i.e., when $\gamma_{sv} > \gamma_{sl}$ or γ_{lv}. Contrastingly, the condition of non-wetting occurs when the contact angle (θ) is obtuse, i.e., when $\gamma_{sv} < \gamma_{sl}$ or γ_{lv}.

Under chemical non-equilibrium conditions, free energy changes depend on both changes in mass and the interfacial areas. Initially, the chemical reaction is confined to the mass transfer through the interface, which reduces the interfacial free energy and in turn, the free energy of the system by $-\Delta G/A$; where ΔG is the change in the free energy and A is the interfacial area. The chemical reaction proceeds into the bulk region by diffusion following its completion at the interface, during which the values of interfacial tension and the specific interfacial free energy increase until a static value is reached, and the reaction is completed. This chemical non-equilibrium condition is encountered during continuous hot-dip galvanizing. The type of chemical

reaction and in turn, the reaction product/intermetallics formed at the steel/coating interface depend on the galvanizing bath composition, temperature, and immersion time.

A galvanizing bath containing pure Zn would result in a coating consisting of several layers of brittle Fe-Zn intermetallics which would deteriorate the coating quality. Hence, small amount of Al is added to the continuous galvanizing bath to temporarily inhibit the formation of the brittle Fe-Zn intermetallics. The continuous galvanizing bath typically contains 0.15–0.25 wt% dissolved Al which is required to form the $Fe_2Al_5Zn_x$ interfacial layer as a product of reactive wetting – often referred to as the "inhibition layer" in the literature – to temporarily "inhibit" or block the formation of brittle Fe-Zn intermetallics at the bath/substrate interface [77]. The formation of Fe-Al intermetallics is thermodynamically and kinetically favoured due to the greater driving force compared to that of Fe-Zn intermetallics [78]. As a result, the formation of brittle Fe-Zn intermetallics is temporarily "inhibited". It should also be noted that the term "dissolved" refers to the Al in solution in the liquid phase and not the Al which participated in forming intermetallic precipitates. Fe is also present in the Zn bath due to Fe dissolution from the steel strip as the strip is not in thermodynamic equilibrium with the bath upon immersion [77].

The Zn-rich corner of the Zn-Al-Fe phase diagram at 460 °C [79] is shown in Figure 2.14. It can be seen that, depending on the bath composition, various intermetallic phases can precipitate due to the limited solubilities of Fe and Al in Zn. With increasing Al content, the equilibrium configuration of the bath changes from L + ζ-$FeZn_{13}$ to L + δ-$FeZn_{10}$ and then to L + η-$Fe_2Al_5Zn_x$. As the continuous galvanizing bath usually contains 0.15–0.25 wt% dissolved Al, the L + η-$Fe_2Al_5Zn_x$ equilibrium configuration is the most relevant one for the CGL. The bath approaches metastable equilibrium – as described by the BCC – Liq equilibrium in Figure 2.15, showing the metastable Fe solubility limit far exceeds the bath equilibrium solubility limit – in the vicinity of

the steel strip upon immersion into the bath due to solid Fe not being in equilibrium with the Zn-Al-Fe bath. As a result, continuous Fe dissolution occurs from the immersed steel strip such that there is local supersaturation of Fe adjacent to the steel strip (Figure 2.15). This is followed by the nucleation and lateral growth of the η-$Fe_2Al_5Zn_x$ or ζ-$FeZn_{13}$ on the steel surface depending on the amount of dissolved aluminium of the zinc bath as the global equilibrium configuration of the zinc bath must be obeyed in the longer term. It should be noted that the formation of ζ-$FeZn_{13}$ is favoured over δ-$FeZn_{10}$ kinetically owing to the well-known epitaxial relationship between ζ-$FeZn_{13}$ and α-Fe [77]. For a 0.2 wt% dissolved Al bath, commonly employed in industrial continuous galvanizing baths, the bath will be supersaturated with respect to $Fe_2Al_5Zn_x$ such that the dissolved Al in the bath is determined from the tie-lines (Figure 2.14) [80].

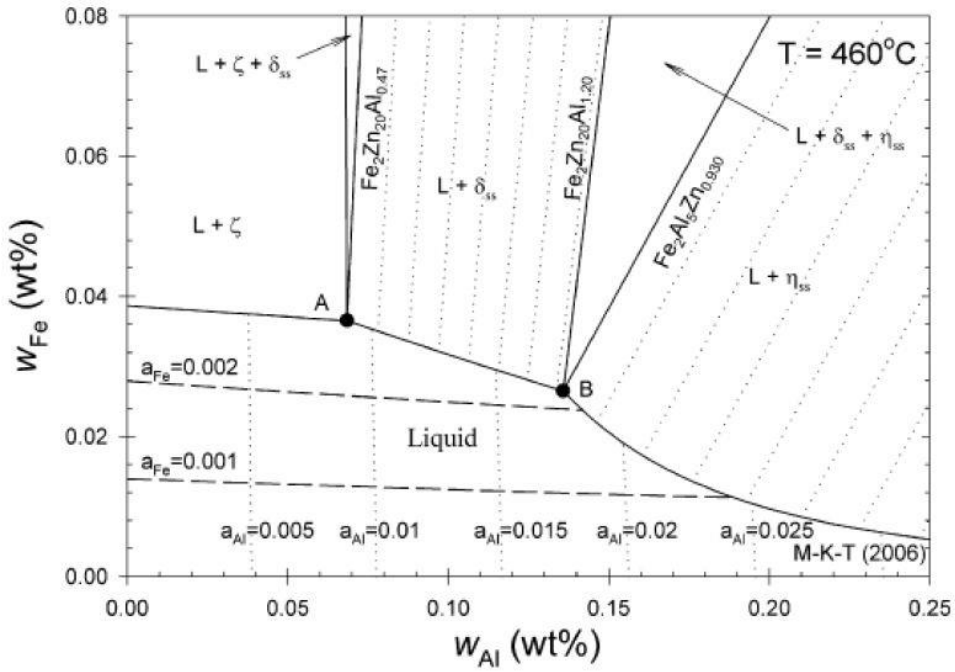

Figure 2.14: Zn rich corner of the Zn-Al-Fe ternary system at 460 °C in Cartesian coordinates; the dotted lines indicate the isoactivity lines of Al and Fe in the liquid phase; L is liquid, ζ is $FeZn_{13}$, δ is $FeZn_{10}$, and η is $Fe_2Al_5Zn_x$ [79].

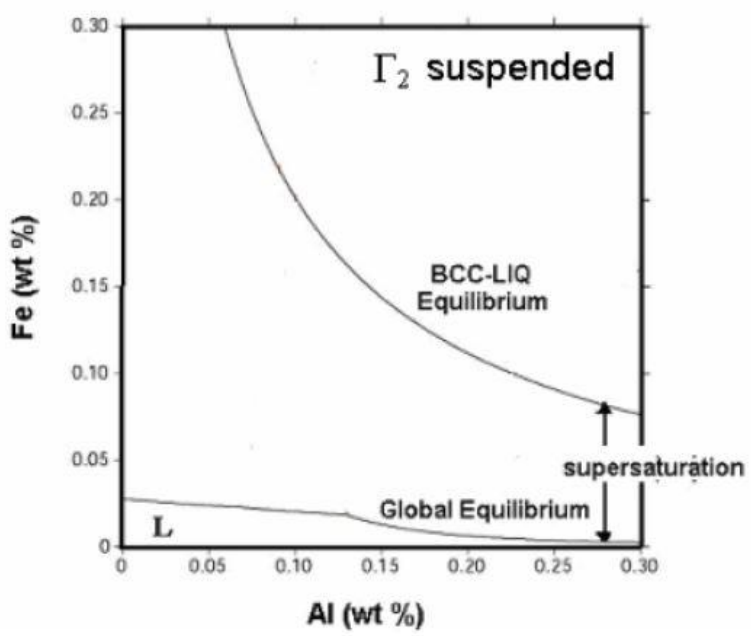

Figure 2.15: Supersaturation of Fe in the Zn(Al, Fe) bath at 450 °C [80].

Tang [81] modelled the inhibition layer formation and reported it to be a two stage process. The first stage is nucleation controlled and associated with a high rate of Al uptake. There is virtually no heterogeneous nucleation barrier (~0.94 eV) for Fe_2Al_5 formation on the steel substrate. The second stage is a diffusion controlled growth stage where the rate controlling step is the long range diffusion of Al in the bath. The steps of inhibition layer formation on an IF steel during galvanizing in a 0.2 wt% Al bath were experimentally investigated by Chen et al. [82] who also reported that the growth of the interfacial layer was diffusion controlled. As mentioned earlier, Fe dissolution occurs from the steel strip when the steel is first immersed in the galvanizing bath, followed by nucleation and growth of metastable $FeAl_3$. A compact layer comprising fine crystals of $FeAl_3$ phase is formed on the steel substrate, as shown in Figure 2.16. This compact layer inhibits further dissolution of Fe from the steel substrate. However, Fe continues to diffuse towards the Zn bath through the intermetallic layer while Zn and Al diffuse towards the steel substrate. As

the reaction proceeds, the metastable $FeAl_3$ begins to transform to $Fe_2Al_5Zn_x$, in order to conform with the local equilibrium (Figure 2.14), per the following reaction,

$$FeAl_3 + 2Al_{(bath)} + Fe_{(substrate)} + xZn_{(bath)} \rightarrow Fe_2Al_5Zn_x \qquad (2.14)$$

This is followed by the growth of an upper, coarser layer of $Fe_2Al_5Zn_x$ precipitating from the supersaturated bath alongside the continued transformation of $FeAl_3$ to $Fe_2Al_5Zn_x$ such that the final morphology of the interfacial layer is comprised of a two layer structure (Figure 2.16). The lower layer is a compact layer of fine and preferentially oriented (i.e., the {200} planes orient parallelly to the substrate surface) $Fe_2Al_5Zn_x$ crystals and the top layer consists of coarse, elongated, and randomly oriented $Fe_2Al_5Zn_x$ crystals, as shown in Figure 2.17 [83]. It should be mentioned that as these reactions happen very rapidly, and the nucleation of the Fe-Al phases has not yet been captured experimentally.

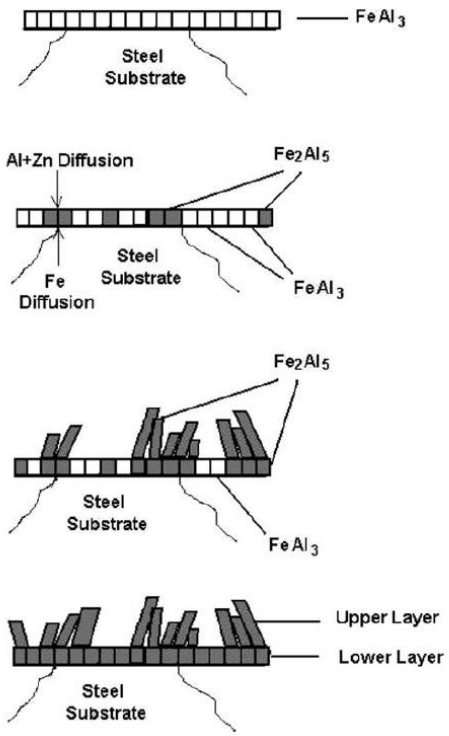

Figure 2.16: Steps in inhibition layer formation on an IF steel galvanized using a 0.2 wt% dissolved Al bath [82].

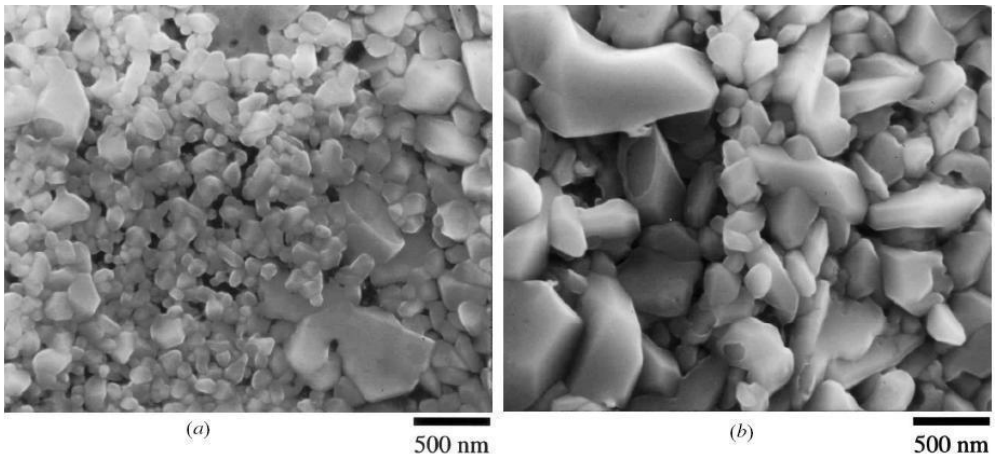

Figure 2.17: Fe-Al interfacial layer morphologies observed at the interface of commercial ultra-low-carbon steel galvanized in a 0.18 wt% Al bath: (a) small equiaxed crystals and (b) coarse elongated crystals [83].

However, the $Fe_2Al_5Zn_X$ inhibition layer is not kinetically stable and will eventually break down if the steel strip is exposed to the liquid bath long enough for Zn diffusion through the inhibition layer [77,83]. $FeZn_{13}$ will nucleate and grow outward from the interface when the interface is saturated with Zn. This usually happens at fast diffusion sites, such as co-incident grain boundaries or triple points. Inhibition breakdown can be problematic as the formation of brittle $FeZn_{13}$ outbursts can be detrimental to coating quality. Chen et al. [82] showed that the dissolved Al content in the galvanizing bath has a significant effect on the inhibition layer breakdown. The authors reported that inhibition layer breakdown and formation of ζ-$FeZn_{13}$ occurred within immersion times associated with industrial galvanizing for a Zn bath containing 0.13 wt% dissolved Al. Contrastingly, a robust $Fe_2Al_5Zn_x$ inhibition layer formed at the steel/coating interface for a galvanizing bath containing 0.2 wt% dissolved Al. Similar effect of low dissolved Al content (< 0.15 wt%) on the inhibition layer breakdown was also reported by Baril and L'Espérance [83]. This suggests that the inhibition layer breakdown within commonly used CGL immersion time is much more difficult for galvanizing bath containing higher dissolved Al.

2.6 Selective Oxidation and Reactive Wetting of AHSSs

A thermodynamic model to predict the selectively oxidized species based on temperature, process atmosphere pO_2, and the Si/Mn ratio of the steel was developed by Suzuki et al. [84]. The authors considered the suppression of SiO_2 film formation to be the necessary condition to achieve good reactive wetting in the CGL. The model was validated by overlaying some reactive wetting results from the literature on the predictions based on the Suzuki et al. [84] model, as shown in Figure 2.18. It was concluded that it was impossible to avoid the deleterious SiO_2 film formation regardless of the process atmosphere pO_2 when the Si/Mn ≥ 1. For a Si/Mn = 1, a dew point of –5 °C or greater was required in a N_2–5vol% H_2 atmosphere to stabilise $MeSiO_3$ + Me_2SiO_4 (where Me = Mn or Fe) instead of SiO_2. On the other hand, a dew point of –25 °C to –10 °C in a N_2–5vol% H_2 process atmosphere, compatible with industrial CGLs, is enough to completely suppress SiO_2 formation and stabilise the system in the desired $MeSiO_3$ + Me_2SiO_4 two phase region when the substrate Si/Mn ratio ≤ 0.5. However, there were some disagreements to the thermodynamic model as it was unable to predict some of the critical factors in reactive wetting such as oxide thickness, morphology, and spatial distribution. For example, Bellhouse and McDermid [29] successfully galvanized a TRIP-assisted steel with conventional CGL parameters where the Si/Mn = 1. The authors attributed this to the widely spaced, nodular type MnO-Mn_2SiO_4/$MnSiO_3$ oxides on the steel surface. The desired $Fe_2Al_5Zn_x$ layer was able to form between the nodules and resulted in high quality galvanized coating.

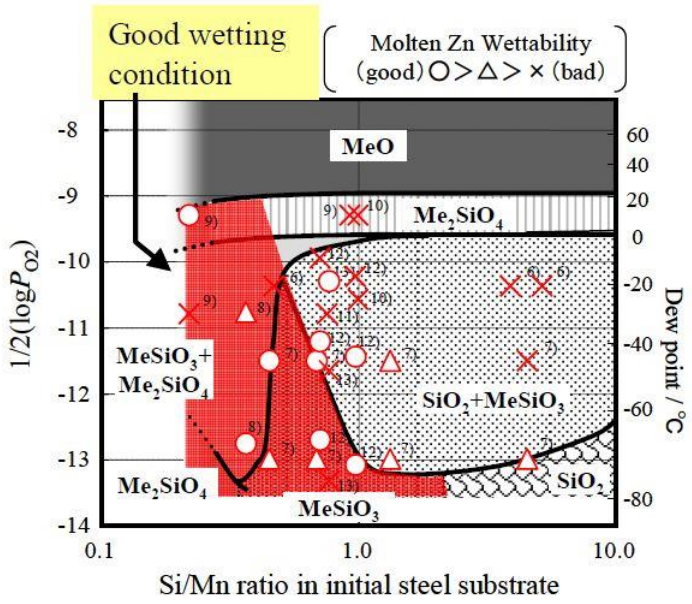

Figure 2.18: The relationship between oxide species and wettability by molten Zn for process atmosphere oxygen potential at 850 °C in a N_2–5vol% H_2 atmosphere for steels with Si content of 1 wt% and Mn content of 0.01–3 wt%; Me = Mn or Fe [84].

A mechanism for the formation of a well-developed interfacial layer regardless of an external MnO layer was first proposed by Khondker et al. [85]. It was hypothesised that aluminothermic reduction of external MnO can occur by the bath dissolved Al during immersion in the Zn(Al, Fe) bath, per Equation (2.15):

$$3MnO + 2[Al] \overset{460°C}{\rightarrow} 3[Mn] + Al_2O_3 \qquad (2.15)$$

where [X] denote species in solution. This mechanism was later validated by Kavitha and McDermid [86], who observed a significant reduction in MnO thickness during immersion in a 0.20 wt% Al (dissolved) galvanizing bath. It was determined that the aluminothermic reduction reaction followed linear kinetics where it could be drawn from the presented data that the MnO layers less than 85 nm in thickness can be reduced within the common CGL dipping time of 4 s, allowing the bath metal to have access to the underlying Fe substrate such that the $Fe_2Al_5Zn_x$

reaction (equation (2.14)) can proceed, and reactive wetting can occur. This is one of the contributing reactive wetting mechanisms that makes it possible to galvanize relatively simple DP and TRIP steels [27,29,85]. Moreover, Liu et al. [87] reported that the ΔG for possible aluminothermic reduction of simple oxides such as MnO, Cr_2O_3, SiO_2, P_2O_5, and Fe_2O_3 at 460 °C are negative, implying that aluminothermic reduction of these oxides is thermodynamically feasible. However, the authors did not address whether the aluminothermic reduction of these simple oxides was kinetically feasible.

Pourmajidian [88] successfully galvanized a model Fe-0.1C-6Mn-2Si (wt%) steel and obtained good reactive wetting and high quality Zn coating with CGL-compatible processing parameters. This was obtained under the combined use of high process atmosphere pO_2 and a 0.05 wt% addition of Sn as a surface active element. Under these conditions, a widely spaced distribution of globular oxides with minimal surface coverage by external MnO was observed, which then contributed to improve reactive wetting upon immersion. Several bath-metal reactions and wetting mechanisms were characterised by TEM+EELS analysis of the Fe-Zn interface. Infiltration of the molten bath and oxide lift-off along with the aluminothermic reduction of surface MnO allowed for partial/full formation of the desired $Fe_2Al_5Zn_x$ layer at the interface.

Recently, Pallisco [89] reported successful reactive wetting during galvanizing a Fe-0.15C-6Mn-1.9Al-1Si (wt%) medium-Mn steel following a two stage heat treatment containing a martensite-ferrite (MF) heat treatment at 890 °C for 600 s and intercritical annealing at 710 °C for 120 s. Pallisco and McDermid [19] previously reported that this thermal processing route was also successful in achieving 3G AHSS general target mechanical properties (UTS × TE ≥ 24000 MPa%). Pallisco [89] summarised the evolution of the substrate surface during the two stage heat treatment and subsequent galvanizing in a schematic diagram, shown in Figure 2.19. It can be seen

that the MF heat treatment resulted in a thick external oxide layer with a near-surface solute-depleted matrix (Figure 2.19b)). However, most of the external oxides were dissolved during the intermediate flash pickling step, leaving some dispersed $MnAl_2O_4$ and extruded Fe nodules on the surface (Figure 2.19c)). This surface remained unchanged during the 120 s intercritical annealing treatment regardless of the process atmosphere pO_2 utilised owing to the solute-depleted layer that formed during the MF heat treatment. This dispersed external oxide distribution and extruded Fe nodules on the surface facilitated successful reactive wetting of the steel substrate *via* direct wetting, oxide wetting, oxide lift-off, and bath metal infiltration. These reactive wetting mechanisms were also reported in literature for successful galvanizing of AHSSs [27,29,90,91].

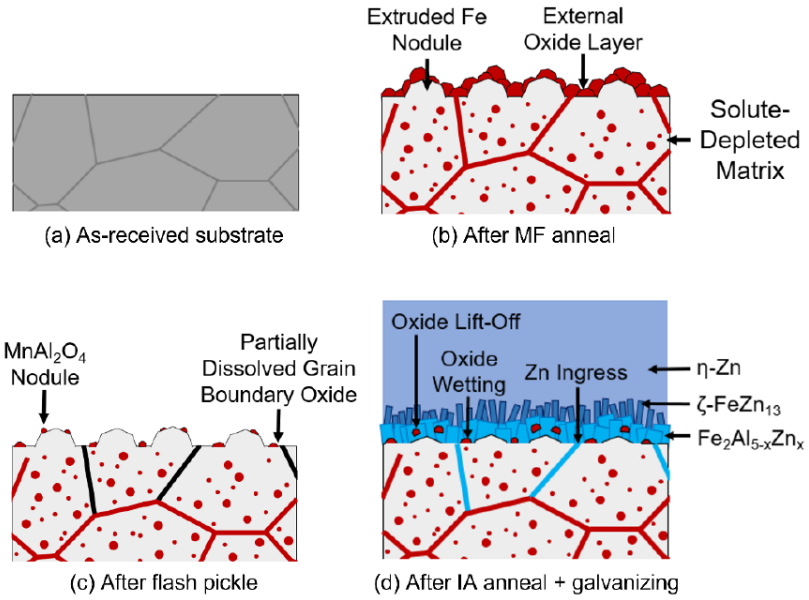

Figure 2.19: Summative schematic showing the evolution of surface and near-surface structures at each stage in the thermal cycle [89].

2.7 Improving Reactive Wetting of AHSSs

Numerous researchers have worked towards finding methods for improving the reactive wetting of the AHSSs by the galvanizing bath. Figure 2.20 shows some of these approaches, which

can also be applicable to the medium-Mn 3G AHSSs [33]. However, oxidation/reduction and flash coating methods are less viable options compared to the high dew point and surface-active element addition as they add more complexity to the process. In case of the oxidation/reduction method, the final microstructure of the surface layer usually consists of a porous, pure iron layer with isolated oxide particles embedded within. This can result in a relatively weak interfacial layer formation during continuous galvanizing [92]. On the other hand, the flash coating method involves depositing a thin layer of pure Ni, Fe or Cu prior to the annealing stage which can prevent the formation of external oxides on the steel substrate [93,94]. However, this method is relatively expensive, thereby limiting its application in the industrial CGL.

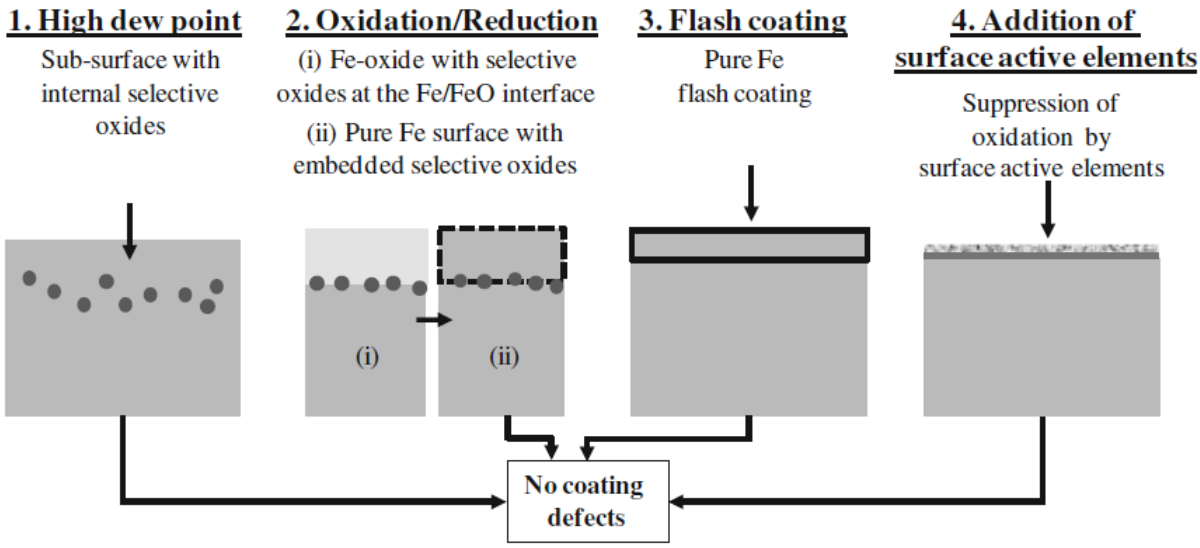

Figure 2.20: Schematic of proposed methods to prevent coating defects resulting from surface selective oxides [33].

2.7.1 High Dew Point Process Atmosphere

External selective oxidation is suppressed at high dew points owing to the greater inward flux of oxygen compared to the outward flux of ignoble alloying elements, resulting in internal selective oxidation. Bellhouse and McDermid [95] studied the effect of the process atmosphere pO_2 on the

selective oxidation and reactive wetting of a 0.2C-1.5Mn-0.5Si-1.0Al (wt%) TRIP-assisted steel. The authors reported good reactive wetting for the steel annealed under both the –53 °C T_{dp} N_2–20 vol% H_2 process atmosphere and the –30 °C T_{dp} N_2–5 vol% H_2 process atmospheres as a result of the formation of a mixture of thin film-like and nodule-like surface oxides. The aluminothermic reduction of the thin film-like oxides enabled the formation of the desired $Fe_2Al_5Zn_x$ interfacial layer. However, the authors also reported that the use of a high process atmosphere (N_2–5 vol% H_2) dew point, i.e., +5 °C T_{dp}, resulted in the formation of relatively thick, localized film-like oxides that acted as a barrier and prevented the complete reduction of the MnO layer by aluminothermic reduction reaction, resulting in poor coating quality. On the contrary, Mousavi and McDermid [91] reported good reactive wetting for a 0.1C-2Mn-1.3Si (wt%) AHSS which was intercritically annealed at 820 °C for 120 s in a +5 °C T_{dp} N_2–5 vol% H_2 process atmosphere and galvanized in a 0.2 wt% (dissolved) Al galvanizing bath at 460 °C for 4 s. Furthermore, Maki et al. [96] reported that the wettability of a 0.1C-1.5Mn-1.3Si (wt%) TRIP steel was improved after annealing in a higher dew point (+10 °C) atmosphere owing to the partial internal oxidation of Si. Cho et al. [97] also concluded that a higher T_{dp} in N_2–10 vol% H_2 process atmosphere would result in improved wettability due to the suppression of surface oxides into the substrate (CMnSi TRIP steel containing 2.2Mn-1.4Si wt%) during annealing.

A series of Mn-containing model steels (2.5, 3.5, and 5.1 wt% Mn) were studied by Alibeigi et al. [20] and the effect of process atmosphere pO_2 on the external oxide thickness and reactive wetting was determined. The results showed that a high oxygen partial pressure resulted in a thin layer of external MnO film along with internal oxidation of Mn. Moreover, it was shown that relatively significant quantities of external MnO could be aluminothermically reduced in the Zn(Al, Fe) bath, the kinetics of which was inversely related to the external MnO layer thickness.

Pourmajidian and McDermid [22] investigated the effect of process atmosphere pO_2 on the spatial distribution and morphology of the oxides formed during annealing of a model 0.1C-6Mn-2Si (wt%) medium-Mn AHSS at 690 °C. The results showed that a +5 °C dew point process atmosphere (N_2–5 vol% H_2) pO_2 yielded a steel surface with nodule-like MnO particles with thin films in between the nodules, as shown in Figure 2.21. This thin and widely spaced external MnO nodules along with a substantially lower surface coverage by the oxides were determined to be the key contributors to the successful reactive wetting and formation of $Fe_2Al_5Zn_x$ intermetallics. As a result, high quality galvanized coating with very few bare spots was achieved for the +5 °C dew point process atmosphere pO_2 (Figure 2.22).

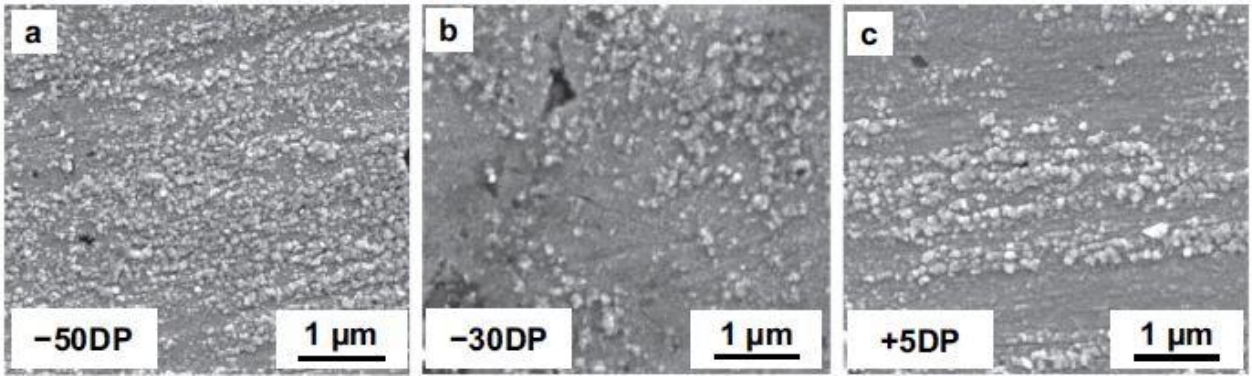

Figure 2.21: SEM of the pre-immersion surface oxides formed on a Fe-0.1C-6Mn-2Si steel intercritically annealed at 690 °C for 120 s in N_2–5vol%H_2 process atmosphere [22].

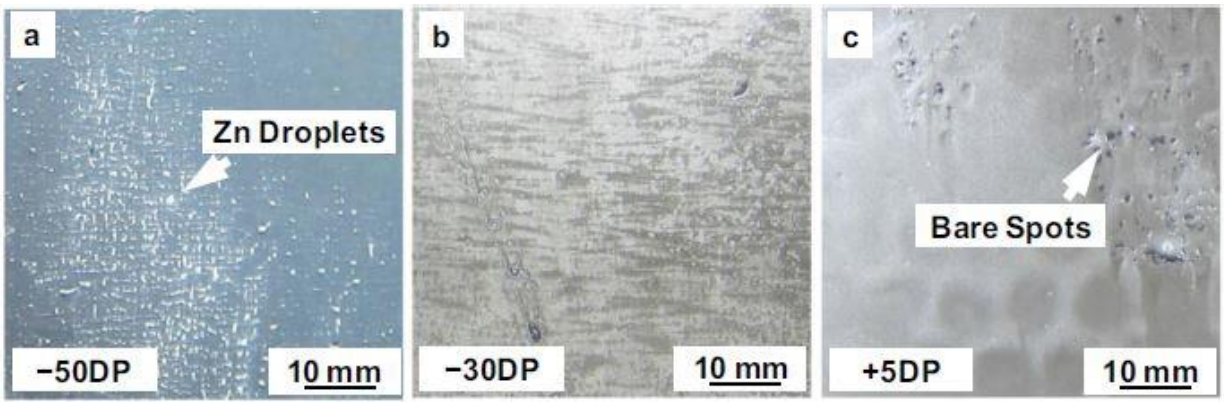

Figure 2.22: Photographs of uniform coating area of the galvanized Fe-0.1C-6Mn-2Si steel panels which were intercritically annealed at 690 °C for 120 s in N_2–5vol%H_2 process atmosphere [22].

2.7.2 Surface Active Element Addition

Another successful method to improve reactive wetting of AHSSs is suppressing the oxidation reaction and modifying the morphology of the oxides by minor additions of surface active elements, such as Sn, Sb, and Bi. A study by Zhang et al. [98] showed that Sb addition in TRIP-assisted steels resulted in a significant decrease in internal oxidation and decarburization rate as well as a reduction in the extent of surface oxidation. It was suggested that Sb could have occupied the adsorption sites on the surface and reduced the inward flux of oxygen to the subsurface. Seah [99] investigated the grain boundary segregation of various elements and suggested an equation to determine the degree of grain boundary or surface segregation of solute atom A in solvent atom B:

$$\ln \beta_A^S = \left\{ 24\left(T_B^m - T_A^m\right) + 1.89\Omega + M\,4.64\times10^7 a_B\left(a_A - a_B\right)^2 \right\} \div RT \pm 1.29 \qquad (2.16)$$

where T is the temperature, T_A^m and T_B^m are melting temperatures of the pure solids A and B, respectively, Ω is the mixing enthalpy of A and B, a_A and a_B are the atomic sizes of A and B,

respectively. According to Tsai et al. [100] the value of M is 1 when $a_A > a_B$ and 0 when $a_A < a_B$. The authors showed that the elastic strain energy in the case of an undersized solute atom is negligible compared to an oversized solute atom. The driving force for this surface segregation is the reduction of surface energy when solute A segregates to the surface. There are two factors in this equation that contribute to this driving force. One is the difference in melting temperature of A and B, which can be measured accurately and are also related to the surface energy reduction. Another is the atomic size difference which affects the driving force due to surface segregation lowering the elastic strain energy in the matrix lattice resulting from the atomic size mismatch of solute A and solvent B. Considering these two factors, Cho et al. [33] plotted the melting point of various elements as a function of their atomic size (Figure 2.23) and suggested that Sb, Bi, and Sn can be credible candidates as surface active elements in steels. Furthermore, the authors investigated the effect of Cr, Ni, Ti, Cu, and Sn on the selective oxidation and reactive wetting of a 0.1C-1.6Mn-1.5Si (wt%) TRIP steel and concluded that Sn had the most significant influence on improving reactive wetting. Minor addition (0.05 wt%) of Sn modified the morphology of the surface oxides from film-like to lens-shaped particles. The lens-shaped oxide particles allowed Fe and dissolved Al to easily react and form the $Fe_2Al_5Zn_x$ interfacial layer at the areas in between the oxide particles. These areas were covered with thinner film-like oxide layers which facilitated successful reactive wetting through aluminothermic reduction and oxide lift-off.

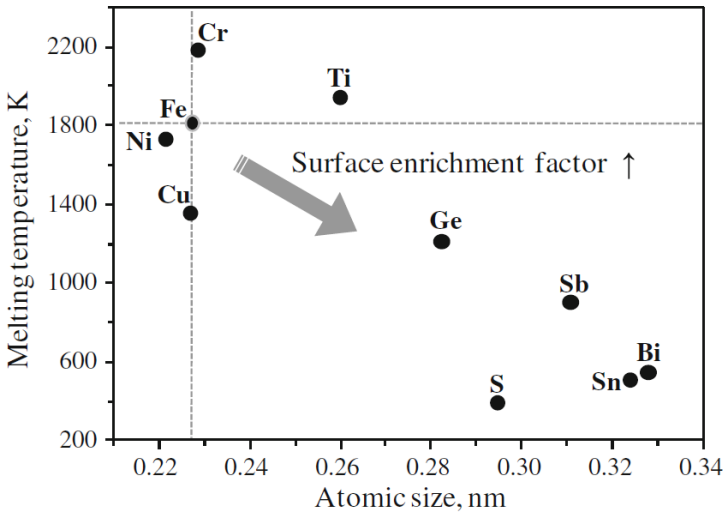

Figure 2.23: Melting temperature of different elements as a function of their atomic sizes [33].

Cho et al. [101] conducted a detailed study with varying amounts of Sn (0.05-1 wt%) to identify the mechanism responsible for modification of the selective oxide morphology in intercritically annealed CMnSi TRIP-assisted steels. The surface of the reference alloy (without Sn) was covered by a thick granular Mn-rich oxide and a thinner Si-rich film-type oxide. Although the 0.05 wt% Sn alloy still contained a thick granular Mn-rich oxide layer, the morphology of the Si-rich oxides changed from film-type to elongated or lens-shaped ones. However, the granular Mn-rich oxide layer was not observed in the 0.5 wt% Sn and 1 wt% Sn containing alloys. Only lens-shaped Si-rich oxide islands were observed in the 0.5 wt% Sn alloy whereas the 1 wt% Sn alloy had lens-shaped oxide islands and film-type Si-rich oxide layers. EDS elemental mapping confirmed that Si was mainly present at the base of lens-shaped oxide whereas Mn was concentrated at the oxide lens surface, as shown in Figure 2.24. The regions underneath the lens-shaped and film-type oxides were enriched with Sn. It was concluded that Sn enrichment at the surface and the interface of the steel/oxide during annealing changed the surface energy of the substrate and interfacial energies, respectively, resulting in the change in morphology of the Si-rich oxides to lens-shaped islands. Moreover, the change in the chemistry of the surface oxides

was also related to the segregation of Sn at the surface. This surface segregated Sn occupied potential adsorption sites for oxygen and reduced the oxygen permeability of the surface.

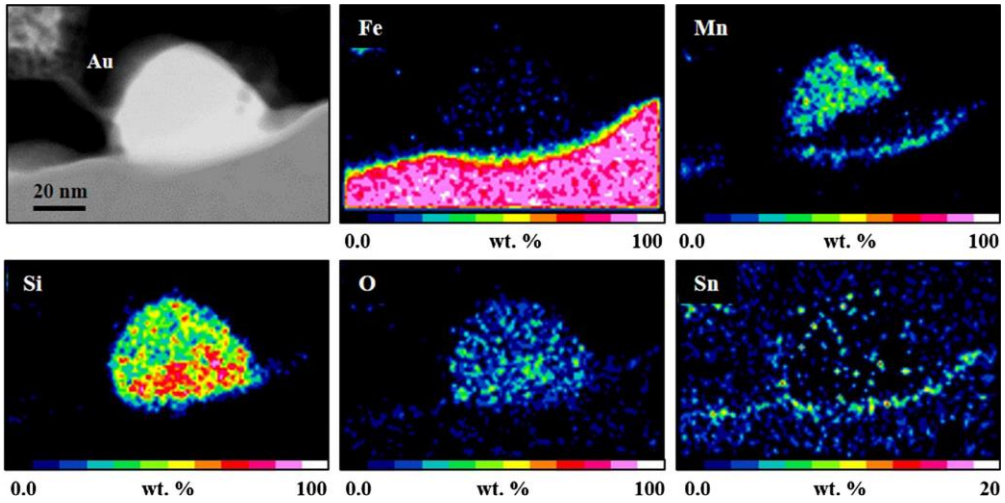

Figure 2.24: EDS elemental mapping of a lens-shaped xMnO.SiO_2 oxide formed on 1 wt% Sn added TRIP steel during annealing [101].

Pourmajidian [88] explored the desirable effect of minor Sn addition (0.05 wt%) on selective oxidation and reactive wetting of a model 0.1C-6Mn-2Si (wt%) medium-Mn steel. Significantly slower external and internal oxidation kinetics were observed owing to Sn segregation to the surface (~10 times compared to its bulk composition) of the annealed samples as shown by atom probe tomography (APT) analysis (Figure 2.25). However, Mousavi et al. [36] reported significantly higher (~150 times compared to its bulk composition) Sn segregation at the oxide/substrate interface during intercritical annealing of a 0.1C-2Mn-1.7Si (wt%) AHSS at 840 °C for 600 s with –50 °C dew point N_2–5 vol% H_2 process atmosphere. Although the annealing parameters were different in those studies, the difference in Sn segregation most likely be attributed to the co-segregation effect of the other alloying elements. Nevertheless, Pourmajidian [88] reported widely spaced, fine, and discrete external oxide nodules on the intercritically annealed Sn-added steel. The author also reported that such an external oxide morphology and

distribution were sufficient for the aluminothermic reduction mechanism to be effective. As a result, a compact and continuous $Fe_2Al_5Zn_x$ interfacial layer formed during galvanizing resulting in high quality galvanized coating.

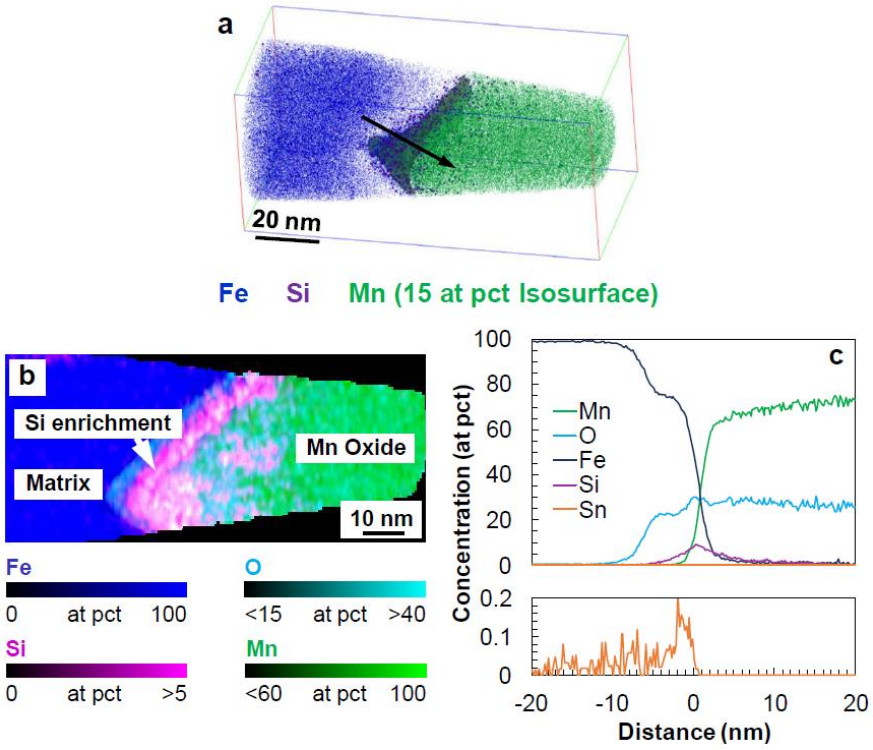

Figure 2.25: APT analysis of the surface oxide/metal interface of the Sn-added steel annealed for 600 s under the –30DP atmosphere (a) 3D atom map of Fe, Mn, Si and 15 at pct Mn isosurface, (b) 5 nm thick 2D section of the reconstructed needle showing the enrichment of alloying elements in the surface oxide and (c) proximity histogram (proxigram) revealing the 1D concentration profiles normal to the isosurface marked with an arrow in (a) [88].

Pourmajidian [88] conducted TEM+EELS analysis of the zinc/steel interface in order to identify the reactive wetting mechanisms. Figure 2.26 and Figure 2.27 show the results for the reference (0.1C-6Mn-2Si wt%) and Sn-added (0.1C-6Mn-2Si-0.05Sn wt%) model medium-Mn steel which were annealed at 690 °C for 120 s with –30 °C dew point N_2–5 vol% H_2 process

atmosphere, respectively. It was concluded that the reference steel had fewer Fe-Al intermetallics at the interface due to either a thicker oxide layer or a larger surface area covered by the oxides. However, good reactive wetting was still observed in the reference steel owing to liquid bath alloy penetration to the steel substrate through the existing gaps or discontinuities in the external MnO layer, resulting in significant oxide lift-off and exposure of the metallic iron of the substrate to the galvanizing bath. In comparison, the Sn-added steel had a more compact and continuous inhibition layer formation at the zinc/steel interface, as shown in Figure 2.27. This was attributed to the thinner, finer, and globular morphology of the widely-spaced oxides on the surface prior to immersion. The external MnO was sufficiently reduced by the dissolved Al in the bath, resulting in full formation of a compact and continuous $Fe_2Al_5Zn_x$ interfacial layer and excellent coating quality in the Sn-added model medium-Mn steel.

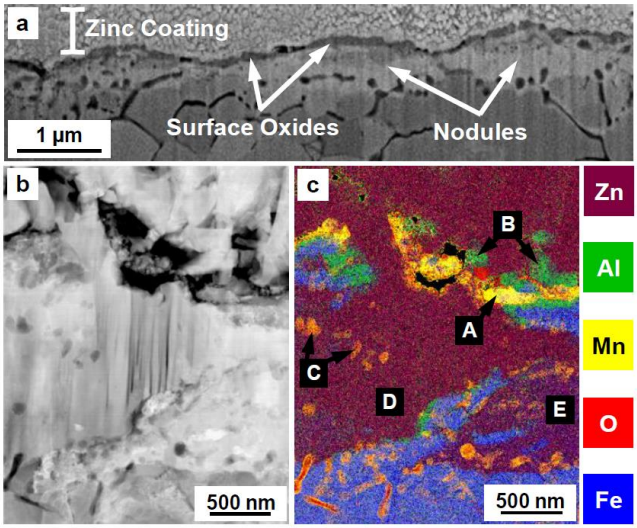

Figure 2.26: (a) SE-FIB image, (b) DF-STEM image and (c) color overlay EELS map showing a nodule-like reaction site and the different reaction products formed at the zinc/steel interface of the galvanized reference steel (0.1C-6Mn-2Si wt%) annealed under the –30DP process atmosphere prior to immersion [88].

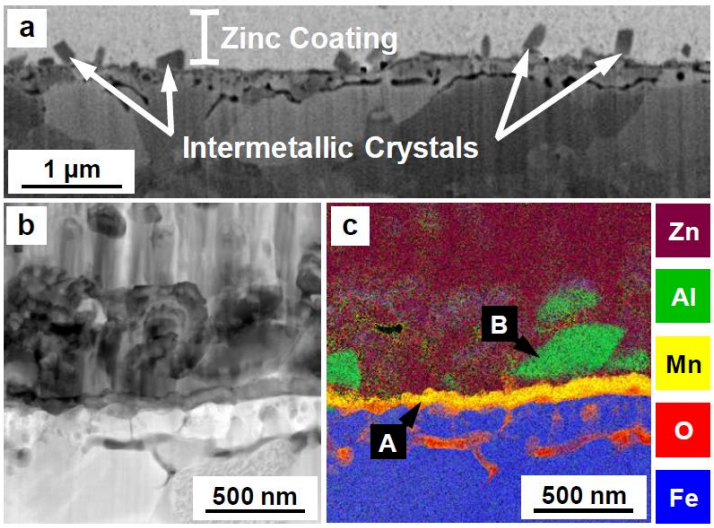

Figure 2.27: (a) SE-FIB image, (b) DF-STEM image and (c) color overlay EELS map showing the reaction products formed at the zinc/steel interface of the galvanized Sn-added steel (0.1C-6Mn-2Si-0.05Sn wt%) annealed under the –30DP process atmosphere prior to immersion [88].

2.8 Summary

To conclude this chapter, although medium-Mn steels are one of the extensively researched 3G AHSSs, most of the research is being conducted on binary or model alloys. Furthermore, the thermal processing parameters utilised in those studies are often not compatible with CGL processing windows. There has been also a lack of comprehensive research which studied the mechanical property development as well as the selective oxidation and reactive wetting of application-oriented medium-Mn steels. Moreover, recent research reported that the martensitic starting microstructure was more robust in achieving 3G AHSS target mechanical properties for medium-Mn steels with CGL-compatible intercritical annealing parameters. However, the effect of two-stage heat treatment, containing austenitizing heat treatment and intercritical annealing, on the selective oxidation and reactive wetting of medium-Mn steels needs to be investigated more thoroughly. On the other hand, effect of surface active element micro-alloying on the mechanical

properties of medium-Mn steels has not been studied. These outstanding questions need to be answered for large-scale industrial production of these promising 3G AHSSs in the existing CGL and their successful integration to the automotive industry.

2.9 References

[1] K. Mukherjee, S.S. Sarkar, M. Militzer, Grain Refinement in Dual-Phase Steels, Metall. Mater. Trans. A. 40 (2009) 2145–2159.

[2] M. Calcagnotto, D. Ponge, D. Raabe, Ultrafine Grained Ferrite/Martensite Dual Phase Steel Fabricated by Large Strain Warm Deformation and Subsequent Intercritical Annealing, ISIJ Int. 48 (8) (2008) 1096–1101.

[3] O. Matsumura, Y. Sakuma, H. Takechi, Enhancement of elongation by retained austenite in intercritical annealed 0.4C–1.5Si–0.8Mn steel, ISIJ Trans. 27 (1987) 570–579.

[4] K. Sugimoto, T. Iida, J. Sakaguchi, T. Kashima, Retained Austenite Characteristics and Tensile Properties in a TRIP Type Bainitic Sheet Steel, ISIJ Int. 40 (9) (2000) 902–908.

[5] C. Garcia-Mateo, F.G. Caballero, H.K.D.H. Bhadeshia, Acceleration of Low-temperature Bainite, ISIJ Int. 43 (11) (2003) 1821–1825.

[6] C. Garcia-Mateo, F.G. Caballero, H.K.D.H. Bhadeshia, Development of Hard Bainite, ISIJ Int. 43 (8) (2003) 1238–1243.

[7] F.G. Caballero, H.K.D.H. Bhadeshia, K.J.A. Mawella, D.G. Jones, P. Brown, Design of novel high strength bainitic steels: Part 2, Mater. Sci. Technol. 17 (5) (2001) 517–522.

[8] C. Garcia-Mateo, F.G. Caballero, Ultra-high-strength Bainitic Steels, ISIJ Int. 45 (11) (2005) 1736–1740.

[9] T. Lolla, G. Cola, B. Narayanan, B. Alexandrov, S.S. Babu, Development of rapid heating and cooling (flash processing) process to produce advanced high strength steel microstructures, Mater. Sci. Technol. 27 (5) (2011) 863–875.

[10] S. Kaar, D. Krizan, J. Schwabe, H. Hofmann, T. Hebesberger, C. Commenda, L. Samek, Influence of the Al and Mn content on the structure-property relationship in density reduced TRIP-assisted sheet steels, Mater. Sci. Eng. A. 735 (2018) 475–486.

[11] H. Yi, Review on δ-Transformation-Induced Plasticity (TRIP) Steels with Low Density: The Concept and Current Progress, JOM 66 (9) (2014) 1759–1769.

[12] J. Speer, D.K. Matlock, B.C. De Cooman, J.G. Schroth, Carbon partitioning into austenite after martensite transformation, Acta Mater. 51 (9) (2003) 2611–2622.

[13] E. De Moor, S. Lacroix, A.J. Clarke, J. Penning, J.G. Speer, Effect of Retained Austenite Stabilised via Quench and Partitioning on the Strain Hardening of Martensitic Steels, Metall. Mater. Trans. A. 39A (2008) 2586–2595.

[14] J.R. McDermid, A. Chakraborty, Identification of Steel Chemistries and Galvanizing Process Design, ZCO-53-1 Project Report, 2012, Hamilton, Canada.

[15] E. De Moor, P.J. Gibbs, J.G. Speer, D.K. Matlock, J.G. Schroth, Strategies for third-generation advanced high-strength steel development, AIST Trans., IST 7 (3) (2010) 133–144.

[16] A. Arlazarov, M. Gouné, O. Bouaziz, A. Hazotte, G. Petitgand, P. Barges, Evolution of microstructure and mechanical properties of medium Mn steels during double annealing, Mater. Sci. Eng. A. 542 (2012) 31– 39.

[17] S. Lee, K. Lee, B.C. De Cooman, Observation of the TWIP + TRIP Plasticity-Enhancement Mechanism in Al-Added 6 Wt Pct Medium Mn Steel, Metall. Mater. Trans. A. 46A (2015) 2356–2363.

[18] K.M.H. Bhadhon, J.R. McDermid, X. Wang, E. McNally, F.E. Goodwin, Fine-scale microstructure characterization and mechanical properties of CGL-compatible heat treated medium-Mn TRIP steel, in: Proc. 11th Conf. Zinc Zinc Alloy Coat. Steel Sheet, Galvatech 2017, ISIJ Int., Tokyo (2017) 493–500.

[19] D.M. Pallisco, J.R. McDermid, Mechanical property development of a 0.15C–6Mn–2Al–1Si third-generation advanced high strength steel using continuous galvanizing heat treatments, Mater. Sci. Eng. A. 778 (2020) 139111.

[20] S. Alibeigi, R. Kavitha, R. J. Meguerian, J.R. McDermid, Reactive wetting of high Mn steels during continuous hot-dip galvanizing, Acta Mater. 59 (9) (2011) 3537–3549.

[21] M. Pourmajidian, J.R. McDermid, Effect of Annealing Temperature on the Selective Oxidation and Reactive Wetting of a 0.1C-6Mn-2Si Advanced High Strength Steel During Continuous Galvanizing Heat Treatments, ISIJ Int. 58 (9) (2018) 1635–1643.

[22] M. Pourmajidian, J.R. McDermid, On the reactive wetting of a medium-Mn advanced high-strength steel during continuous galvanizing, Surf. Coat. Technol. 357 (2019) 418–426.

[23] R.A. Grange, C.R. Hribal, Low-Carbon 6% Manganese Martensitic Steels, Edgar C. Bain Lab. Fundam. Res. Rep. No. 1453, USS, November 1968.

[24] R.L. Miller, Ultrafine-grained microstructures and mechanical properties of Alloy Steels, Metall. Trans. 3 (1972) 905–912.

[25] Y. Ma, Medium-manganese steels processed by austenite-reverted-transformation annealing for automotive applications, Mater. Sci. Technol. 33 (2017) 1713–1727.

[26] F.B. Pickering, Physical metallurgy and the design of steels, Applied Science Publishers, 1978.

[27] E.M. Bellhouse, J.R. McDermid, Selective Oxidation and Reactive Wetting during Galvanizing of a CMnAl TRIP-Assisted Steel, Metall. Mater. Trans. A. 42A (9) (2011) 2753–2768.

[28] M. De Meyer, D. Vanderschueren, B.C. De Cooman, The Influence of the Substitution of Si by Al on the Properties of Cold Rolled C-Mn-Si TRIP Steels, ISIJ Int. 39 (8) (1999) 813–822.

[29] E.M. Bellhouse, J.R. McDermid, Selective Oxidation and Reactive Wetting of 1.0 Pct Si-0.5 Pct Al and 1.5 Pct Si TRIP-Assisted Steels, Metall. Mater. Trans. A. 41A (2010) 1539–1553.

[30] J. Mahieu, J. Maki, B.C. De Cooman, S. Claessens, Phase Transformation and Mechanical Properties of Si-Free CMnAl Transformation-Induced Plasticity–Aided Steel, Metall. Mater. Trans. A. 33A (2002) 2573- 2580.

[31] B. Ehrhardt, T. Gerber, H. Hofmann, T.W. Schaumann, Property related design of advanced cold rolled steels with induced plasticity, Steel Grips. 2 (2004) 247–255.

[32] H.K.D.H. Bhadeshia, R.W.K. Honeycombe, Steels: Microstructure and Properties, 4th Ed., Elsevier Ltd, Oxford, United Kingdom, 2017.

[33] L. Cho, M.S. Kim, Y.H. Kim, B.C. De Cooman, Influence of Minor Alloying Elements on Selective Oxidation and Reactive Wetting of CMnSi TRIP Steel during Hot Dip Galvanizing, Metall. Mater. Trans. A. 45 (2014) 4484–4498.

[34] L. Cho, E.J. Seo, G.S. Jung, D.W. Suh, B.C. De Cooman, Surface Selective Oxidation of Sn-Added CMnSi TRIP Steel, Metall. Mater. Trans. A. 47 (2016) 1705–1719.

[35] J. Oh, L. Cho, M.S. Kim, K. Kang, B.C. De Cooman, The Effect of Bi on the Selective Oxide Formation on CMnSi TRIP Steel, Metall. Mater. Trans. A. 47 (2016) 5474–5486.

[36] G.S. Mousavi, B. Langelier, J.R. McDermid, Effect of Sn Addition, Process Atmosphere pO_2, and Annealing Time on the Selective Oxidation of a C-2Mn-1.7Si (Wt Pct) Advanced High-Strength Steel During Continuous Galvanizing, Metall. Mater. Trans. A. 50 (2019) 2898–2911.

[37] M. Pourmajidian, B. Langelier, J.R. McDermid, Effect of Process Atmosphere Dew Point and Tin Addition on Oxide Morphology and Growth for a Medium-Mn Third Generation Advanced Steel During Intercritical Annealing, Metall. Mater. Trans. A. 49 (2018) 5561–5573.

[38] H. Hofmann, D. Mattissen, T.W. Schaumann, Advanced Cold Rolled Steels for Automotive Applications, Steel Research Int. 80 (1) (2009) 22–28.

[39] S. Lee, B.C. De Cooman, Annealing Temperature Dependence of the Tensile Behavior of 10 pct Mn Multi-phase TWIP-TRIP Steel, Metall. Mater. Trans. A. 45A (2014) 6039–6052.

[40] P.J. Jacques, Transformation-induced plasticity for high strength formable steels, Curr. Opin. Solid State Mater. Sci. 8 (3–4) (2004) 259–265.

[41] F. Spenger, T. Hebesberger, A. Pichler, C. Krempaszky, E.A. Werner, AHSS steel grades: strain hardening and damage as material design criteria, Int. Conf. in New Developments in AHSS, (2008), Orlando, USA.

[42] E.M. Bellhouse, J.R. McDermid, Effect of Continuous Galvanizing Heat Treatments on the Microstructure and Mechanical Properties of High Al-Low Si Transformation Induced Plasticity Steels, Metall. Mater. Trans. A. 41 (2010) 1460–1473.

[43] J.R. McDermid, H.S. Zurob, Y. Bian, Stability of Retained Austenite in High-Al, Low-Si TRIP-Assisted Steels Processed via Continuous Galvanizing Heat Treatments, Metall. Mater. Trans. A. 42A (2011), 3627–3637.

[44] H. Luo, H. Dong, New ultrahigh-strength Mn-alloyed TRIP steels with improved formability manufactured by intercritical annealing, Mater. Sci. Eng. A. 626 (2015) 207–212.

[45] G.B. Olson, M. Cohen, A mechanism for the strain-induced nucleation of martensitic transformations, J. Less Common Met. 28 (1) (1972) 107–118.

[46] B.C. De Cooman, Y. Estrin, S.K. Kim, Twinning-induced plasticity (TWIP) steels, Acta Mater. 142 (2018) 283–362.

[47] B.C. De Cooman, L. Chen, H.S. Kim, Y. Estrin, S.K. Kim, H. Voswinckel, State-of-the-Science of High Manganese TWIP Steels for Automotive Applications, Microstructure and Texture in Steels. (2009) 165–183.

[48] Y.-K. Lee, C. Choi, Driving force for γ→ε martensitic transformation and stacking fault energy of γ in Fe-Mn binary system, Metall. Mater. Trans. A. 31 (2000) 355–360.

[49] S. Allain, J.-P. Chateau, O. Bouaziz, S. Migot, N. Guelton, Correlations between the calculated stacking fault energy and the plasticity mechanisms in Fe–Mn–C alloys, Mater. Sci. Eng. A. 387–389 (2004) 158–162.

[50] A. Dumay, J.-P. Chateau, S. Allain, S. Migot, O. Bouaziz, Influence of addition elements on the stacking-fault energy and mechanical properties of an austenitic Fe–Mn–C steel, Mater. Sci. Eng. A. 483–484 (2008) 184–187.

[51] A. Saeed-Akbari, J. Imlau, U. Prahl, W. Bleck, Derivation and Variation in Composition-Dependent Stacking Fault Energy Maps Based on Subregular Solution Model in High-Manganese Steels, Metall. Mater. Trans. A. 40 (2009) 3076–3090.

[52] S. Lee, B.C. De Cooman, On the Selection of the Optimal Intercritical Annealing Temperature for Medium Mn TRIP Steel, Metall. Mater. Trans. A. 44A (2013) 5018–5024.

[53] P.J. Gibbs, E. De Moor, M.J. Merwin, B. Clausen, J.G. Speer, D.K. Matlock, Austenite Stability Effects on Tensile Behavior of Manganese-Enriched-Austenite Transformation-Induced Plasticity Steel, Metall. Mater. Trans. A. 42A (2011) 3691–3702.

[54] D.W. Suh, J.H. Ryu, M.S. Joo, H.S. Yang, K. Lee, H.K.D.H. Bhadeshia, Medium-Alloy Manganese-Rich Transformation-Induced Plasticity Steels, Metall. Mater. Trans. A. 44 (2013) 286–293.

[55] A. Arlazarov, A. Hazotte, O. Bouaziz, M. Gouné, F. Kegel, Characterization of microstructure formation and mechanical behavior of an advanced medium Mn steel, Proc. MS&T 2012. (2012) 1124–1131.

[56] Q. Lai, M. Gouné, A. Perlade, T. Pardoen, P. Jacques, O. Bouaziz, Y. Bréchet, Mechanism of Austenite Formation from Spheroidized Microstructure in an Intermediate Fe-0.1C-3.5Mn Steel, Metall. Mater. Trans. A. 47A (2016) 3375–3386.

[57] A. Mehrabi, J.R. McDermid, H.S. Zurob, F.E. Goodwin, Austenite Nucleation and Growth as a Function of Starting Microstructure in a Fe-0.15C-5.56Mn-1.1Si-1.89Al Medium-Mn Steel, Extended Abstracts of HMnS 2022 Conf., Linz, Austria, (2022).

[58] N. Nakada, K. Mizutani, T. Tsuchiyama, S. Takaki, Difference in Transformation Kinetics between Ferrite and Austenite Formation in 0.1%C-5%Mn Steel, Extended Abstracts of HMnS 2014 Conf., Aachen, Germany, (2014) K2-89.

[59] R. Wei, M. Enomoto, R. Hadian, H.S. Zurob, G.R. Purdy, Growth of austenite from as-quenched martensite during intercritical annealing in an Fe–0.1C–3Mn–1.5Si alloy, Acta Mater. 61 (2013) 697–707.

[60] J. Shi, X. Sun, M. Wang, W. Hui, H. Dong, W. Cao, Enhanced work-hardening behavior and mechanical properties in ultrafine-grained steels with large-fractioned metastable austenite, Scr. Mater. 63 (8) (2010) 815–818.

[61] E.A. Silva, private communication (2005), U.S. Steel Research.

[62] W.Q. Cao, C. Wang, J. Shi, M.Q. Wang, W.J. Hui, H. Dong, Microstructure and mechanical properties of Fe–0.2C–5Mn steel processed by ART-annealing, Mater. Sci. Eng. A. 528 (22–23) (2011) 6661–6666.

[63] Morris, FREED Thermodynamic Database v7.8.1 (2013).

[64] I.H. Jung, Y.B. Kang, S.A. Decterov, A.D. Pelton, Thermodynamic evaluation and optimization of the MnO-Al_2O_3 and MnO-Al_2O_3-SiO_2 systems and applications to inclusion engineering, Metall. Mater. Trans. B. 35 (2004) 259–268.

[65] I.H. Jung, Critical evaluation and thermodynamic modeling of the Mn–Cr–O system for the oxidation of SOFC interconnect, Solid State Ion. 177 (2006) 765–777.

[66] C. Wagner, Reaktionstypen bei der Oxydation von Legierungen, Zeitschrift für Elektrochemie. 63 (7) (1959) 772–782.

[67] R.A. Rapp, Kinetics, Microstructures and Mechanism of Internal Oxidation - Its Effect and Prevention in High Temperature Alloy Oxidation, Corrosion. 21 (12) (1965) 382–402.

[68] V.A. Lashgari, C. Kwakernaak, W.G. Sloof, Transition from Internal to External Oxidation of Mn Steel Alloys, Oxid. Met. 81 (2014) 435–451.

[69] N. Birks, G.H. Meier, F.S. Pettit, Introduction to the High-Temperature Oxidation of Metals. Cambridge, UK: Cambridge University Press, 2006.

[70] J.M. Mataigne, M. Lamberigts, V. Leroy, Developments in the Annealing of Sheet Steels, Warrendale, PA, USA: Minerals, Metals & Materials Society, 1992.

[71] D. Huin, P. Flauder, J.-B. Leblond, Numerical Simulation of Internal Oxidation of Steels during Annealing Treatments, Oxid. Met. 64 (2005) 131–167.

[72] C.R. Shastry, J.A. Rotole, T.W. Kaiser, Characterization of selective oxidation of alloying elements in an advanced high strength steel from theoretical and experimental viewpoints, 7th Int. Conf. Zinc Zinc Alloy Coat. Steel Sheet. (2007) Paper B-6-2, 403–408.

[73] J-B. Leblond, J-M. Bergheau, R. Lacroix, D. Huin, Implementation and application of some nonlinear models of diffusion/reaction in solids, Finite Elem. Anal. Des. 132 (2017) 8–26.

[74] G.S. Mousavi, J.R. McDermid, Selective Oxidation of a C-2Mn-1.3Si (Wt Pct) Advanced High-Strength Steel During Continuous Galvanizing Heat Treatments, Metall. Mater. Trans. A. 49A (2018) 5546–5560.

[75] I.A. Aksay, C.E. Hoge, J.A. Pask, Wetting under chemical equilibrium and nonequilibrium conditions, J. Phys. Chem. 78 (1974) 1178–1183.

[76] T. Young, An Essay on the Cohesion of Fluids, Phil. Trans. R. Soc. Lond. 95 (1805) 65–87.

[77] M. Guttmann, Diffusive Phase Transformations in Hot Dip Galvanizing, Mater. Sci. Forum. 155–156 (1994) 527–548.

[78] C.E. Jordan, A.R. Marder, Fe-Zn phase formation in interstitial-free steels hot-dip galvanized at 450°C: Part II 0.20 wt% Al-Zn baths, J. Mater. Sci. 32 (1997) 5603–5610.

[79] J.R. McDermid, M.H. Kaye, W.T. Thompson, Fe Solubility in the Zn-Rich Corner of the Zn-Al-Fe System for Use in Continuous Galvanizing and Galvannealing, Metall. Mater. Trans. B. 38 (2) (2007) 215–230.

[80] J. Nakano, PhD Thesis, McMaster University, Hamilton, ON, Canada, 2006.

[81] N.-Y. Tang, Modeling AI Enrichment in Galvanized Coatings, Metall. Mater. Trans. A. 26A (1995) 1699–1704.

[82] L. Chen, R. Fourmentin, J.R. McDermid, Morphology and Kinetics of Interfacial Layer Formation during Continuous Hot-Dip Galvanizing and Galvannealing, Metall. Mater. Trans. A. 39A (2008) 2128–2142.

[83] E. Baril, G. L'Espérance, Studies of the Morphology of the Al-Rich Interfacial Layer Formed during the Hot Dip Galvanizing of Steel Sheet, Metall. Mater. Trans. A. 30 (1999) 681–695.

[84] Y. Suzuki, T. Yamashita, Y. Sugimoto, S. Fujita, Thermodynamic Analysis of Selective Oxidation Behavior of Si and Mn-added Steel during Recrystallization Annealing, in: Proc. 8th Conf. Zinc Zinc Alloy Coat. Steel Sheet, Galvatech 2011, Genova (2011).

[85] R. Khondker, A.I.M. Mertens, J.R. McDermid, Effect of annealing atmosphere on the galvanizing behavior of a dual-phase steel, Mater. Sci. Eng. A. 463 (2007) 157–165.

[86] R. Kavitha, J.R. McDermid, On the in-situ aluminothermic reduction of manganese oxides in continuous galvanizing baths, Surf. Coat. Technol. 212 (2012) 152–158.

[87] H. Liu, Y. He, L. Li, Application of thermodynamics and Wagner model on two problems in continuous hot-dip galvanizing, J. Appl. Surf. Sci. 256 (5) (2009) 1399–1403.

[88] M. Pourmajidian, Selective Oxidation and Reactive Wetting of Fe-0.1C-6Mn-2Si-xSn Advanced High Strength Steels During Continuous Hot-Dip Galvanizing, PhD Thesis, McMaster University, Hamilton, ON, Canada, 2018.

[89] D.M. Pallisco, Mechanical Property Development and Galvanizing of Medium-Mn Third Generation Advanced High Strength Steel, PhD Thesis, McMaster University, Hamilton, ON, Canada, 2021.

[90] R. Sagl, A. Jarosik, D. Stifter, G. Angeli, The role of surface oxides on annealed high-strength steels in hot-dip galvanizing, Corros. Sci. 70 (2013) 268–275.

[91] G. Seyed Mousavi, J.R. McDermid, Effect of dew point on the reactive wetting of a C-2Mn-1.3Si (wt%) advanced high strength steel during continuous galvanizing, Surf. Coat. Technol. 351 (2018) 11–20.

[92] Y.F. Gong, B.C. De Cooman, Influence of the Oxidation-Reduction Process on the Surface and Sub-surface Microstructure of Intercritically Annealed CMnSi TRIP Steel, ISIJ Int. 51 (2011) 630–637.

[93] Y.I. Choi, W.J. Beom, C.J. Park, D. Paik, M.H. Hong, Surface Oxidation of the High-Strength Steels Electrodeposited with Cu or Fe and the Resultant Defect Formation in Their Coating during the Following Galvanizing and Galvannealing Processes, Metall. Mater. Trans. A. 41A (2010) 3379–3385.

[94] R. Sa-nguanmoo, E. Nisaratanaporn, Y. Boonyongmaneerat, Hot-dip galvanization with pulse-electrodeposited nickel pre-coatings, Corros. Sci. 53 (2011) 122–126.

[95] E.M. Bellhouse, J.R. McDermid, Selective Oxidation and Reactive Wetting During Hot-Dip Galvanizing of a 1.0 pct Al-0.5 pct Si TRIP-Assisted Steel, Metall. Mater. Trans. A. 43 (7) (2012) 2426–2441.

[96] J. Maki, J. Mahieu, B.C. De Cooman, S. Claessens, Galvanisability of silicon free CMnAl TRIP steels, Mater. Sci. Technol. 19 (1) (2003) 125–131.

[97] L. Cho, J.S. Lee, M.S. Kim, Y.H. Kim, B.C. De Cooman, Influence of Gas Atmosphere Dew Point on the Selective Oxidation and the Reactive Wetting During Hot Dip Galvanizing of CMnSi TRIP Steel, Metall. Mater. Trans. A. 44A (2013) 362–371.

[98] Z. Zhang, I. Sohn, F. Pettit, G. Meier, S. Sridhar, Investigation of the Effect of Alloying Elements and Water Vapor Contents on the Oxidation and Decarburization of Transformation-Induced Plasticity Steels, Metall. Mater. Trans. B. 40B (2009) 567–584.

[99] M. Seah, Adsorption-induced interface decohesion, Acta Metall. 28 (1980) 955–962.

[100] N. Tsai, G. Pound, F. Abraham, Comment on the prediction of segregation to alloy surfaces, J. Catal. 50 (1977) 200–202.

[101] L. Cho, E.J. Seo, G.S. Jung, D.W. Suh, B. C. De Cooman, Surface Selective Oxidation of Sn-Added CMnSi TRIP Steel, Metall. Mater. Trans. A. 47 (2016) 1705–1719.

3 Effects of CGL-Compatible Thermal Processing, Starting Microstructure, and Sn Micro-alloying on the Mechanical Properties of a Medium-Mn Third Generation Advanced High Strength Steel

K.M.H. Bhadhon, X. Wang, J.R. McDermid
Department of Materials Science and Engineering, McMaster University, Hamilton, Ontario, Canada
Materials Science and Engineering A 833 (2022) 142563.

3.1 Abstract

Two prototype medium-Mn third generation advanced high strength steels (Fe-0.2C-6Mn-1.5Si-0.5Al-0.5Cr-xSn wt%, x = 0 or 0.05) were annealed with continuous galvanizing line (CGL) compatible thermal processing parameters. It was found that the starting microstructure, intercritical annealing (IA) parameters and Sn micro-alloying had a significant effect on the volume fraction, stability, and deformation-induced transformation kinetics of the retained austenite and, therefore, the resultant mechanical properties of the steels. It was shown that Sn segregation at the carbide/matrix interface inhibited C diffusion and consequently, reduced carbide dissolution and precipitation kinetics during intercritical annealing. This resulted in lower volume fraction of retained austenite with lower stability after intercritical annealing of the as-received cold-rolled Sn-containing alloy. CGL-compatible IA treatments, therefore, were only able to produce target 3G-AHSS mechanical properties in the as-received cold-rolled alloy without Sn micro-alloying. However, the martensitic starting microstructures were more robust in achieving the 3G-AHSS target mechanical properties for both alloys. A martensitic starting microstructure resulted in higher volume fraction of stable retained austenite for 650 °C and 675 °C IA treatments. Gradual transformation of this stable retained austenite to martensite (TRIP effect) and mechanical

twinning (TWIP effect) resulted in high sustained work hardening rates during plastic deformation. As a result, a favourable strength/ductility balance was achieved in the prototype steels. Moreover, Sn micro-alloying did not have a significant detrimental effect on the mechanical properties for the martensitic starting microstructure heat treatments which achieved target 3G-AHSS properties. This is promising in terms of developing a CGL-compatible processing route for these prototype steels.

3.2 Introduction

Medium-Mn steels are promising candidates to achieve third generation advanced high strength steel (3G-AHSS) mechanical property targets. A general mechanical property target range for 3G-AHSSs was outlined by Matlock and Speer [1], where a UTS × TE product of 24,000 – 40,000 MPa% was suggested. Additionally, specific UTS and TE targets have been proposed by the U.S. Department of Energy (i.e., 1200 MPa UTS × 30% TE and 1500 MPa UTS × 25% TE) [2] and the AutoSteel Partnership (1500 MPa UTS × 20% TE) [3]. The high strength – ductility balance of this new generation of advanced steels will allow the use of thinner cross-sections for structural autobody parts – thereby helping to meet legislated fuel efficiency targets for petroleum powered vehicles [1,4] and enabling longer battery ranges for electric vehicles – while meeting or improving passenger safety.

Recent research [5-16] has shown that medium-Mn steels can achieve 3G-AHSSs target mechanical properties through a variety of thermal processing routes and starting microstructures. High strength and ductility combinations were obtained by successful activation of multiple plasticity-enhancing mechanisms, which in turn maintained the instantaneous work-hardening rate at high values and allowed for continued increase in both the strength and elongation by delaying

the onset of necking. Two plasticity enhancing mechanisms cited in the medium-Mn literature are the TRansformation Induced Plasticity (TRIP) and TWinning Induced Plasticity (TWIP) effects.

In the case of the TRIP effect, chemically stable retained austenite gradually transforms to martensite during deformation, thereby continuously introducing a strong second phase into the microstructure while also generating geometrically necessary dislocations (GNDs) owing to the volumetric expansion associated with the retained austenite to martensite transformation [17-19]. Both of these deformation products impede dislocation movement and assist in maintaining high instantaneous work hardening rates. However, the activation of and transformation kinetics for the TRIP effect depend significantly on the chemical and mechanical stability of the retained austenite. Moreover, a balance between these factors is necessary to achieve the desired, gradual retained austenite to martensite transformation with applied deformation and, thereby, achieve the desired mechanical properties [5-16].

The Twinning-Induced Plasticity (TWIP) effect can also be activated if the retained austenite stacking fault energy (SFE) falls within a nominal range of ~15-45 mJ/m^2 [20]. Strengthening due to the TWIP effect is a result of the so-called "dynamic Hall-Petch effect" whereby twin boundaries are continuously introduced into the austenite grains, thereby decreasing the dislocation mean free path and enhancing the instantaneous work hardening rate [21-26]. Recently, numerous reports have shown that it is possible to activate both the TRIP and TWIP effects in medium-Mn steels when the retained austenite SFE is approximately 15-20 mJ/m^2 [7,13-16].

Several studies have determined that the steel starting microstructure has a strong effect on retained austenite formation kinetics, its volume fraction and stability during the deformation [10-16]. It was found that a martensitic starting microstructure can result in faster austenite reversion kinetics and higher volume fractions of retained austenite at lower intercritical annealing

temperatures versus a non-martensitic starting microstructures [10-16]. Moreover, martensite-derived retained austenite tends to have a very fine (less than 500 nm), lath-like morphology, which is known to be more mechanically stable versus blocky retained austenite due to the plastic constraints imposed from the surrounding martensite. In addition, the relatively fine lath-type retained austenite is likely more chemically stable than blocky retained austenite due to its higher C and Mn content arising from the shorter diffusion distances involved [10,18].

However, the annealing times used in much of the above literature were quite long, often on the order of hours, which far exceeds the typical heating and soaking times of 3-5 minutes used by continuous galvanizing lines (CGL) [27]. Thus, some research must be devoted to make medium-Mn 3G-AHSS thermal treatments compatible with CGL capabilities. Furthermore, it is well established that alloying elements such as Mn, Si, Al, and Cr will selectively oxidize in the dew point (dp) – and, therefore, oxygen partial pressure (pO_2) – controlled N_2–(5-20 vol%) H_2 CGL process atmosphere [28,29], where any external oxides formed can lead to poor reactive wetting by the Zn-alloy CGL bath [30,31]. However, using a higher process atmosphere pO_2 (i.e., higher dp) to promote internal oxidation, combined with micro-additions (0.05 wt%) of surface active Sn, has been found to promote successful reactive wetting for a model medium-Mn Fe-0.1C-6Mn-2Si-xSn (wt%) alloy [32]. However, the effect of Sn additions on the steel mechanical properties was not determined. Thus, the objective of this investigation is to determine the effects of starting microstructure, annealing parameters, and micro-alloying of Sn on the microstructural evolution and mechanical properties of a prototype, application-oriented medium-Mn 3G-AHSS steel. The global goal is to develop a CGL-compatible thermal processing route for the prototype alloy which would meet target 3G-AHSS mechanical properties and which can be reactively wetted by a

conventional galvanizing bath. The latter objective is beyond the scope of the present contribution and will be addressed in a subsequent publication.

3.3 Materials and Methods

3.3.1 Starting Materials and Thermal Treatments

The chemical compositions of the prototype medium-Mn steels, as determined by inductively coupled plasma (ICP) and combustion analysis, are shown in Table 3.1. These prototype steels were produced by U.S. Steel R&D (Munhall, PA), the detailed thermo-mechanical processing (TMP) route of which is shown in Figure 3.1. It should be noted that the TMP routes and compositions of the steels are insignificantly different other than the Sn micro-addition to steel F.

Table 3.1: Chemical Composition of the Prototype Medium-Mn 3G-AHSSs (wt%).

Steel	C	Mn	Si	Al	Cr	Ti	S	Sn	Si/Mn
A	0.18	5.91	1.46	0.43	0.59	0.008	0.0056	0.003	0.25
F	0.19	5.86	1.51	0.51	0.49	0.010	0.0025	0.049	0.25

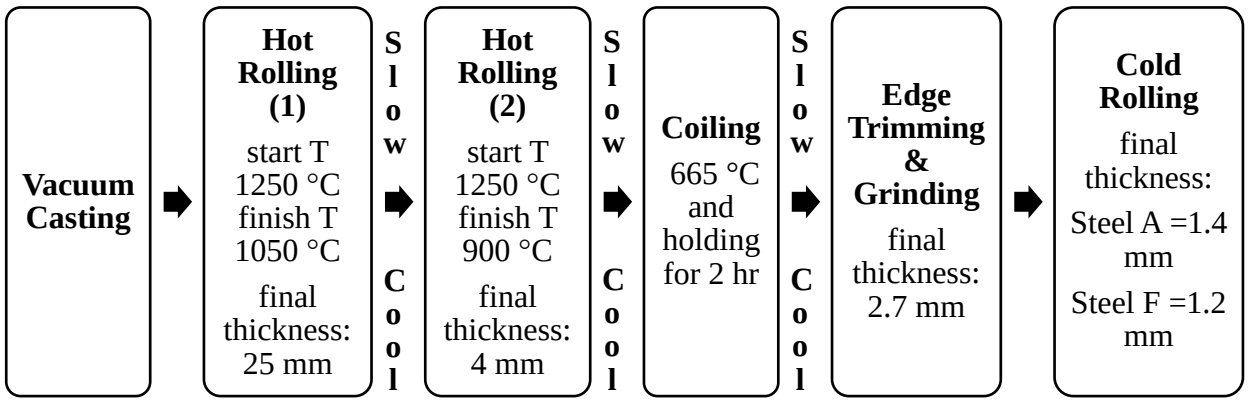

Figure 3.1: Thermo-mechanical processing route of the prototype medium-Mn steels.

Heat treatments were carried out to alter the microstructure and mechanical properties of the as received, cold-rolled (CR) steel sheets. All heat treatments were carried out using the McMaster Galvanizing Simulator (MGS, Iwatani-Surtec) under a N_2–5vol% H_2, –30 °C dew point process atmosphere. The MGS consists of an atmosphere-controlled column with an external quartz lamp infrared furnace – used for all heat treatments – and a cooling section comprising parallel platens fed by N_2. All heat treatments employed 120 mm × 200 mm panels such that the longitudinal axis of the panel was parallel to the rolling direction (RD). In all cases, the sample temperature was controlled *via* a 0.5 mm diameter type K thermocouple spot welded to the sample prior to heat treatment and a conventional feedback controller. The cooling rate of the samples was controlled by adjusting N_2 gas flow in the cooling platens.

As discussed above, it has been established that a martensitic starting microstructure can affect retained austenite evolution and the resultant mechanical properties in medium-Mn steels. In this regard, the as-received CR starting microstructures were subjected to a 775 °C 600 s austenitizing heat treatment, known to be above the alloy Ac_3 temperature, as determined *via* dilatometry. The samples were then gas quenched at –30 °C/s to room temperature. This resulted in a fully martensitic (M) starting microstructure for both steels, as will be discussed below.

Both the CR and M starting microstructures were subjected to a simulated CGL heat treatment cycle (shown schematically in Figure 3.2), where the samples were first heated to a target intercritical annealing temperature (IAT), held isothermally at the IAT for either 60 or 120 s, and then cooled at –10 °C/s to an overaging temperature (OT) of 460 °C, where the samples were held for 20 s. This latter step simulates the industrial CGL practice of thermally equilibrating the substrate with the 460 °C Zn bath [27]. Finally, the samples were cooled to room temperature at –10 °C/s. Table 3.2 provides a summary of the heat treatment parameters used. It should be noted

that the IATs were selected to produce greater than 0.5 volume fraction of intercritical austenite during annealing, as determined from dilatometry data. It should be further noted that the sample nomenclature used in Table 3.2 – e.g. A-CR and A-M denoting steel A with the CR and M starting microstructures – will be employed in all subsequent discussions.

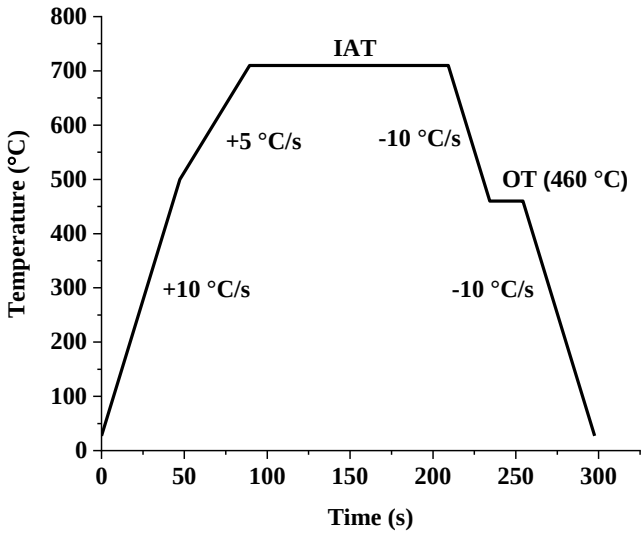

Figure 3.2: Schematic diagram of the heat treatment profile.

Table 3.2: Summary of Intercritical Annealing Parameters.

Sample ID	IAT (°C)	IAT Holding Time (s)	OT (°C)	OT Holding Time (s)
A-CR	675	60, 120	460	20
F-CR	690			
	710			

	650			
A-M	675	60, 120	460	20
F-M	690			
	710			

3.3.2 Mechanical Testing

All mechanical property tests used ASTM E8M-01ε2 [33] sub-size uniaxial tensile specimens (gauge dimensions = 25 mm × 6 mm). Mechanical testing samples were cut from the uniform heating area of the intercritically annealed panels (see Table 3.2) using electric discharge machining (EDM), where the tensile direction of the specimens was parallel to the rolling direction (RD). EDM was used in order to avoid any induced transformation of retained austenite in the gauge length prior to tensile testing. All tensile tests were conducted with an Instron 100 kN tensile frame at room temperature with a crosshead speed of 1 mm/min. A conventional extensometer (25 mm gauge) was used to measure sample elongation. All intercritical heat treatment samples were tested to failure and selected heat treatments which yielded promising properties were subjected to interrupted tensile tests, discussed below.

The true strain at fracture (ε_f) for the tensile samples tested to failure was calculated based on the reduction in the sample cross-sectional area using equation (3.1), where A_O is the original sample cross-sectional area and A_f is the cross-sectional area of the fracture surface. The area of the fracture surface was determined using a Keyence VHX-5000 optical microscope. The true stress at fracture (σ_f) was determined using equation (3.2), where L_f is the load prior to

fracture. The Hollomon power law equation was used to fit the true stress-true strain curves up to true strain at fracture (ε_f).

$$\varepsilon_f = \ln\left(\frac{A_O}{A_f}\right) \tag{3.1}$$

$$\sigma_f = \frac{L_f}{A_f} \tag{3.2}$$

Interrupted tensile tests were performed for selected intercritical annealing conditions in order to determine the deformation-induced retained austenite to martensite transformation kinetics. For these tests, samples were deformed to pre-determined levels of true tensile strain (e.g. 0.05, 0.10, 0.15, etc.), after which the sample cross-sections in the uniform elongation region of the gauge length were analysed using X-ray diffraction (XRD) and ASTM E975-13 [34] to determine the retained austenite volume fraction as a function of applied true strain.

3.3.3 Microstructural Characterisation

The as-annealed and tensile samples were examined at a variety of length scales to determine their microstructural evolution. The intercritically annealed samples were analysed using XRD in order to determine the retained austenite volume fraction *via* ASTM E975-13 [34] using the austenite (111), (200), and (220) peaks. The mounted sample cross-sections were polished with a series of SiC papers to remove approximately 500 μm from the cross-sectioned surfaces and eliminate any effects arising from cutting the sample. A Bruker D8 DISCOVER with a Co Kα (λ = 1.79026 Å) radiation source in a DAVINCI X-ray detector system was used for data collection. The sample was rotated during data acquisition to minimize any texture effect. DIFFRAC.EVA (v.4.0) software was used to process the diffraction data and obtain intensity *vs.* 2θ plots, which were then analysed using the TOPAS (v.4.2) software (Bruker). The measured

intensity was normalized with respect to the calculated structure factor for each phase and then the entire diffraction pattern was used to determine the volume fractions of each phase. The analytical error was computed based on the calculated and measured diffraction patterns.

The microstructures of the steels were determined as a function of thermal processing treatment and at a variety of length scales. The micron-scale structures of the steels were analysed using a JEOL 7000F field emission scanning electron microscope (FE-SEM). The samples were prepared in cross-section using standard metallographic techniques and etched using 2% nital. Prior to analysis, the samples were coated with a thin layer of carbon to avoid charging. An acceleration voltage of 10 keV, a working distance of 10 mm, and secondary electron image (SEI) mode were used in all cases.

The transmission electron microscope (TEM) was used to determine the nano-scale microstructure of the samples as a function of heat treatment. TEM was used to determine the carbide size and size distribution in the starting microstructures and for selected IA heat treatments using C-film extraction replicas prepared using standard techniques. A Talos L120C TEM was used to examine the extraction replicas using an acceleration voltage of 120 keV. The TEM micrographs were analysed with ImageJ (v.1.52a) to determine the carbide size distribution and area fraction (a.f.).

The carbides in the F-CR starting microstructure intercritically annealed at 675 °C for 120 s were analysed at the atomic scale using 3D atom probe tomography (APT) to determine possible Sn segregation to the carbide particle/matrix interface. A Cameca LEAP 4000X HR atom probe was used in all cases. The APT needles were prepared in a Zeiss NVision 40 focused ion beam (FIB). The sample surfaces were sputter-coated with Cr (~300 nm thick) to facilitate specimen preparation. The FIB lift-outs were sectioned and mounted onto silicon posts using W deposition

and sharpened into needles by annular milling at 30 keV using the technique of Thompson et al. [35]. Final sharpening was done at 10 keV to remove any FIB damage. The APT analysis of the needles was conducted in laser pulsing mode (λ = 355 nm, 60 pJ/pulse) with a stage temperature of ~60 K. The target detection rate was set at 0.005 ions/pulse (0.5%), which was maintained by an applied DC voltage. The laser pulsing rate was 200 kHz, as dictated by the applied voltage and maximum range of the mass spectrum. IVAS (v3.8.0) software was used for reconstruction and analysis of the APT data.

The fine-scale microstructures of selected intercritically annealed samples deformed to various strains (i.e., selected interrupted tensile tests) were also examined *via* TEM using conventional thin foils. TEM samples were prepared by electropolishing samples excised from the intercritically annealed panels and from the uniform elongation portion of selected interrupted tensile test samples. The excised samples were first ground to approximately 100 μm thickness using fine SiC papers and were then electropolished at 16 V in a twin jet electropolisher using an electrolyte comprising 10% perchloric acid in methanol held at –40 °C. Selected area diffraction (SAD) patterns and dark field (DF) TEM micrographs of the samples were analysed to identify the retained austenite in the samples and to detect the presence of mechanical twins therein as a function of applied strain. All microstructural analysis samples were analysed with a PHILIPS CM12 analytical TEM using an acceleration voltage of 200 keV.

Both the fracture surfaces and the fracture surface cross-sections of selected intercritically annealed A-M and F-M starting microstructures were analysed using SEM to determine the fracture mode – i.e., ductile, brittle or mixed mode fracture – and the microstructural origin of damage in the material. For the former, all fracture surfaces were examined using a JEOL 6610LV SEM in SEI mode at an acceleration voltage of 10 keV and a working distance of 20 mm. In the

latter case, fractured tensile samples were longitudinally cross-sectioned along the sample mid-width, cold mounted, and polished using conventional metallographic techniques. Prior to examination, the samples were etched using 2% nital and C coated to prevent charging. SEM examination was performed using a JEOL 7000F FE-SEM in SEI mode. In all cases, an acceleration voltage of 10 keV and a working distance of 10 mm were employed. Samples were examined from the fracture surface backwards into the uniform elongation portion of the fractured sample and the microstructural features associated with damage events were documented.

3.4 Results

3.4.1 Microstructural Evolution

The as-received (CR) and as-quench martensitic (M) starting microstructures for steels A and F were analysed with SEM. The results are shown in Figure 3.3. The CR microstructure for both steels consisted of tempered martensite and carbides whereas the M sample microstructures comprised martensite with no significant evidence of other phases visible at this length scale. TEM analysis was performed on the carbon extraction replicas for both starting microstructures to evaluate the carbide size distribution and area fraction within the microstructure. Representative results for the CR and M starting microstructures are provided in Appendix A, which includes a montage of low magnification bright field (BF) TEM micrographs and the corresponding carbide size distributions. As discussed above, the carbide area fractions (a.f.) were determined by analysing multiple BF TEM micrographs, a summary of which can be found in Figure 3.6. From these data, it can be seen that A-CR staring microstructure had approximately ten times the area fraction of carbide particles compared to the F-CR starting microstructure (Figure 3.6) without a significant difference in the carbide size distribution (i.e., see Appendix A Figure 3.24a *vs.* Figure 3.24e).

Contrastingly, the A-M and F-M starting microstructures had significantly finer carbides and lower area fractions of carbide particles in the microstructure, as shown in Appendix A and Figure 3.6. As documented in Table 3.3, significant carbide dissolution occurred during austenization, with the C remaining in the martensite as supersaturated carbon after quenching. However, examination of Figure 3.6 and Table 3.3 will show that the dissolution of carbides during the austenitizing + quenching heat treatment of the A-CR (i.e., A-CR → A-M thermal treatment) and F-CR starting microstructures was significantly different, with approximately 90% of the carbide particles being dissolved during A-CR austenization whereas only 40% of the F-CR carbides dissolved in the case of F-CR austenization (Table 3.3 and Figure 3.6).

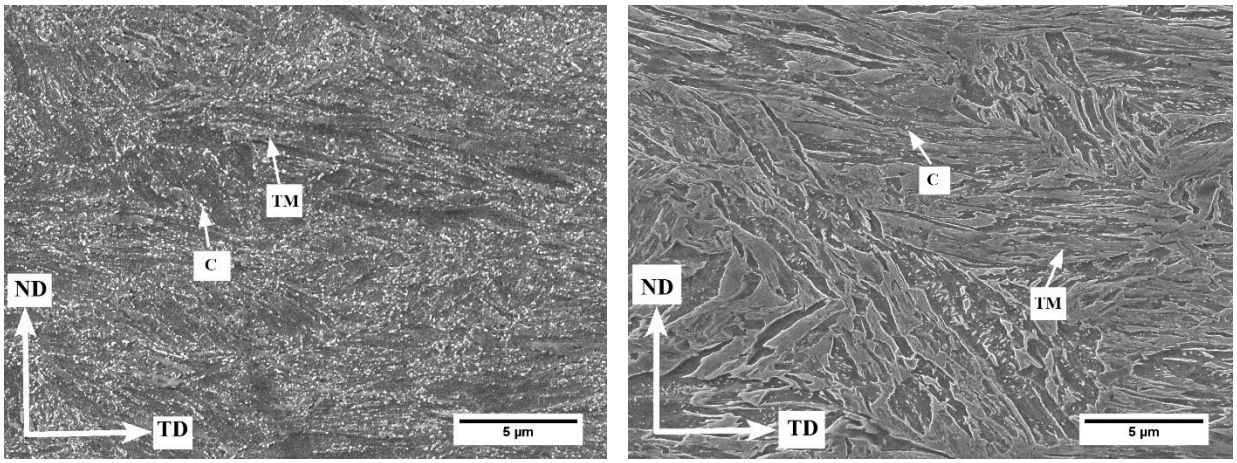

a) b)

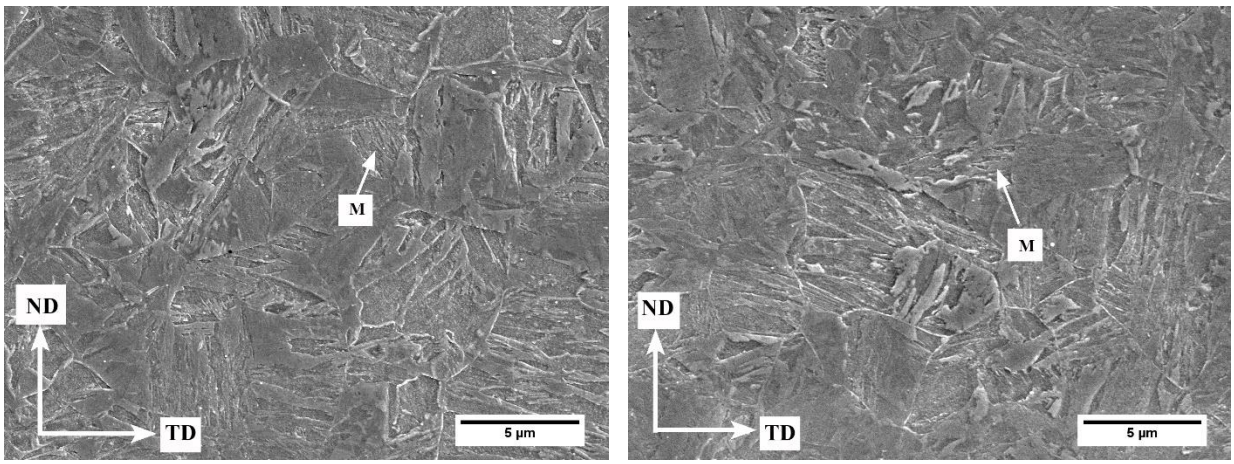

c) d)

Figure 3.3: SEM images of as-received cold-rolled a) steel A-CR, b) steel F-CR and as-quenched martensitic c) steel A-M and d) steel F-M microstructures; ND = Normal Direction, TD = Transverse Direction, C = Carbides, TM = Tempered Martensite, M = Martensite.

The microstructures of the intercritically annealed samples were determined using SEM. Figure 3.4 shows the microstructures of the A-CR and F-CR starting microstructures intercritically annealed for 120 s at 690 ℃ and 710 ℃. The IA microstructures consisted of various fine-grained phases (ferrite, retained austenite, and martensite) with carbide particles precipitated largely at the grain boundaries. Although it was difficult to distinguish between martensite and retained austenite with SEM, the morphology of the martensite/retained austenite islands were identified as blocky-type. The microstructures of the A-M and F-M starting microstructures intercritically annealed at 650 ℃, 675 ℃, and 710 ℃ for 120 s are shown in Figure 3.5. These microstructures consisted of polygonal ferrite and both blocky- and lath-type martensite/retained austenite with carbide particles at the grain boundaries. This general microstructure as a function of starting microstructure is consistent with the observations of other researchers [10,13-16].

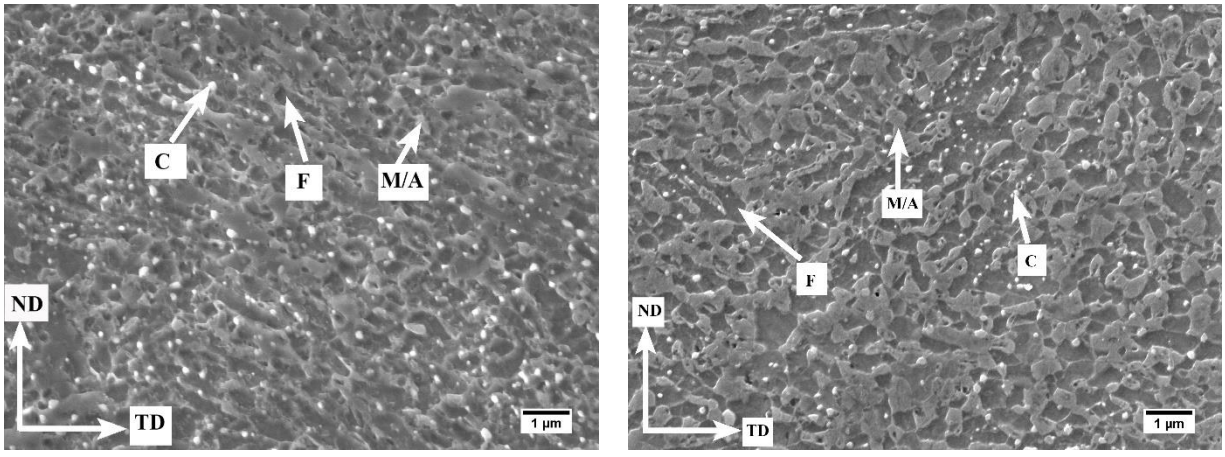

a) b)

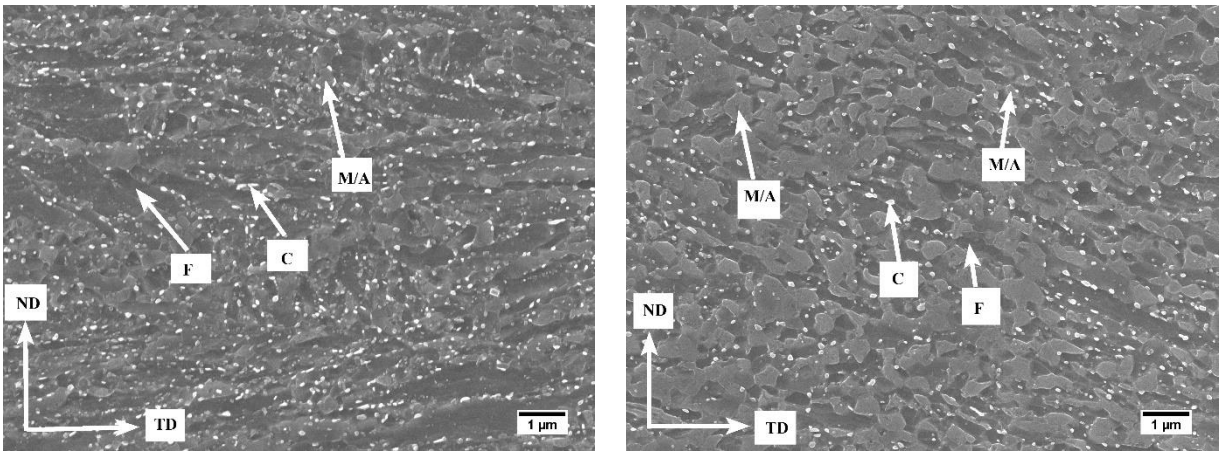

c) d)

Figure 3.4: SEM micrographs of A-CR starting microstructures intercritically annealed for 120 s at a) 690 °C and b) 710 °C; F-CR starting microstructures intercritically annealed for 120 s at c) 690 °C and d) 710 °C; ND = Normal Direction, TD = Transverse Direction, F = Ferrite, M = Martensite, A = Retained Austenite, and C = Carbides.

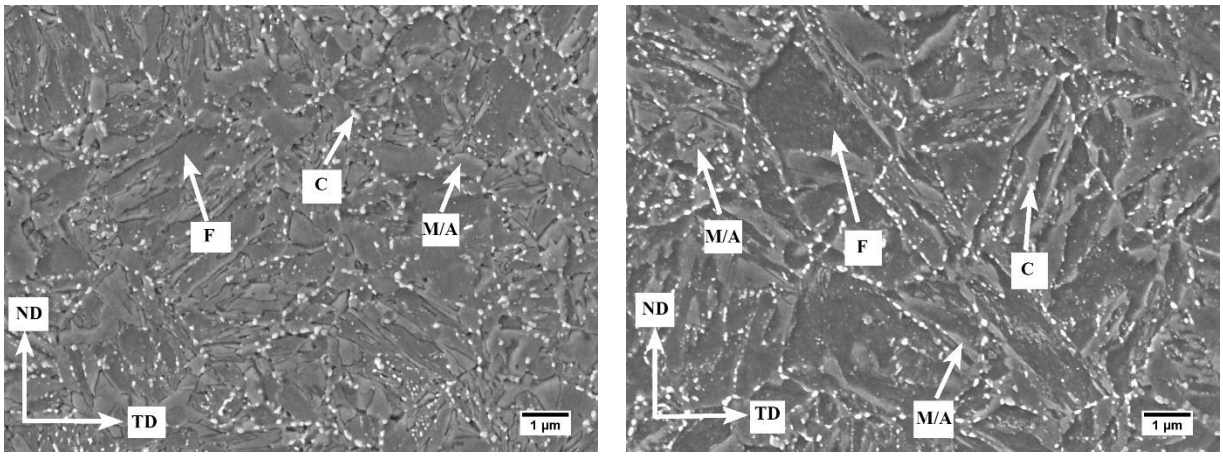

a) d)

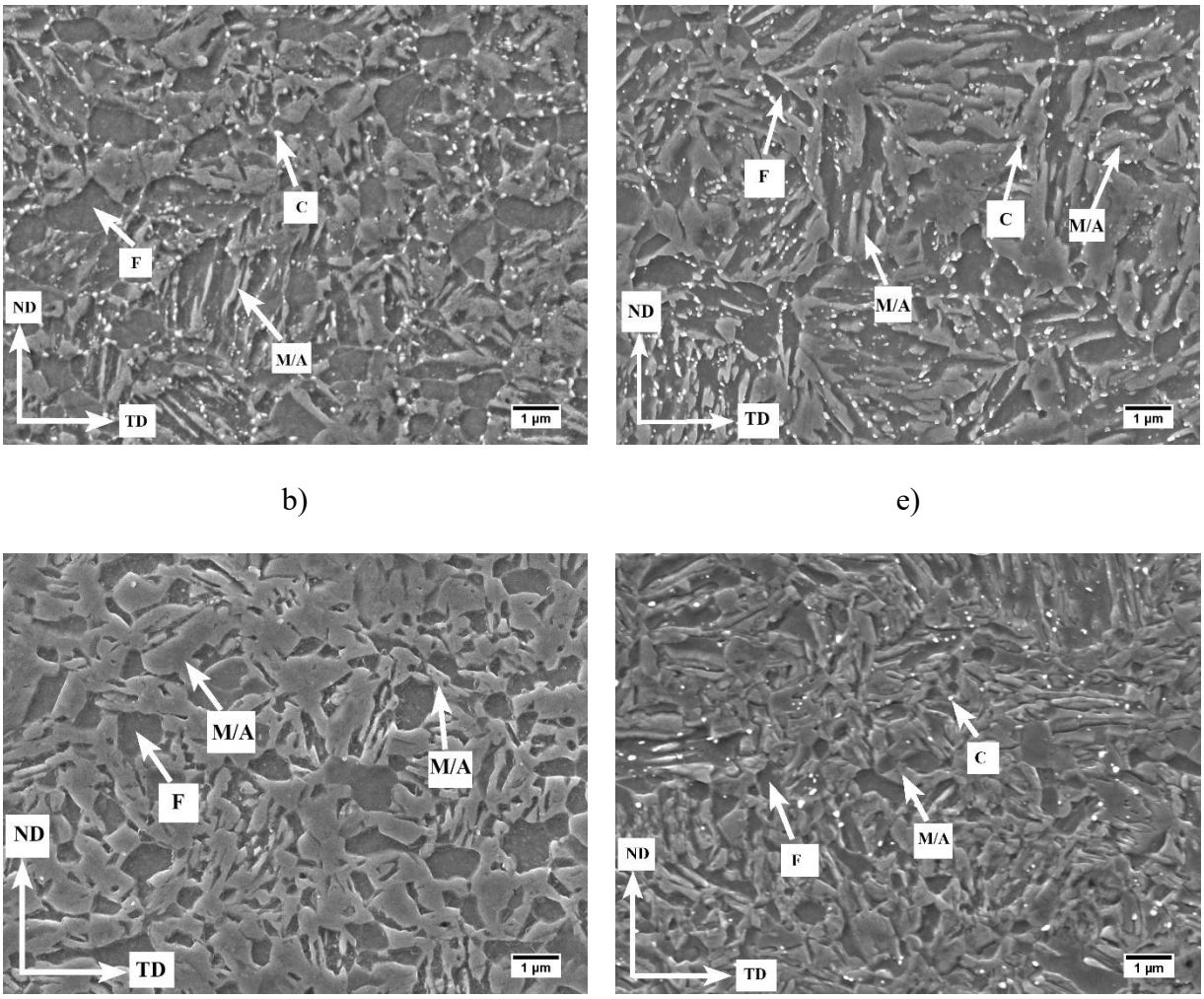

Figure 3.5: SEM micrographs of A-M starting microstructures intercritically annealed for 120 s at a) 650 °C, b) 675 °C, and c) 710 °C; F-M starting microstructures intercritically annealed for 120 s at d) 650 °C, e) 675 °C, and f) 710 °C; ND = Normal Direction, TD = Transverse Direction, F = Ferrite, M = Martensite, A = Retained Austenite, and C = Carbides.

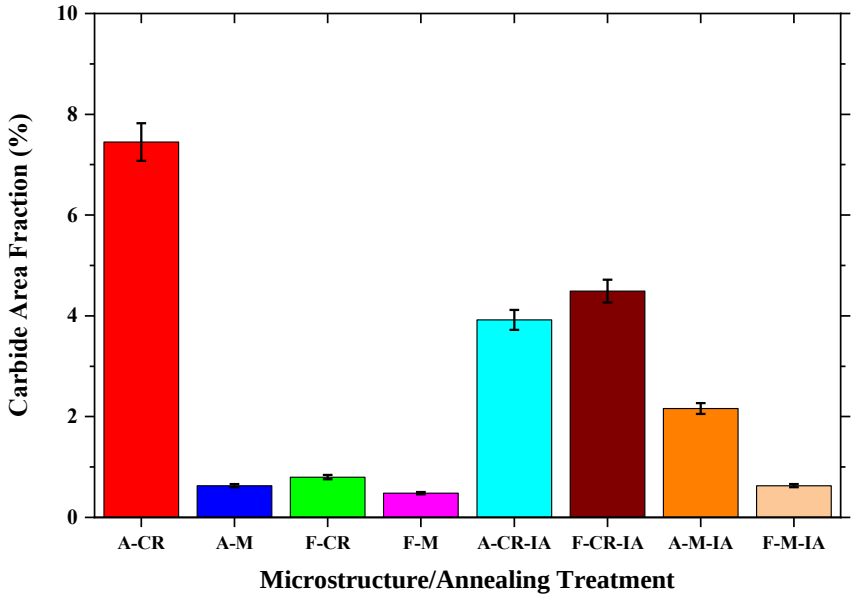

Figure 3.6: Carbide area fraction for steels A and F as a function of microstructure/heat treatment. Note that all intercritically annealed samples utilized the 675 ℃ 120 s IA treatment.

Table 3.3: Change in carbide area fraction and size distribution as a function of thermal treatment.

Steel ID.	Thermal Process	Δ carbide area fraction (%)	Carbide Evolution
A	A-CR → A-M	–6.9 ± 0.4	major carbide dissolution + minor reprecipitation and growth of carbides
	A-CR → A-CR-IA	–3.6 ±0.6	major carbide dissolution + minor reprecipitation and growth of carbides
	A-M → A-M-IA	+1.6 ± 0.1	significant carbide precipitation + minor growth of carbides

F	F-CR → F-M	–0.3 ± 0.06	minor carbide dissolution + minor fine carbide precipitation (possible Sn inhibition effect)
	F-CR → F-CR-IA	+3.7 ± 0.2	significant precipitation and growth of carbides (different from A-CR)
	F-M → F-M-IA	+0.1 ± 0.05	minor precipitation and growth of carbides (possible Sn inhibition effect)

The carbide distribution of all starting microstructures intercritically annealed at 675 °C × 120 s was determined *via* carbon extraction replicas and TEM analysis. The findings of these analyses are summarized in Figure 3.6 and Table 3.3. Representative collages of the carbon extraction replicas and size distribution analyses are provided in Appendix A. In the case of the A-CR starting microstructure, the carbide particle size and area fraction of carbides decreased significantly after the 675 °C × 120 s IA treatment, as shown by examining Figure 3.6, Appendix A, and the A-CR → A-CR-IA treatment in Table 3.3. This suggests that the carbides either partially or completely dissolved during the IA anneal into carbide-nucleated growing austenite [36,37]. Thus, the dissolving carbide particles were likely a significant source of carbon that assisted in chemically stabilizing the intercritical austenite. Contrastingly, in the case of the F-CR starting microstructure, significant carbide precipitation and particle growth were observed after the 675 °C × 120 s IA (i.e., F-CR → F-CR-IA (Table 3.3), Appendix A, and Figure 3.6) with this microstructure ultimately having a higher area fraction of carbides versus the A-CR-IA

microstructure (Figure 3.6). This suggests that there was slightly less carbon available in the F-CR-IA microstructure to chemically stabilize the intercritical austenite.

Fine carbide particles precipitated at grain boundaries during the intercritical annealing treatment of the A-M and F-M starting microstructures (Appendix A), where Figure 3.6 and Table 3.3 show an increase in carbide area fraction after the 675 °C × 120 s IA of the martensitic starting microstructures. It should be noted that, as documented in Table 3.3, this increase was significant in the case of the A-M → A-M-IA treatment whereas it was less significant in the case of the F-M → F-M-IA treatment with the carbide fraction being significantly higher in the A-M-IA microstructure. These results suggest the source of C in the A-M and F-M starting microstructures was the supersaturated C in the martensite phase. This supersaturated C partitioned into the growing intercritical austenite – likely the interlath retained austenite – and provided the required chemical stabilization of the retained austenite in the final microstructure. This is consistent with the austenite reversion mechanism proposed by various researchers [10,36,37] for C partitioning during intercritical annealing of a martensitic medium-Mn steel.

As the F-CR 675 °C 120 s sample had the highest area fraction of carbides among the steel F samples, it was chosen for APT analysis to determine possible Sn segregation to the carbide particles. The results are shown in Figure 3.7. The 3D atom map for carbon confirmed the presence of a (Cr,Nb) carbide particle in the APT needle, as shown in Figure 3.7a). A higher magnification map of the APT needle (Figure 3.7b)) also revealed that Sn segregation occurred to the carbide/matrix interface. Furthermore, a 1D compositional profile taken across the carbide particle, along the arrow marked in Figure 3.7a), showed an approximately 10× increase in Sn concentration at the carbide/matrix interface versus the bulk Sn content.

Further examination of Table 3.3 and Figure 3.6 will show that there are significant differences in the carbide dissolution and precipitation processes occurring in steel A and steel F during the thermal processing of these steels, despite the fact that there are no significant differences in the TMP route (Figure 3.1 and Figure 3.2) and the only significant compositional difference being the presence of the Sn micro-addition in steel F (Table 3.1). As shown in Figure 3.7, it is very likely that Sn has segregated to the surface of the carbide particles in steel F and may acted as a diffusion barrier for carbon diffusion as well as carbide nucleation and diffusion-driven growth. These observations are consistent with the results of previous researchers who reported significant reduction in oxidation and decarburization kinetics owing to Sn segregation to grain boundaries and external surfaces [38-41]. For example, when comparing the A-CR to F-CR microstructures, the very small volume fraction of carbides in the F-CR microstructure can be attributed to the presence of a nucleation and growth barrier, which may have been Sn. The carbide precipitation observed for the F-CR → F-M treatment can be accounted for by an inhibition for carbide dissolution during austenization annealing and an inhibited carbide nucleation and growth mechanism. The differences in the carbide growth observed during the intercritical anneals are also consistent with an inhibiting effect on carbide dissolution, nucleation, and growth. Furthermore, as will be discussed below, this inhibiting effect would also have implications for C partitioning into the growing intercritical austenite and the chemical stability of the retained austenite.

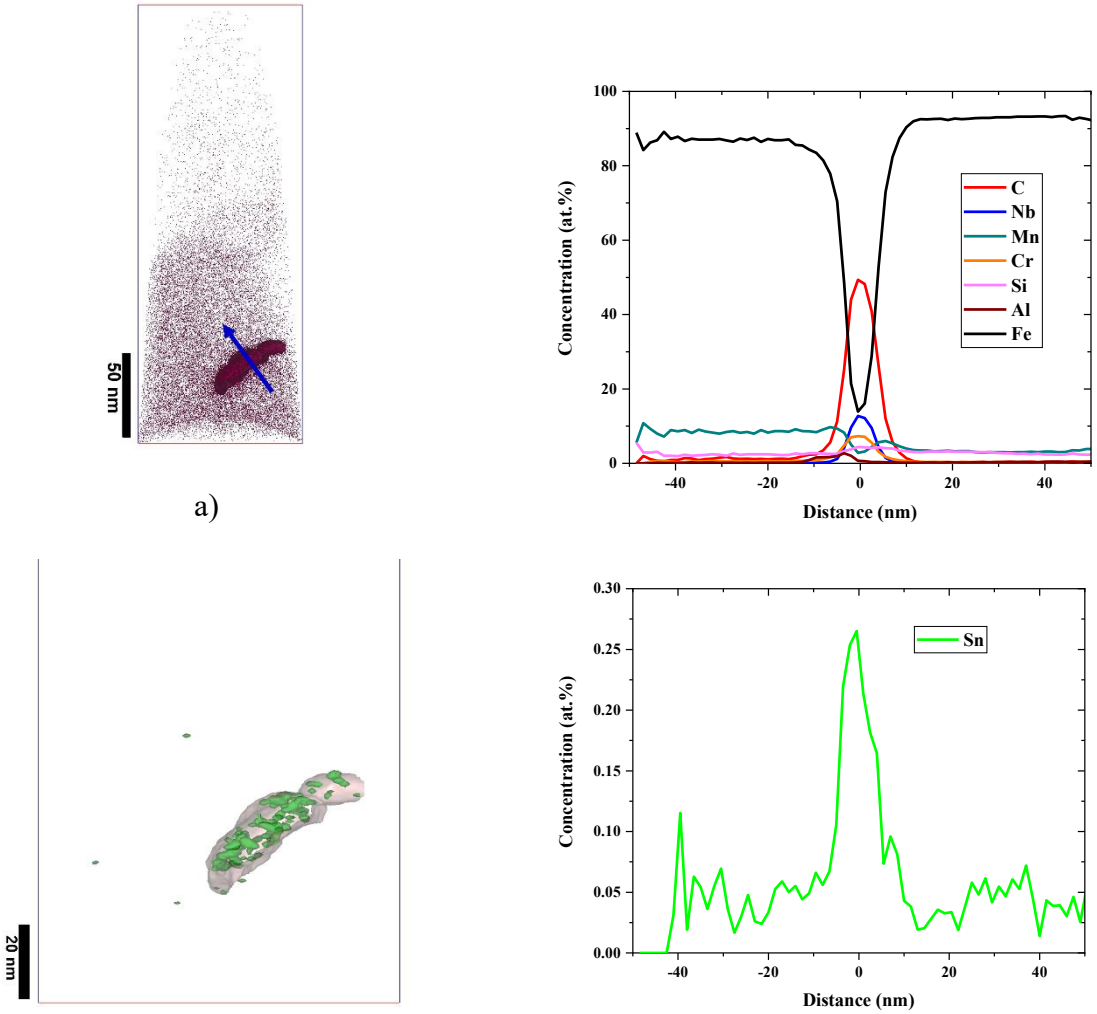

Figure 3.7: APT analysis of a carbide particle in the F-CR starting microstructure sample intercritically annealed at 675 °C × 120 s; a) C atom map, b) magnified map (0.8 at.% Sn + 20 at.% C isosurface) showing the carbide particle with interfacial Sn segregation shown in green, and c) proxigram showing 1D concentration profiles along the blue arrow in a).

3.4.2 Retained Austenite after Intercritical Annealing

The retained austenite volume fraction of the intercritically annealed CR starting microstructures as a function of IAT and IA holding times are shown in Figure 3.8a). For both the A-CR and F-CR starting microstructures, the retained austenite volume fraction increased with

increasing IAT and IA holding time. These results are consistent with increased partitioning of C to the intercritical austenite with increasing temperature and time. This trend agrees with the results reported by previous research [6,8,13-16]. However, the retained austenite volume fractions for the F-CR starting microstructures were significantly lower than those of the A-CR starting microstructures processed with the same annealing conditions. This is attributed to the smaller mass of C available to stabilize the retained austenite, as can be implied from the higher area fraction of carbides in the F-CR-IA microstructure (Figure 3.6) and the inhibiting effect of the Sn in steel F. This resulted in reduced chemical stability of the intercritical austenite, resulting in a larger fraction of intercritical austenite being transformed to martensite during final cooling and lower retained austenite fractions.

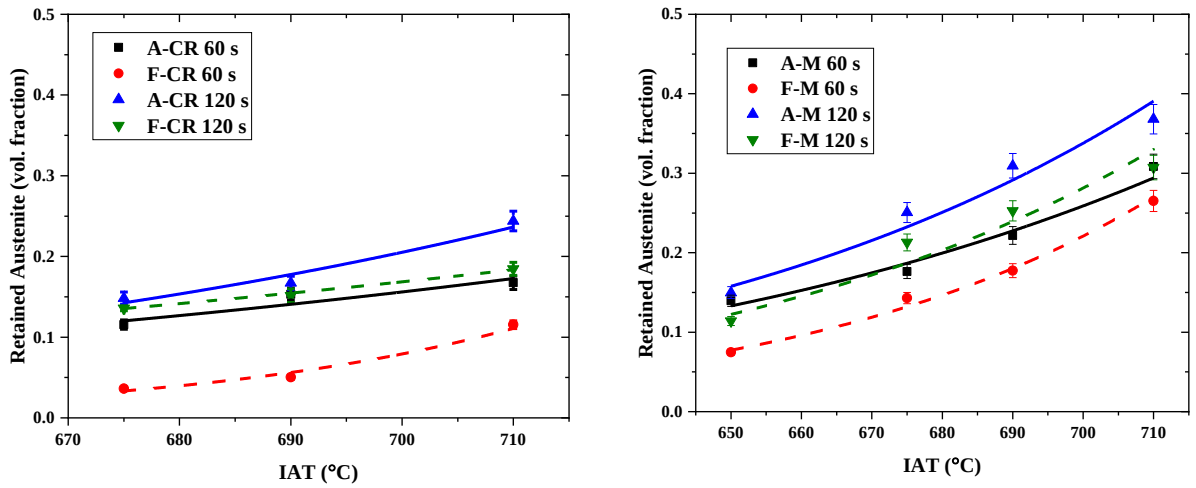

a) b)

Figure 3.8: Retained austenite volume fraction as a function of IAT and IA holding time for a) A-CR and F-CR and b) A-M and F-M starting microstructures.

A similar analysis was carried out for the annealed A-M and F-M starting microstructures, the results of which are shown in Figure 3.8b). An increasing trend in retained austenite volume fraction with increasing IAT and IA holding time was observed, with greater than 0.30 volume

fraction of retained austenite observed at the 710 °C IAT regardless of holding times and steel chemistry. Moreover, similar to the results for the CR starting microstructures (Figure 3.8a)), the retained austenite volume fraction for the F-M starting microstructures was significantly less than that for the A-M starting microstructures for the same annealing conditions due to reduced carbon diffusion kinetics owing to Sn segregation.

Furthermore, comparing the same IATs (675, 690, and 710 °C) for the same steel chemistry as a function of starting microstructure (i.e., Figure 3.8a) *vs.* Figure 3.8b)), it can be seen that the martensitic starting microstructure yielded higher volume fractions of retained austenite for both steels. This was due to faster austenite reversion kinetics from the martensitic starting microstructure, consistent with results reported in the literature [10-16,36,37]. The faster austenite reversion kinetics are attributed to two factors: i) a lower nucleation barrier as there are significant interlath retained austenite films and ii) a C supersaturated martensitic starting microstructure with a significant amount of stored elastic energy in the form of dislocations, both of which help drive the partitioning of C to the growing interlath retained austenite and, thereby, increase its chemical stability [10,36,37].

The stability of the retained austenite, as characterised by the deformation-induced martensite start $\left(M_S^{\sigma}\right)$ temperature, is an important factor in determining the retained austenite to martensite deformation-induced transformation kinetics. As stated by Lee et al. [42], the M_S^{σ} temperature is a strong function of the retained austenite composition, particularly the C and Mn contents, and grain size. The authors also reported that the retained austenite M_S^{σ} temperature increases (i.e., stability decreases) at higher annealing temperature owing to lower retained austenite C contents, resulting in early activation and rapid exhaustion of the TRIP effect at low strains [42]. In this regard, the ThermoCalc® (TCFE 6 database) was used to calculate the alloy phase diagram and

determine the equilibrium C content of the intercritical austenite as a function of intercritical annealing temperature assuming negligible partitioning of the other solutes (e.g. Mn, Si, Al, Cr) versus the bulk composition listed in Table 3.1. The recently published equation of Karr et al. [43] for 3G steels, equation (3.3), was used to compute the M_S temperature of the resultant intercritical austenite:

$$M_S\left(^{\circ}\mathrm{C}\right) = 692 - 502\left(C + 0.86N\right)^{0.5} - 37Mn - 14Si + 20Al - 11Cr \qquad (3.3)$$

where all compositions are in wt%. The results of intercritical austenite C content and the M_S temperature are provided in Figure 3.9.

Using the results of Figure 3.9 to qualitatively assess the retained austenite M_S^{σ}, it can be seen that the intercritical austenite has a minimum M_S temperature and, by implication, a minimum M_S^{σ} temperature, for intercritical annealing temperatures of between 650 and 670 °C. This result suggests that the chemical and mechanical stability of the intercritical austenite formed in both steels at IATs greater than 675 °C may be significantly lower compared to that formed at 650 °C and 675 °C. Furthermore, the lower intercritical austenite C content at IATs greater than 675 °C may have resulted in the transformation of significant volume fraction of intercritical austenite to martensite during final cooling. This trend is shown in Figure 3.10, which indicates that there was a significant increase in the fresh martensite volume fraction (determined based on the difference between the equilibrium intercritical austenite and retained austenite volume fractions) with increasing IAT and IA holding times. Moreover, although the 710 °C IAT resulted in higher volume fractions of retained austenite in both alloys (Figure 3.8), the findings from Figure 3.9 suggest that the resultant retained austenite may be less stable during deformation owing to a qualitative increase in the M_S^{σ} of the retained austenite (Figure 3.9b)).

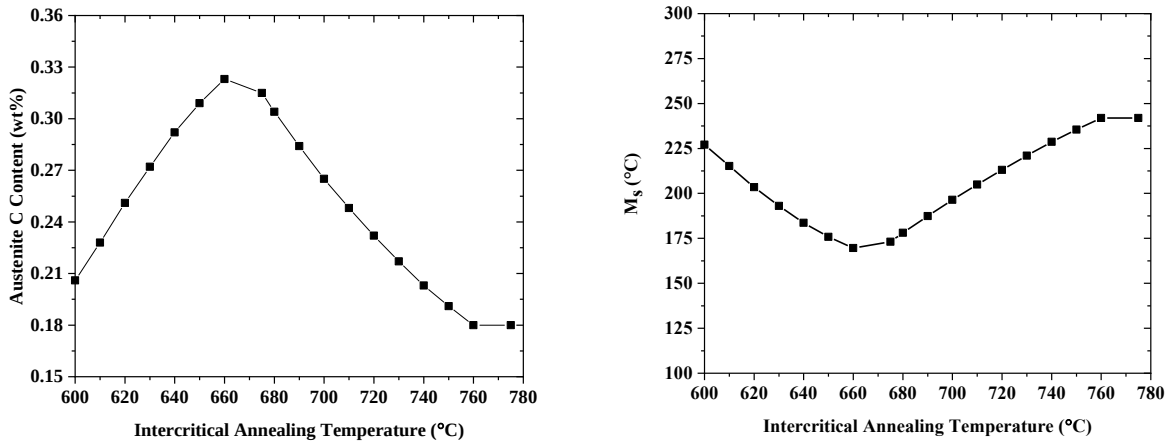

a) b)

Figure 3.9: a) Equilibrium intercritical austenite C content as a function of IAT and (b) M_s temperature of the retained austenite assuming full C partitioning and negligible partitioning of Mn, Si, Al, and Cr versus the bulk concentrations in Table 3.1.

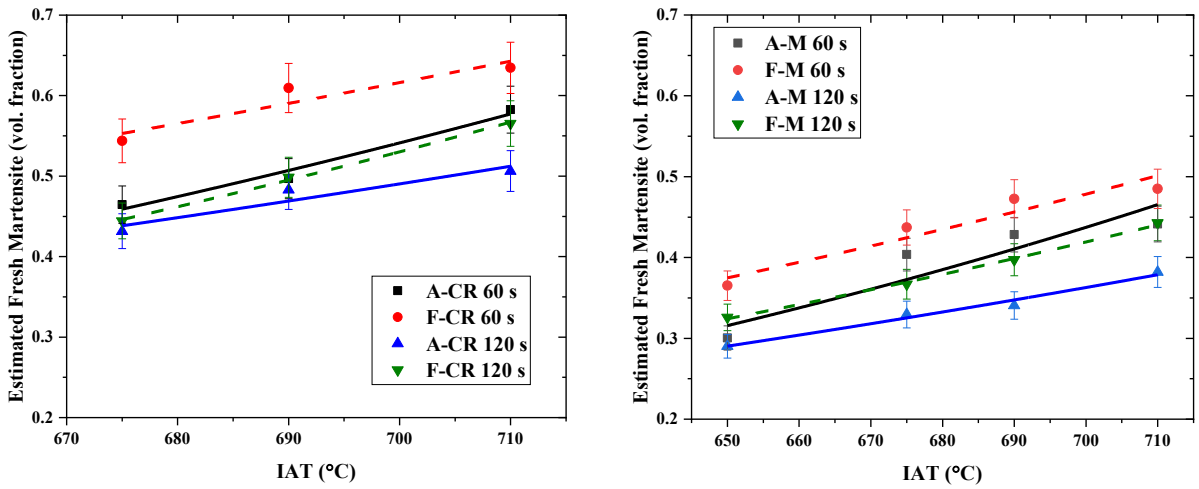

a) b)

Figure 3.10: Estimated fresh martensite volume fraction as a function of IAT and IA holding time for a) A-CR and F-CR and b) A-M and F-M starting microstructures.

3.4.3 Mechanical Properties

Uniaxial tensile tests were conducted on all intercritically annealed samples. The resulting engineering stress – engineering strain, true stress – true strain curves, and the calculated work hardening rate curves ($d\sigma/d\varepsilon$, calculated from the true stress – true strain curves) plotted as a function of true strain are shown in Figure 3.11, Figure 3.12, Figure 3.14, and Figure 3.15. In addition, the retained austenite transformation kinetics of selected samples as a function of starting microstructure and applied true strain are shown in Figure 3.13 and Figure 3.16.

The mechanical properties of the intercritically annealed steels were a strong function of the IA parameters. Two general trends were observed in the engineering stress – engineering strain and true stress – true strain curves regardless of the starting microstructure and steel chemistry. Lower IATs – i.e., 675 °C and 690 °C for the A-CR and F-CR starting microstructures and 650 °C and 675 °C for the A-M and F-M starting microstructures – resulted in relatively high yield strengths (YS) and significant yield point elongations (YPE), as shown in Figure 3.11a), Figure 3.12a), Figure 3.14a), and Figure 3.15a), respectively. Similar high YPE has also been reported by other researchers [8,9,14-16]. In the case of the 710 °C IAT for all starting microstructures it can be seen that the yield strength dropped significantly.

Following the YPE, an increase in the work hardening rate was observed for all CR starting microstructures intercritically annealed at 675 °C and 690 °C (marked by arrows in Figure 3.11c) and Figure 3.12c)) and the M starting microstructures intercritically annealed at 650 °C and 675 °C (similarly marked in Figure 3.14c) and Figure 3.15c)) owing to the activation of plasticity enhancing mechanisms such as the TRIP and/or TWIP effects. Figure 3.13 and Figure 3.16 show that all starting microstructures intercritically annealed at 675 °C × 120 s exhibited gradual retained austenite to martensite transformation kinetics, with the TRIP effect being exhausted at relatively

high strains. This indicates that the retained austenite from these treatments had sufficient chemical and mechanical stability to sustain the high work hardening rates such that the onset of necking was delayed and the desired high strength/ductility balance was obtained (Figure 3.11c), Figure 3.12c), Figure 3.14c), and Figure 3.15c)). It should also be noted that a significant amount (~0.06 volume fraction) of retained austenite remained untransformed at fracture for the A-CR-IA 675 °C 120 s samples (Figure 3.13). This is an indication of a higher chemical and mechanical retained austenite stability than desired. In addition, the true stress-true strain curves (Figure 3.11b), Figure 3.12b), Figure 3.14b), and Figure 3.15b)), plotted to the true strain at fracture (ε_f), showed significant post-uniform elongation ($\varepsilon_f \geq 0.40$) for the samples intercritically annealed at ≤ 690 °C for the CR and ≤ 675 °C for the M starting microstructures. This is promising in terms of the potential formability of these steels as post-uniform elongation has been shown to have a reasonably good correlation with material formability [44,45].

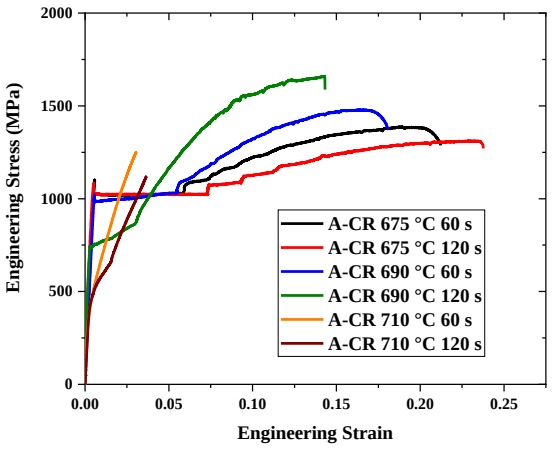

a)

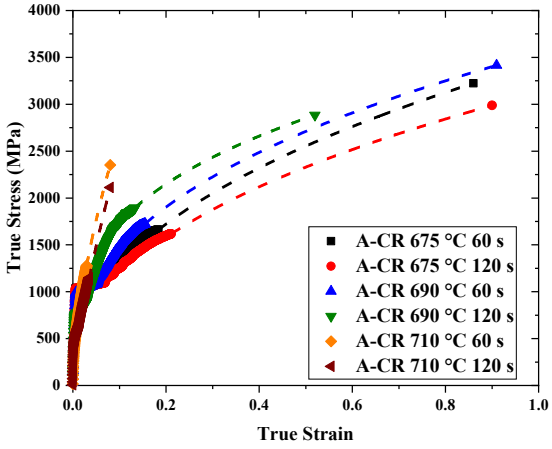

b)

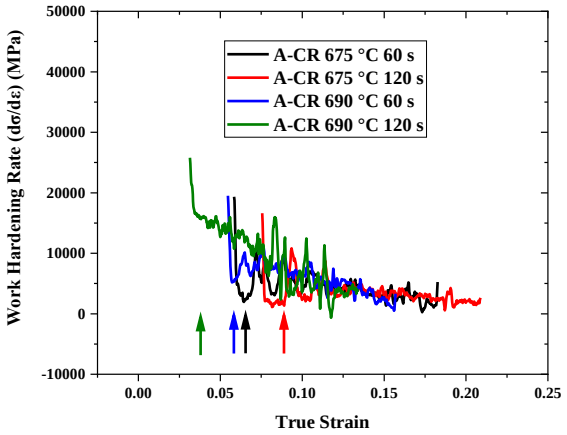

c)

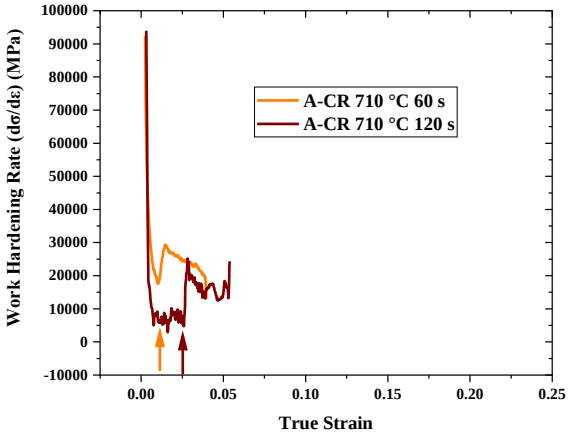

d)

Figure 3.11: a) Engineering stress *vs.* strain b) true stress *vs.* strain curves as a function of IAT and IA holding time for A-CR starting microstructures, and c) and d) corresponding work hardening rate *vs.* true strain curves.

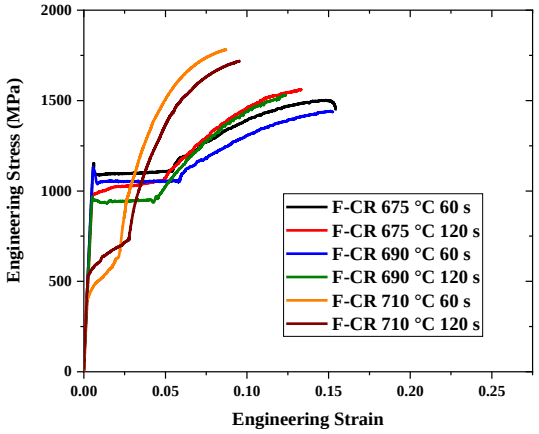

a)

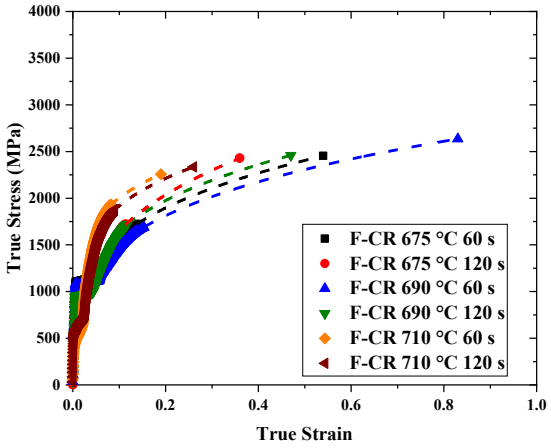

b)

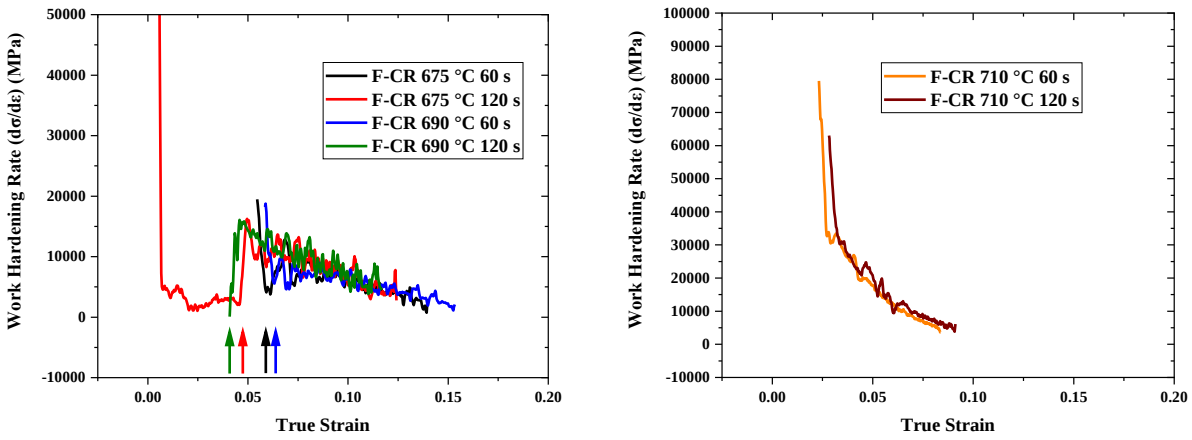

c) d)

Figure 3.12: a) Engineering stress *vs.* strain b) true stress *vs.* strain curves as a function of IAT and IA holding time for F-CR starting microstructures, and c) and d) corresponding work hardening rate *vs.* true strain curves.

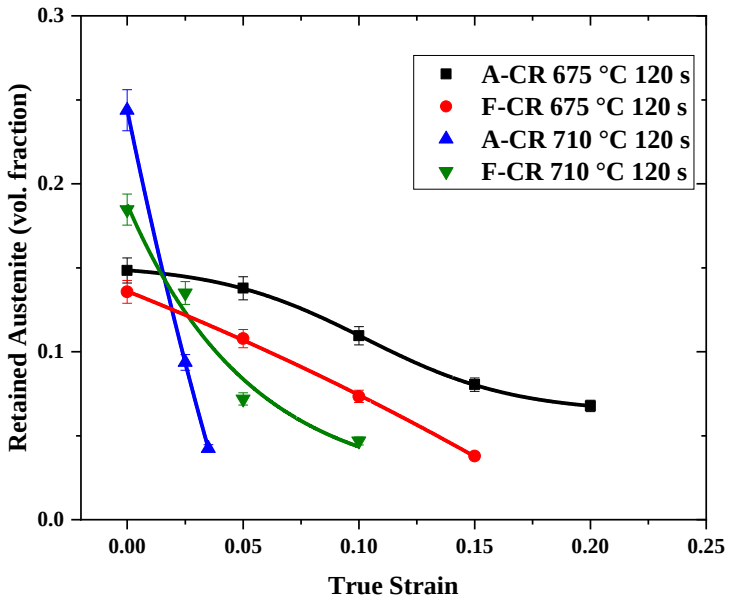

Figure 3.13: Retained austenite transformation kinetics for A-CR and F-CR starting microstructures annealed for 120 s as a function of IAT.

On the other hand, the YS and total elongation (TE) decreased while the ultimate tensile strength (UTS) increased significantly for all starting microstructures intercritically annealed at

710 °C, as shown in Figure 3.11a), Figure 3.12a), Figure 3.14a), and Figure 3.15a). This decrease in YS and TE, along with increased UTS, was also observed for the A-CR-IA 690 °C 120 s sample (Figure 3.11a)). It is expected that the higher volume fractions of retained austenite present in these samples (Figure 3.8) would have lower C contents to satisfy the C mass balance and have, consequently, lower retained austenite stability and a more rapid exhaustion of the TRIP effect (Figure 3.13 and Figure 3.16). These observations are consistent with the results reported by Gibbs et al. [8]. This rapid exhaustion of the TRIP effect at low strains resulted in the rapid continuous decrease in work hardening rate with increasing true strain (Figure 3.11d), Figure 3.12d), Figure 3.14c), and Figure 3.15c)) more characteristic of dual phase steels versus the starting microstructures intercritically annealed at 675 °C or lower [9,13-16,42,46-48]. The rapid retained austenite transformation kinetics along with increased fresh martensite volume fraction (Figure 3.10) which formed during final cooling from higher IAT (≥ 675 °C) resulted in high UTS and low TE in these annealed samples. It should be noted that there was not any significant difference in the mechanical properties of A-M and F-M starting microstructures intercritically annealed at 690 °C and 710 °C. Hence, only the mechanical properties of A-M and F-M starting microstructures intercritically annealed at 710 °C are presented in Figure 3.14 and Figure 3.15.

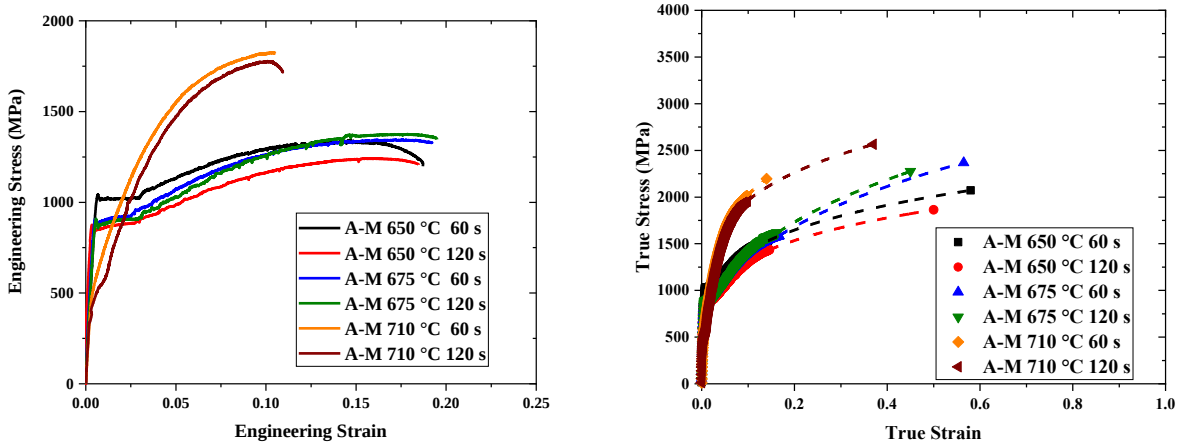

a) b)

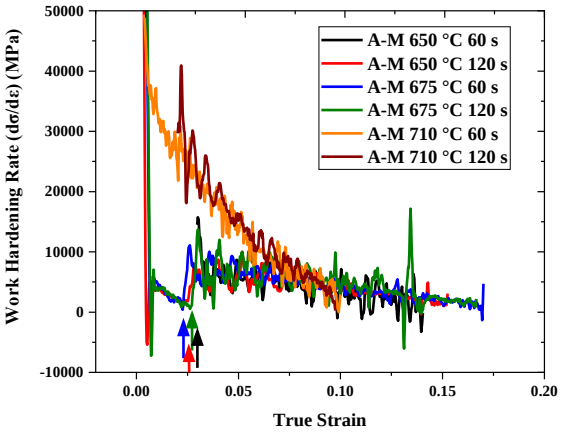

c)

Figure 3.14: a) Engineering stress *vs.* strain, b) true stress *vs.* strain curves as a function of IAT and IA holding time for A-M starting microstructures, and c) corresponding work hardening rate *vs.* true strain curves.

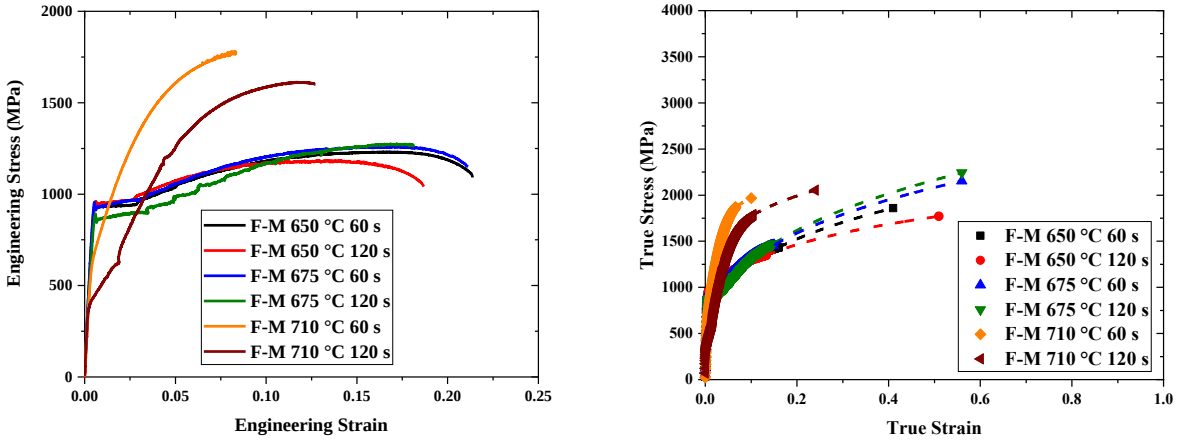

a) b)

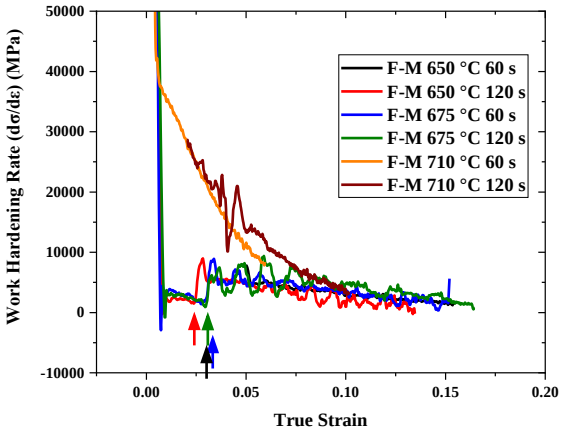

c)

Figure 3.15: a) Engineering stress *vs.* strain, b) true stress *vs.* strain curves as a function of IAT and IA holding time for F-M starting microstructures, and c) corresponding work hardening rates *vs.* true strain curves.

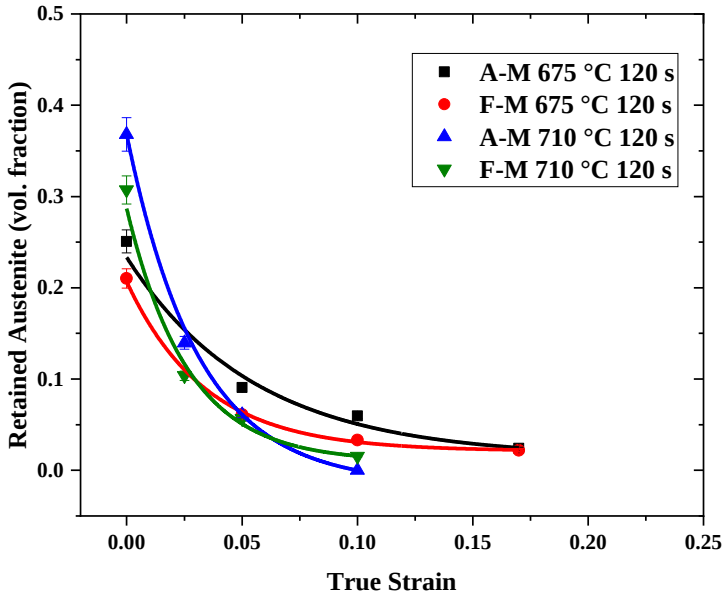

Figure 3.16: Retained austenite transformation kinetics for A-M and F-M starting microstructures annealed for 120 s as a function of IAT.

A summary of the starting microstructures and intercritical annealing parameters that resulted in the prototype steels meeting the 3G-AHSS target property envelope of UTS × TE ≥

24,000 MPa% is provided in Table 3.4. It can be seen that the IATs of 675 °C and 690 °C for the A-CR starting microstructure and 650 °C and 675 °C for the A-M and F-M starting microstructures met the target 3G-AHSS mechanical properties. It is notable that none of the F-CR intercritical heat treatments met the target property envelope. Further examination of the summative mechanical property trends as a function of steel composition, starting microstructure, and intercritical annealing parameters (Figure 3.17) will show that the mechanical properties of the CR starting microstructures – particularly the UTS and TE – were sensitive to the IA temperature, where the latter declined sharply with increasing IA. Table 3.4, Figure 3.17c), and Figure 3.17d) also revealed that there were only slight differences in the mechanical properties of the A-M and F-M starting microstructures annealed under the same conditions. This suggests Sn micro-alloying did not have any detrimental effect on the mechanical properties of the prototype steel with a martensitic starting microstructure. From these trends and the UTS × TE information in Table 3.4, it was concluded that the M starting microstructures possessed a more robust thermal stability and were, therefore, selected as the focus of detailed characterisation work. In particular, the A-M-IA and F-M-IA 675 °C 120 s treatments were selected for more detailed investigations as these resulted in 3G-AHSS properties for both alloys.

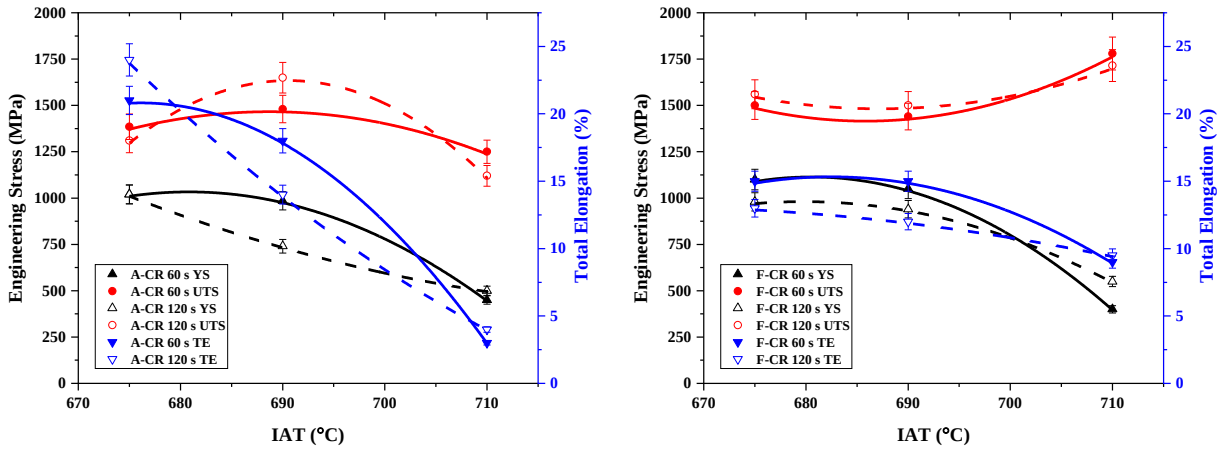

a) b)

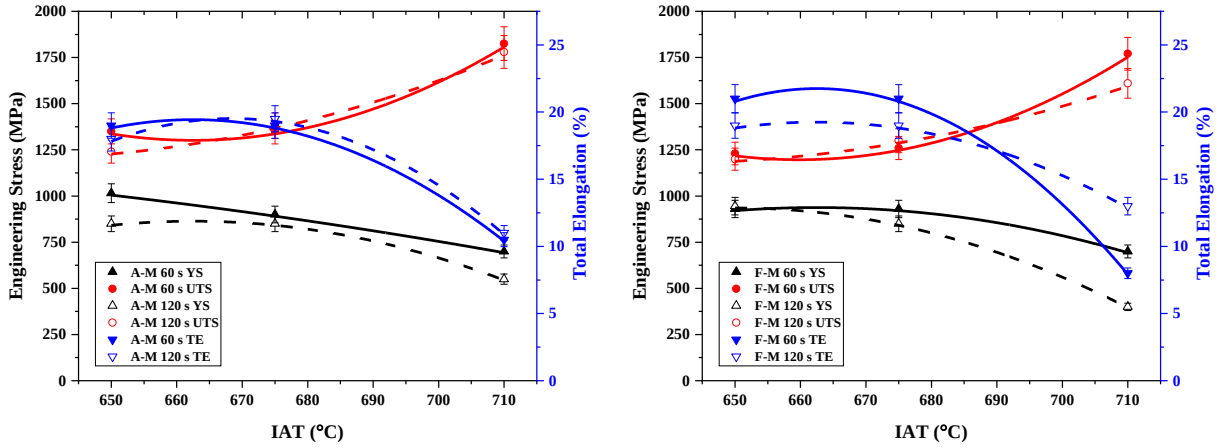

c) d)

Figure 3.17: Summary of tensile properties as a function of IAT and IA holding time for a) A-CR, b) F-CR, c) A-M, and d) F-M starting microstructures.

Table 3.4: Summary of Mechanical Properties for Steels that met the 3G-AHSS UTS × TE Target.

Steel ID	Yield Stress (YS), MPa	Ultimate Tensile Stress (UTS), MPa	Total Elongation (TE), %	UTS × TE, MPa%	True Strain at Fracture (ε_f)
A-CR-IA 675 °C 60 s	1020	1385	21	29085	0.86
A-CR-IA 675 °C 120 s	1020	1310	24	31440	0.90
A-CR-IA 690 °C 60 s	985	1480	18	26640	0.91
A-M-IA 650 °C 60 s	1015	1350	19	25650	0.58
A-M-IA 675 °C 60 s	900	1350	19	25650	0.56
A-M-IA 675 °C 120 s	850	1380	19.5	26910	0.45
F-M-IA 650 °C 60 s	930	1230	21	25830	0.41
F-M-IA 675 °C 60 s	930	1260	21	26460	0.56
F-M-IA 675 °C 120 s	850	1300	19	24700	0.56

3.4.4 TEM Analysis

TEM analysis was performed on interrupted tensile test samples from the A-M 675 ℃ 120 s and F-M 675 ℃ 120 s treatments – both of which meet 3G-AHSS property requirements (Table 3.4) – in order to assess the microstructural development of the retained austenite during plastic deformation. Figure 3.18 and Figure 3.19 show TEM micrographs and SAD patterns for the A-M-IA 675 °C 120 s samples deformed to true strains of $\varepsilon = 0.05$ and $\varepsilon = 0.10$, respectively. Bright field (BF) and dark field (DF) micrographs confirmed the presence of nano-twins (average spacing < 10 nm) in the lath-type retained austenite. The satellite spots (marked by red arrows) and the 180° lattice rotation corresponding to twinning of the retained austenite were confirmed in the SAD patterns (Figure 3.18c) and Figure 3.19c)). This data and the retained austenite to martensite transformation kinetics data in Figure 3.16 suggest that both the TWIP and TRIP effects contributed to sustaining the high work hardening rates observed during deformation of these samples (Figure 3.14c)). Further analysis of the SAD patterns also revealed Kurdjumov-Sachs (K–S) [49] and Nishiyama-Wassermann (N–W) [50,51] orientation relationship between the retained austenite and surrounding martensite. This suggests the austenite grew from the parent martensite lath boundaries or from interlath retained austenite films during intercritical annealing, which is also consistent with previous research conducted on various AHSSs with martensitic starting microstructure [13-16,36,37].

Figure 3.20 and Figure 3.21 show the TEM micrographs and SAD patterns for the F-M-IA 675 °C 120 s samples strained to $\varepsilon = 0.05$ and to fracture ($\varepsilon = 0.16$), respectively. A lath-type retained austenite morphology was also confirmed in these samples by analysing the BF and DF TEM micrographs. Moreover, similar to the A-M starting microstructures that underwent the same annealing conditions, nano-twins (average spacing < 10 nm) were observed in the strained F-M-

IA 675 °C 120 s samples. SAD pattern analysis of the sample pulled to fracture also confirmed strong satellite spots (marked by red arrows) and 180° lattice rotation corresponding to twinning of the retained austenite (Figure 3.21c)). Furthermore, the N-W orientation relationship [50,51] between the retained austenite and martensite was observed in these samples.

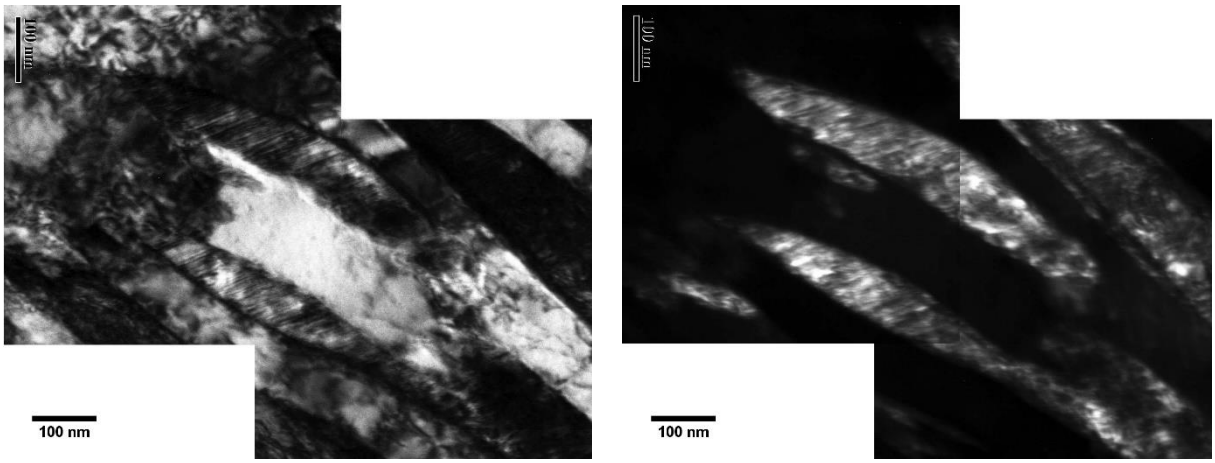

a) b)

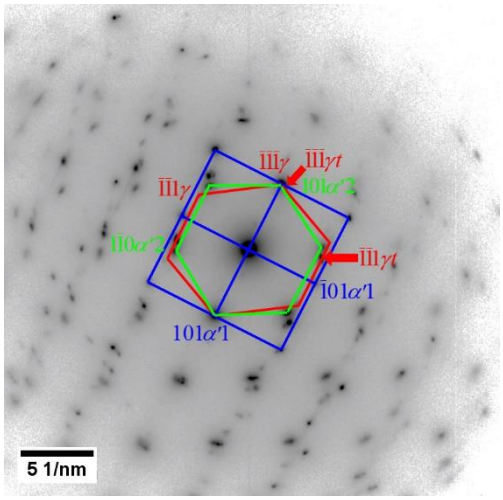

c)

Figure 3.18: a) Bright Field (BF) image, b) dark field (DF) image corresponding to $\langle \bar{1}\bar{1}1 \rangle \gamma$ and c) SAD pattern corresponding to $[100]\alpha'1 \| [111]\alpha'2 \| [110]\gamma$ for the A-M-IA 675 °C 120 s sample with ε = 0.05.

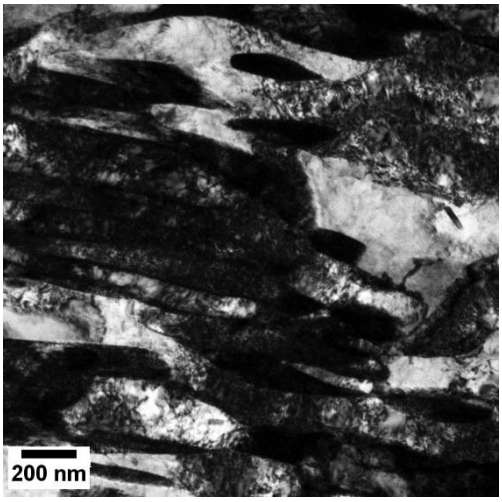

a)

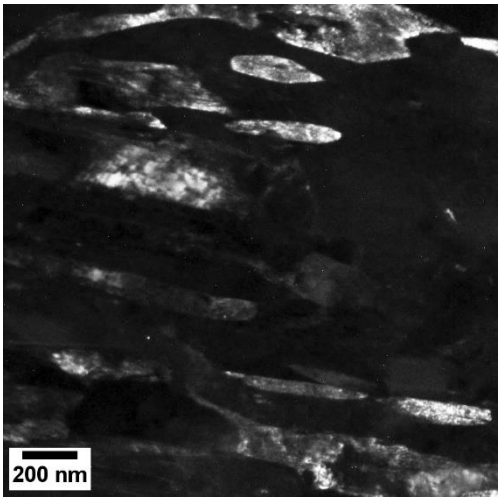

b)

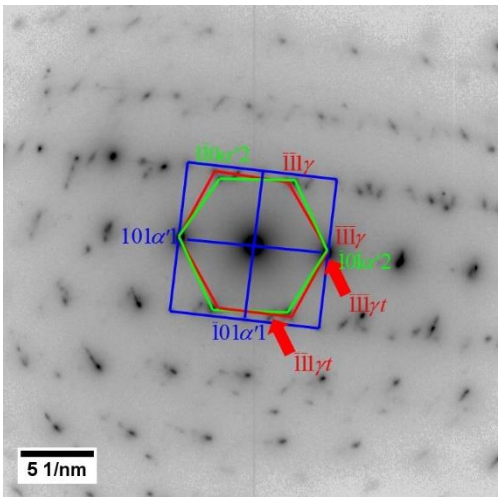

c)

Figure 3.19: a) Bright Field (BF) image, b) dark field (DF) image corresponding to $\langle\bar{1}\bar{1}1\rangle\gamma$ and c) SAD pattern corresponding to $[100]\alpha'1||[111]\alpha'2||[110]\gamma$ for the A-M-IA 675 °C 120 s sample with ε = 0.10.

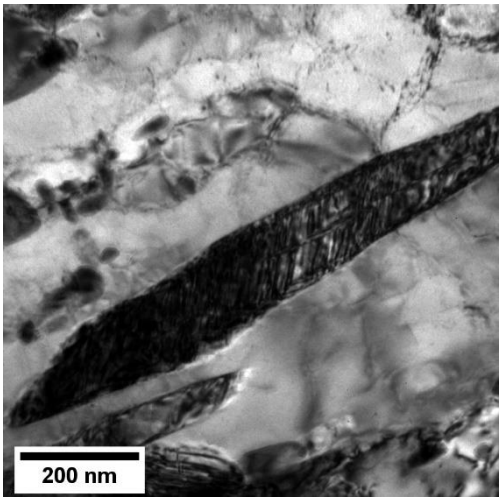

a)

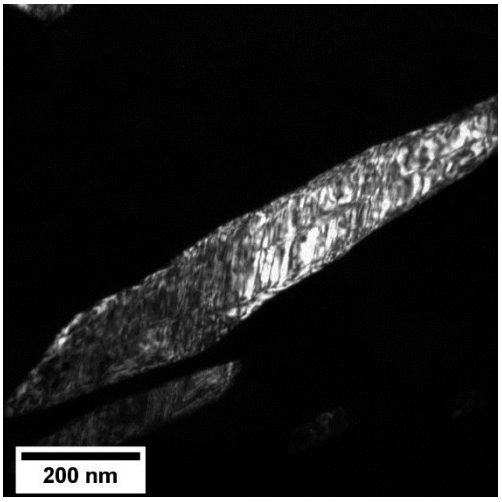

b)

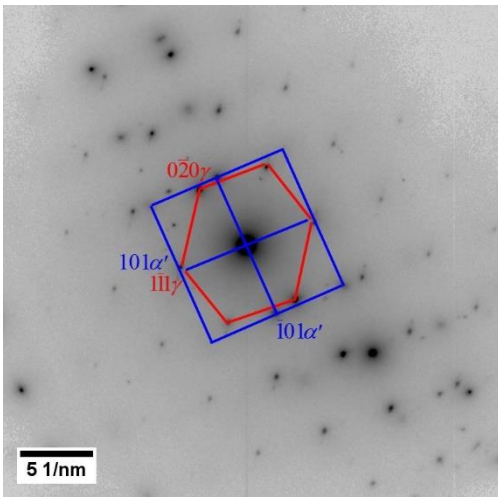

c)

Figure 3.20: a) Bright Field (BF) image, b) dark field (DF) image corresponding to $\langle \bar{1}\bar{1}1 \rangle \gamma$ and c) SAD pattern corresponding to $[100]\alpha' \| [110]\gamma$ for the F-M-IA 675 ℃ 120 s sample with ε = 0.05.

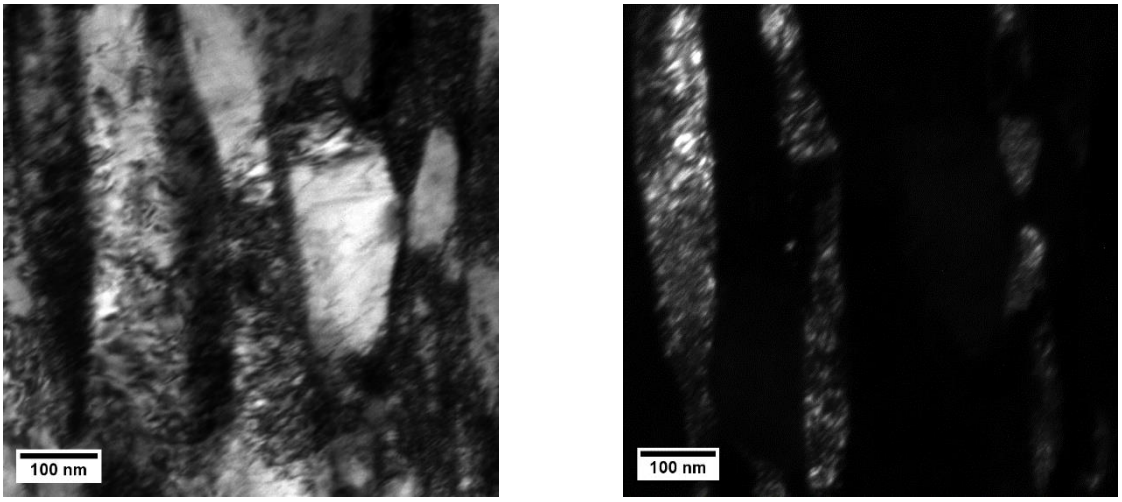

a) b)

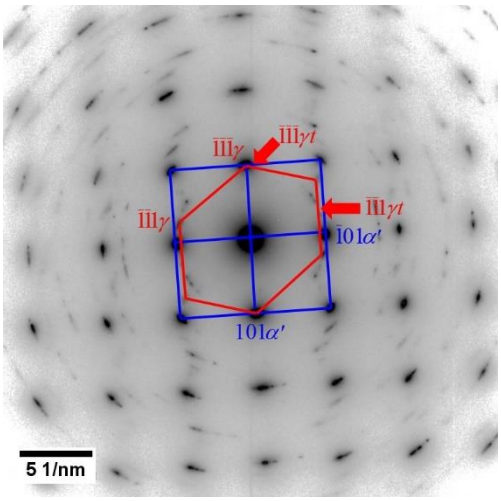

c)

Figure 3.21: a) Bright Field (BF) image, b) dark field (DF) image corresponding to $\langle \bar{1}\bar{1}1 \rangle \gamma$ and c) SAD pattern corresponding to $[100]\alpha' \| [110]\gamma$ for the fractured (ε = 0.16) F-M-IA 675 °C 120 s sample.

3.4.5 Fracture Analysis

Fracture surface cross-sections were analysed with SEM in order to determine the critical damage event and global fracture mode. Figure 3.22 shows SEM micrographs of selected A-M-IA

and F-M-IA samples. It can be seen that shear voids nucleated at the ferrite/martensite/retained austenite interfaces regardless of steel chemistry or heat treatment parameters, as shown by the red arrows in Figure 3.22. These shear voids coalesced and resulted in interfacial decohesion. This is consistent with the fracture surface analysis which confirmed that the cracks propagated mainly by interfacial decohesion and ductile tearing (Figure 3.23). This critical damage mechanism and global fracture mode are consistent with results observed by other medium-Mn steel researchers [15,16,52].

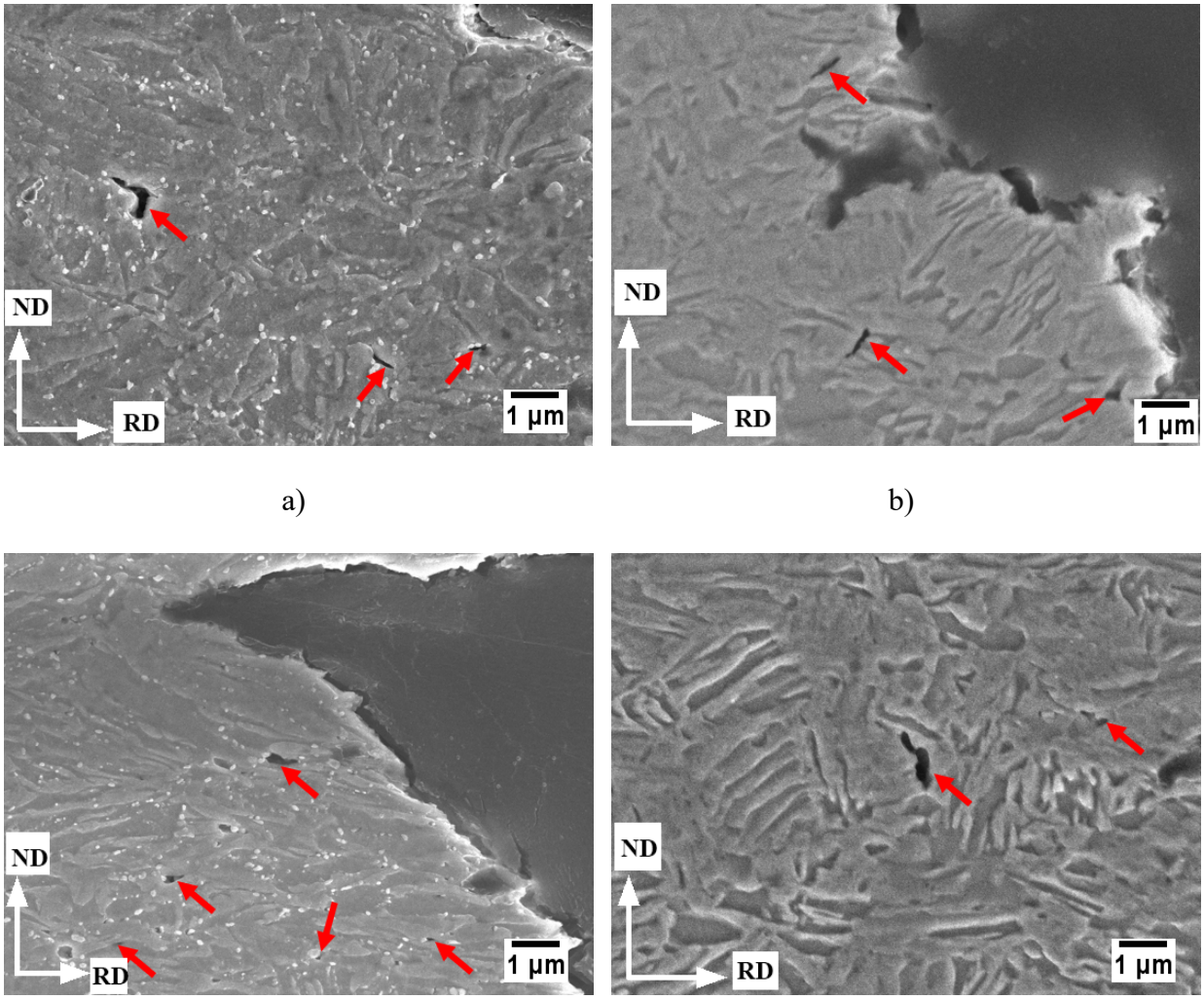

Figure 3.22: SEM micrographs of the fracture surface cross-sections for a) A-M-IA 675 °C 120 s, b) A-M-IA 710 °C 120 s, c) F-M-IA 675 °C 120 s and d) F-M-IA 710 °C 120 s samples; ND = Normal Direction, RD = Rolling Direction.

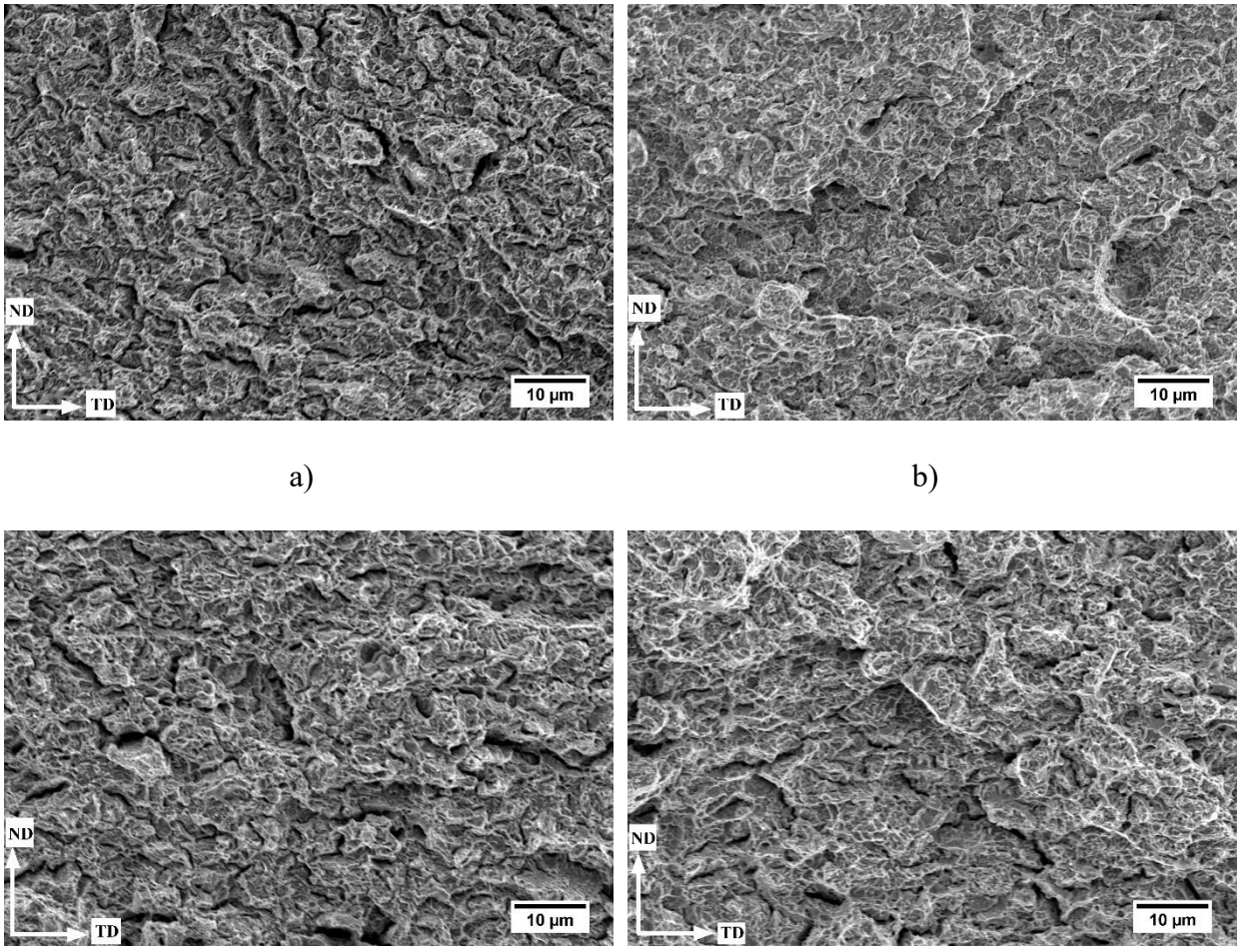

Figure 3.23: SEM micrographs of the fracture surface for a) A-M-IA 675 °C 120 s, b) A-M-IA 710 °C 120 s, c) F-M-IA 675 °C 120 s and d) F-M-IA 710 °C 120 s samples; ND = Normal Direction, TD = Transverse Direction.

3.5 Discussion

The retained austenite volume fraction, morphology, and stability were a strong function of the intercritical annealing parameters and starting microstructures of the prototype medium-Mn

steels. XRD (Figure 3.8) and SEM (Figure 3.4 and Figure 3.5) results showed that the retained austenite volume fraction increased with increasing IAT and IA holding time for both steel compositions as well as both starting microstructures. However, intercritical annealing of the martensitic starting microstructure resulted in a significantly higher volume fraction of retained austenite due to faster austenite reversion kinetics (Figure 3.8a) *vs.* Figure 3.8b)) being driven by C partitioning from the supersaturated martensitic matrix and decreasing strain energy associated with the growing interlath austenite films [10-12]. Wei et al. [53] have reported that the growth of interlath retained austenite did not have a nucleation barrier as these structures were pre-existing along the martensite lath boundaries. Furthermore, lath-type retained austenite is known to be more chemically and mechanically stable compared to blocky retained austenite [10,18]. Thus, both the A-M and F-M starting microstructures contained relatively high volume fractions of stable retained austenite which gradually transformed to martensite during straining (Figure 3.16), resulting in 3G-AHSS mechanical properties being realised for a wider variety of intercritical heat treatments.

This is in contrast with the CR starting microstructures, where only a slight increase in retained austenite volume fraction was observed with increasing IAT (Figure 3.8). In this case, the carbide dissolution kinetics and the resultant soluble C supply played a critical role, particularly in the case of the Sn-containing F-CR starting microstructures. The carbide extraction replica analysis (Table 3.3) revealed that intercritical annealing of the A-CR starting microstructures resulted in significant carbide dissolution whereas that of the F-CR starting microstructure resulted in significant carbide precipitation (Figure 3.6 and Table 3.3). These findings suggest that the mechanism for austenite growth in the A-CR starting microstructures comprised austenite nucleation and growth on dissolving carbide particles, resulting in the blocky morphology observed (Figure 3.4) [36,37]. In the case of the F-CR starting microstructure, there was significant

carbide precipitation and coarsening ((Figure 3.6 and Table 3.3), with less soluble C being available for partitioning to the retained austenite. As shown in Figure 3.7, the Sn segregated to the carbide/matrix interfaces likely inhibited the dissolution and diffusion processes, resulting in lesser volume fraction of chemically stable retained austenite and mechanical properties versus its A-CR counterparts (Figure 3.8a), Figure 3.11 *vs.* Figure 3.12, Figure 3.13, Table 3.4). This mechanism would be consistent with the effect Sn has on oxidation and decarburization kinetics [38-41]. The lesser chemical stability of the F-CR intercritical austenite is also apparent from the estimated volume fraction of fresh martensite produced during cooling from the IAT, as shown in Figure 3.10.

In the case of the A-M and F-M starting microstructures, the volume fractions of chemically stable retained austenite were considerably greater versus the CR starting microstructures (Figure 3.8a) *vs.* Figure 3.8b)), likely due to the lack of a nucleation barrier for the formation of intercritical austenite from pre-existing interlath retained austenite films and the more rapid partitioning of C from the adjacent, C supersaturated martensitic microstructures. This resulted in the martensitic starting microstructures being more stable than their CR counterparts – per the fresh martensite made during cooling (Figure 3.10) – which exhibited a more gradual deformation-induced retained austenite to martensite transformation (Figure 3.16) and exhausted itself at higher strains versus their CR starting microstructure counterparts. Both factors resulted in the properties of the M starting microstructures meeting the 3G property window over a larger range of IATs and IA holding times than was seen for the CR microstructures (Table 3.4). It should also be noted that the highest properties observed – as characterised by the UTS × TE product (Table 3.4) – were observed in the instances of maximum potential partitioning of C to the intercritical austenite for the 650 °C and 675 °C IATs, resulting in a minimum M_S temperature and, by implication,

minimum M_S^{σ} (Figure 3.9). This correlates well with the retained austenite transformation kinetics in Figure 3.13 and Figure 3.16. Furthermore, it can be seen from Table 3.4 that the Sn micro-alloying had only a minor effect on the overall mechanical property profile in the case of the M starting microstructures. It is also apparent from the carbide data that the Sn micro-addition had some effect on the carbide precipitation kinetics during intercritical annealing, with a significantly smaller volume of carbides precipitating versus the A-M starting microstructure (Figure 3.6 and Table 3.3). In this case, it is hypothesized that the Sn micro-alloying reduced diffusion of C to the retained austenite, making it slightly less chemically stable.

As evidenced by the TRIP kinetics documented in Figure 3.16 and the TEM micrographs in Figure 3.18 – Figure 3.21, both the TRIP and TWIP effects assisted in enhancing the mechanical properties of the prototype medium-Mn 3G-AHSSs. The TRIP and TWIP effects and their influence on mechanical properties of the intercritically annealed steels, in turn, depend significantly on the retained austenite SFE, volume fraction, and chemical/mechanical stability. In fact, a balance between these factors is required for sustaining high work hardening rates during deformation and in delaying the onset of necking such that the target 3G-AHSS properties can be attained.

In order to be successfully employed as a plasticity enhancement mechanism, the TRIP effect must employ retained austenite of sufficient stability to transform gradually during deformation, optimally exhausting itself at high strains in order to maintain the desired high instantaneous work hardening rates at high strains. An examination of the retained austenite transformation kinetics correlated with the mechanical property curves (Figure 3.11 – Figure 3.16) and the summative results in Table 3.4 will show that 3G-compabible properties were only obtained when a gradual transformation of retained austenite to martensite transformation was obtained such that it was not

exhausted at low strains. In the case of the CR starting microstructures, this was the case for the A-CR-IA treatments at 675 ℃ for 60 s and 120 s and at 690 ℃ for 60 s. In the case of the 710 ℃ IA treatments, the TRIP effect was exhausted at very low strains (Figure 3.13), resulting in failure to sustain high work hardening rates during deformation (Figure 3.11d) and Figure 3.12d)) and a relatively low strength – ductility balance, similar to that observed in DP steels. This trend is consistent with the higher volume fractions of fresh martensite made in these microstructures (Figure 3.10). Similar observations have been reported by numerous researchers [6,8,9,14-16,42,46].

In the case of the M starting microstructures, sufficiently stable retained austenite was created for a wider range of heat treatments at 650 ℃ and 675 ℃ for both the A-M and F-M prototype alloys (Table 3.4) *via* the mechanisms documented above. However, as was the case for the CR starting microstructures, the higher volume fractions of retained austenite formed in the 690 ℃ and 710 ℃ intercritical heat treatments was of insufficient stability – per the retained austenite transformation curves in Figure 3.16. This was likely due to insufficient C partitioning to the larger volume fractions of the retained austenite, as shown in the trends provided in Figure 3.9 and its implications for M_S^{σ} as well as in the higher percentages of fresh martensite (Figure 3.10b)). These results reaffirm that a balance between retained austenite volume fraction and stability is necessary to achieve a high strength/ductility balance in medium-Mn steels. In addition, it was shown that mechanical twinning – i.e., the TWIP effect – occurred in the retained austenite in the instances where higher mechanical properties (Figure 3.18 – Figure 3.21) were realised. Thus, it can be concluded that the stacking fault energy of the retained austenite in these materials was of a suitable range – often cited as 15 – 45 mJ/m^2 [20] – to activate mechanical twinning. From the present data, however, the relative contributions of the TRIP and TWIP effects to sustaining the

instantaneous work hardening rate are very difficult to deconvolute, but it is very likely that both plasticity-enhancing mechanisms contributed to the observed behaviour.

Overall, it was found that CGL-compatible heat treatments could be employed with the prototype medium-Mn alloys to produce 3G-AHSS mechanical properties. In particular, it was determined that, for the martensitic starting microstructure, the thermal processing schemes used in the present contribution were reasonably robust in producing 3G-AHSS properties. Furthermore, it was determined that the addition of surface-active Sn had only a very slight effect on the mechanical properties in the case of the martensitic starting microstructures. As a result, the martensitic starting microstructure and 650 °C and 675 °C intercritical annealing conditions will be used in on-going research to determine the selective oxidation behaviour and reactive wetting of these prototype medium-Mn steels.

3.6 Conclusions

The effects of intercritical annealing parameters, starting microstructure, and Sn micro-alloying (~0.05 wt%) on the microstructural evolution and mechanical properties of two prototype Fe-0.2C-6Mn-1.5Si-0.5Al-0.5Cr-xSn (wt%) (x = 0 and 0.05 wt%) medium-Mn steels subjected to continuous galvanizing line (CGL)-compatible heat treatments were determined. It can be concluded that:

1. CGL-compatible intercritical annealing treatments were able to produce target 3G-AHSS mechanical properties (UTS × TE ≥ 24,000 MPa%) in the prototype medium-Mn steels for the CR starting microstructure without Sn micro-alloying and for the M starting microstructure, both with and without Sn micro-alloying. However, the martensitic starting microstructures were more robust in achieving 3G-AHSS mechanical properties,

where both the 650 °C and 675 °C intercritical annealing treatments met the mechanical property targets.

2. The retained austenite volume fraction, morphology, and stability were a strong function of intercritical annealing parameters and starting microstructure, where the austenite formation mechanism was strongly affected by the carbide fraction in the CR starting microstructures and the degree of C supersaturation in the martensite for the M starting microstructures. This difference resulted in the more rapid formation of larger fractions of more stable retained austenite which gradually transformed to martensite during deformation for the M starting microstructures and the more robust process window observed for producing 3G-AHSS properties.
3. Both the TRIP and TWIP plasticity enhancing mechanisms were observed in the alloys/heat treatments which resulted in 3G-AHSS mechanical properties.
4. The effect of Sn micro-alloying on the mechanical properties depended on the starting microstructure. Sn micro-alloying had a significant impact on the carbide dissolution and precipitation kinetics, particularly in the case of the Sn-containing CR starting microstructure. This led to the inhibition of C dissolution and partitioning to the intercritical austenite and poor retained austenite stability, ultimately resulting in the Sn-containing CR alloy not meeting the 3G property targets for any of the thermal treatments employed. However, Sn micro-alloying did not have a significant detrimental effect on the mechanical properties of the martensitic starting microstructure heat treatments which achieved the target 3G-AHSS properties.

3.7 Acknowledgements

This study was financially supported by the International Zinc Association Galvanized Autobody Partnership (IZA-GAP) program and the Natural Sciences and Engineering Research Council of Canada (NSERC, grant CRDPJ 522309 – 17). The authors gratefully acknowledge U.S. Steel Research for the provision of the sheet steels used in this study. The authors also thank Dr. Maedeh Pourmajidian, Jonas Wagner, and the staff of the Canadian Centre for Electron Microscopy (CCEM), the Brockhouse Institute for Materials Research (BIMR), the McMaster Steel Research Centre (SRC), and the Centre for Automotive Materials and Corrosion (CAMC) for their technical support.

3.8 Appendix A

Carbide Extraction Replicas and Size Distribution Analyses:

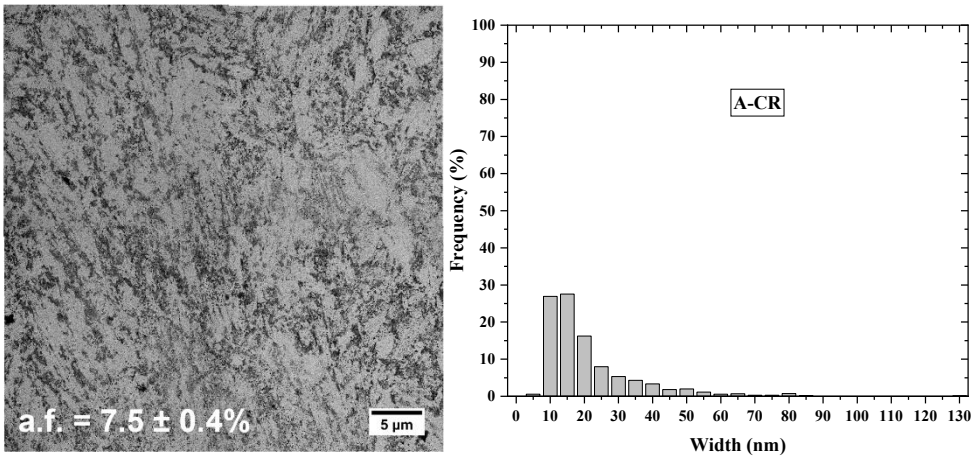

a)

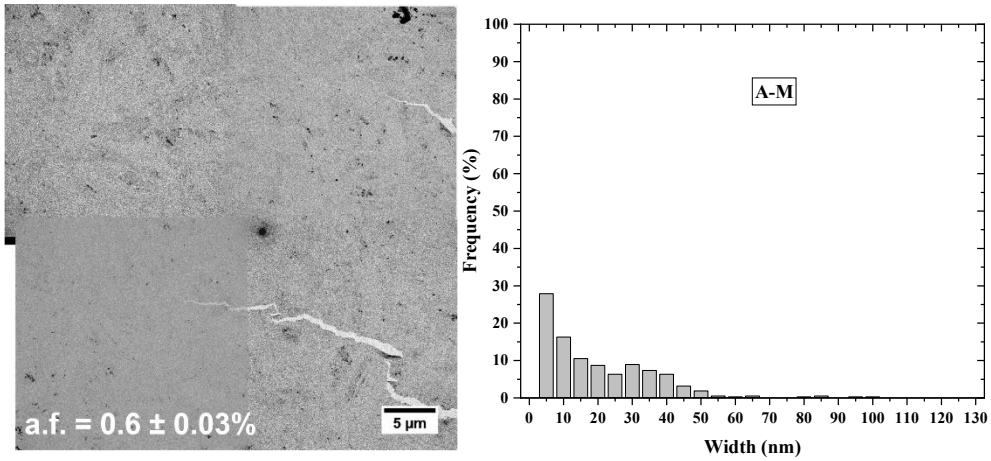
a.f. = 0.6 ± 0.03%
5 µm
A-M
Frequency (%)
Width (nm)

b)

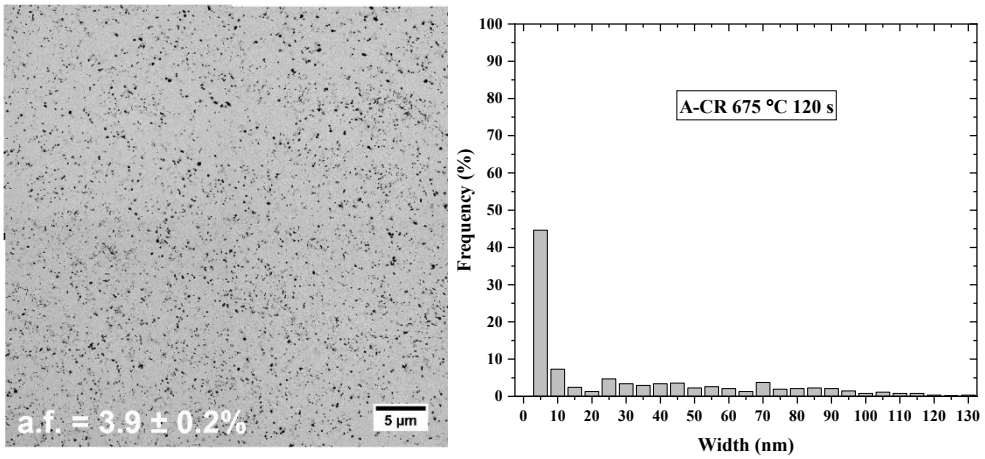
a.f. = 3.9 ± 0.2%
5 µm
A-CR 675 °C 120 s
Frequency (%)
Width (nm)

c)

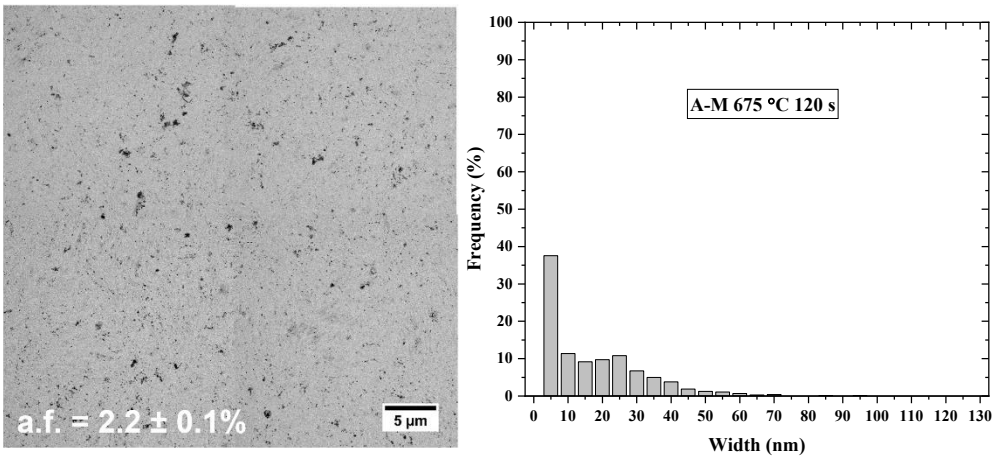
a.f. = 2.2 ± 0.1%
5 µm
A-M 675 °C 120 s
Frequency (%)
Width (nm)

d)

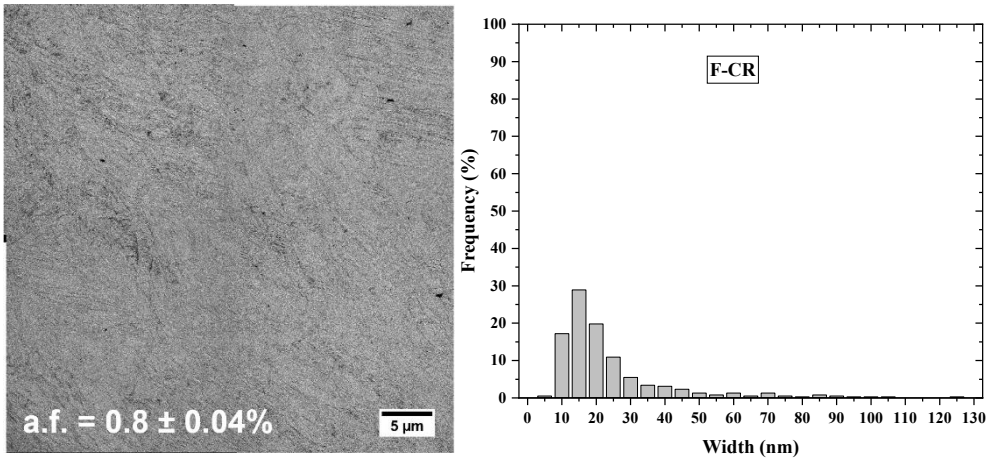
a.f. = 0.8 ± 0.04%
5 µm
F-CR
Frequency (%)
Width (nm)

e)

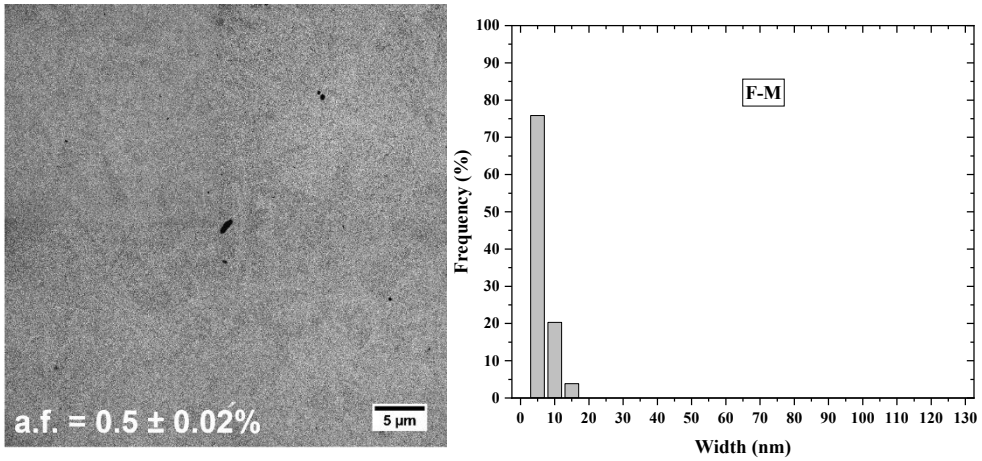
a.f. = 0.5 ± 0.02%
5 µm
F-M
Frequency (%)
Width (nm)

f)

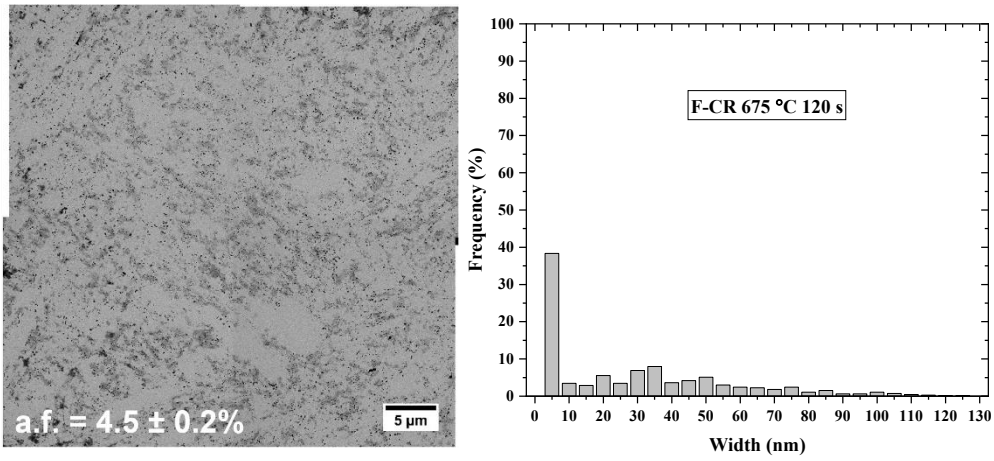
a.f. = 4.5 ± 0.2%
5 µm
F-CR 675 °C 120 s
Frequency (%)
Width (nm)

g)

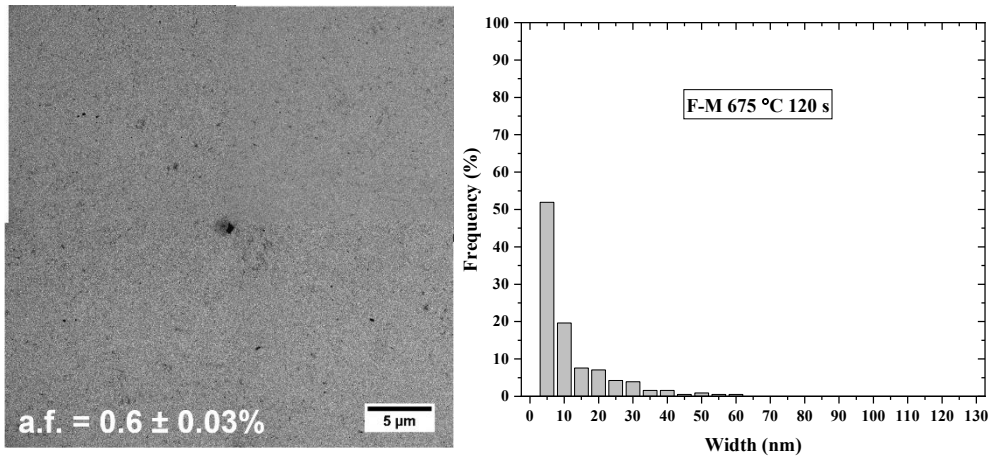

h)

Figure 3.24: Montage of low magnification TEM micrographs and corresponding carbide size distribution from extraction replicas of a) A-CR, b) A-M, c) A-CR-IA, d) A-M-IA, e) F-CR, f) F-M, g) F-CR-IA, and h) F-M-IA samples; a.f. = carbide area fraction, IA = 675 ℃ × 120 s.

3.9 References

[1] D.K. Matlock, J.G. Speer, Design considerations for the next generation of advanced high strength steel sheets, in: Proc. 3rd Inter. Conf. Advanced High Strength Steels (2006) 774–781.

[2] C. Schutte, DOE Focuses on Developing Materials to Improve Vehicle Efficiency, SAE Technical Paper 2015-01-0405 (2015), https://doi.org/10.4271/2015-01-0405.

[3] L.G. Hector Jr., The Next Generation of Advanced High Strength Steels – Computation, Product Design and Performance, 12th Annual Great Designs in Steel Seminar, Livonia, MI (2013).

[4] E. De Moor, P.J. Gibbs, J.G. Speer, D.K. Matlock, Strategies for third-generation advanced high strength steel development, AIST Trans. 7 (2010) 133–144.

[5] W.Q. Cao, C. Wang, J. Shi, M.Q. Wang, W.J. Hui, H. Dong, Microstructure and mechanical properties of Fe–0.2C–5Mn steel processed by ART-annealing, Mater. Sci. Eng. A. 528 (2011) 6661–6666.

[6] S. Lee, B.C. De Cooman, On the selection of the optimal intercritical annealing temperature for medium Mn TRIP steel, Metall. Mater. Trans. A. 44A (2013) 5018–5024.

[7] S. Lee, K. Lee, B.C. De Cooman, Observation of the TWIP + TRIP plasticity-enhancement mechanism in Al-added 6 wt pct medium Mn steel, Metall. Mater. Trans. A. 46A (2015) 2356–2363.

[8] P.J. Gibbs, E. De Moor, M.J. Merwin, B. Clausen, J.G. Speer, D.K. Matlock, Austenite stability effects on tensile behavior of manganese-enriched-austenite transformation induced plasticity steel, Metall. Mater. Trans. A. 42A (2011) 3691–3702.

[9] D.W. Suh, J.H. Ryu, M.S. Joo, H.S. Yang, K. Lee, H.K.D.H. Bhadeshia, Medium-alloy Manganese-rich transformation-induced plasticity steels, Metall. Mater. Trans. A. 44A (2013) 286–293.

[10] H. Luo, H. Dong, New ultrahigh-strength Mn-alloyed TRIP steels with improved formability manufactured by intercritical annealing, Mater. Sci. Eng. A. 626 (2015) 207–212.

[11] J. Shi, X. Sun, M. Wang, W. Hui, H. Dong, W. Cao, Enhanced work-hardening behavior and mechanical properties in ultrafine-grained steels with large-fractioned metastable austenite, Scr. Mater. 63 (2010) 815–818.

[12] A. Arlazarov, M. Gouné, O. Bouaziz, A. Hazotte, G. Petitgand, P. Barges, Evolution of microstructure and mechanical properties of medium Mn steels during double annealing, Mater. Sci. Eng. A. 542 (2012) 31– 39.

[13] K.M.H. Bhadhon, J.R. McDermid, X. Wang, E. McNally, F.E. Goodwin, Fine-scale microstructure characterization and mechanical properties of CGL-compatible heat treated medium-Mn TRIP steel, in: Proc. 11th Conf. Zinc Zinc Alloy Coat. Steel Sheet, Galvatech 2017, ISIJ Int., Tokyo (2017) 493–500.

[14] D.M. Pallisco, K.M.H. Bhadhon, V. Patel, M. Pourmajidian, F.E. Goodwin, J.R. McDermid, Galvanizing of medium-Manganese third generation advanced high strength steels, in: Proc. 4th Int. Conf. Mediu. High-Manganese Steels. 9-11 (2019) 375–378.

[15] D.M. Pallisco, J.R. McDermid, Mechanical property development of a 0.15C–6Mn–2Al–1Si third-generation advanced high strength steel using continuous galvanizing heat treatments, Mater. Sci. Eng. A. 778 (2020) 139111, doi: https://doi.org/10.1016/j.msea.2020.139111.

[16] V. Patel, Microstructure and mechanical properties of medium Mn steel, McMaster University (2019), Hamilton, Canada.

[17] P.J. Jacques, Transformation-induced plasticity for high strength formable steels, Curr. Opin. Solid State Mater. Sci. 8 (2004) 259–265.

[18] J.R. McDermid, H.S. Zurob, Y. Bian, Stability of retained austenite in high-Al, low-Si TRIP-assisted steels processed via continuous galvanizing heat treatments, Metall. Mater. Trans. A. 42A (2011) 3627–3637.

[19] F. Spenger, T. Hebesberger, A. Pichler, C. Krempaszky, E.A. Werner, AHSS steel grades: strain hardening and damage as material design criteria, Int. Conf. in New Developments in AHSS, (2008), Orlando, USA.

[20] B.C. De Cooman, Y. Estrin, S.K. Kim, Twinning-induced plasticity (TWIP) steels, Acta Mater. 142 (2018) 283–362.

[21] R.E. Schramm, R.P. Reed, Stacking fault energies of seven commercial austenitic stainless steels, Metall. Trans. A. 6A (1975) 1345–1351.

[22] S. Allain, J. Chateau, O. Bouaziz, S. Migot, N. Guelton, Correlations between the calculated stacking fault energy and the plasticity mechanisms in Fe–Mn–C alloys, Mater. Sci. Eng. A. 387–389 (2004) 158–162.

[23] A. Dumay, J.-P. Chateau, S. Allain, S. Migot, O. Bouaziz, Influence of addition elements on the stacking-fault energy and mechanical properties of an austenitic Fe–Mn–C steel, Mater. Sci. Eng. A. 484 (2008), 184–187.

[24] A. Saeed-Akbari, J. Imlau, U. Prahl, W. Bleck, Derivation and variation in composition-dependent stacking fault energy maps based on Subregular Solution Model in high-Manganese steels, Metall. Mater. Trans. A. 40A (2009) 3076–3090.

[25] O. Bouaziz, S. Allain, C. Scott, Effect of grain and twin boundaries on the hardening mechanisms of twinning-induced plasticity steels, Scr. Mater. 58 (2008) 484–487.

[26] M. Ghasri-Khouzani, J.R. McDermid, Effect of carbon content on the mechanical properties and microstructural evolution of Fe–22Mn–C steels, Mater. Sci. Eng. A. 621 (2015) 118–127.

[27] J.R. McDermid, A. Chakraborty, Identification of steel chemistries and galvanizing process design, ZCO-53-1 Project Report, (2012), Hamilton, Canada.

[28] M. Pourmajidian, J.R. McDermid, Selective oxidation of a 0.1C-6Mn-2Si third generation advanced high-strength steel during dew-point controlled annealing, Metall. Mater. Trans. A. 49A (2018) 1795–1808.

[29] M. Pourmajidian, J.R. McDermid, Effect of annealing temperature on the selective oxidation and reactive wetting of a 0.1C-6Mn-2Si advanced high strength steel during continuous galvanizing heat treatments, ISIJ Int. 58(9) (2018) 1635–1643.

[30] Y. Suzuki, T. Yamashita, Y. Sugimoto, S. Fujita, S. Yamaguchi, Thermodynamic analysis of selective oxidation behavior of Si and Mn-added steel during recrystallization annealing, ISIJ Int. 49(4) (2009) 564–573.

[31] E.M. Bellhouse, J.R. McDermid, Selective oxidation and reactive wetting during galvanizing of a CMnAl TRIP-assisted steel, Metall. Mater. Trans. A. 42A(9) (2011) 2753–2768.

[32] M. Pourmajidian, J.R. McDermid, On the reactive wetting of a medium-Mn advanced high-strength steel during continuous galvanizing, Surf. Coat. Technol. 357 (2019) 418–426.

[33] ASTM E8/E8M-16a: Standard Test Methods for Tension Testing of Metallic Materials, West Conshohocken, PA, USA, 2016.

[34] ASTM E975-13: Standard Practice for X-Ray Determination of Retained Austenite in Steel with Near Random Crystallographic Orientation, West Conshohocken, PA, USA, 2013.

[35] K. Thompson, D. Lawrence, D.J. Larson, J.D. Olson, T.F. Kelly, B. Gorman, In situ site-specific specimen preparation for atom probe tomography, Ultramicroscopy 107 (2007) 131–139.

[36] A. Arlazarov, A. Hazotte, O. Bouaziz, M. Goune, F. Kegel, Characterization of microstructure formation and mechanical behavior of an advanced medium Mn steel, Proc. MS&T 2012, Pittsburgh (2012) 1124–1131.

[37] J.I. Kim, J.H. Ryu, S.W. Lee, K. Lee, Y.-U. Heo, D.-W. Suh, Influence of the Initial Microstructure on the Reverse Transformation Kinetics and Microstructural Evolution in Transformation-Induced Plasticity – Assisted Steel, Metall. Mater. Trans. A. 47 (2016) 5352–5361.

[38] E.D. Hondros, M.P. Seah, Segregation to interfaces, Int. Met. Rev. 22 (1977) 262–301.

[39] M. Seah, Quantitative prediction of surface segregation, J. Catal. 57 (1979) 450–457.

[40] L. Cho, E.J. Seo, G.S. Jung, D.W. Suh, B.C. De Cooman, Surface selective oxidation of Sn-added CMnSi TRIP steel, Metall. Mater. Trans. A. 47(4) (2016) 1705-1719.

[41] M. Pourmajidian, B. Langelier, J.R. McDermid, Effect of process atmosphere dew point and Tin addition on oxide morphology and growth for a medium-Mn third generation advanced steel during intercritical annealing, Metall. Mater Trans. A. 49 (2018) 5561–5573.

[42] S. Lee, S. Shin, M. Kwon, K. Lee, B.C. De Cooman, Tensile Properties of Medium Mn Steel with a Bimodal UFG $\alpha + \gamma$ and Coarse δ-Ferrite Microstructure, Metall. Mater. Trans. A 48A (2017) 1678–1700.

[43] S. Kaar, K. Steineder, R. Schneider, D. Krizan, C. Sommitsch, New Ms-formula for exact microstructural prediction of modern 3rd generation AHSS chemistries, Scr. Mater. 200 (2021) 113923.

[44] J. Sarkar, T.R.G. Kutty, D.S. Wilkinson, J.D. Embury, D.J. Lloyd, Tensile properties and bendability of T4 treated AA6111 aluminum alloys, Mater. Sci. Eng. A. 369 (2004) 258–266.

[45] P. Larour, J. Freudenthaler, T. Weissböck, Reduction of cross section area at fracture in tensile test: Measurement and applications for flat sheet steels, J. Phys. Conf. Ser. 896 (2017).

[46] K.O. Findley, J. Hidalgo, R.M. Huizenga, M.J. Santofimia, Controlling the work hardening of martensite to increase the strength/ductility balance in quenched and partitioned steels, Mater. Des. 117 (2017) 248–256.

[47] E.M. Bellhouse, J.R. McDermid, Effect of Continuous Galvanizing Heat Treatments on the Microstructure and Mechanical Properties of High Al-Low Si Transformation Induced Plasticity Steels, Metall. Mater. Trans. A. 41 (2010) 1460–1473.

[48] P. Jacques, Q. Furnémont, A. Mertens, F. Delannay, On the sources of work hardening in multiphase steels assisted by transformation-induced plasticity, Philos. Mag. A. 81 (2001) 1789–1812.

[49] G. Kurdjumov, G. Sachs, Uber der Mechanismus der Stahlhartung (On the mechanism of hardening of steel), Z. Phys. 64 (1930) 325–343.

[50] Z. Nishiyama, X -ray investigation of the mechanism of the transformation from face-centered cubic lattice to body- centered cubic, Sci. Rep. Tohoku Univ. 23 (1934) 637–664.

[51] G. Wassermann, Influence of the α-γ transformation of an irreversible Ni steel onto crystal orientation and tensile strength, Arch. Eisenhuttenwes. 126 (1933) 647–654.

[52] B. Sun, D. Palanisamy, D. Ponge, B. Gault, F. Fazeli, C. Scott, S. Yue, D. Raabe, Revealing fracture mechanisms of medium manganese steels with and without delta-ferrite, Acta Mater. 164 (2019) 683–696.

[53] R. Wei, M. Enomoto, R. Hadian, H.S. Zurob, G.R. Purdy, Growth of austenite from as-quenched martensite during intercritical annealing in an Fe–0.1C–3Mn–1.5Si alloy, Acta Mater. 61 (2013) 697–707.

4 Selective Oxidation of a Medium-Mn Third Generation Advanced High Strength Steel during Austenitizing and Intercritical Annealing

K.M.H. Bhadhon, J.R. McDermid
Centre for Automotive Materials and Corrosion, Department of Materials Science and Engineering, McMaster University, Hamilton, Ontario, Canada
Submitted to *Journal of The Electrochemical Society* on April 9, 2022.

4.1 Abstract

The effect of the simulated continuous galvanizing line N_2-5 vol% H_2 process atmosphere oxygen partial pressure (pO_2) on the external and internal selective oxidation of a prototype medium-Mn third generation (3G) advanced high strength steel was determined during a two-stage heat treatment cycle (i.e., austenitizing and intercritical annealing) which had previously yielded 3G properties. Thick external oxides (~ 200 nm) were observed after the austenitizing heat treatment, regardless of the process atmosphere pO_2 employed. An intermediate flash pickling step was successful in reducing the external oxide thickness significantly (to ~ 30 nm) along with revealing some extruded metallic Fe nodules on the surface. The austenitizing heat treatment also resulted in a solute-depleted surface layer with a minimum thickness of 2 μm. This solute-depleted layer inhibited the formation of external oxides during intercritical annealing, resulting in a surface similar to that observed after flash pickling comprising a near-pure Fe surface with isolated, nodular external oxides. These surfaces are promising in terms of successful reactive wetting of this prototype medium-Mn steel during subsequent continuous hot-dip galvanizing.

4.2 Introduction

Design of lighter automotive body structures to increase fuel efficiency and reduce greenhouse gas emissions while improving passenger safety has motivated the research and development of

third generation advanced high strength steels (3G AHSS) [1,2]. The overall objective is to develop a new generation of AHSS with a higher strength-ductility balance compared to 1G AHSSs with lower alloy contents compared to the 2G AHSSs, making them less expensive to produce and easier to galvanize. Medium-Mn (med-Mn) steels have been in the forefront of this research. Recent research [3-12] has shown that med-Mn steels can meet 3G AHSS target mechanical properties, as defined by Matlock and Speer [2], in terms of the ultimate tensile strength (UTS) × tensile elongation (TE) product of 24,000 ≤ UTS × TE ≤ 40,000 MPa%. Through the judicious selection of intercritical annealing time/temperature and starting microstructure, it is also possible to obtain 3G mechanical properties with continuous galvanizing line (CGL)-compatible processing parameters [9-12], typically comprising peak annealing temperatures (PAT) of approximately 650 – 750 °C and PAT soaking times of 60 – 120 s. Furthermore, some authors have reported that med-Mn steels with martensitic starting microstructures were more robust in attaining 3G mechanical properties compared to an as-received cold-rolled starting microstructure [9-12].

Continuous hot-dip galvanizing using a molten Zn(Al, Fe) bath is amongst the most cost-effective method to provide corrosion protection to automotive steels exposed to the external environment [13]. However, the alloying elements present in AHSSs can make these steels challenging to galvanize. In particular, the alloying elements Mn, Si, Al, and Cr will selectively oxidize in the dew point controlled (i.e., fixed water vapour partial pressure, pH_2O) CGL N_2–(5-20 vol%) H_2 process atmosphere during the pre-galvanizing heat treatment required to obtain the desired substrate microstructure and mechanical properties. These external oxides, depending on their chemistry, morphology, and spatial distribution, can prevent reactive wetting during immersion in the CGL bath by blocking direct contact between the Zn(Al, Fe) bath and steel substrate, the dissolution of surface Fe and the formation of the desired $Fe_2Al_5Zn_X$ reactive wetting

product [14-27]. Suzuki et al. [28] developed a thermodynamic model to predict the oxidized species based on temperature, process atmosphere pO_2, and the steel Si/Mn ratio (calculated based on wt%). The authors advocated that tailoring the CGL process atmosphere oxygen partial pressure (pO_2) such that SiO_2 film formation was supressed to be a necessary condition to achieve good reactive wetting. It was concluded that it was not possible to avoid deleterious SiO_2 film formation, regardless of the process atmosphere pO_2, when the alloy Si/Mn ≥ 1. On the other hand, when the substrate Si/Mn ≤ 0.5, a process atmosphere dew point of –25 °C to –10 °C in a N_2–5 vol% H_2 process atmosphere, commonly employed in industrial CGLs, would suppress SiO_2 formation and stabilise the system in the desired $MeSiO_3$ + Me_2SiO_4 two phase region (where Me = Mn or Fe). However, thermodynamic models are unable to predict some of the critical factors in the selective oxidation/reactive wetting interaction such as oxide thickness, morphology, and spatial distribution. For example, Bellhouse and McDermid [18] successfully galvanized two low alloy Si/Al TRIP-assisted steels using conventional CGL process atmospheres, where the substrate Si/Mn = 1 and 0.67, respectively. The authors attributed successful reactive wetting to having widely spaced, nodular MnO-Mn_2SiO_4/$MnSiO_3$ on the steel surface. The desired $Fe_2Al_5Zn_x$ layer was able to form between the nodules and resulted in a defect-free Zn coating. Similarly, Mousavi and McDermid [22] successfully galvanized a 0.1C-2Mn-1.3Si (wt%) AHSS (i.e., Si/Mn = 0.65) through intercritically annealed at 820 °C for 120 s in a N_2–5 vol% H_2 process atmosphere with dew points of –30 °C and +5 °C using a 460 °C 0.2 wt% dissolved Al zinc bath.

One of the effective ways to improve reactive wetting during the continuous galvanizing of 1G AHSSs has been employing higher process atmosphere dew points (i.e., higher pO_2, as dictated by the H_2-H_2O-O_2 equilibrium with fixed pH_2, pH_2O and process temperature T) during the pre-galvanizing heat treatment [14,16,22,23,29,30]. External selective oxidation is suppressed at high

dew points owing to the greater inward flux of oxygen compared to the outward flux of ignoble alloying elements, resulting in internal selective oxidation. High process atmosphere dew points have also been found to be beneficial for the successful galvanizing of med-Mn steels [27,31]. For example, Pourmajidian and McDermid [27] investigated the effect of process atmosphere pO_2 on oxide spatial distribution and morphology during the annealing of a model 0.1C-6Mn-2Si (wt%) med-Mn AHSS at 690 °C. The results showed that a +5 °C dew point process atmosphere pO_2 (2.26×10^{-23} atm) yielded a steel surface with nodule-like MnO particles with thin inter-nodular films. The relatively thin inter-nodular MnO films and widely spaced external MnO nodules were determined to be the key contributors for the formation of an integral $Fe_2Al_5Zn_x$ intermetallic layer through successful reactive wetting by the Zn(Al, Fe) bath. Similar findings were also presented by Alibeigi et al. [31] for a series of Mn (0.14 – 5.1 wt%) containing steels.

However, the majority of the above studies were conducted on model alloys. The effect of process atmosphere pO_2 on the selective oxidation of application-oriented med-Mn steels has not been extensively researched [25,26,32,33]. Moreover, although recent research has shown that a martensitic starting microstructure is more robust in achieving 3G AHSS target mechanical properties [4,8-12,34], there has been scarce literature on the effect of process atmosphere pO_2 on selective oxidation during the austenitizing heat treatments necessary to produce the martensitic starting microstructure. For example, the current authors have documented the microstructural evolution and mechanical property development of a prototype med-Mn steel (0.2C-6Mn-1.5Si-0.5Al-0.5Cr wt%) and have reported that CGL-compatible intercritical annealing (675 °C × 120 s) from a martensitic starting microstructure was successful in producing 3G AHSS target mechanical properties (i.e., UTS × TE ≈ 26,900 MPa%) [12]. Thus, the objective of this investigation is to determine the effect of process atmosphere pO_2 on the selective oxidation using

the two-stage austenitizing and intercritical annealing heat treatments of the above med-Mn steel known to produce 3G mechanical properties [12]. In particular, the present investigation will assess the morphology, distribution, and chemistry of the external and internal oxides formed during these heat treatments within the context of producing a pre-immersion surface which can be successfully reactively wetted using a conventional CGL galvanizing bath.

4.3 Experimental

The chemical composition of the prototype med-Mn steel (as determined by inductively coupled plasma optical emission spectroscopy (ICP-OES (Varian Vista Pro) and C/S combustion analysis (LECO CS744)) is shown in Table 4.1. The prototype med-Mn steel was produced at U.S. Steel R&D (Munhall, PA) where the steel was melted in an induction furnace using electrolytic Fe (Armco) and alloying additions of 99.99%+ purity. Figure 4.1 shows the detailed thermo-mechanical processing (TMP) route utilised to produce the as-received cold-rolled steels.

Table 4.1: Chemical Composition of the Prototype Med-Mn 3G AHSS (wt%). Note that the Ac_1 and Ac_3 were measured via Quench Dilatometry.

	C	Mn	Si	Al	Cr	Ti	S	Si/Mn	Ac_1	Ac_3
wt%	0.18	5.91	1.46	0.43	0.59	0.008	0.0056	0.25	520 °C	765 °C
at%	0.82	5.86	2.84	0.87	0.62	0.009	0.010	--		

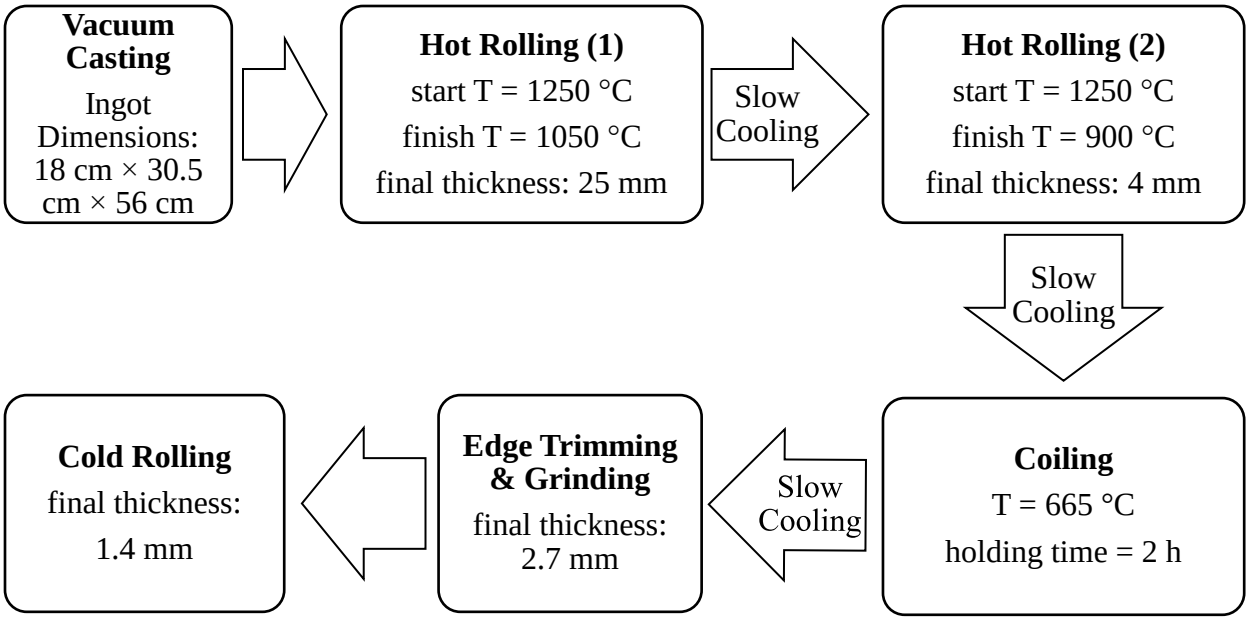

Figure 4.1: Thermo-mechanical processing route of the prototype med-Mn steel.

Sample coupons, measuring 10 mm × 50 mm with the longitudinal axis parallel to the rolling direction (RD), were used throughout this study. The coupons were lightly ground with a series of SiC papers, with 4000 grit SiC being the final step, to mitigate the effects of the as-received cold-rolled finish roughness on subsequent surface analyses. As discussed in [12], the thermal processing route which yielded the most promising mechanical properties (i.e., UTS = 1380 MPa, TE = 19.5%, UTS × TE = 26,910 MPa%, [12]) was used for all experiments. All thermal treatments were carried out in the McMaster Galvanizing Simulator (MGS, Iwatani-Surtec). When annealing only, the MGS comprises an atmosphere-controlled column equipped with a quartz lamp infrared furnace. A schematic of the thermal processing cycle used can be found in Figure 4.2. As pictured, the as-received cold-rolled sheet was first austenitized at 775 °C × 600 s, followed by high velocity N_2 gas cooling at –30 °C/s to room temperature to produce the desired martensitic starting

microstructure for subsequent intercritical annealing [12]. The martensitic starting microstructure samples will be referred to as the M samples, as specified in Table 4.2.

Following the austenitizing heat treatment, the steel was flash pickled to remove any external oxides (Figure 4.2). Flash pickling consisted of a 60 s immersion in a 30 °C solution comprising 64.5 mL DI water, 59.6 mL HCl, and 0.25 g hexamethylenetetramine [35], followed by rinsing and drying. Flash pickled samples were then intercritically annealed at 675 °C × 120 s (Figure 4.2) followed by cooling at –10 °C/s to the overaging temperature (OT) isothermal hold of 460 °C × 20 s. This latter is common practice in the CGL to thermally equilibrate the substrate with that of the resident molten Zn-alloy galvanizing bath [36]. Following the OT treatment, samples were then cooled to room temperature and stored in anhydrous isopropanol (99.9% purity) to minimize atmospheric contamination and oxidation. As specified in Table 4.3, the intercritically annealed samples will be referred to as M-IA in the subsequent text.

As specified in Table 4.2 and Table 4.3, both the austenitizing and intercritical annealing treatment process atmospheres were varied across three dew point controlled (i.e., T_{dp}) simulated N_2–5 vol% H_2 CGL process atmospheres, where T_{dp} = –30 °C, –10 °C and +5 °C. In this case, a premixed dry and water saturated N_2-5 vol % H_2 gas streams were mixed via mass flow controllers before entering the MGS such that the gas flow was counter-current to the sample movement. The process atmosphere pO_2 for the annealing temperatures and their fixed pH_2O/pH_2 ratios are documented in Table 4.2 and Table 4.3 for the austenitizing and intercritical annealing treatments, respectively. It should be further noted that all of the process atmospheres enumerated in Table 4.2 and Table 4.3 are reducing with respect to Fe-oxides but are oxidizing with respect to the primary alloying elements Mn, Si, Al, and Cr (Table 4.1).

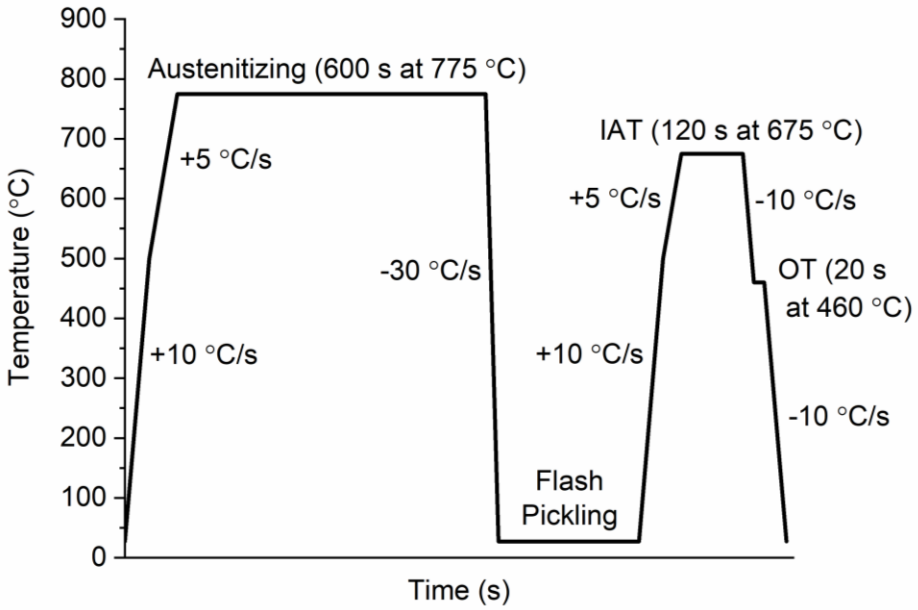

Figure 4.2: Schematic diagram of the experimental thermal profile.

Table 4.2: Summary of Austenitizing Heat Treatment Parameters and Process Atmosphere Characteristics.

Sample ID	Austenitizing Temperature (°C)	Holding Time (s)	T_{dp} (°C)	pO_2 (atm)	pH_2O/pH_2
M	775	600	–30	1.15×10^{-23}	1.0×10^{-2}
			–10	3.65×10^{-22}	5.6×10^{-2}
			+5	3.38×10^{-21}	1.7×10^{-1}

Table 4.3: Summary of Intercritical Annealing Heat Treatment Parameters and Process Atmosphere Characteristics.

Sample ID	IAT (°C)	Holding Time (s)	OT (°C)	Holding Time (s)	T_{dp} (°C)	pO_2 (atm)	pH_2O/pH_2
M-IA	675	120	460	20	–30	2.85×10^{-26}	1.0×10^{-2}
					–10	9.03×10^{-25}	5.6×10^{-2}
					+5	8.38×10^{-24}	1.7×10^{-1}

A JEOL 7000F field-emission scanning electron microscope (FE-SEM) was used to analyse the external oxide distribution and morphology. Secondary electron images (SEI) of the surface were taken using an acceleration voltage of 10 keV and a working distance of 10 mm. All samples were sputter coated with C to minimize charging from the incident electron beam. Furthermore, the cross-sections of the heat-treated samples were analysed with energy dispersive X-ray spectroscopy (EDS) using the JEOL 7000F FE-SEM. An acceleration voltage of 15 keV and a working distance of 10 mm were used in this case. All samples were polished using standard metallographic methods to a 0.04 μm finish using colloidal silica. EDS line scans were performed in order to determine elemental depth profiles, which were then assessed with respect to the bulk concentration to determine the depth of the solute-depleted layer formed during the austenitizing heat treatment.

The heat-treated sample external oxide thickness and depth of internal oxidation were determined by using a Zeiss NVision 40 focused ion beam scanning electron microscope (FIB-SEM). The FIB-SEM was used to make ~ 15 μm wide trench cuts via Ga^+ ion beam milling. Prior to ion milling, the region of interest (ROI) was coated with W in order to protect the external oxides. High magnification SEI were acquired along the length of the trench cut using an in-lens detector. The SEI micrographs were analysed using ImageJ (v.1.52a) to determine the external oxide layer thickness and the depth of internal oxidation using a defined grid system (as shown in Appendix A). At least 200 measurements per sample were taken. The average external oxide thickness and depth of internal oxidation are reported using a 95% confidence interval of the mean.

A PHI Quantera II Scanning X-ray Photoelectron Spectroscope (XPS) equipped with an Al Kα X-ray source (1486.7 eV) was used for obtaining high-resolution surface spectra of the heat-treated M and M-IA samples. Elemental XPS depth profiles were obtained for the as-austenitized and

flash pickled M samples to determine the effects of flash pickling. The spot size and take-off angle of the X-ray beam were 100 µm and 45°, respectively. A pass energy of 140 eV (N, O, and C) and 55 eV (Al, Si, Fe, Cr, and Mn) and step size of 0.25 eV (N, O, and C) and 0.1 eV (Al, Si, Fe, Cr, and Mn) were used when acquiring the spectra. The sample surface was gently sputtered with Ar to remove any contamination prior to acquiring the high-resolution spectra. All spectra were calibrated using the metallic iron binding energy of 706.8 eV. For elemental depth profiling, a 1 mm × 1 mm area on the heat-treated sample surface was analysed after Ar sputtering at different time intervals. The acquired data was processed using MultiPak (v.9.5.1) software.

A FEI Titan 80-300HB TEM was used for high-resolution scanning transmission electron microscopy (HR-STEM) characterisation of selected heat-treated sample cross-sections to determine the fine-scale characteristics of the external and internal oxides. An acceleration voltage of 300 keV was used in all cases. Site-specific TEM samples were prepared using the FIB-SEM. Electron energy loss spectroscopy (EELS) was used to obtain elemental maps of the sample cross-sections. EELS spectra were acquired using Gatan Quantum GIF and were analysed with Gatan Digital Micrograph software (v. 3.43) to extract the elemental maps.

4.4 Results

4.4.1 Effect of process atmosphere pO_2 during austenitizing heat treatments

The external oxide morphology and distribution were determined by SEM for the M samples austenitized under the –30 °C, –10 °C, and +5 °C T_{dp} process atmospheres. SEM micrographs of the M samples, before and after flash pickling, are shown in Figure 4.3. The austenitizing time of 600 s resulted in significant external oxidation of the M samples. Nodule-type external oxides were observed for all M samples prior to flash pickling (Figure 4.3a) – Figure 4.3c)) regardless of process atmosphere T_{dp}. However, the distribution and surface coverage of the

external oxide nodules varied with process atmosphere T_{dp} (pO_2). For the M (–30 °C T_{dp}) sample, compact, nodule-type external oxides covered the surface, as shown in Figure 4.3a). Contrastingly, some thin film-type oxides were observed alongside the nodule-type oxides for the M (–10 °C T_{dp}) sample (Figure 4.3b)). Surface coverage of the nodule-type oxides decreased significantly with increased process atmosphere pO_2 (i.e., M (+5 °C T_{dp}), Figure 4.3c)) whereas the thin film-type oxide coverage increased. Extruded metallic Fe nodules were also observed for the M (+5 °C T_{dp}) sample. This was due to the higher process atmosphere pO_2 (Table 4.2) promoting internal oxidation of the solutes, resulting in extrusion of the Fe nodules due to the volume change. Similar Fe nodules were observed by Pourmajidian and McDermid [25] for a model 0.1C-6Mn-2Si (wt%) med-Mn steel which was annealed at –30 and +5 °C T_{dp} for 600 s. After flash pickling, most of the nodular external oxides were removed, irrespective of annealing process atmosphere. Thin film-type oxides along with metallic Fe nodules were observed on the pickled M surfaces (Figure 4.3d) – Figure 4.3f)), suggesting that flash pickling was effective at eliminating most of the external oxides for the M treatment, regardless of the austenitizing process atmosphere pO_2.

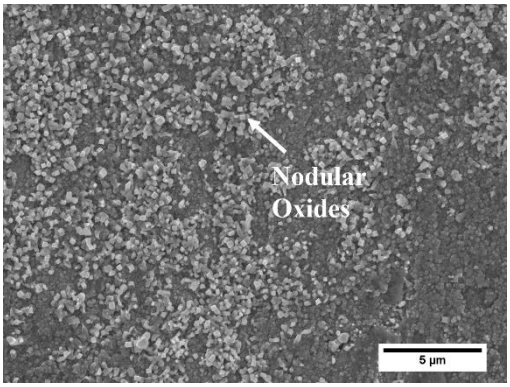

a)

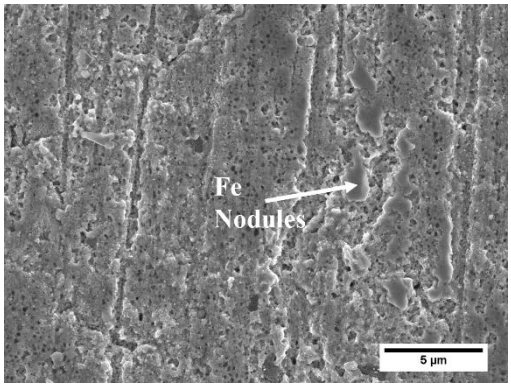

d)

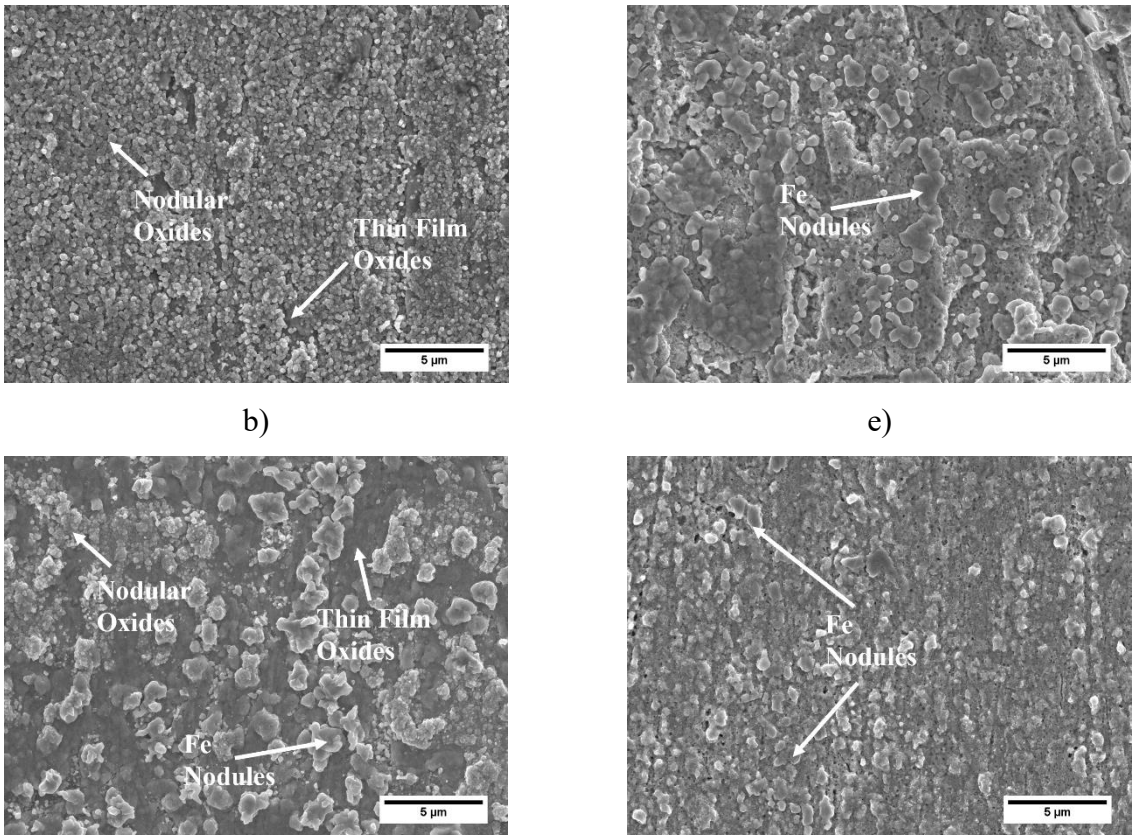

Figure 4.3: SEM images of as-austenitized steels a) M (–30 °C T_{dp}), b) M (–10 °C T_{dp}), and c) M (+5 °C T_{dp}); flash pickled d) M (–30 °C T_{dp}), e) M (–10 °C T_{dp}), and f) M (+5 °C T_{dp}).

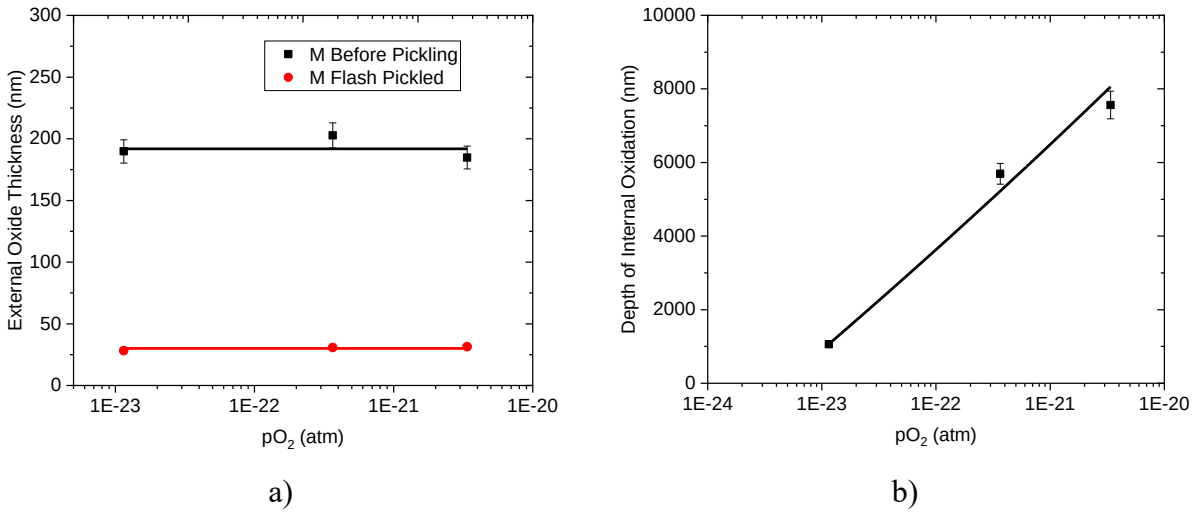

Figure 4.4: a) External oxide thickness and b) depth of internal oxidation as a function of process atmosphere pO_2 during the austenitizing heat treatment (775 °C × 600 s).

The external oxide thickness and the depth of internal oxidation for the M treatment were determined by FIB trench cut analysis (details of which are provided in Appendix A). The results are shown in Figure 4.4. Figure 4.4a) shows that the average external oxide thickness (~ 200 nm) did not change significantly with increasing process atmosphere pO_2. However, flash pickling largely eliminated the external oxide (to less than 50 nm) for all austenitizing process atmosphere pO_2 (Figure 4.4a)). On the other hand, the depth of internal oxidation increased significantly with increasing process atmosphere pO_2 (Figure 4.4b)). As would be expected, the higher process atmosphere pO_2 resulted in a higher inward flux of oxygen, which in turn resulted in a deeper internal oxidation layer for the M samples.

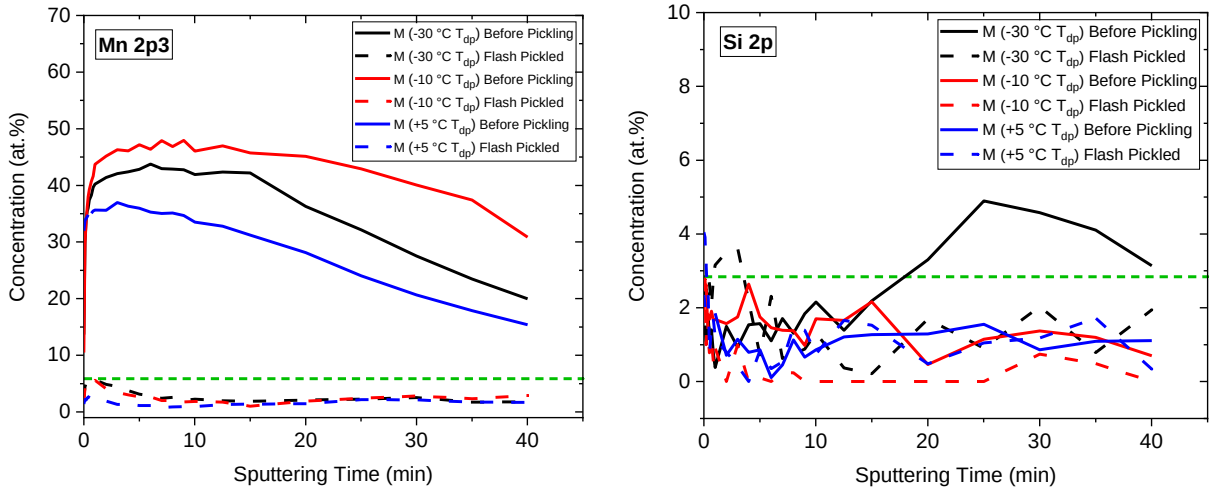

a) b)

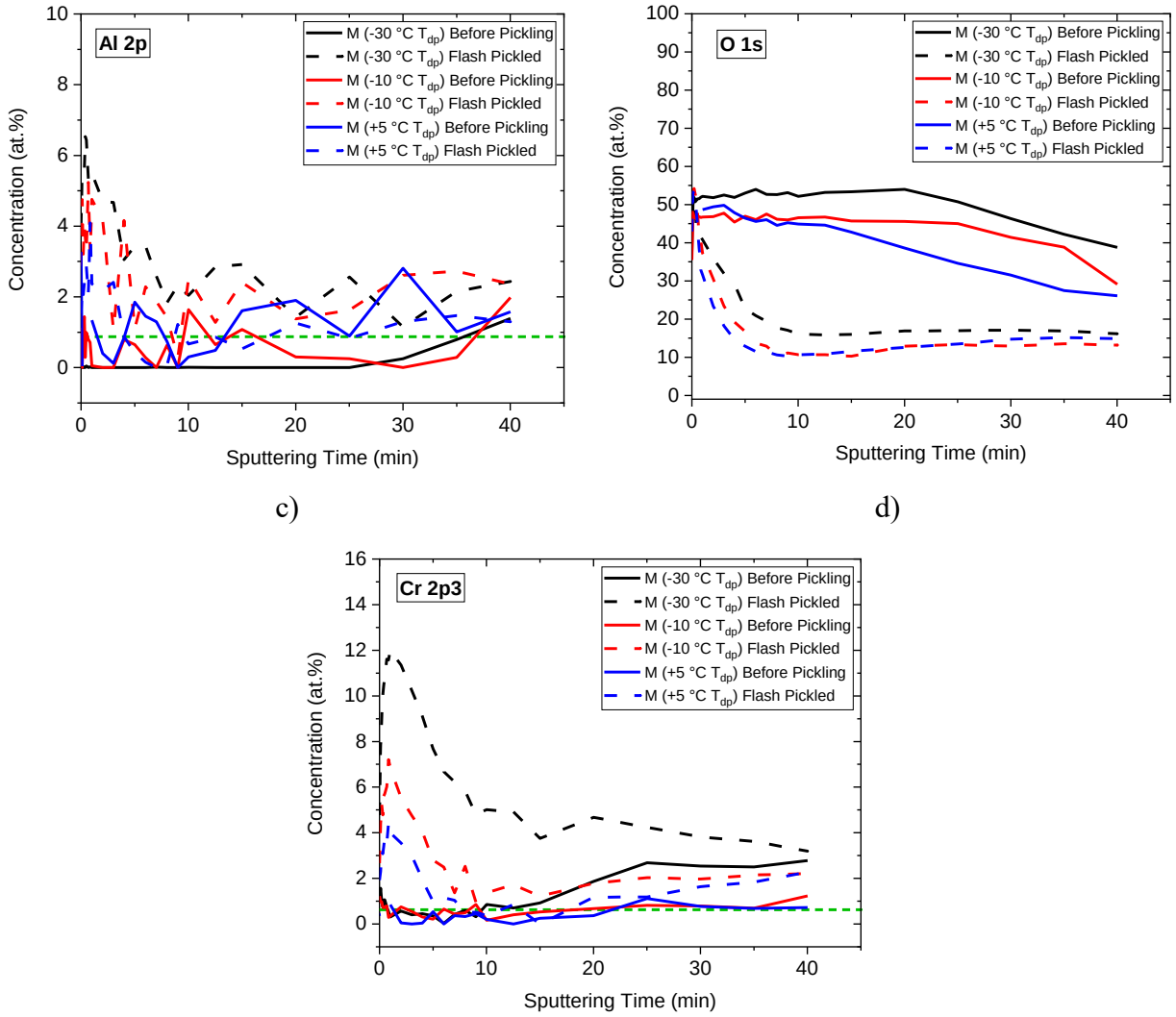

Figure 4.5: XPS elemental depth profiles of a) Mn, b) Si, c) Al, d) O, and e) Cr as a function of process atmosphere pO_2 for the austenitizing heat treatment. The green dashed lines represent the bulk concentration of the respective elements, per Table 4.1.

Table 4.4: XPS Binding Energies used for M Sample Surface Oxide Species Identification. Note that the Flash Pickled M (–30 °C T_{dp}) Sample is Representative of all Flash Pickled M samples.

Steel ID	Measured XPS Binding Energies (eV)				Oxide Species Present	Ref.
	Mn $2p_{3/2}$	Al 2s	Si 2p	Cr 2p		

M (–30 °C T_{dp})	640.8	-	-	-	MnO	[37-43]
M (–10 °C T_{dp})	641.5	119.3	102.6	576.6	MnO, $MnAl_2O_4$, $MnSiO_3/Mn_2SiO_4$, $MnCr_2O_4$	
M (+5 °C T_{dp})	641.7	119.5	102.5	576.9		
Flash Pickled M (–30 °C T_{dp})	641.3	119.3	102.5	576.6		

XPS was used to determine elemental depth profiles to assess alloying element enrichment at the surface and subsurface of the as-austenitized and flash pickled M samples. Figure 4.5 shows the depth profiles for the major alloying elements as a function of sputtering time and austenitizing process atmosphere pO_2. The green dashed line in each plot represents the nominal bulk concentration of the alloying element, per Table 4.1. Before pickling, the surface of the M (–30 °C T_{dp}) treatment was enriched in Mn (Figure 4.5a), suggesting the formation of Mn-rich oxides. XPS binding energy analysis of the high-resolution spectra (Table 4.4) confirmed that the nodular oxides were MnO. These MnO nodules were also observed for the M (–10 °C T_{dp}) and M (+5 °C T_{dp}) treatments along with $MnAl_2O_4$, $MnSiO_3/Mn_2SiO_4$, and $MnCr_2O_4$ (Table 4.4). Further analysis of Figure 4.5 revealed that Cr, Si, and Al enrichment occurred at longer sputtering times, suggesting that these oxides formed either as external oxides below the nodular MnO or as internal oxides in the subsurface. Moreover, it was also revealed that the external oxides were largely removed during flash pickling (Figure 4.5). High-resolution surface spectra analysis confirmed that some MnO, $MnAl_2O_4$, $MnSiO_3/Mn_2SiO_4$, and $MnCr_2O_4$ oxides remained on the flash pickled samples, as shown in Table 4.4. Further analysis of Figure 4.5 revealed significant Cr and Al enrichment with comparatively lower Si enrichment in the flash pickled samples. This suggests the external oxides after pickling were mainly $MnCr_2O_4$ with some $MnAl_2O_4$ also being present along with very minor Mn-silicates (i.e., $MnSiO_3/Mn_2SiO_4$). Furthermore, XPS (Figure 4.5) also

showed lower than bulk levels of Mn and Si in the subsurface for some distance into the steel, suggesting that there was significant solute depletion of the near-surface region.

The external and internal oxide chemistry was determined by analysing the cross-sectional microstructures of the M samples with TEM + EELS elemental maps. Figure 4.6 shows the high angle annular dark field (HAADF) image and composite elemental map for the M (–30 °C T_{dp}) sample cross-section prior to flash pickling. It should be noted that Figure 4.6 does not show the entirety of the internal oxidation zone as it is focussed on the M (–30 °C T_{dp}) external oxides morphology and chemistry. Two oxide morphologies were identified in the M (–30 °C T_{dp}) sample, as shown in Figure 4.6a). The external oxides were designated type 1 whereas type 2 oxides were the thick sub-surface internal oxides. Per Table 4.4 and XPS binding energy analysis, the type 1 external oxides comprised MnO with a thin layer of $MnCr_2O_4$ oxides underneath the MnO layer, as shown in Figure 4.6b). Samanta et al. [44] reported similar Mn and Cr-rich external oxides in Cr containing AHSSs (~ 0.50 wt%) annealed at 800 °C in a N_2–5 vol% H_2 process atmosphere with –40 °C T_{dp}. Further analysis of Figure 4.6 determined that Al and Si predominantly formed internal oxides. Moreover, the TEM analysis confirmed the SEM finding of extruded metallic Fe nodules being present on the surface of the M (–30 °C T_{dp}) sample [19,45-47]. TEM EELS analysis was also performed on the cross-section of the flash pickled M (–30 °C T_{dp}) sample and the results are shown in Figure 4.7. Comparison of Figure 4.7 to Figure 4.6 will reveal that the thick external MnO present on the M (–30 °C T_{dp}) surface prior to flash pickling was largely dissolved. The remaining external oxides comprised of a thin layer of Mn and Cr-rich oxides (Figure 4.7b)). Furthermore, another internal oxide morphology – type 3 oxides, comprising core-shell type grain boundary oxides – was identified in the flash pickled M (–30 °C T_{dp}) sample (Figure 4.7a)). The core of the internal oxides was enriched with Al. The shell of the internal oxide, on the other hand,

was Si-rich. However, Mn and Cr enrichment were also observed in some of the internal oxide network. Similar core-shell type internal oxides have been reported in annealed AHSSs [21,25]. However, the chemistry of the core-shell structure depended on the steel chemistry.

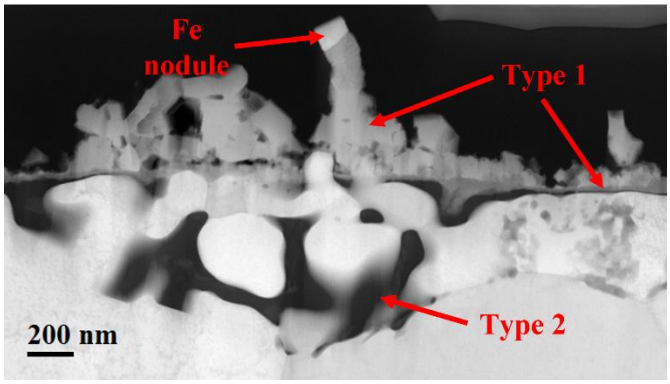

a)

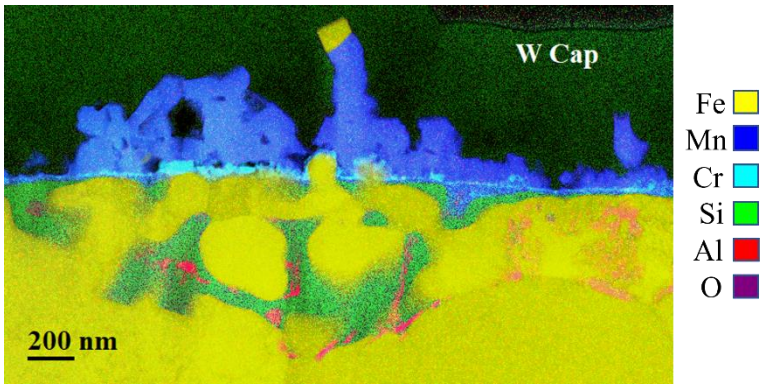

b)

Figure 4.6: a) HAADF image and b) corresponding TEM EELS composite map for the M (–30 °C T_{dp}) sample before flash pickling.

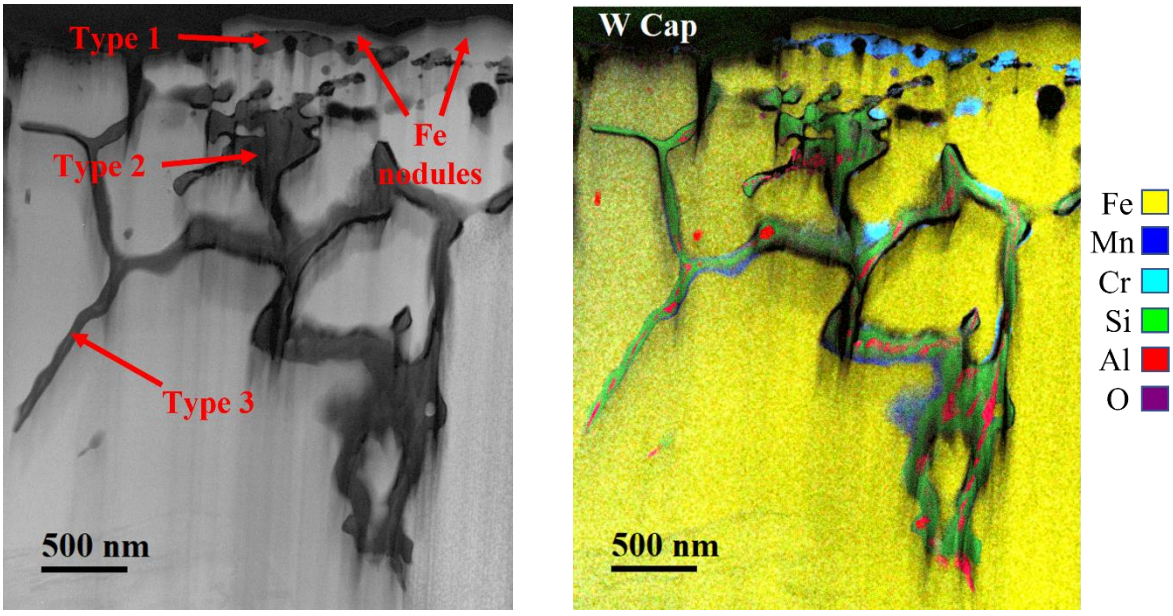

a) b)

Figure 4.7: a) HAADF image and b) corresponding TEM EELS composite map for the M (–30 °C T_{dp}) sample after flash pickling.

SEM-EDS line scans were performed on the cross-section of M samples to determine the depth of the solute-depleted layer formed during the austenitizing heat treatment. Figure 4.8 shows the result for the M (–10 °C T_{dp}) sample, from which Mn, Al, Si, Cr, and O depth profiles were acquired. From the Mn depth profile, it was found that the depth of solute-depleted layer was approximately 6 µm and coincided with the internal oxide zone formed during the austenitizing heat treatment. A similar solute-depleted layer was also identified for the M (–30 °C T_{dp}) and M (+5 °C T_{dp}) samples. Furthermore, the presence of Mn and Si-rich grain boundary oxides was also ascertained through the Mn, Si, and O profiles in Figure 4.8 (marked by the vertical dashed lines).

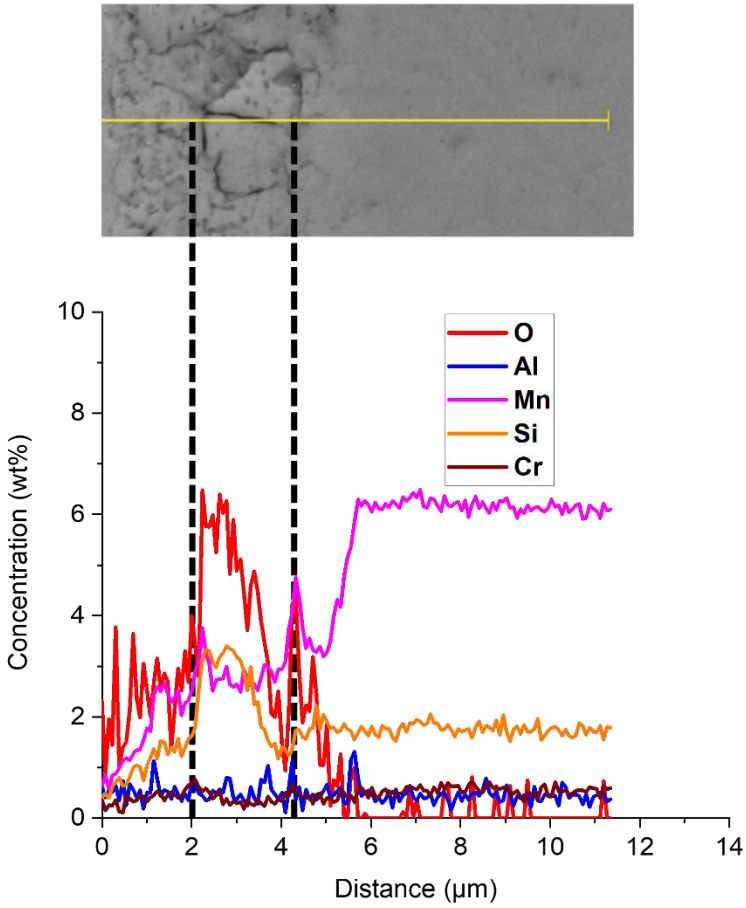

Figure 4.8: SEM-EDS line scan showing the depth of solute-depleted layer in M (–10 °C T_{dp}) sample.

4.4.2 Effect of process atmosphere pO_2 during intercritical annealing

The flash pickled M samples were subsequently subjected to a CGL-compatible intercritical annealing heat treatment [12], per Table 4.3. As was the case for the austenitizing heat treatment, three process atmosphere dew points (–30, –10, and +5 °C T_{dp}) were used to determine the effect of process atmosphere pO_2 on substrate external and internal oxidation. The external oxide morphology and distribution for the intercritically annealed M samples (M-IA) are shown in Figure 4.9. For the M (–30 °C T_{dp}) samples (Figure 4.9a) – Figure 4.9c)), the surface comprised fine nodule-type oxides alongside discreate patches of thin film-type oxides, regardless of the

process atmosphere dew point employed during intercritical annealing. Contrastingly, for the M samples austenitized at the higher process atmosphere T_{dp} of –10 °C and +5 °C, Figure 4.9d) – Figure 4.9i), the surface was covered with thin, film-type oxides with some scattered fine nodular oxides. Furthermore, significant quantities of extruded metallic Fe nodules were observed on the surfaces of these higher T_{dp} annealed M-IA samples owing to deeper internal oxidation during austenitizing and intercritical annealing. These Fe nodules would likely be beneficial for reactive wetting during galvanizing as they will likely react preferentially with the galvanizing bath due to their higher surface/volume ratio to initiate the formation of the $Fe_2Al_5Zn_x$ interfacial layer.

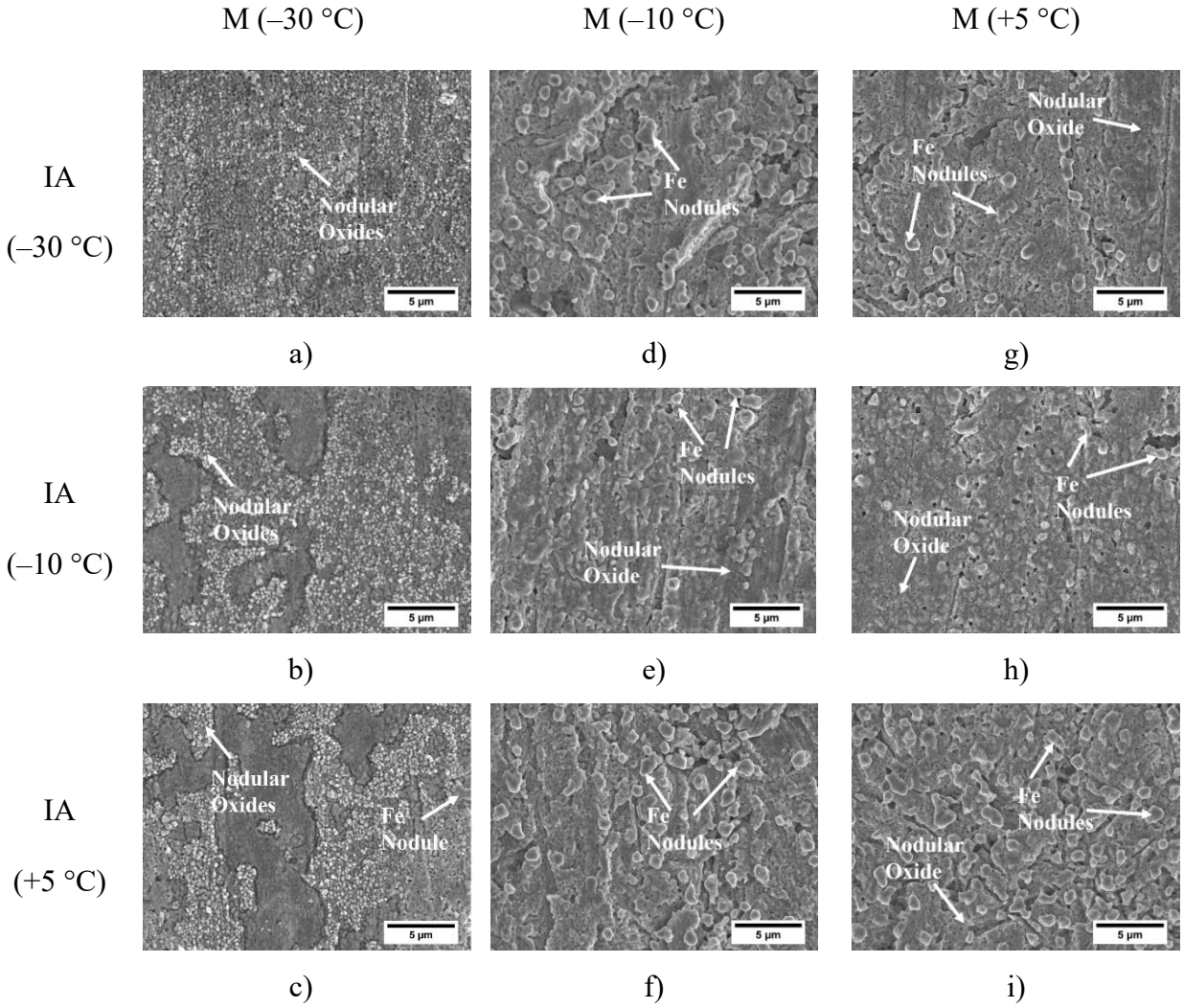

Figure 4.9: SEM images of the surfaces of M-IA samples austenitized, flash pickled, and intercritically annealed as a function of process atmosphere T_{dp} (pO_2).

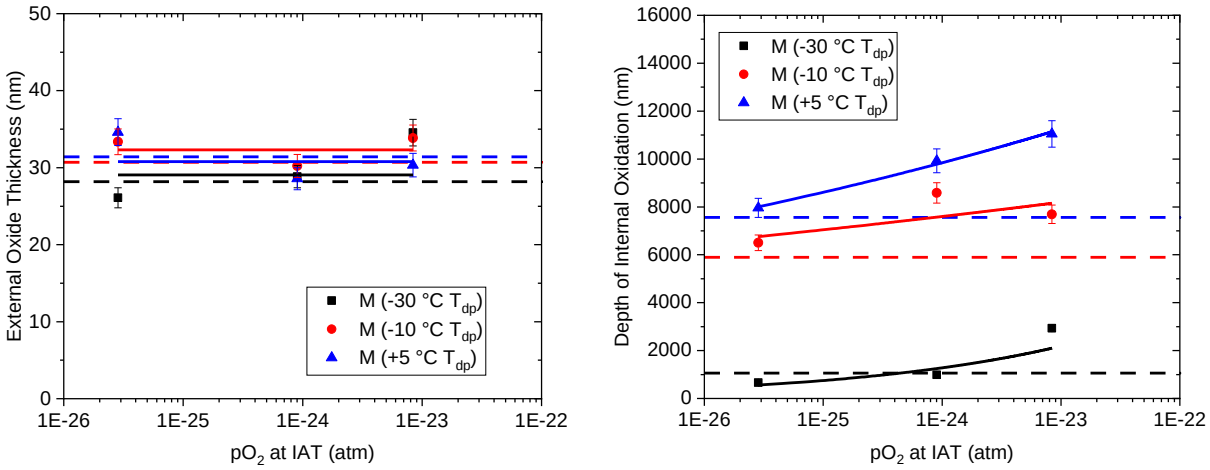

a) b)

Figure 4.10: a) External oxide thickness and b) depth of internal oxidation as a function of intercritical annealing process atmosphere pO_2; the dashed lines represent the external oxide thickness and depth of internal oxidation of the flash pickled samples for their respective austenitizing heat treatment process atmosphere pO_2.

The external oxide thickness and depth of internal oxidation for the M-IA samples were determined by FIB trench cut analysis and the results are shown in Figure 4.10. The dashed lines in Figure 4.10 represent the average external oxide thickness and depth of internal oxidation of the flash pickled M samples for their respective process atmosphere T_{dp} (pO_2) during the austenitizing heat treatment. These dashed lines were used to determine if further growth of the external and internal oxide layers had occurred during intercritical annealing. As can be seen in Figure 4.10a), no significant change in external oxide thickness was observed for the intercritically annealed samples, regardless of process atmosphere pO_2 during intercritical annealing. As a result, a thin (~ 30 nm) external oxide layer was present for all M-IA samples and is likely indicative of relatively

large portions of the substrate Fe being boldly exposed to the environment. In the case of MnO films, this finding is promising as Kavitha and McDermid [48] have reported that it is possible to aluminothermically reduce up to 85 nm of external MnO within the common CGL dipping time of 4 s. On the other hand, the depth of internal oxidation increased significantly with increasing process atmosphere pO_2 during intercritical annealing, regardless of austenitizing process atmosphere (Figure 4.10b)). The deepest internal oxidation zone (~ 11 μm) was observed in for the M (+5 °C T_{dp})-IA (+5 °C T_{dp}) sample (Figure 4.10b)). It should be noted that this relatively deep internal oxidation zone can affect AHSS resistance spot welding (RSW) such that the weld lobe is shifted to higher currents or longer welding times [49].

The external oxide species on the intercritically annealed surfaces were identified by analysing the XPS binding energies from the high-resolution spectra collected. Appendix B shows the XPS binding energy analysis for the M (–30 °C T_{dp})-IA (–30 °C T_{dp}) sample. This analysis is representative of all the M-IA samples. In all cases, MnO, $MnAl_2O_4$, $MnSiO_3$/Mn_2SiO_4, and $MnCr_2O_4$ were identified on the sample surface. It should be noted that these external oxide species corresponded to those identified for the flash pickled M surfaces, as shown in Table 4.4.

TEM EELS analysis was conducted on cross-sections of the M (–30 °C T_{dp})-IA samples to determine the external and internal oxide chemistry and morphology. These samples were chosen as they had a shallower internal oxide zone (Figure 4.10b)), which is expected to have benefits with respect to the RSW of the present med-Mn steel [49]. All three oxide morphologies, as identified above, were observed in the M (–30 °C T_{dp})-IA samples, as shown in Figure 4.11 – Figure 4.13. The type 1 external oxides were mainly Mn and Cr-rich oxides (Figure 4.11b), Figure 4.12h), and Figure 4.13h)). Comparison of Figure 4.11b), Figure 4.12h), and Figure 4.13h) to the TEM EELS maps of the flash pickled M (–30 °C T_{dp}) surface (Figure 4.7) will show no significant

difference between the two and indicates that no significant growth of the external oxide layer occurred during intercritical annealing, consistent with the results shown in Figure 4.10.

TEM EELS analysis also revealed that the type 2 oxides were mainly comprised of Si and Al (Figure 4.11 – Figure 4.13). However, some Mn and Cr enrichment was also observed in all the samples, particularly in the oxide shells. Furthermore, it should be noted that this relatively thick sub-surface internal oxide layer was similar to that observed in the M (–30 °C T_{dp}) sample (Figure 4.6).

Further analysis of the TEM EELS elemental maps for the M (–30 °C T_{dp})-IA (–10 °C T_{dp}) (Figure 4.12) and M (–30 °C T_{dp})-IA (+5 °C T_{dp}) samples (Figure 4.13) established that the type 3 internal oxides had a core-shell type structure. However, the chemistry of this core-shell internal oxide was different as compared to those observed in the flash pickled M (–30 °C T_{dp}) samples (Figure 4.7). A Si-rich oxide core was observed in the M (–30 °C T_{dp})-IA (–10 °C T_{dp}) and M (–30 °C T_{dp})-IA (+5 °C T_{dp}) samples (Figure 4.12e) and Figure 4.13e), respectively). The shell of the internal oxide was Mn-containing with some scattered Cr, as shown in Figure 4.12c), Figure 4.12g), Figure 4.13c), and Figure 4.13g). However, Al-rich oxides were not observed in these type 3 internal oxides. Moreover, it should be noted that extruded Fe nodules were also observed on the surface of the M (–30 °C T_{dp})-IA samples (Figure 4.11b), Figure 4.12b), and Figure 4.13b)).

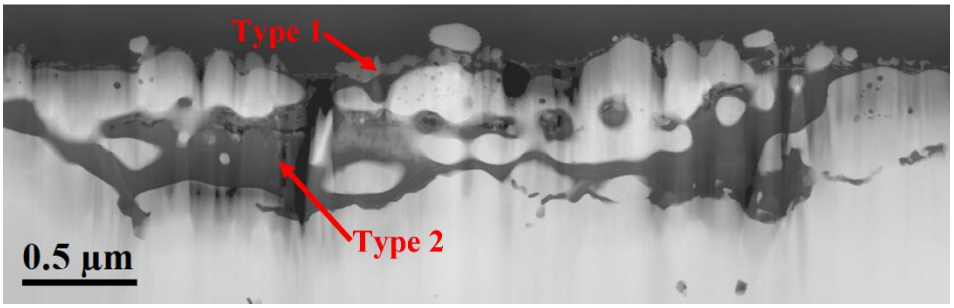

a)

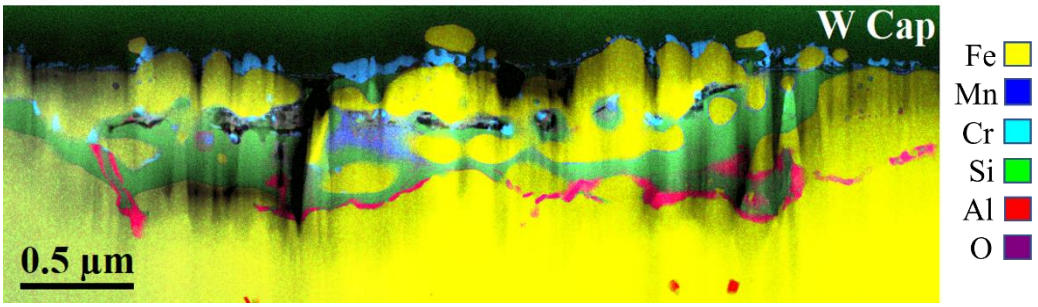

b)

Figure 4.11: a) HAADF image and b) corresponding TEM EELS composite elemental map for the M (–30 °C T_{dp})-IA (–30 °C T_{dp}) sample.

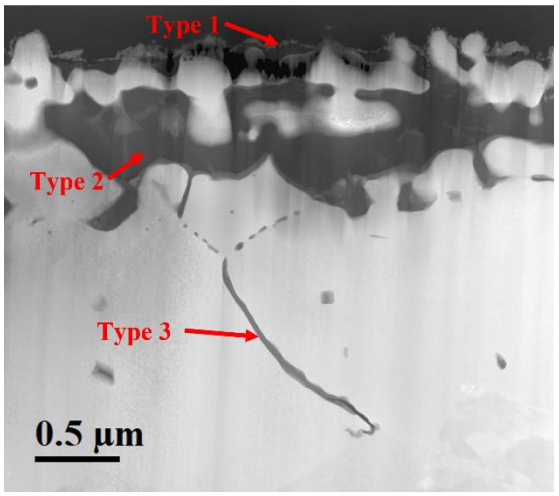

a)

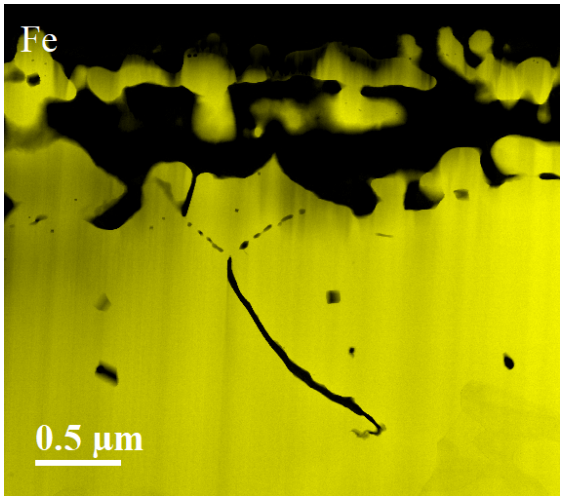

b)

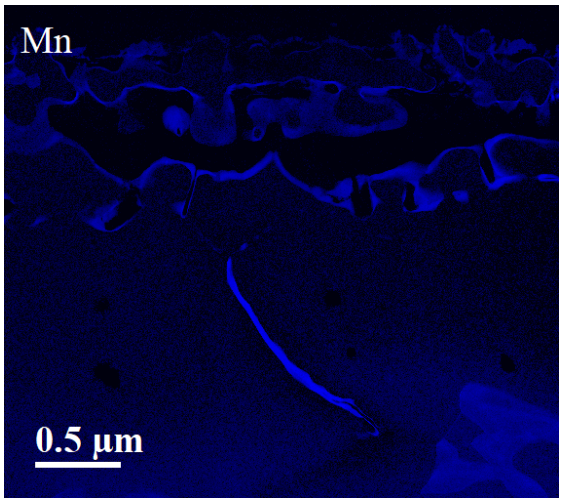

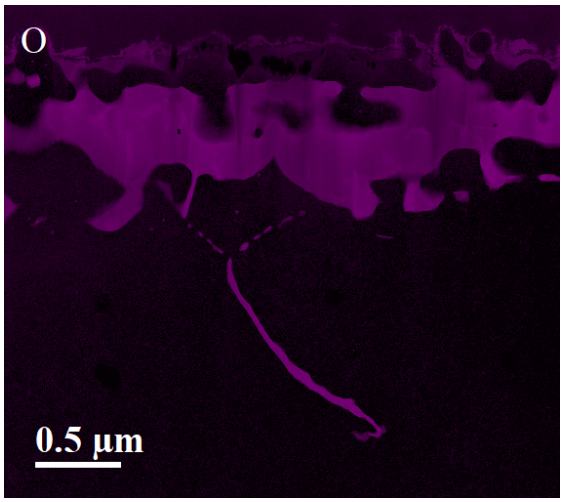

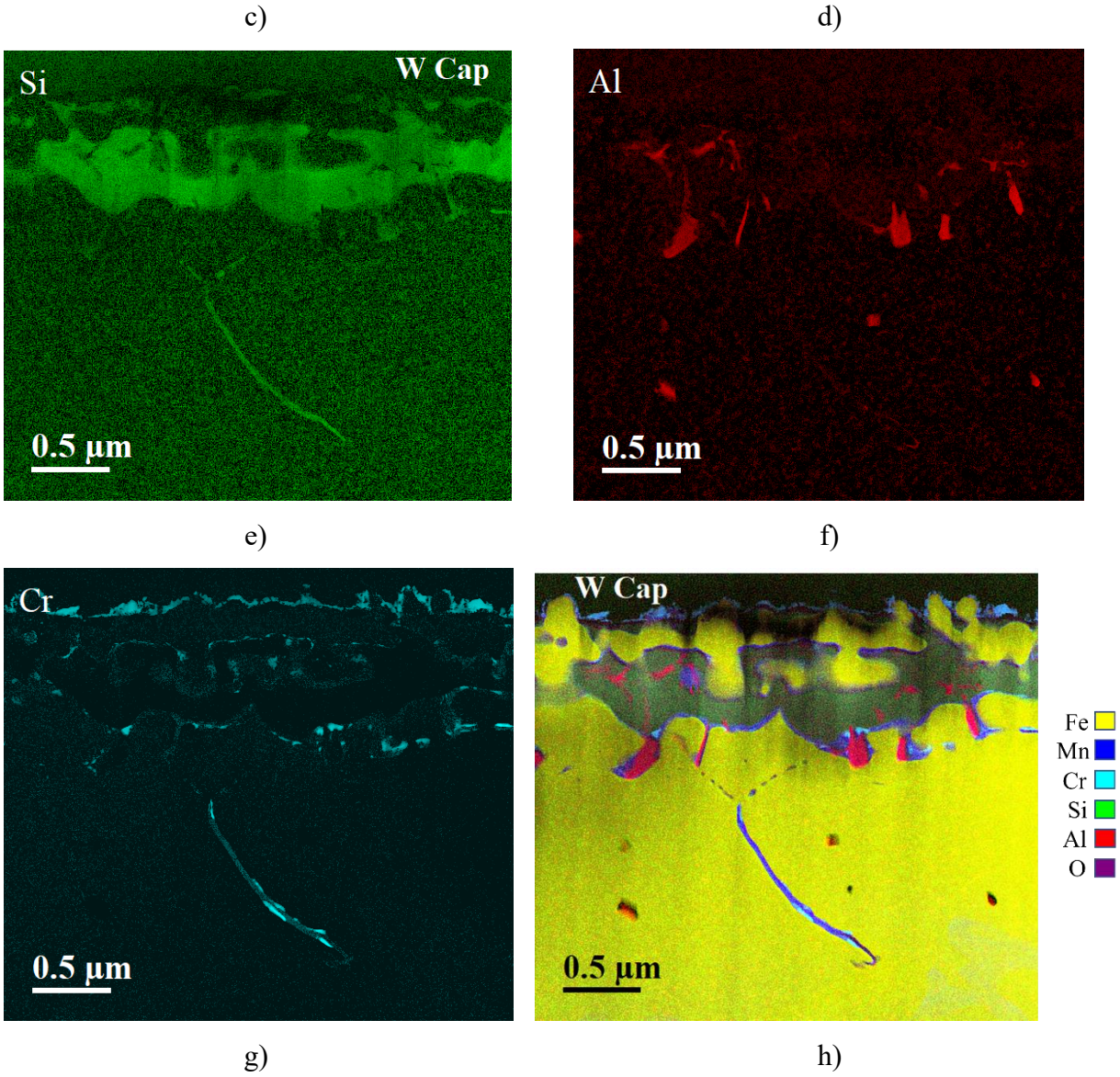

Figure 4.12: a) HAADF image and TEM EELS elemental maps of b) Fe, c) Mn, d) O, e) Si, f) Al, g) Cr, and h) corresponding composite elemental map for the M (–30 °C T_{dp})-IA (–10 °C T_{dp}) sample.

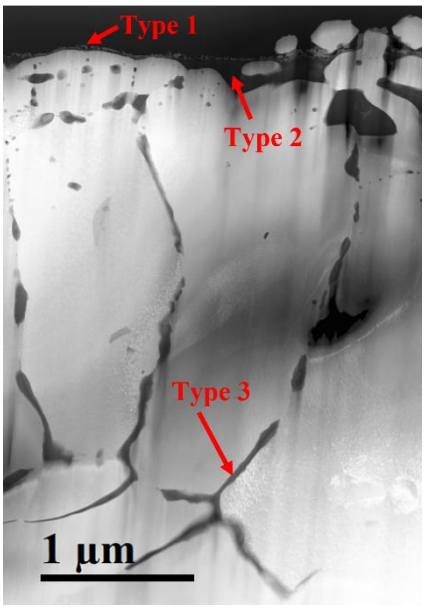

a)

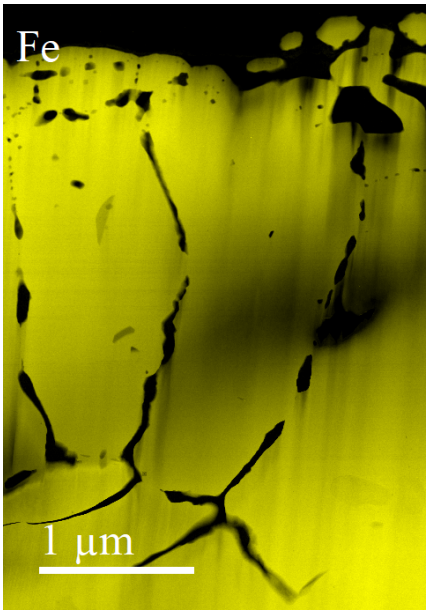

b)

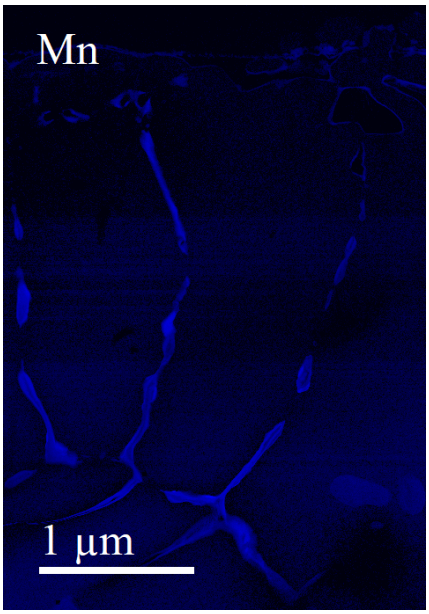

c)

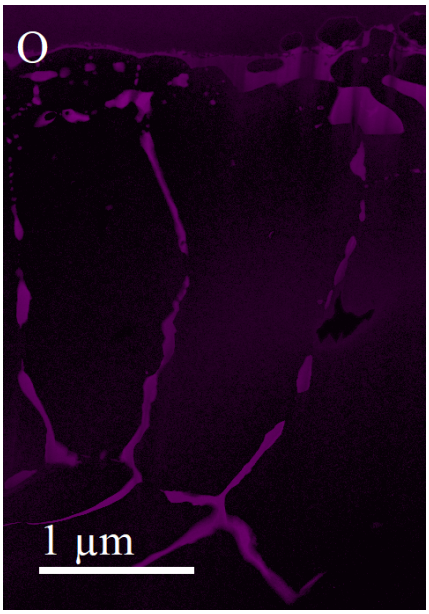

d)

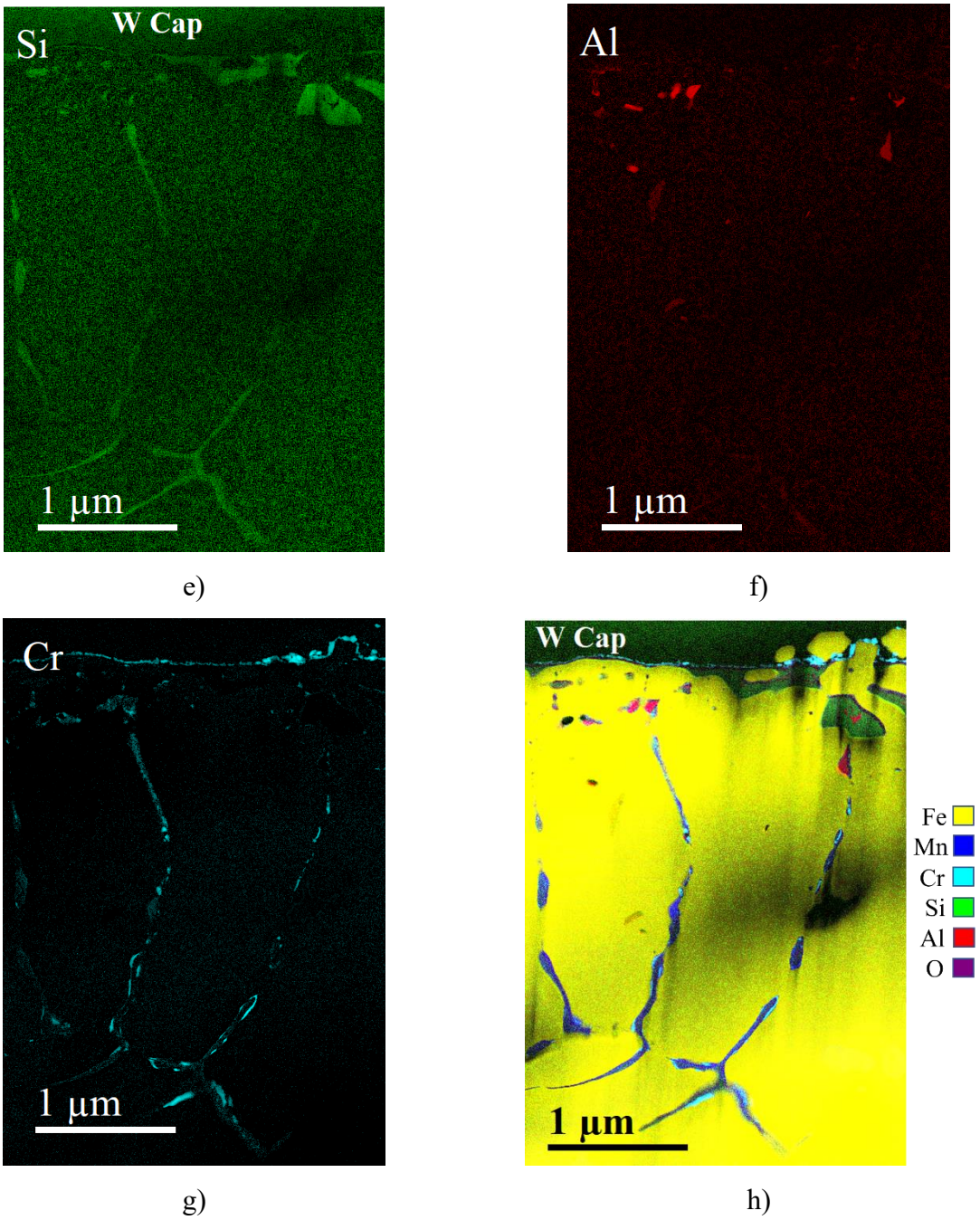

Figure 4.13: a) HAADF image and TEM EELS elemental maps of b) Fe, c) Mn, d) O, e) Si, f) Al, g) Cr, and h) corresponding composite elemental map for M (–30 °C T_{dp})-IA (+5 °C T_{dp}) sample.

4.5 Discussion

A prototype med-Mn steel was subjected to a two-stage CGL-compatible austenitizing and intercritical annealing heat treatment under three process atmosphere T_{dp} (–30, –10, and +5 °C) to determine the effect of process atmosphere pO_2 on selective external and internal oxidation. The heat treatment parameters were chosen based on a previous study of this prototype steel which yielded 3G AHSS target mechanical properties [12].

It was found that the austenitizing heat treatment resulted in external oxides with an average thickness of approximately 200 nm regardless of the process atmosphere pO_2, as shown in Figure 4.4a). It should be noted that a simple Wagner [50] analysis (using the diffusion data from Table 4.6 and thermodynamic data from Appendix C) predicts that the oxidation mode for Mn changes from external to internal oxidation at $T_{dp} \geq$ –30 °C for the austenitizing temperature of 775 °C. Nevertheless, external oxides formed during the austenitizing heat treatment for all process atmosphere T_{dp} explored, belying this prediction. The external oxides grew to an approximately equal thickness after the 600 s holding time, indicating that they likely formed during sample heating. Contrastingly, the predominant internal oxidation mode resulted in a significant increase in the internal oxidation depth with increasing process atmosphere T_{dp} (pO_2) (Figure 4.4b)). SEM examination of the external oxides revealed that the morphology, distribution, and surface coverage of the external oxides varied with process atmosphere pO_2 (Figure 4.3a) - Figure 4.3c)). For the –30 °C T_{dp} process atmosphere, the surface was covered with nodular oxides (Figure 4.3a)). XPS revealed that these nodular oxides were MnO (Table 4.4). Fine-scale TEM+EELS analysis of the sample cross-section established that MnO overlayed a thin $MnCr_2O_4$ layer (Figure 4.6b)). However, the Wagner model [50] predicts internal oxidation of Cr, thereby not being consistent with the TEM observation. It should be noted that one of the limitations of the Wagner model [50]

is its applicability in complex alloy and oxide systems. Hence, formation of the complex $MnCr_2O_4$ instead of simple binary oxide (i.e., Cr_2O_3) is likely the reason for this disagreement. Nevertheless, this result is consistent with the observations reported by various researchers with Mn and Cr containing AHSSs [43,44,51]. For example, Swaminathan [51] reported external $MnCr_2O_4$ formation owing to chemical interactions between Mn and Cr at higher process atmosphere $T_{dp} \geq$ –40 °C for a Fe-2Mn-0.8Cr (wt%) alloy. In the present research, thin film-type external $MnCr_2O_4$ were observed alongside nodule-type MnO for the M (–10 °C T_{dp}) and M (+5 °C T_{dp}) samples (Figure 4.3b) and Figure 4.3c)). However, only nodular MnO was observed for the M (–30 °C T_{dp}) sample (Figure 4.3a)). As explained above, this change in morphology of the external oxides was likely due to the change in predominant Mn oxidation mode from external to internal for the higher pO_2 process atmospheres, as shown in Figure 4.4b). Extruded Fe nodules resulting from the volume expansion associated with internal oxidation were also observed for the M (+5 °C T_{dp}) sample austenitized under the highest process atmosphere pO_2 of 3.38×10^{-21} atm (Table 4.2). Similar external oxide distribution and surface coverage was reported by Pourmajidian and McDermid [25] for a model 0.1C-6Mn-2Si (wt%) med-Mn steel which was annealed for 600 s at +5 °C T_{dp}. XPS binding energy analysis revealed that the film-type oxides alongside the nodular MnO were complex oxides comprising $MnAl_2O_4$, $MnSiO_3$/Mn_2SiO_4, and $MnCr_2O_4$.

The intermediate flash pickling step significantly reduced the average thickness of the external oxides to approximately 30 nm, as shown in Figure 4.4a). Furthermore, SEM analysis (Figure 4.3d) – Figure 4.3f)) and XPS Mn depth profiling (Figure 4.5a)) confirmed a significant reduction of the MnO layer thickness. XPS depth profiling (Figure 4.5) and TEM EELS analysis (Figure 4.7) also showed that the external oxides comprised $MnCr_2O_4$ with some $MnAl_2O_4$ and minor $MnSiO_3$/Mn_2SiO_4. This is consistent with literature which reported that MnO, $MnSiO_3$, and

Mn_2SiO_4 oxides are highly soluble in HCl [52-54]. Furthermore, the presence of Fe nodules was observed on the flash pickled surface of not only the M (+5 °C T_{dp}) sample but also the M (–30 °C T_{dp}) and M (–10 °C T_{dp}) samples owing to the dissolution of the relatively thin external oxides covering the Fe nodules (Figure 4.3d) - Figure 4.3f)).

TEM EELS analysis of the M (–30 °C T_{dp}) sample, both before and after flash pickling (Figure 4.6 and Figure 4.7), revealed that the near-surface internal oxide layer was enriched with Al and Si. This would be expected for Al as Wagner model [50] predicts internal oxidation of Al for all three process atmosphere T_{dp}. However, Si is expected to oxidize externally for the –30 °C T_{dp} process atmosphere, as predicted by the Wagner model [50]. This inconsistency was likely due to the fact that Si formed complex $MnSiO_3/Mn_2SiO_4$ (Table 4.4) instead of simple SiO_2. Further analysis of Figure 4.7b) revealed that the internal oxides, particularly those formed at the grain boundaries, had a core-shell type structure. The core of these internal oxides was enriched with Al whereas the shell was enriched in Si with some Mn and Cr enrichment. This structure can be explained in terms of the thermodynamic driving force for oxide formation, solubility of the oxides in austenite, and the relative diffusivities of these elements during the austenitizing heat treatment.

Figure 4.14 provides the relevant thermodynamic information for the equilibrium pO_2 of the relevant metal-oxide reactions and experimental process atmosphere dew points as a function of temperature. Figure 4.14a) provides a comprehensive compilation for a large temperature range, where the red box highlights the temperature range of relevance for the current experiments and Figure 4.14b) provides a more detailed (and slightly simplified) version of Figure 4.14a). In the case of continuous galvanizing process atmospheres, the relevant reaction for the formation of a general ternary oxide ($M_xN_yO_z$) is the reaction of the general metallic solute(s) *M* and *N* with water vapour, as provided by equation (4.1):

$$xM + yN + zH_2O = M_xN_yO_z + zH_2 \quad (4.1)$$

At equilibrium, the standard Gibbs energy of equation (4.1) $\left(\Delta G^o_{4.1}\right)$ is given by:

$$\Delta G^o_{4.1} = -RT\ln K_{4.1} = -RT\ln\left[\frac{\left(pH_2\right)^z}{a_M^x a_N^y \left(pH_2O\right)^z}\right] \quad (4.2)$$

where *R* and *T* are the gas constant and absolute temperature, respectively, pH_2 and pH_2O are the partial pressures of hydrogen and water vapour, respectively, a_i is the activity of a general solute species, where it is assumed that the oxide is a pure condensed species with unit activity. For the present experiments, it should be noted that pH_2 = 0.05 in all cases. Furthermore, for a given process atmosphere with a fixed dew point, it should be noted that the $\left(\frac{pH_2}{pH_2O}\right)$ ratio is constant for all *T*. The reader should note that equations (4.1) and (4.2) can be easily modified for a binary oxide by removing the terms related to the second solute species, *N*. Equation (4.1) can be considered to be the sum of two sub-reactions, in this case the decomposition of water vapour and the formation of the general ternary oxide:

$$zH_2O = zH_2 + \frac{z}{2}O_2 \qquad \Delta G^o_{4.3} = -RT\ln K_{4.3} = -RT\ln\left[\frac{\left(pH_2\right)^z \left(pO_2\right)^{z/2}}{\left(pH_2O\right)^z}\right] \quad (4.3)$$

$$xM + yN + \frac{z}{2}O_2 = M_xN_yO_z \qquad \Delta G^o_{4.4} = -RT\ln K_{4.4} = -RT\ln\left[\frac{1}{a_M^x a_N^y \left(pO_2\right)^{z/2}}\right] \quad (4.4)$$

and

$$\Delta G^o_{4.1} = \Delta G^o_{4.3} + \Delta G^o_{4.4} = -RT\ln\left(K_{4.3}\bullet K_{4.4}\right) \quad (4.5)$$

where equations (4.3) and (4.4) can easily be solved to yield the equilibrium pO_2 associated with the applicable process atmosphere or oxide as a function of *T*. A complete listing of the thermodynamic data used to calculate Figure 4.14 can be found in Appendix C.

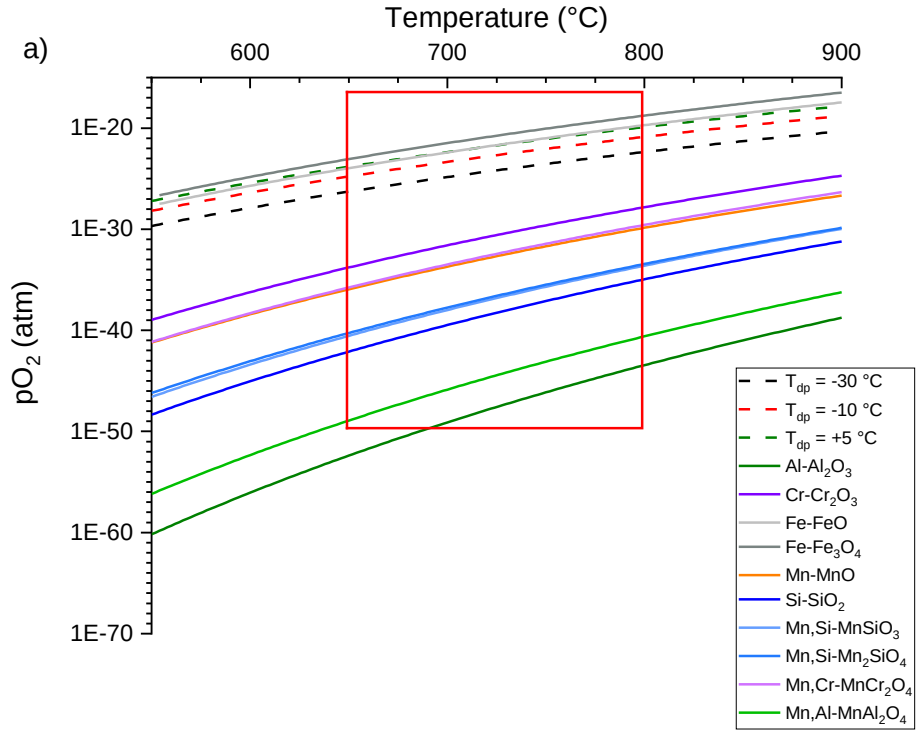
a)
Temperature (°C)
600
700
800
900
1E-20
1E-30
1E-40
1E-50
1E-60
1E-70
pO2 (atm)
Tdp = -30 °C
Tdp = -10 °C
Tdp = +5 °C
Al-Al2O3
Cr-Cr2O3
Fe-FeO
Fe-Fe3O4
Mn-MnO
Si-SiO2
Mn,Si-MnSiO3
Mn,Si-Mn2SiO4
Mn,Cr-MnCr2O4
Mn,Al-MnAl2O4

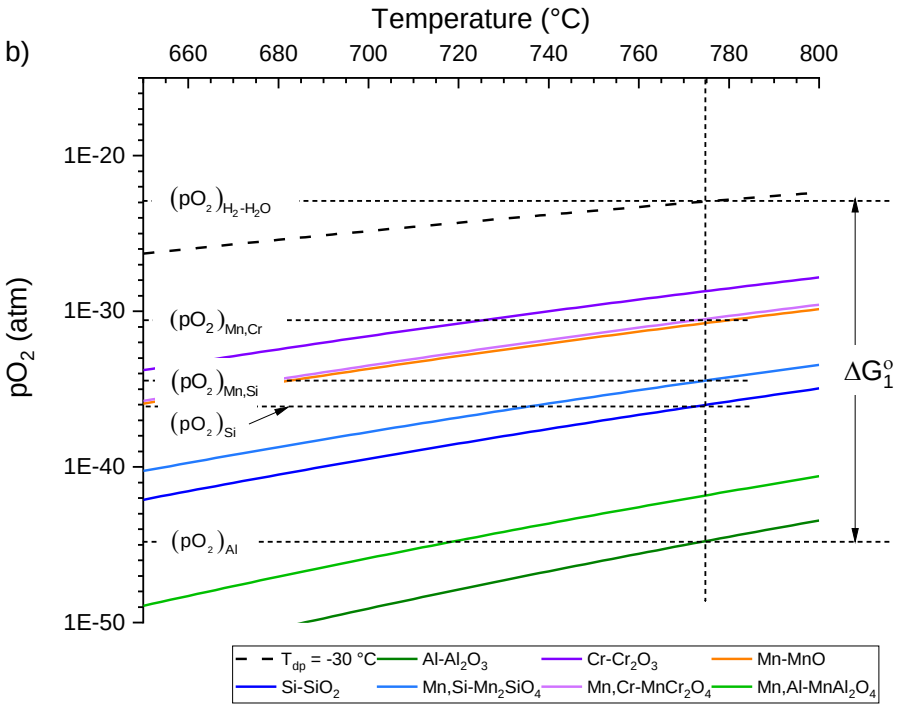
b)
Temperature (°C)
660
680
700
720
740
760
780
800
1E-20
1E-30
1E-40
1E-50
pO2 (atm)
(pO2)H2-H2O
(pO2)Mn,Cr
(pO2)Mn,Si
(pO2)Si
(pO2)Al
ΔG°1
Tdp = -30 °C
Al-Al2O3
Cr-Cr2O3
Mn-MnO
Si-SiO2
Mn,Si-Mn2SiO4
Mn,Cr-MnCr2O4
Mn,Al-MnAl2O4

Figure 4.14: Oxygen partial pressure *vs* temperature for the formation of (a) relevant oxides and all experimental dew points (b) detailed view of the experimental region with the –30 °C T_{dp} process atmosphere, emphasizing the austenitizing temperature of 775 °C.

Figure 4.14a) shows that all three process atmospheres (–30 °C, –10 °C, and +5 °C T_{dp}) are reducing with respect to any Fe-oxides present on the as-received substrates but are oxidizing with respect to the primary alloying elements Mn, Si, Al, and Cr. For the austenitizing heat treatments, Figure 4.14b) provides a detailed view of the thermodynamic driving forces for the oxidation reactions. It has been argued by Zhang et al. [55] that the selective oxidation reactions are driven by the pO_2 of the process atmosphere, but this is not a complete picture. As can be seen in Figure 4.14b), the pO_2 of the –30 °C T_{dp} N_2–5 vol% H_2 process atmosphere is approximately 10^{-23} atm. However, the equilibrium pO_2 of the solute oxides are many orders of magnitude less than that of the process atmosphere, indicative of a significant thermodynamic driving force for their formation, with the driving force for the reaction being proportional to the difference in the equilibrium pO_2 between the process atmosphere and oxide formation reaction (Figure 4.14b)). From this graphic, it is clear that the driving force for the oxides of concern for the ternary oxide formation (reaction (4.1)) increases in the order:

$$Cr_2O_3 < MnCr_2O_4 < MnO < (Mn,Si) - oxides \leq SiO_2 < MnAl_2O4 < Al_2O_3 \quad (4.6)$$

where (Mn,Si) oxides refer to both $MnSiO_3$ and Mn_2SiO_4.

However, another factor which must be considered is the solubility of the oxide in the matrix. Table 4.5 lists the solubility products of the relevant oxides in both austenite at 775 °C for the austenitizing heat treatment and in ferrite at 675 °C for the IA heat treatment. As the near-surface region has been decarburized and also de-alloyed (Figure 4.8) during the austenitizing heat treatment, the most relevant solubility data for the IA treatment are those for ferrite. It should be

noted that an exceptionally high solubility product for an oxide would suggest that precipitation of the oxide will be delayed versus that of a low solubility product oxide, despite having a substantial thermodynamic driving force. From Table 4.5, it can be seen that most of the oxides observed in the present experiments have very low solubility products in both austenite and ferrite, with the solubility product of MnO being considerably higher than that of the other oxides suggesting that precipitation of MnO in austenite and ferrite matrix would be delayed versus the other oxides.

Table 4.5: Solubility Products of Oxide Species in Austenite at 775 °C and Ferrite at 675 °C.

Oxide Species	Solubility Product		Ref.
	Austenite at 775 °C	Ferrite at 675 °C	
MnO	$4.13\ (ppm)^2$	$0.34\ (ppm)^2$	[56-60]
SiO_2	$9.96 \times 10^{-6}\ (ppm)^3$	$6.06 \times 10^{-8}\ (ppm)^3$	
$MnAl_2O_4$	$6.59 \times 10^{-21}\ (ppm)^7$	$3.04 \times 10^{-27}\ (ppm)^7$	
Mn_2SiO_4	$6.87 \times 10^{-7}\ (ppm)^7$	$1.32 \times 10^{-11}\ (ppm)^7$	
Al_2O_3	$1.67 \times 10^{-19}\ (ppm)^5$	$1.70 \times 10^{-24}\ (ppm)^5$	
$MnCr_2O_4$	$1.08 \times 10^{-6}\ (ppm)^7$	$3.65 \times 10^{-6}\ (ppm)^7$	

Kinetic factors must also be taken into account when discussing selective oxidation under relatively transient CGL conditions. Table 4.6 and Table 4.7 list the diffusion data, diffusivities, and molar fluxes of the solute elements in austenite at 775 °C and ferrite at 675 °C, respectively. It can be seen that Al has significantly higher diffusivity in austenite compared to Si, Cr, and Mn, resulting in Al enrichment at the grain boundaries and formation of the internal oxide cores (Figure 4.6 and Figure 4.7). On the other hand, due to relatively slow diffusivity versus Al (but still greater

than Mn and Cr) and high driving force for oxide formation, Si enrichment occurs after Al enrichment, forming the shell of the internal oxides.

Table 4.6: Diffusivity Data for Si, Mn, Al, Cr, and O in Austenite at 775 °C. Note that the flux (J) was calculated considering steady-state conditions and diffusion from the mid-thickness to the surface of the sheet steel (i.e., $\Delta x = 0.0007$ m).

Element	Pre-exponential constant (D_i') (10^{-4} m^2/s)	Activation energy (Q_i) (10^3 J/mol)	Diffusion coefficient (D) (m^2/s)	Flux (J) (mol/m^2-s)	Ref.
Si	0.07	243	5.4×10^{-18}	4.01×10^{-12}	[61]
Mn	0.178	264.2	1.2×10^{-18}	1.84×10^{-12}	[62]
Al	5.9	241.58	5.4×10^{-16}	12.31×10^{-11}	[63]
Cr	1.69	263.9	1.2×10^{-17}	1.94×10^{-12}	[62]
O	5.75	168	2.43×10^{-12}		[60]

Further growth of the internal oxides during intercritical annealing was only observed for (−10 °C T_{dp}) and (+5 °C T_{dp}) process atmospheres owing to the higher inward O flux compared to (−30 °C T_{dp}) process atmosphere (Figure 4.10b)). It is expected that the immediate sub-surface layer would be ferritic after significant decarburization and de-alloying during the 600 s austenitizing heat treatment (Figure 4.8); indicating that the relevant diffusion data and solubility products should be those of ferrite. The TEM analysis of Figure 4.12 and Figure 4.13 indicated that the type 3 internal oxides formed during intercritical annealing were grain boundary oxides.

The internal oxides had a core-shell type structure; however, the chemical composition was different compared the internal oxides observed in the M (–30 °C T_{dp}) sample (Figure 4.7b)). A Si-rich oxide core with Mn-rich oxide shell was observed in the deeper grain boundary oxides of the M (–30 °C T_{dp})-IA (–10 °C T_{dp}) and M (–30 °C T_{dp})-IA (+5 °C T_{dp}) samples (Figure 4.12 and Figure 4.13). This is consistent with higher diffusivity of Si compared to Mn, Cr, and Al in ferrite at 675 °C, as shown in Table 4.7, and with the thermodynamic driving force for oxide formation (Figure 4.14b)). Furthermore, the solubility products of the observed oxide species, calculated in ferrite at 675 °C (Table 4.5), suggest that internal oxide shell is Mn_2SiO_4 instead of MnO, the latter of which has significantly higher solubility in ferrite.

Table 4.7: Diffusivity Data for Si, Mn, Al, Cr, and O in Ferrite at 675 °C. Note that the flux (J) was calculated considering steady-state condition and diffusion from the mid-thickness to the surface of the sheet steel (i.e., $\Delta x = 0.0007$ m).

Element	Pre-exponential constant ($D_i´$) (10^{-4} m^2/s)	Activation energy (Q_i) (10^3 J/mol)	Diffusion coefficient (D) (m^2/s)	Flux (J) (mol/m^2-s)	Ref.
Si	0.93	219.79	7.2×10^{-17}	53.38×10^{-12}	[64]
Mn	0.76	224.35	3.3×10^{-17}	50.82×10^{-12}	[62]
Al	5.15	245.8	1.5×10^{-17}	3.41×10^{-12}	[65]
Cr	2.33	238.8	1.6×10^{-17}	2.60×10^{-12}	[62]
O	0.037	98	1.47×10^{-11}		[60]

Contrastingly, no significant growth of the external oxides was observed during the intercritical annealing heat treatment, regardless of the process atmosphere pO_2 (Figure 4.10a)). Moreover, TEM EELS (Figure 4.7, Figure 4.11 – Figure 4.13) and XPS binding energy analysis (Table 4.4 and Appendix B) determined that similar external oxide species were present after flash pickling and intercritical annealing. This is very likely due to the solute-depleted layer that formed during the austenitizing heat treatment. The SEM-EDS line scan (Figure 4.8) showed that the thickness of the solute-depleted layer was consistent with the depth of internal oxidation of the M samples (Figure 4.4b)). This confirmed that solute-depleted layer was several microns thick, with the lowest thickness (~ 2 µm) being observed for the M (–30 °C T_{dp}) sample. Appendix D shows the concentration profiles of Al, Cr, Mn, and Si as a function of diffusion distance in ferrite after the 675 °C × 120 s IA treatment. From this, it can be seen that the maximum distance that the solutes can diffuse is significantly lower than 1 µm. Hence, with a multi-micron deep solute-depleted layer, growth of the external oxides was not observed after intercritical annealing for all process atmosphere pO_2. In addition, extruded Fe nodules were observed on the surfaces along with thin (~ 30 nm) external oxides.

As mentioned previously, obtaining surfaces suitable for reactive wetting by the molten Zn(Al, Fe) continuous galvanizing bath was one of the objectives of this research. To this end, it must be commented that the above results are promising in this respect. Fundamentally, the substrates processed using the present thermal processing parameters and process atmospheres, due to decarburization and dealloying of the near-surface layer, will present a Fe-rich surface with fine, widely dispersed $MnCr_2O_4$ nodules with relatively thin internodular oxides. This surface is almost ideal for reactive wetting as it will react with the dissolved Al in the molten bath to either aluminothermically reduce the thin oxides or react directly with the boldly exposed Fe to form the

desired $Fe_2Al_5Zn_X$ interfacial intermetallic, resulting in a robust, high-quality Zn coating on the prototype med-Mn 3G AHSS. The reactive wetting of the present steel by a simulated CGL Zn(Al, Fe) bath will be the subject of a subsequent publication by the present authors.

4.6 Conclusions

The external and internal oxides formed during austenitizing and intercritical annealing heat treatment as a function of process atmosphere dew point were determined for a prototype med-Mn 3G AHSS. Moreover, the effect of an intermediate flash pickling step on the external oxides was also determined. Based on the results, it can be concluded that

1) The austenitizing heat treatment resulted in MnO, $MnAl_2O_4$, $MnSiO_3$/Mn_2SiO_4, and $MnCr_2O_4$ external oxide formation with an average thickness of approximately 200 nm. TEM EELS analysis determined that nodule-type MnO oxides formed on top of $MnAl_2O_4$, $MnSiO_3$/Mn_2SiO_4, and $MnCr_2O_4$ oxides. However, the surface coverage of these oxides depended on the process atmosphere dew point. The +5 °C T_{dp} process atmosphere promoted deeper internal oxidation, which resulted in significant quantity of extruded Fe nodules on the surface alongside the selective external oxides.
2) Flash pickling significantly reduced the thickness of the external oxides formed during the austenitizing heat treatment. Complete dissolution of the compact nodular MnO oxides in some areas during flash pickling revealed metallic Fe nodules on the external surfaces of M samples.
3) No significant growth of the external oxide was observed during intercritical annealing, regardless of the process atmosphere dew point, owing to the solute-depleted layer that formed during the austenitizing heat treatment. Discreate MnO, $MnCr_2O_4$, $MnAl_2O_4$, and

$MnSiO_3$/Mn_2SiO_4 oxides, similar to those present after flash pickling (average thickness ~ 30 nm), were also observed after intercritical annealing.

4) Overall, the presence of fine, nodular oxides with thin internodular external oxides, the boldly exposed Fe surface, and extruded metallic Fe nodules on the pre-immersion steel surface is expected to be beneficial during continuous hot-dip galvanizing and producing high-quality galvanized coating in this prototype med-Mn 3G AHSS.

4.7 Acknowledgements

This research was financially supported by the International Zinc Association Galvanized Autobody Partnership (IZA-GAP) program and the Natural Sciences and Engineering Research Council of Canada (NSERC, grant CRDPJ 522309 – 17). The authors greatly acknowledge U.S. Steel Research for the provision of the steel substrates used in this study. The authors also thank the staff of the Canadian Centre for Electron Microscopy (CCEM), the Brockhouse Institute for Materials Research (BIMR), the Biointerfaces Institute, the McMaster Steel Research Centre (SRC), and the Centre for Automotive Materials and Corrosion (CAMC) for their technical support.

4.8 Appendix A

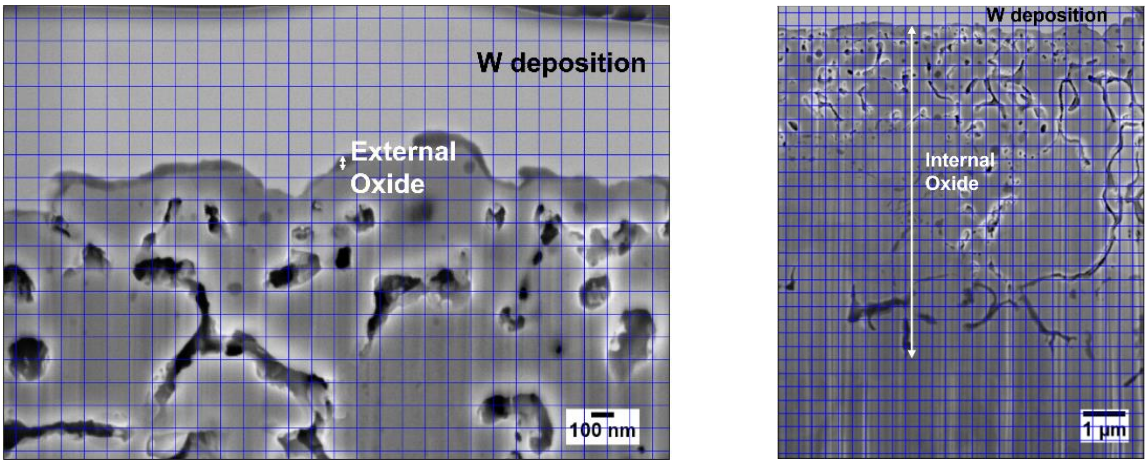

a) b)

Figure 4.15: High magnification SEI along the FIB trench cut showing the process of determining a) external oxide thickness and b) depth of internal oxidation for the flash pickled M (–10 °C T_{dp}) sample.

4.9 Appendix B

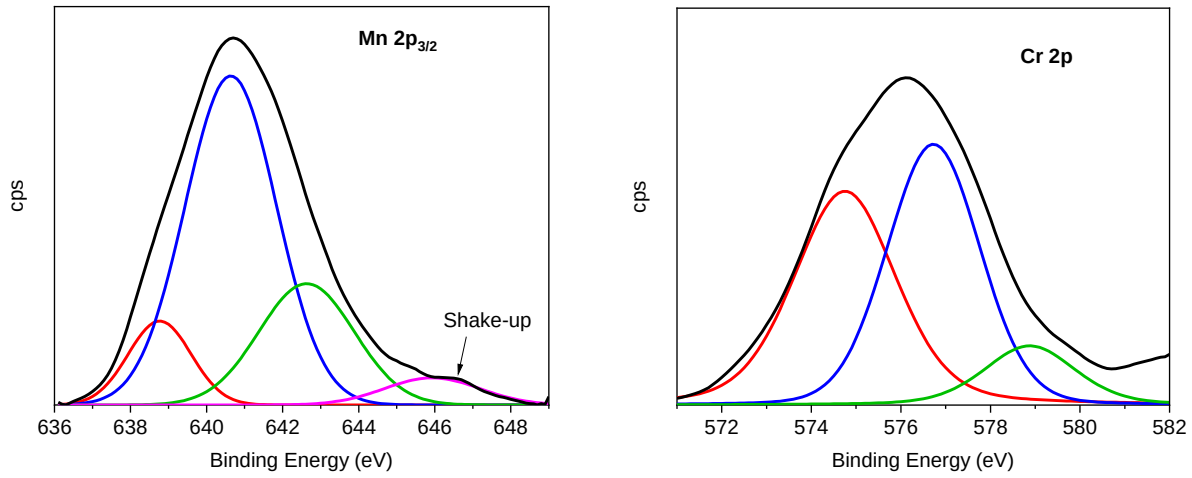

a) b)

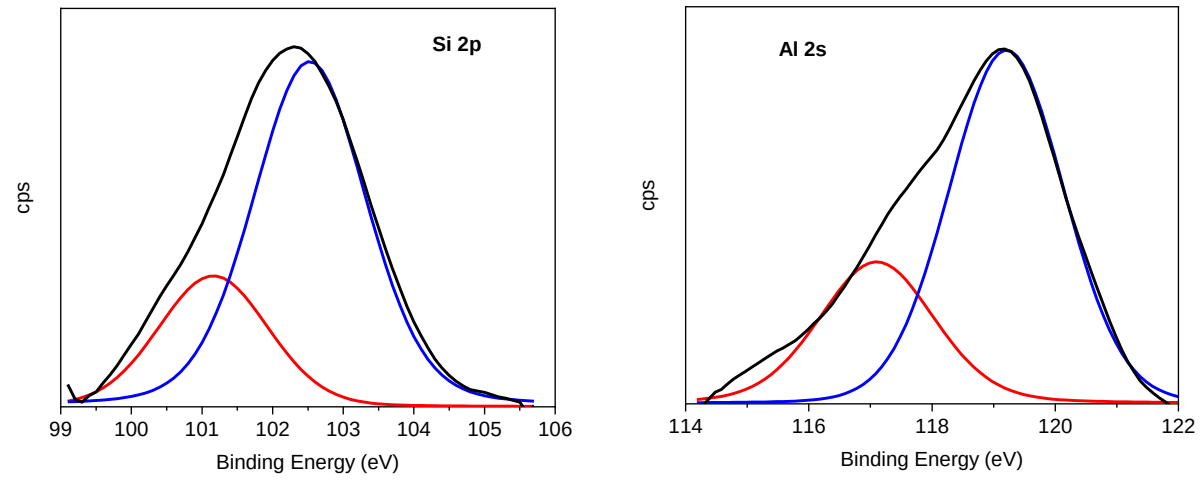

c) d)

Figure 4.16: Background subtracted high-resolution XPS spectrum of a) Mn $2p_{3/2}$, b) Cr 2p, c) Si 2p, and d) Al 2s from M (–30 °C T_{dp})-IA (–30 °C T_{dp}) sample surface. Note that these are representative of all the M-IA samples.

4.10 Appendix C

Table 4.8: Thermodynamic Data used for Constructing Figure 4.14.

Formation Reaction	ΔG^f (Jmol^{-1})	Ref.
$2Al+\frac{3}{2}O_2=Al_2O_3$	$-11.49866T\ln T+441.7964T-(3.572678E-03)T^2$ $+14.34315T^{-1}-677.7411T^{\frac{1}{2}}+2.03343\times10^{-7}T^3-1700491$	[66]
$2Cr+\frac{3}{2}O_2=Cr_2O_3$	$297.799334T\ln T-2306.3214T-0.1006328T^2$ $+4175977.18T^{-1}+23712.6364T^{\frac{1}{2}}$ $+119.406\times10^{-7}T^3-1292002.1$	
$Fe+\frac{1}{2}O_2=FeO$ $T=800-1000K$	$-312.37974T\ln T+2289.59246T+0.1296543T^2$ $+35023345.2T^{-1}+1042.28461T^{\frac{1}{2}}$ $+5.85664\times10^{-7}T^3-536965.33$	

$Fe+\frac{1}{2}O_2=FeO$ $T=1000-1043K$	$-330.66382T\ln T+2311.46177T+0.17360722T^2$ $+212465.196T^{-1}+1042.28461T^{\frac{1}{2}}$ $+5.85664\times10^{-7}T^3-441674.76$
$3Fe+2O_2=Fe_3O_4$ $T=800-1000K$	$-819.5096T\ln T+6020.9804T+0.3753117T^2$ $+62252807.2T^{-1}+4169.1384T^{\frac{1}{2}}$ $+2.69232\times10^{-7}T^3-1722055.5$
$3Fe+2O_2=Fe_3O_4$ $T=1000-1043K$	$-874.3619T\ln T+6086.58860T+0.50717045T^2$ $-42179833T^{-1}+4169.1384T^{\frac{1}{2}}$ $+2.69232\times10^{-7}T^3-1436183.8$
$H_2+\frac{1}{2}O_2=H_2O(l)$	$-2304.0466T\ln T+18256.7583T+1.44162570T^2$ $-8161063.5T^{-1}-121879.48T^{\frac{1}{2}}$ $-3158.67\times10^{-7}T^3+245617.101$
$H_2+\frac{1}{2}O_2=H_2O(g)$	$14.5914916T\ln T-49.440744T-0.0053297T^2$ $-122643.5T^{-1}-76.542088T^{\frac{1}{2}}$ $+3.47762\times10^{-7}T^3-236434.09$
$Mn+\frac{1}{2}O_2=MnO$ $T=298-980K$	$1.3662852T\ln T+36.6929348T+0.00481023T^2$ $+352614.968T^{-1}+1042.28461T^{\frac{1}{2}}$ $-3.9889179\times10^{-7}T^3-395773.02$
$Mn+\frac{1}{2}O_2=MnO$ $T=980-1360K$	$10.4915884T\ln T-23.449655T+(2.79219E-05)T^2$ $+534200.568T^{-1}+1042.28461T^{\frac{1}{2}}$ $-3.9889179\times10^{-7}T^3-394019.63$
$Mn+Si+\frac{3}{2}O_2$ $=MnSiO_3$ $T=298-980K$	$19.5054352T\ln T+67.1685256T-0.0053862T^2$ $+1431376.95T^{-1}+3126.85382T^{\frac{1}{2}}$ $+8.75848121\times10^{-7}T^3-1352103.4$
$Mn+Si+\frac{3}{2}O_2$ $=MnSiO_3$ $T=980-1360K$	$28.6307384T\ln T+7.02593581T-0.0101685T^2$ $+1612962.54T^{-1}+3126.85382T^{\frac{1}{2}}$ $+8.75848121\times10^{-7}T^3-1350350.0$

$2Mn + Si + 2O_2 = Mn_2SiO_4$ $T = 298 - 980K$	$15.7885788T\ln T + 129.671271T + 0.00445223T^2 + 1980786.36T^{-1} + 4169.13843T^{\frac{1}{2}} + 0.17576147\times10^{-7}T^3 - 1774679.2$	[59, 66]
$2Mn + Si + 2O_2 = Mn_2SiO_4$ $T = 980 - 1360K$	$34.0391851T\ln T + 9.38609148T - 0.0051124T^2 + 2343957.56T^{-1} + 4169.13843T^{\frac{1}{2}} + 0.17576147\times10^{-7}T^3 - 1771172.4$	
$Si + O_2 = SiO_2$	$8.21930022T\ln T + 79.2570095T - 0.0009297T^2 + 1322689.18T^{-1} + 2084.56922T^{\frac{1}{2}} - 1.1798608\times10^{-7}T^3 - 932891.64$	
$Mn + 2Cr + 2O_2 = MnCr_2O_4$ $T = 298 - 980K$	$299.1656T\ln T - 2269.63T - 0.09582T^2 + 4528592T^{-1} + 24754.92T^{\frac{1}{2}} + 115.4171\times10^{-7}T^3 - 1738775$	
$Mn + 2Cr + 2O_2 = MnCr_2O_4$ $T = 980 - 1360K$	$308.2909T\ln T - 2329.77T - 0.1006T^2 + 4710178T^{-1} + 24754.92T^{\frac{1}{2}} + 115.4171\times10^{-7}T^3 - 1737022$	
$Mn + 2Al + 2O_2 = MnAl_2O_4$ $T = 298 - 980K$	$-10.1324T\ln T + 480.7093T + 0.001238T^2 + 352629.3T^{-1} + 364.5435T^{\frac{1}{2}} - 1.95549\times10^{-7}T^3 - 2121266$	[66, 67]
$Mn + 2Al + 2O_2 = MnAl_2O_4$ $T = 980 - 1360K$	$-1.00707T\ln T + 420.5667T - 0.00354T^2 + 534214.9T^{-1} + 364.5435T^{\frac{1}{2}} - 1.95549\times10^{-7}T^3 - 2119513$	

4.11 Appendix D

The solute concentration profiles are determined based on solving Fick's second law for diffusion between two semi-infinite solids with different initial solute concentrations. The solution is given in equation (4.7):

$$C(y,t) = C_1 + \frac{C_2 - C_1}{2}\left[1 + erf\left(\frac{y}{2\sqrt{Dt}}\right)\right] \quad (4.7)$$

where $C(y,t)$ = concentration of solute at position y and time t (in s); y = 0 represents the interface of the two solids

C_1 = bulk concentration of the solute (in mole fraction)

C_2 = concentration of solute (in mole fraction) in the near surface region = 0

D = diffusion coefficient of the solute in ferrite at 675 °C (Table 4.7)

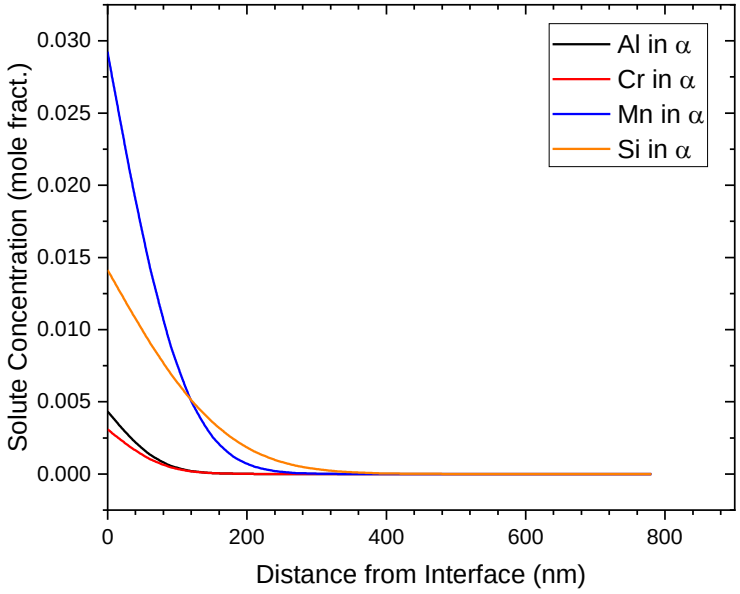

Figure 4.17: Concentration profiles of Al, Cr, Mn, and Si in ferrite as a function of distance from the interface after 675 °C × 120 s IA treatment.

4.12 References

[1] E. De Moor, P.J. Gibbs, J.G. Speer, D.K. Matlock, Strategies for third-generation advanced high strength steel development, AIST Trans. 7 (2010) 133–144.

[2] D.K. Matlock, J.G. Speer, Design Considerations for the Next Generation of Advanced High Strength Sheet Steels, in: H.C. Lee (Ed.), Proc. 3rd Int. Conf. Struct. Steels, Seoul, Korea (2006) 774–781.

[3] S. Lee, B.C. De Cooman, On the selection of the optimal intercritical annealing temperature for medium Mn TRIP steel, Metall. Mater. Trans. A. 44A (2013) 5018–5024.

[4] W.Q. Cao, C. Wang, J. Shi, M.Q. Wang, W.J. Hui, H. Dong, Microstructure and mechanical properties of Fe–0.2C–5Mn steel processed by ART-annealing, Mater. Sci. Eng. A. 528 (2011) 6661–6666.

[5] P.J. Gibbs, E. De Moor, M.J. Merwin, B. Clausen, J.G. Speer, D.K. Matlock, Austenite stability effects on tensile behavior of manganese-enriched-austenite transformation induced plasticity steel, Metall. Mater. Trans. A. 42A (2011) 3691–3702.

[6] S. Lee, K. Lee, B.C. De Cooman, Observation of the TWIP + TRIP plasticity-enhancement mechanism in Al-added 6 wt pct medium Mn steel, Metall. Mater. Trans. A. 46A (2015) 2356–2363.

[7] A. Arlazarov, M. Gouné, O. Bouaziz, A. Hazotte, G. Petitgand, P. Barges, Evolution of microstructure and mechanical properties of medium Mn steels during double annealing, Mater. Sci. Eng. A. 542 (2012) 31– 39.

[8] J. Shi, X. Sun, M. Wang, W. Hui, H. Dong, W. Cao, Enhanced work-hardening behavior and mechanical properties in ultrafine-grained steels with large-fractioned metastable austenite, Scr. Mater. 63 (2010) 815–818.

[9] K.M.H. Bhadhon, J.R. McDermid, X. Wang, E. McNally, F.E. Goodwin, Fine-scale microstructure characterization and mechanical properties of CGL-compatible heat treated

medium-Mn TRIP steel, in: Proc. 11th Conf. Zinc Zinc Alloy Coat. Steel Sheet, Galvatech 2017, ISIJ Int., Tokyo (2017) 493–500.

[10] D.M. Pallisco, J.R. McDermid, Mechanical property development of a 0.15C–6Mn–2Al–1Si third-generation advanced high strength steel using continuous galvanizing heat treatments, Mater. Sci. Eng. A. 778 (2020) 139111, doi: https://doi.org/10.1016/j.msea.2020.139111.

[11] V. Patel, Microstructure and mechanical properties of medium Mn steel, McMaster University (2019), Hamilton, Ontario, Canada.

[12] K.M.H. Bhadhon, X. Wang, J.R. McDermid, Effects of CGL-Compatible Thermal Processing, Starting Microstructure, and Sn Micro-alloying on the Mechanical Properties of a Medium-Mn Third Generation Advanced High Strength Steel, Mater. Sci. Eng. A. 833 (2022) 142563, doi: https://doi.org/10.1016/j.msea.2021.142563.

[13] M. Guttmann, Diffusive phase transformation in hot dip galvanizing, Mater. Sci. Forum 155–156 (1994) 527–548.

[14] R. Sagl, A. Jarosik, D. Stifter, G. Angeli, The role of surface oxides on annealed high strength steels in hot-dip galvanizing, Corros. Sci. 70 (2013) 268–275.

[15] J. Mahieu, S. Claessens, B.C. De Cooman, Galvanizability of high-strength steels for automotive applications, Metall. Mater. Trans. A. 32A (2001) 2905–2908.

[16] J. Maki, J. Mahieu, B.C. De Cooman, S. Claessens, Galvanisability of silicon free CMnAl TRIP steels, Mater. Sci. Technol. 19 (2003) 125–131.

[17] M. Blumenau, M. Norden, F. Friedel, K. Peters, Use of pre-oxidation to improve reactive wetting of high manganese alloyed steel during hot-dip galvanizing, Surf. Coat. Technol. 206 (2011) 559–567.

[18] E.M. Bellhouse, J.R. McDermid, Selective Oxidation and Reactive Wetting of 1.0 Pct Si-0.5 Pct Al and 1.5 Pct Si TRIP-Assisted Steels, Metall. Mater. Trans. A. 41A (2010) 1539–1553.

[19] E.M. Bellhouse, J.R. McDermid, Selective Oxidation and Reactive Wetting during Galvanizing of a CMnAl TRIP-Assisted Steel, Metall. Mater. Trans. A. 42 (2011) 2753–2768.

[20] R. Khondker, A. Mertens, J.R. McDermid, Development of the surface structure of TRIP steels prior to hot-dip galvanizing, Mater. Sci. Eng. A. 463 (2007) 157–165.

[21] G.S. Mousavi, J.R. McDermid, Selective oxidation of a C-2Mn-1.3Si (Wt Pct) advanced high-strength steel during continuous galvanizing heat treatments, Metall. Mater. Trans. A. 49 (2018) 5546–5560.

[22] G.S. Mousavi, J.R. McDermid, Effect of dew point on the reactive wetting of a C-2Mn-1.3Si (wt%) advanced high strength steel during continuous galvanizing, Surf. Coat. Technol. 351 (2018) 11–20.

[23] L. Cho, G.S. Jung, B.C. De Cooman, On the Transition of Internal to External Selective Oxidation on CMnSi TRIP Steel, Metall. Mater. Trans. A. 45A (2014) 5158–5172.

[24] L. Cho, M.S. Kim, Y.H. Kim, B.C. De Cooman, Influence of Minor Alloying Elements on Selective Oxidation and Reactive Wetting of CMnSi TRIP Steel during Hot Dip Galvanizing, Metall. Mater. Trans. A. 45A (2014) 4484–4498.

[25] M. Pourmajidian, J.R. McDermid, Selective Oxidation of a 0.1C-6Mn-2Si Third Generation Advanced High-Strength Steel During Dew-Point Controlled Annealing, Metall. Mater. Trans. A. 49 (2018) 1795–1808.

[26] M. Pourmajidian, J.R. McDermid, Effect of Annealing Temperature on the Selective Oxidation and Reactive Wetting of a 0.1C-6Mn-2Si Advanced High Strength Steel During Continuous Galvanizing Heat Treatments, ISIJ Int. 58(9) (2018) 1635–1643.

[27] M. Pourmajidian, J.R. McDermid, On the reactive wetting of a medium-Mn advanced high-strength steel during continuous galvanizing, Surf. Coat. Technol. 357 (2019) 418–426.

[28] Y. Suzuki, T. Yamashita, Y. Sugimoto, S. Fujita, S. Yamaguchi, Thermodynamic Analysis of Selective Oxidation Behavior of Si and Mn-added Steel during Recrystallization Annealing, ISIJ Int. 49(4) (2009) 564–573.

[29] L. Cho, S.J. Lee, M.S. Kim, Y.H. Kim, B.C. De Cooman, Influence of Gas Atmosphere Dew Point on the Selective Oxidation and the Reactive Wetting During Hot Dip Galvanizing of CMnSi TRIP Steel, Metall. Mater. Trans. A. 44A (2013) 362–371.

[30] Y.F. Gong, H.S. Kim, B.C. De Cooman, Internal Oxidation during Intercritical Annealing of CMnSi TRIP Steel, ISIJ Int. 49(4) (2009) 557–563.

[31] S. Alibeigi, R. Kavitha, R.J. Meguerian, J.R. McDermid, Reactive wetting of high Mn steels during continuous hot-dip galvanizing, Acta Mater. 59(9) (2011) 3537–3549.

[32] Z. Chen, Y. He, W. Zheng, H. Wang, Y. Zhang, L. Li, Effect of Hot-Dip Galvanizing Process on Selective Oxidation and Galvanizability of Medium Manganese Steel for Automotive Application, Coatings 10(12) (2020) 1265.

[33] T. Yang, Y. He, H. Wang, L. Li, L. Wang, Selective Oxidation Behavior of Medium Manganese Steel in Hot-Dip Galvanizing Process, Mater. Sci. Forum 960 (2019) 51–57.

[34] H. Luo, H. Dong, New ultrahigh-strength Mn-alloyed TRIP steels with improved formability manufactured by intercritical annealing, Mater. Sci. Eng. A. 626 (2015) 207–212.

[35] S. Dionne, B. Voyzelle, J. Li, E. Essadiqi, É. Baril, J.R. McDermid, F. Goodwin, Effect of Reheating Parameters on Galvanizing Behaviour and Properties of High Strength Hot Rolled Steels, in: Proc. 6th Conf. Zinc Zinc Alloy Coat. Steel Sheet, Galvatech 2004, AIST, Chicago (2004) 751–762.

[36] J.R. McDermid, A. Chakraborty, Identification of steel chemistries and galvanizing process design, ZCO-53-1 Project Report, (2012), Hamilton, Ontario, Canada.

[37] B.R. Strohmeier, D.M. Hercules, Surface Spectroscopic Characterization of Mn/Al_2O_3 Catalysts, J. Phys. Chem. 88 (1984) 4922–4929.

[38] M.C. Biesinger, B.P. Payne, A.P. Grosvenor, L.W.M. Lau, A.R. Gerson, R.St.C. Smart, Resolving surface chemical states in XPS analysis of first row transition metals, oxides and hydroxides: Cr, Mn, Fe, Co and Ni, Appl. Surf. Sci. 257 (2011) 2717–2730.

[39] A. Aoki, X-ray photoelectron spectroscopic studies on ZnS: MnF_2 Phosphors, Jpn. J. Appl. Phys. 15 (1976) 305–311.

[40] H. Liu, Y. He, S. Swaminathan, M. Rohwerder, L. Li, Effect of dew point on the surface selective oxidation and subsurface microstructure of TRIP-aided steel, Surf. Coat. Technol. 206 (2011) 1237–1243.

[41] A.P. Grosvenor, E.M. Bellhouse, A. Korinek, M. Bugnet, J.R. McDermid, XPS and EELS characterization of Mn_2SiO_4, $MnSiO_3$ and $MnAl_2O_4$, Appl. Surf. Sci. 379 (2016) 242–248.

[42] M.G. Frith, J.D. Wnuk, C.M. Chun, T.A. Ramanarayanan, S.L. Bernasek, The Kinetics and Mechanism of the Selective Oxidation of 20Fe–40Ni–10Mn–30Cr Alloy, Oxid. Met. 83 (2015) 71–88.

[43] S. Swaminathan, M. Spiegel, Thermodynamic and kinetic aspects on the selective surface oxidation of binary, ternary and quarternary model alloys, Appl. Surf. Sci. 253 (2007) 4607–4619.

[44] S. Samanta, A.K. Halder, Y. Deo, S. Guha, M. Dutta, Effect of Mn and Cr on the selective oxidation, surface segregation and hot-dip Zn coatability, Surf. Coat. Technol. 377 (2019) 124908.

[45] J.R. Mackert, R.D. Ringle, C.W. Fairhurst, High-temperature Behavior of a Pd-Ag Alloy for Porcelain, J. Dent. Res. 62 (1983) 1229–1235.

[46] S. Guruswamy, S.M. Park, J.P. Hirth, R.A. Rapp, Internal oxidation of Ag-In alloys: Stress relief and the influence of imposed strain, Oxid. Met. 26 (1986) 77–100.

[47] Z.T. Zhang, I.R. Sohn, F.S. Pettit, G.H. Meier, S. Sridhar, Investigation of the Effect of Alloying Elements and Water Vapor Contents on the Oxidation and Decarburization of Transformation-Induced Plasticity Steels, Metall. Mater. Trans. B. 40 (2009) 567–584.

[48] R. Kavitha, J.R. McDermid, On the in-situ aluminothermic reduction of manganese oxides in continuous galvanizing baths, Surf. Coat. Technol. 212 (2012) 152–158.

[49] X. Han, C. DiGiovanni, J. McDermid, E. Biro, N.Y. Zhou, Effect of internal oxidation on the weldability of CMnSi steels, Weld. World. 63 (2019) 1633–1639.

[50] C. Wagner, Reaktionstypen bei der Oxydation von Legierungen, Zeitschrift für Elektrochemie. 63 (7) (1959) 772–782.

[51] S. Swaminathan, Selective surface oxidation and segregation upon short term annealing of model alloys and industrial steel grades, Ruhr University (2007), Bochum, Germany.

[52] C.F. Jones, R.S.C. Smart, P.S. Turner, Dissolution kinetics of manganese oxides. Effects of preparation conditions, pH and oxidation/reduction from solution, J. Chem. Soc. Faraday Trans. 86 (1990) 947–953.

[53] J.F. Banfield, G.G. Ferruzzi, W.H. Casey, H.R. Westrich, HRTEM study comparing naturally and experimentally weathered pyroxenoids, Geochim. Cosmochim. Acta. 59 (1995) 19–31.

[54] W.H. Casey, M.F. Hochella, H.R. Westrich, The surface chemistry of manganiferous silicate minerals as inferred from experiments on tephroite (Mn2SiO4), Geochim. Cosmochim. Acta. 57 (1993) 785–793.

[55] X. Zhang, C.C. da Silva, C. Liu, M. Prabhakar, M. Rohwerder, Selective Oxidation of Ternary Fe-Mn-Si Alloys during Annealing Process, Corr. Sci. 174 (2020) 108859.

[56] G. Eriksson, P. Wu, M. Blander, A.D. Pelton, Critical Evaluation and Optimization of the Thermodynamic Properties and Phase Diagrams of the MnO-SiO2 and CaO-SiO2 Systems, Can. Metall. Q. 33 (1994) 13–21.

[57] D. Huin, P. Flauder, J.-B. Leblond, Numerical Simulation of Internal Oxidation of Steels during Annealing Treatments, Oxid. Met. 64 (2005) 131–167.

[58] O. Kubaschewski, C.B. Alcock, P.J. Spencer, Metallurgical Thermochemistry, sixth ed., Pergamon Press, Oxford, 1993.

[59] I.-H. Jung, Critical evaluation and thermodynamic modeling of the Mn–Cr–O system for the oxidation of SOFC interconnect, Solid State Ion. 177 (2006) 765–777.

[60] J.H. Swisher, E.T. Turkdogan, Solubility, permeability, and diffusivity of oxygen in solid iron, Trans. AIME 239 (1967) 426.

[61] Z. He, Y. He, Y. Gao, L. Li, S. Huang, O.V. der Biest, Computer Simulation of Fe-Al-Si System Diffusion Couples, J. Mater. Sci. Technol. 27(8) (2011) 729–734.

[62] H. Oikawa, Technology Reports, 1983.

[63] Diffusion Information Center, Diffusion Data: A Continuous Compilation of New Reference Data on Diffusion Processes in Inorganic Solids and Their Melts, 1969.

[64] R.J. Borg, D.Y.F. Lai, Diffusion in α-Fe-Si Alloys, J. Appl. Phys. 41 (1970) 5193–5200.

[65] J. Takada, S. Yamamoto, S. Kikuchi, M. Adachi, Internal oxidation of Fe-Al alloys in the α-phase region, Oxid. Met. 25 (1986) 93–105.

[66] Morris, FREED Thermodynamic Database v7.8.1 (2013).

[67] I.H. Jung, Y.B. Kang, S.A. Decterov, A.D. Pelton, Thermodynamic evaluation and optimization of the MnO-Al_2O_3 and MnO-Al_2O_3-SiO_2 systems and applications to inclusion engineering, Metall. Mater. Trans. B. 35 (2004) 259–268.

5 On Continuous Hot-Dip Galvanizing of a Prototype Medium-Mn Third Generation Advanced High Strength Steel

K.M.H. Bhadhon, J.R. McDermid
Centre for Automotive Materials and Corrosion, Department of Materials Science and Engineering, McMaster University, Hamilton, Ontario, Canada
Draft Manuscript.

5.1 Abstract

A prototype medium-Mn steel (Fe-0.2C-6Mn-1.5Si-0.5Al-0.5Cr wt%) with a martensitic starting microstructure was subjected to a continuous galvanizing line (CGL)-compatible processing route to achieve target mechanical properties for third generation advanced high strength steel (3G AHSS) and form high-quality galvanized coatings. The austenitizing heat treatment which was used to produce the martensitic starting microstructure also resulted in complete surface coverage with Mn-rich nodular external oxides. However, flash pickling was successful in dissolving these external oxides along with revealing extruded Fe nodules and exposed substrate. Furthermore, no significant growth of the external oxide was observed during the CGL-compatible intercritical annealing regardless of the process atmosphere pO_2 owing to the solute-depleted layer formed during the austenitizing heat treatment. The discrete external oxide nodules, exposed substrate, and extruded Fe nodules present on the pre-immersion surface of the annealed substrate were beneficial in terms of promoting successful reactive wetting. A robust $Fe_2Al_5Zn_x$ inhibition layer formed at the steel/coating interface of the galvanized steel samples owing to the direct wetting mechanism. Additionally, oxide wetting, oxide lift-off, bath metal ingress, and aluminothermic reduction were identified as secondary reactive wetting mechanisms that operated during galvanizing of the medium-Mn steel. These multiple reactive wetting

mechanisms resulted in good coating adherence as revealed by the three-point bend tests. Furthermore, the galvanized prototype medium-Mn steels met 3G AHSS general target mechanical properties (24,000 MPa% ≤ UTS × TE ≤ 40,000 MPa%).

5.2 Introduction

Medium-Mn (med-Mn) steels have been promising candidates to achieve the third generation advanced high strength steel (3G AHSS) target mechanical properties and meet automotive weight reduction demands through the optimal selection of intercritical annealing parameters and starting microstructure [1-11]. Although med-Mn steels contain lower alloy content compared to the second generation advanced high strength steels (2G AHSS), these steels are still challenging to galvanize in a continuous galvanizing line (CGL) owing to the selective oxidation of alloying elements in the dew point controlled N_2–(5-20 vol%) H_2 process atmosphere during the pre-galvanizing heat treatment required to achieve the desired microstructure and mechanical properties. Research on different generations of AHSS have shown that the external oxides formed during the annealing stage can lead to poor reactive wetting during continuous galvanizing depending on the oxide chemistry, morphology, and distribution [12-25]. In particular, the formation of SiO_2 films is considered to be detrimental for successful reactive wetting. Suzuki et al. [26] considered this criterion for developing a thermodynamic model to predict the selectively oxidized species and successful reactive wetting for AHSS. The authors concluded that it was impossible to avoid the deleterious SiO_2 film formation regardless of the process atmosphere pO_2 when the Si/Mn ratio is greater than 1. However, the thermodynamic model is unable to predict some of the critical factors in reactive wetting such as oxide thickness, morphology, and spatial distribution. Hence, the model had some disagreements with the results reported in literature. For example, Bellhouse and McDermid [16] successfully galvanized two Si/Al TRIP-assisted steels

using conventional CGL process atmospheres where the Si/Mn ratio was equal to 1 and 0.67, respectively. The authors attributed this to the widely spaced, nodule-type MnO-Mn_2SiO_4/$MnSiO_3$ on the steel surface. The desired $Fe_2Al_5Zn_x$ layer was able to form between the nodules and resulted in a high-quality Zn coating.

Extensive research on different generations of AHSS has identified various reactive wetting mechanisms that can lead to high-quality galvanized coating *via* successful formation of the $Fe_2Al_5Zn_x$ interfacial layer. A mechanism for the formation of a well-developed interfacial layer despite an external MnO layer was first proposed by Khondker et al. [18]. It was hypothesised that aluminothermic reduction of MnO can occur by the dissolved bath Al during immersion in the Zn(Al,Fe) bath. This mechanism was later validated by Kavitha and McDermid [27] who reported that it is possible to aluminothermically reduce up to 85 nm thick MnO layer within the conventional CGL dipping time of 4 s. Moreover, Liu et al. [28] reported that the ΔG for possible aluminothermic reduction of simple oxides such as MnO, Cr_2O_3, SiO_2, P_2O_5, and Fe_2O_3 at 460 °C are negative, implying that aluminothermic reduction of these oxides is thermodynamically feasible. Aluminothermic reduction of MnO was also reported by Alibeigi et al. [29] for steels containing higher Mn contents (2.5, 3.5, and 5.1 wt% Mn). Direct wetting is another reactive wetting mechanism where any exposed substrate and extruded Fe nodules on the pre-immersion surface come in direct contact with the bath metals and form $Fe_2Al_5Zn_x$ intermetallics at the steel/coating interface [30]. Additionally, liquid bath metal infiltration through the cracks at the oxide-substrate interface, oxide bridging by the $Fe_2Al_5Zn_X$ intermetallics, and oxide flaking/spalling are some of the other reactive wetting mechanisms that can operate during continuous hot-dip galvanizing of AHSS [12,17,20,30,31]. Recently, Pourmajidian and McDermid [25] reported successful reactive rewetting of a model med-Mn steel (0.1C-6Mn-2Si wt%) owing

to several of these above mentioned reactive wetting mechanisms operating simultaneously during hot-dip galvanizing in a 0.20 wt% Al (dissolved) galvanizing bath. The authors showed higher process atmosphere (N_2–5 vol% H_2) dew point (+5 °C) during intercritical annealing resulted in widely spaced external MnO nodules along with a substantially lower surface coverage by the oxides. These were determined to be the key contributors to the successful reactive wetting which resulted in the robust high-quality galvanized coating for the model med-Mn steel. Furthermore, Pallisco [30] also reported successful reactive wetting of a med-Mn steel (0.15C-5.6Mn-1.9Al-1.1Si wt%) which went through a two-stage heat treatment – a partial austenitization at 890 °C for 600 s and intercritical annealing at 710 °C for 120 s – with an intermediate flash pickling stage, and galvanizing in a conventional 0.20 wt% Al (dissolved) Zn(Al,Fe) bath. The author reported that bath metal infiltration during galvanizing was facilitated by both oxide cracking and spalling owing to the difference in the coefficient of thermal expansion between the oxides and the substrate [32], and partial dissolution of internal oxides during an intermediate flash pickling treatment.

However, it should be noted that most of the selective oxidation and reactive wetting studies on med-Mn steels were conducted on binary and model alloys. Effect of process atmosphere pO_2 on the reactive wetting of application-oriented med-Mn steels has not been researched extensively. Furthermore, although recent research has shown that martensitic starting microstructures are more robust in achieving the target 3G AHSS mechanical properties in med-Mn steels [2,5,7-11], there is lack of research on the evolution of external oxides during the austenitizing heat treatment – used to achieve the martensitic starting microstructure – and intercritical annealing, and its effect on the subsequent reactive wetting of med-Mn steels. In that regard, the first objective of this investigation is to determine the external oxide chemistry, morphology, and distribution during the austenitizing heat treatment and the subsequent flash pickling treatment of a prototype,

application-oriented 0.2C-6Mn-1.5Si-0.5Al-0.5Cr (wt%) med-Mn steel. The flash pickling was conducted as it has been reported to dissolve significant amount of thick external oxides formed during the austenitizing heat treatment [30]. The second objective is to determine the effect of intercritical annealing process atmosphere pO_2 on the selective oxidation and reactive wetting of the prototype med-Mn steel. The goal is to assess the external oxides formed during the heat treatments along with the steel/coating interface of the successfully galvanized panels within the context of producing high-quality Zn coating with conventional CGL-compatible processing parameters.

5.3 Material and Experimental Methods

The chemical composition of the prototype med-Mn steel is listed in Table 5.1. The prototype steel was produced at U.S. Steel R&D (Munhall, PA) where it was cast as ingots in a vacuum induction furnace. The ingots were reheated to 1250 °C and hot rolled to a thickness of 25 mm with a hot roll finish temperature of 1050 °C. The roughed ingots were slow cooled in vermiculite. The roughed ingots went through a second hot rolling step where they were reheated to 1250 °C and hot rolled to a thickness of 4 mm with a hot roll finish temperature of 900 °C. The hot rolled steels were coiled at 665 °C and held at that temperature for 2 hours followed by slow cooling (7 °C/hr) to room temperature. Afterwards, 18 mm was trimmed from each edge followed by surface grinding to a thickness of 2.7 mm. Finally, the steels were cold rolled to a thickness of 1.4 mm.

Table 5.1: Chemical Composition of the Prototype Med-Mn 3G AHSS (wt%)

C	Mn	Si	Al	Cr	Ti	S	Si/Mn
0.18	5.91	1.46	0.43	0.59	0.008	0.0056	0.25

Two sample geometries, 10 mm × 50 mm coupons and 120 mm × 200 mm panels, were used in this research. In both cases, the longitudinal axis was parallel to the rolling direction (RD). The sample coupons were used for the selective oxidation study whereas the panels were used for the galvanizing trials. The sample coupons were ground with a series of SiC papers, with 4000 grit SiC being the final step, to remove the effect of surface roughness on the subsequent surface analyses after the heat treatments. The steel substrates were cleaned using a nylon brush while the samples were immersed in an 80 °C 2% NaOH aqueous solution, followed by rinsing in DI water, ultrasonic cleaning in isopropanol, and drying using a warm air stream. All heat treatments were carried out in the McMaster Galvanizing Simulator (Iwatani-Surtec) with a N_2–5 vol% H_2 process atmosphere with a controlled pO_2. The temperature of the steel samples was monitored by a type K thermocouple (0.5 mm) that was spot welded to the sample prior to the heat treatments. The cooling rate of the annealed samples was controlled by N_2 gas flow which was adjusted accordingly to conform to the target cooling rates *via* feedback control from the sample thermocouple readings.

A two-stage heat treatment was used in this study. The first stage was the austenitizing heat treatment to produce the martensitic starting microstructure which has been found to be more robust in achieving the 3G AHSS target mechanical properties [2,5,7-11]. In that regard, the as-received cold-rolled samples were subjected to a 600 s austenitizing heat treatment at 775 °C (above the Ac_3 temperature). The samples were then gas quenched at –30 °C/s to room temperature. This resulted in a fully martensitic microstructure for the prototype med-Mn steel [11]. A process atmosphere dew point of –30 °C was used during the austenitizing heat treatment. Prior to the intercritical annealing heat treatment of the martensitic (M) samples, flash pickling was conducted in order to dissolve the thick external oxide formed during the austenitizing heat

treatment. The M samples were pickled at 30 °C for 60 s in a flash pickling solution containing 64.5 mL DI water, 59.6 mL HCl, and 0.25 g hexamethylenetetramine. The flash pickled M samples were intercritically annealed at 675 °C for 120 s, and then cooled at –10 °C/s to an overaging temperature (OT) of 460 °C, where the samples were held for 20 s. The intercritical annealing parameters were chosen based on the microstructure and mechanical property analysis of this prototype med-Mn steel conducted by the present authors [11]. The overaging section of the heat treatment was used to obtain thermal equilibrium in the steel substrate prior to entering the molten Zn bath. As the zinc pot is generally kept at 460–465 °C [33], the overaging temperature was selected to support the thermal stability of the Zn pot. Finally, the samples were cooled to room temperature at –10 °C/s. For the galvanizing trials, the steel panels were immersed in a Fe saturated 0.2 wt% Al (dissolved) galvanizing bath for 4 s at 460 °C after the OT treatment. Three different process atmosphere dew points (T_{dp}) of –30 °C, –10 °C, and +5 °C were used during the intercritical annealing to determine their effect on the selective oxidation and the subsequent reactive wetting of the prototype med-Mn steel. A schematic diagram of the heat treatment profile is shown in Figure 5.1. Table 5.2 and Table 5.3 show a summary of the heat treatment parameters along with the process atmosphere pO_2 and pH_2O/pH_2 used in this study.

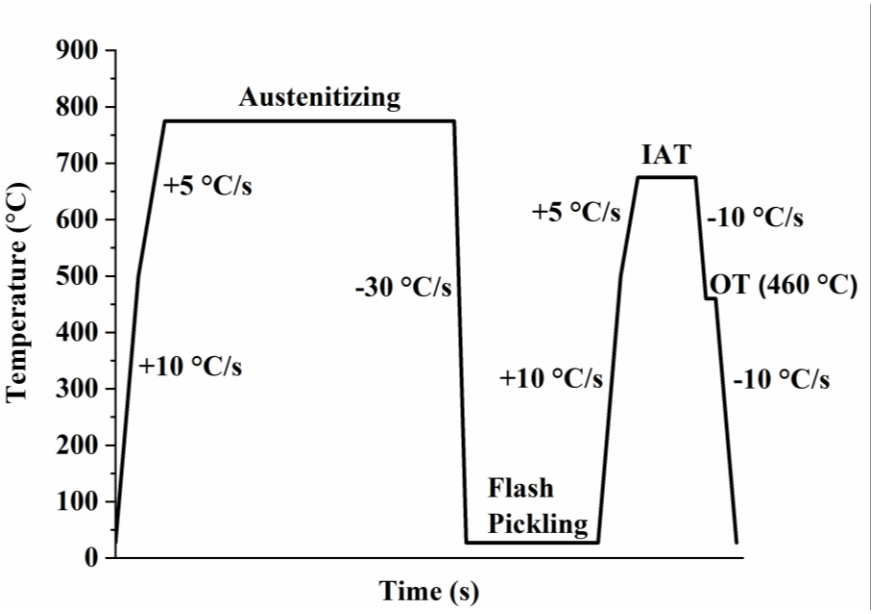

Figure 5.1: Schematic diagram of the two-stage heat treatment profile.

Table 5.2: Summary of Austenitizing Heat Treatment Parameters.

Sample ID	Austenitizing Temperature (°C)	Holding Time (s)	T_{dp} (°C)	pO_2 (atm)	pH_2O/pH_2
M	775	600	–30	1.15×10^{-23}	1.0×10^{-2}

Table 5.3: Summary of Intercritical Annealing Heat Treatment Parameters.

Sample ID	IAT (°C)	Holding Time (s)	OT (°C)	Holding Time (s)	T_{dp} (°C)	pO_2 (atm)	pH_2O/pH_2
M (–30 °C T_{dp})-IA	675	120	460	20	–30	2.85×10^{-26}	1.0×10^{-2}
					–10	9.03×10^{-25}	5.6×10^{-2}
					+5	8.38×10^{-24}	1.7×10^{-1}

The morphology and distribution of the external oxides formed during austenitizing and intercritical annealing were analysed with a JEOL 7000F field emission scanning electron microscope (FE-SEM). Secondary electron images (SEI) of the surface were taken using an

acceleration voltage of 10 keV and a working distance of 10 mm. The chemistry of the external oxides, both before and after flash pickling of the M samples, was determined by a JEOL JAMP-9500F field emission scanning Auger microscope (FE-SAM). Elemental maps of the surface were obtained after gently sputtering the sample surface with Ar to remove any contamination. Image Investigator (v.1.04) software was used to process the Auger elemental spectra and generate the Auger elemental maps.

The external and internal oxides of the M (–30 °C T_{dp})-IA samples were investigated with high-resolution scanning transmission electron microscopy (HR-STEM). An FEI Titan 80-300HB TEM was used for analysing the M (–30 °C T_{dp})-IA sample cross-sections. The site-specific TEM samples were prepared using a Zeiss NVision 40 focused ion beam scanning electron microscope (FIB-SEM). Tungsten coating was used to protect the external oxides of the region of interest (ROI) during FIB milling. Electron energy loss spectroscopy (EELS) was used to obtain elemental maps of the sample cross-sections. The electron energy loss spectra were acquired using Gatan Quantum GIF which were analysed with Gatan Digital Micrograph software (v.3.43) to extract the elemental maps.

After the galvanizing trials, the steel/coating interface was analysed with a JEOL 7000F FE-SEM in order to investigate the potential reactive wetting of the substrates (i.e., formation of $Fe_2Al_5Zn_x$ intermetallics) by the galvanizing bath. In that regard, the steel/coating interface was exposed by: 1) chemically stripping the Zn overlay with 10 vol% H_2SO_4 in water which would retain the interfacial Fe-Al and Fe-Zn intermetallics, and 2) chemically stripping both the Zn overlay and Fe-Zn intermetallics with fuming HNO_3, leaving any Fe-Al intermetallics formed intact. Furthermore, low angle x-ray diffraction (LA-XRD) was used to characterise the intermetallics and oxides that remained on the steel/coating interface after the chemical stripping

of the zinc overlay. A D8 DISCOVER (Bruker AXS) diffractometer equipped with a Co source (λ = 1.79026 Å) and a Vantec 500 (MiKroGap TM technology) or Eiger2 R 500K (Bruker AXS) area detector that was operated in the 2D mode was used to collect the XRD data. DIFFRAC.EVA software (Bruker AXS) (v.4.0) was used to analyse the diffraction pattern (2θ range of 10° to 64°). The diffraction peaks were identified using the International Centre for Diffraction Data Powder Diffraction File PDF-4 database [34]. The steel/coating interface was also analysed using HR-STEM. Elemental maps were obtained from EELS analysis of the galvanized sample cross-sections which were prepared by FIB milling. This was done to confirm successful reactive wetting and determine the reactive wetting mechanisms that operated during galvanizing.

The coating adherence was assessed by a customised three-point bend test which was adopted from the ASTM A 653/A 653M-05 standard [35]. An Instron 5566 universal tensile machine with a 10 kN load capacity was used for the bend tests. The punch radius and the steel thickness were 3.18 mm and 1.4 mm, respectively. Coating adhesion was evaluated by examining the outer bend surface with a Keyence VHX-5000 digital optical microscope. The cross-sections of the bend test samples were also analysed with a JEOL 7000F FE-SEM to evaluate the growth of any crack that might have formed during bending of the galvanized samples.

Uniaxial tensile tests were conducted for the galvanized samples with an Instron 100 kN tensile frame. Sub-size tensile specimens (ASTM E8M- 01ε2 [36]) were cut from the galvanized panels using electric discharge machining (EDM) where the tensile direction of the specimens was parallel to the RD. EDM was used to avoid any deformation-induced transformation of retained austenite in the gauge length prior to tensile testing. All tensile tests were performed at room temperature with a crosshead speed of 1 mm/min. An extensometer (25 mm gauge length) was

used to measure the engineering strain. The cross-sections of the fracture surfaces were analysed using a JEOL 7000F FE-SEM to determine the fracture mechanism.

5.4 Results

5.4.1 Characterisation of External Oxide after Austenitizing and IA treatment

The morphology and distribution of the external oxides, formed during the austenitizing heat treatment and present after flash pickling, were analysed by SEM. Figure 5.2 shows the SEM micrographs of the M (–30 °C T_{dp}) sample. It can be seen that the surface of the M (–30 °C T_{dp}) sample was completely covered with nodule-type oxide particles before flash pickling (Figure 5.2a)). This suggests significant external oxidation occurred during the 600 s austenitizing heat treatment under the –30 °C process atmosphere dew point. However, flash pickling was able to dissolve most of these compact nodule-type external oxides and reveal some metallic Fe nodules on the surface which were previously trapped under the compact external oxides, as shown in Figure 5.2b). These Fe nodules were extruded owing to volumetric expansion associated with internal oxidation during the austenitizing heat treatment [17,37-39].

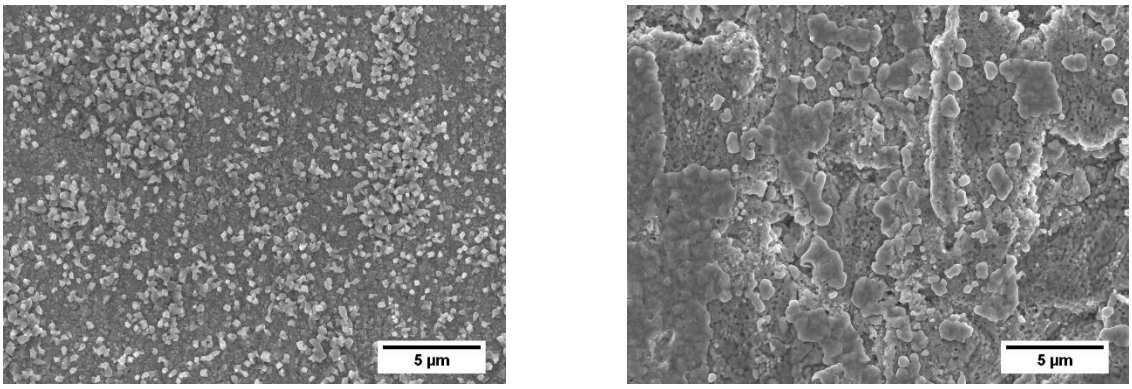

a) b)

Figure 5.2: SEM micrographs showing the surface of M (–30 °C T_{dp}) sample a) before and b) after flash pickling.

The chemistry of the external oxides was determined by using an FE-SAM. Auger elemental maps were collected from the surface of the M (–30 °C T_{dp}) sample, before and after flash pickling, as shown in Figure 5.3 and Figure 5.4, respectively. Before flash pickling, the surface of the M (–30 °C T_{dp}) sample was covered with Mn-rich external oxides, confirmed by the Mn (Figure 5.3b)) and O (Figure 5.3c)) elemental maps. On the other hand, after flash pickling, the Mn-rich oxides were mostly dissolved, and a significant Fe signal was detected on the surface, as shown in Figure 5.4d). These regions contained both the extruded Fe nodules and exposed substrate which resulted from complete dissolution of relatively thin external oxides during flash pickling. Furthermore, it can be seen that the Si, Al, and Cr elemental maps detected some signal along with the Mn from the flash pickled external surface of the M (–30 °C T_{dp}) sample (Figure 5.4). This suggests the nodule-type discrete external oxides observed on the flash pickled surface of the M (–30 °C T_{dp}) sample (Figure 5.2b)) were Mn, Si, Al, and Cr-rich oxides which were trapped underneath the Mn-rich external oxides prior to the flash pickling treatment. Furthermore, it should be noted that thick film-type external oxides were not detected in the M (–30 °C T_{dp}) sample, both before and after the flash pickling treatment. This is consistent with the results reported by Pallisco [30] for a prototype med-Mn steel (0.15C-5.6Mn-1.9Al-1.1Si wt%) that went through a similar flash pickling treatment after a partial austenitization heat treatment at 890 °C for 600 s.

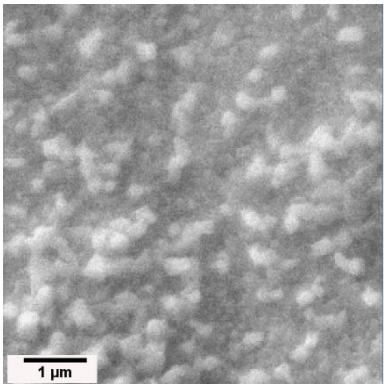

a)

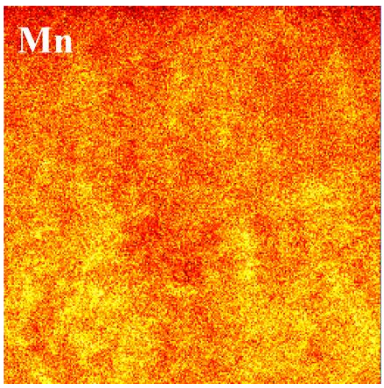

b)

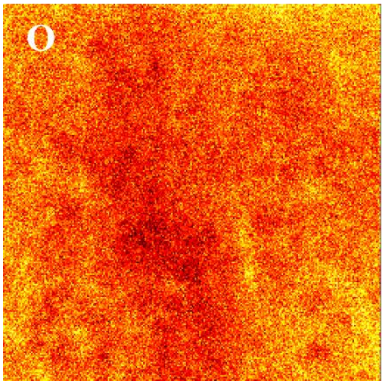

c)

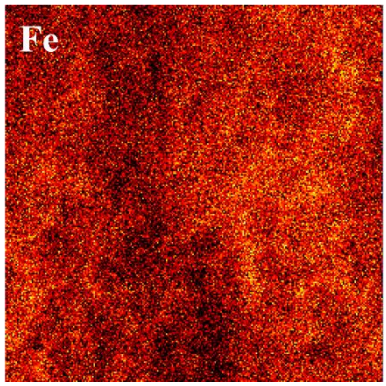

d)

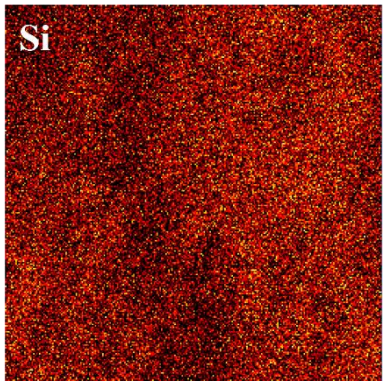

e)

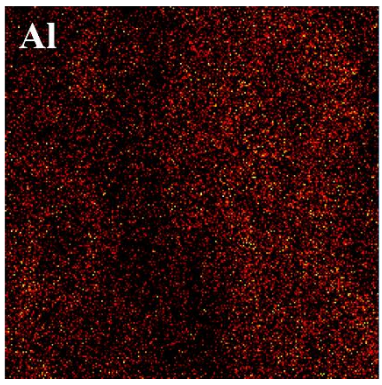

f)

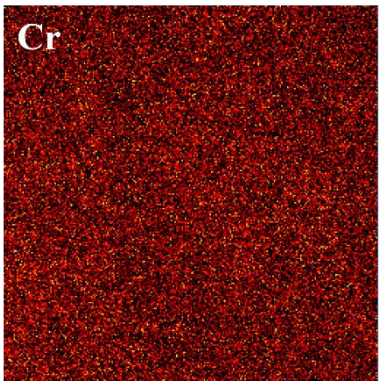

g)

Figure 5.3: a) SEM micrograph and corresponding SAM elemental maps of b) Mn, c) O, d) Fe, e) Si, f) Al, and g) Cr for M (–30 °C T_{dp}) sample before flash pickling.

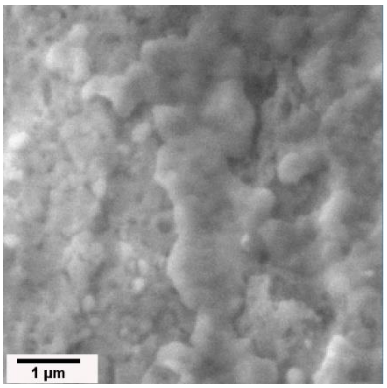

a)

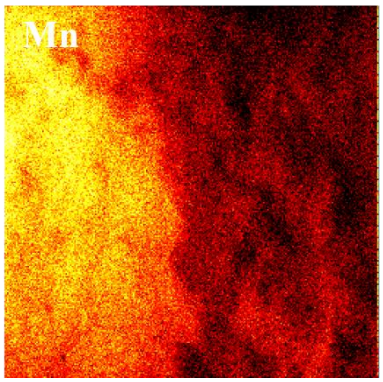

b)

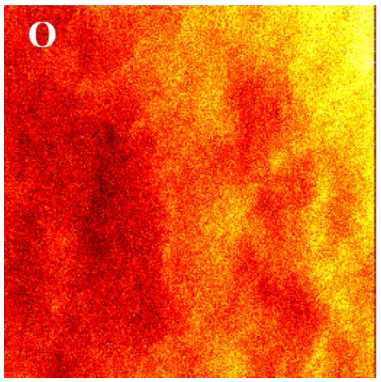

c)

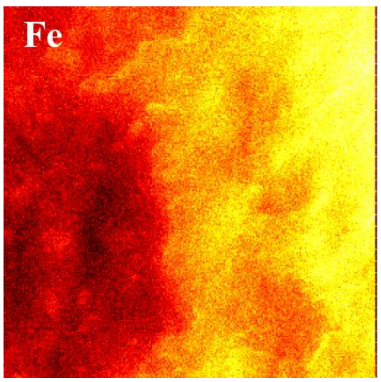

d)

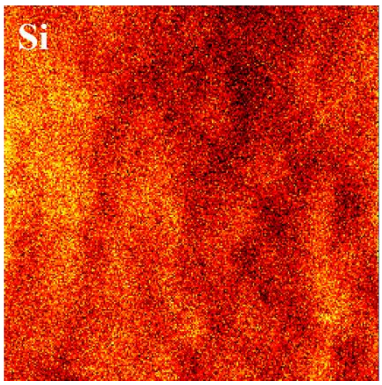

e)

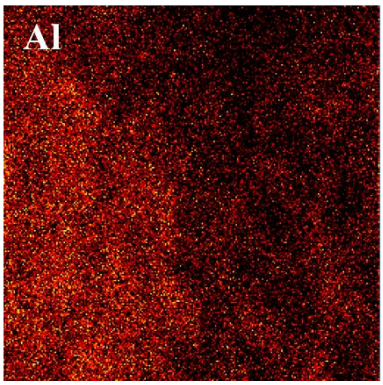

f)

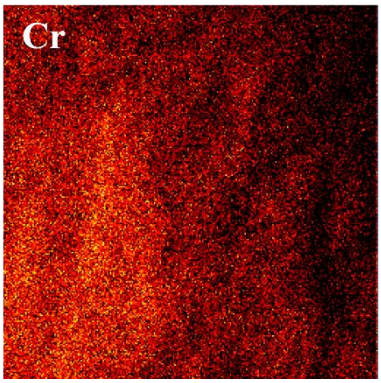

g)

Figure 5.4: a) SEM micrograph and corresponding SAM elemental maps of b) Mn, c) O, d) Fe, e) Si, f) Al, and g) Cr for M (–30 °C T_{dp}) sample after flash pickling.

The external oxide morphology and distribution were also analysed by SEM after intercritical annealing of the M (–30 °C T_{dp}) samples under –30 °C, –10 °C, and +5 °C process atmosphere T_{dp}. The results are shown in Figure 5.5. A similar distribution of nodule-type oxides and extruded Fe nodules were observed on the surface of the intercritically annealed M (–30 °C T_{dp}) samples regardless of the process atmosphere T_{dp}. This suggests no significant growth of the external oxides occurred during the 120 s intercritical annealing heat treatment. It is expected that a multi-micron deep solute-depleted layer formed during the austenitizing heat treatment. Outward flux of the alloying elements from the bulk could not diffuse through the solute-depleted layer and

reach the surface during the short (120 s) holding time at this intercritical annealing temperature. This is also consistent with the results reported in the literature [30].

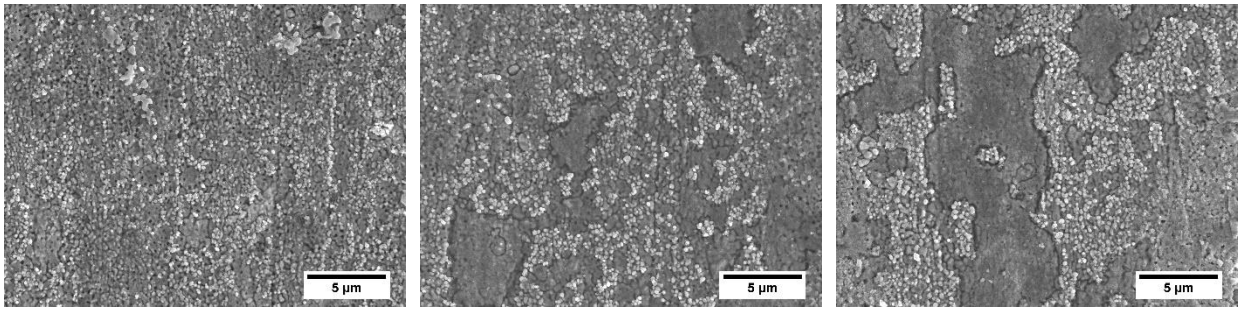

a) b) c)

Figure 5.5: SEM micrographs showing the surfaces of a) M (–30 °C T_{dp})-IA (–30 °C T_{dp}), b) M (–30 °C T_{dp})-IA (–10 °C T_{dp}), and c) M (–30 °C T_{dp})-IA (+5 °C T_{dp}) samples.

The external and internal oxide chemistries were determined by TEM EELS analysis of the M (–30 °C T_{dp})-IA sample cross-sections. Figure 5.6 shows the high angle annular dark field (HAADF) TEM image and the corresponding TEM EELS composite map for M (–30 °C T_{dp})-IA (–30 °C T_{dp}) sample. TEM EELS analysis confirmed that the external oxides were mainly comprised of Mn- and Cr-rich oxides. This is consistent with the observations reported by researchers who investigated selective oxidation of Cr containing AHSSs [40,41]. Moreover, the presence of extruded Fe nodules and exposed substrate was also confirmed on the surface, as shown in Figure 5.6b). The internal oxides were mainly comprised of Si and Al. However, some Mn and Cr enrichment was also observed in the internal oxide network. It should be noted that the surface after the intercritical annealing heat treatment did not contain any continuous thick Si-rich amorphous oxides. This is promising in terms of successful reactive wetting of this prototype med-Mn steel [13,14,17,42].

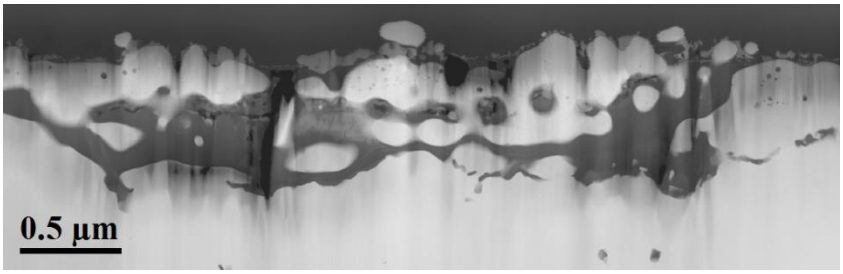

a)

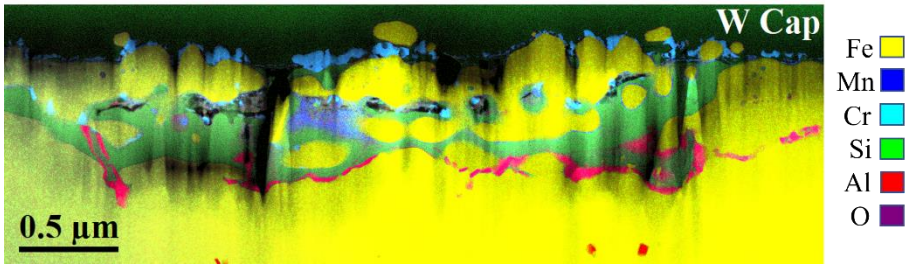

b)

Figure 5.6: a) HAADF image and b) corresponding TEM EELS composite map for M (–30 °C T_{dp})-IA (–30 °C T_{dp}) sample [43].

5.4.2 Reactive Wetting

The macroscopic views of the uniform temperature and coating area of the M (–30 °C T_{dp}) samples following intercritical annealing under three process atmosphere pO_2 and continuous hot-dip galvanizing are shown in Figure 5.7. In all cases, the steel surfaces were completely coated with Zn alloy. Furthermore, no significant bare spots or coating defects were observed (Figure 5.7).

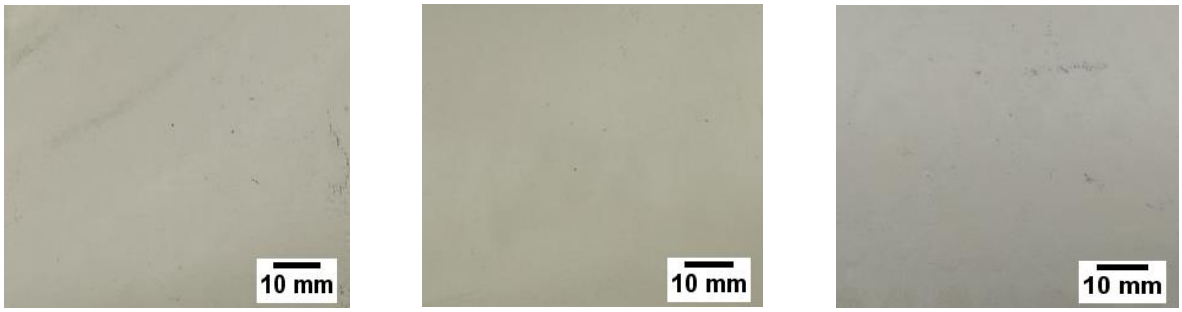

a) b) c)

Figure 5.7: Uniform coating area of galvanized a) M (–30 °C T_{dp})-IA (–30 °C T_{dp}), b) M (–30 °C T_{dp})-IA (–10 °C T_{dp}), and c) M (–30 °C T_{dp})-IA (+5 °C T_{dp}) panels.

The steel/coating interface was analysed using various techniques in order to verify successful reactive wetting during the galvanizing stage. In that regard, the Zn overlay was chemically stripped with 10 vol% H_2SO_4 in water and the steel/coating interface was analysed using SEM. The results are shown in Figure 5.8. It can be seen that in all three cases, a significant amount of Fe-Zn and Fe-Al intermetallics formed during galvanizing. SEM was also used to observe the steel/coating interface after chemical stripping of the Zn overlay with fuming HNO_3 which only retained Fe-Al intermetallics at the interface. Figure 5.9 shows the SEM images of the steel/coating interface after chemical stripping with fuming HNO_3. $Fe_2Al_5Zn_x$ crystals were observed at the steel/coating interface in all three galvanized M (–30 °C T_{dp})-IA samples. Although the $Fe_2Al_5Zn_x$ crystals covered the steel/coating interface completely in the M (–30 °C T_{dp})-IA (+5 °C T_{dp}) sample (Figure 5.9c)), there were some holes along with the $Fe_2Al_5Zn_x$ crystals in the M (–30 °C T_{dp})-IA (–30 °C T_{dp}) and the M (–30 °C T_{dp})-IA (–10 °C T_{dp}) samples, as shown in Figure 5.9a) and Figure 5.9b), respectively. These holes might be associated with ζ phase ($FeZn_{13}$) outbursts which have been chemically stripped with fuming HNO_3. This is consistent with SEM results shown in Figure 5.8a) and Figure 5.8b). The steel/coating interfaces were also analysed with LA-XRD to identify the intermetallics present in each galvanized sample after chemical

stripping using the two methods mentioned above. The XRD diffractograms for the galvanized M (–30 °C T_{dp})-IA (+5 °C T_{dp}) sample, representative of the three galvanized M (–30 °C T_{dp})-IA samples, are shown in Figure 5.10. The Powder Diffraction File (PDF-4) database [34] was used to identify the peaks observed in the XRD diffractograms. Fe_2Al_5 (PDF 00-047-1435), $FeZn_{13}$ (PDF 00-034-1314), and $FeZn_{10}$ (PDF 04-009-6619) intermetallics were identified at the steel/coating interfaces along with some Mn_2SiO_4 (PDF 00-035-0748) and Al_2O_3 (PDF 00-046-1215) [34]. However, it should be noted that the $FeZn_{10}$ diffraction peaks overlap with other intermetallics. Nevertheless, these SEM and LA-XRD results confirm successful reactive wetting occurred during galvanizing of M (–30 °C T_{dp})-IA samples regardless of process atmosphere pO_2 employed during intercritical annealing.

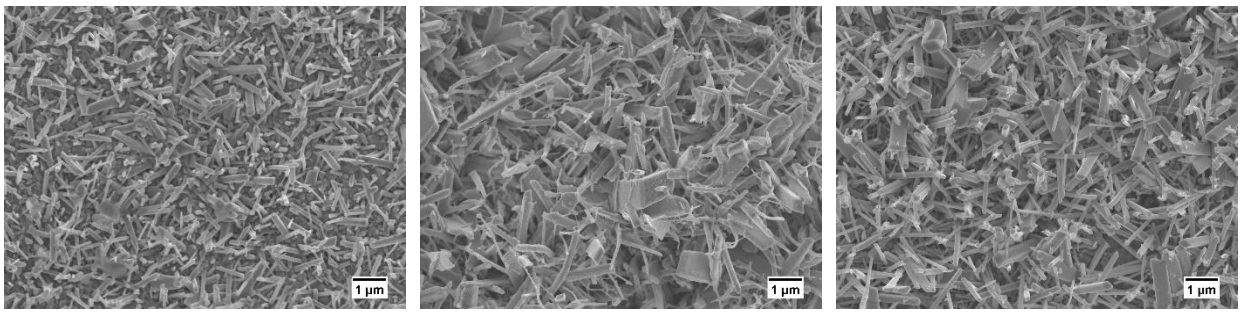

a) b) c)

Figure 5.8: Steel/coating interface of galvanized a) M (–30 °C T_{dp})-IA (–30 °C T_{dp}), b) M (–30 °C T_{dp})-IA (–10 °C T_{dp}), and c) M (–30 °C T_{dp})-IA (+5 °C T_{dp}) samples after chemical stripping with 10 vol% H_2SO_4 in water.

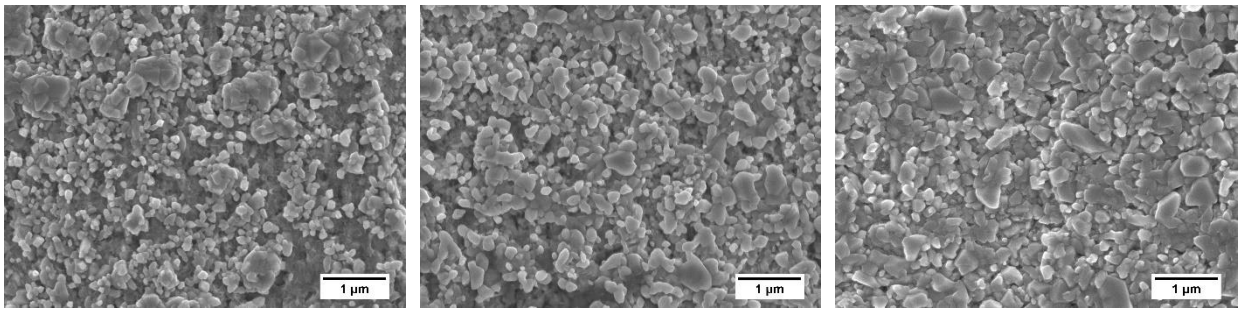

a) b) c)

Figure 5.9: Steel/coating interface of galvanized a) M (–30 °C T_{dp})-IA (–30 °C T_{dp}), b) M (–30 °C T_{dp})-IA (–10 °C T_{dp}), and c) M (–30 °C T_{dp})-IA (+5 °C T_{dp}) samples after chemical stripping with fuming HNO_3.

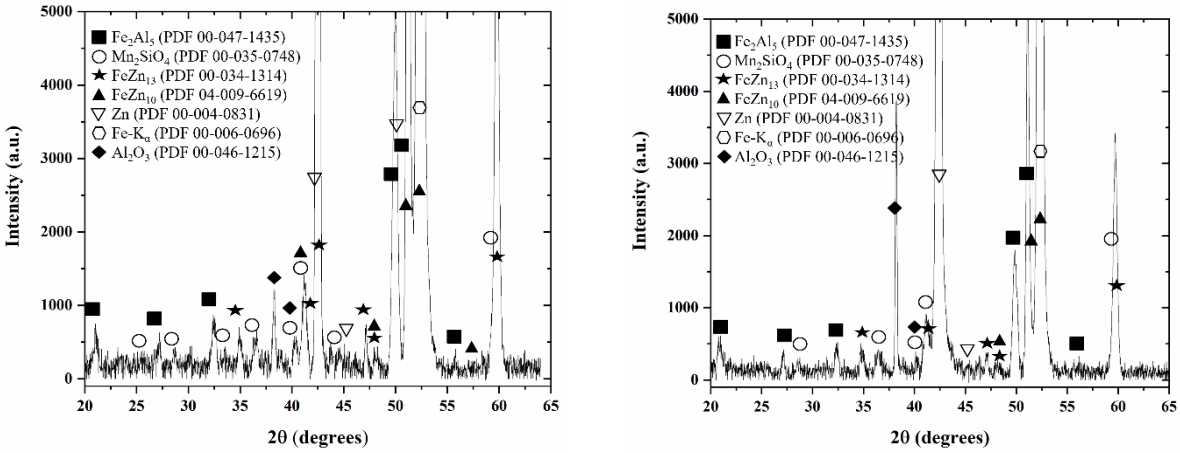

a) b)

Figure 5.10: LA-XRD diffraction patterns collected from the steel/coating interface of galvanized M (–30 °C T_{dp})-IA (+5 °C T_{dp}) samples which were chemically stripped with a) 10 vol% H_2SO_4 in water and b) fuming HNO_3.

TEM EELS analysis was conducted on the steel/coating interface cross-sections to further verify $Fe_2Al_5Zn_x$ intermetallic formation and determine the reactive wetting mechanisms that operated during galvanizing of M (–30 °C T_{dp})-IA samples. The HAADF images and the

corresponding TEM EELS composite maps for each galvanized sample are shown in Figure 5.11 – Figure 5.13. Formation of $Fe_2Al_5Zn_x$ intermetallics was confirmed in all three sample cross-sections (Figure 5.11b), Figure 5.12b), and Figure 5.13b)) which correlates well with SEM (Figure 5.8 and Figure 5.9) and LA-XRD (Figure 5.10) results confirming successful reactive wetting during continuous hot-dip galvanizing. This also suggests that dissolution of the exposed substrate and extruded Fe nodules present on the pre-immersion surface occurred during galvanizing and promoted the inhibition layer ($Fe_2Al_5Zn_x$) formation. This is evidence of "direct wetting" of the steel substrate. Furthermore, bath metal (Zn) ingress was also observed in all three galvanized M (–30 °C T_{dp})-IA samples (Figure 5.11 – Figure 5.13). Other reactive wetting mechanisms, oxide lift-off (Figure 5.12b)) and oxide wetting (i.e., direct contact between the $Fe_2Al_5Zn_x$ and oxide nodules) (Figure 5.13b)), were also identified by analysing the TEM EELS composite maps. Moreover, Si and Cr signals were not identified in the TEM EELS maps, as shown in Figure 5.11b), Figure 5.12b), and Figure 5.13b). This suggests the Mn and Cr-rich discrete oxide nodules that were present after intercritical annealing (Figure 5.6b)) were aluminothermically reduced during galvanizing. It should be also noted that the holes identified in each sample cross-sections were an artefact of the FIB milling process which was used for TEM sample preparation.

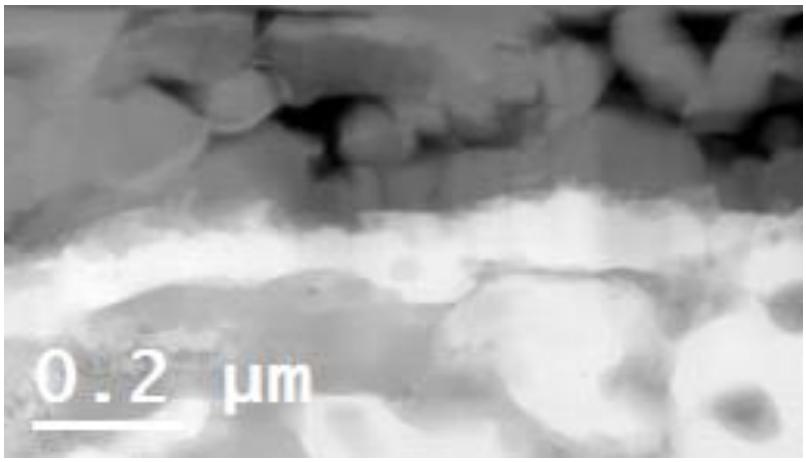

a)

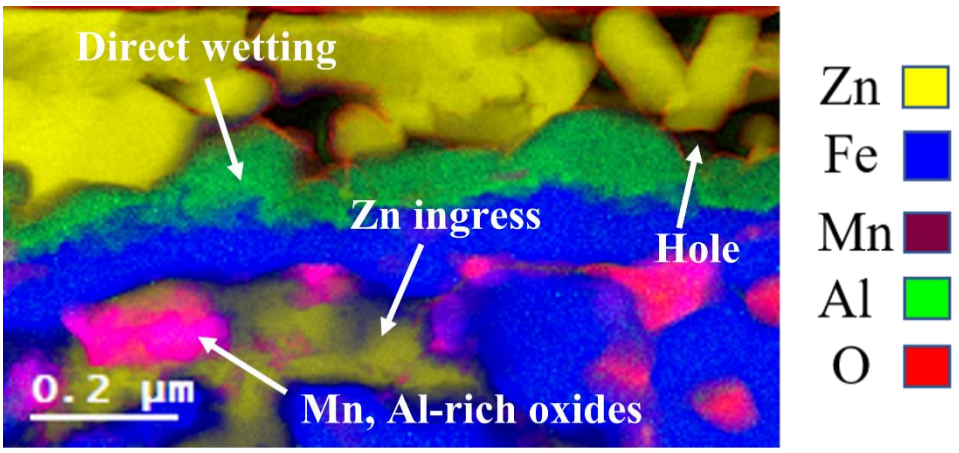

b)

Figure 5.11: a) HAADF image and b) corresponding TEM EELS composite map of steel/coating interface for galvanized M (–30 °C T_{dp})-IA (–30 °C T_{dp}) sample.

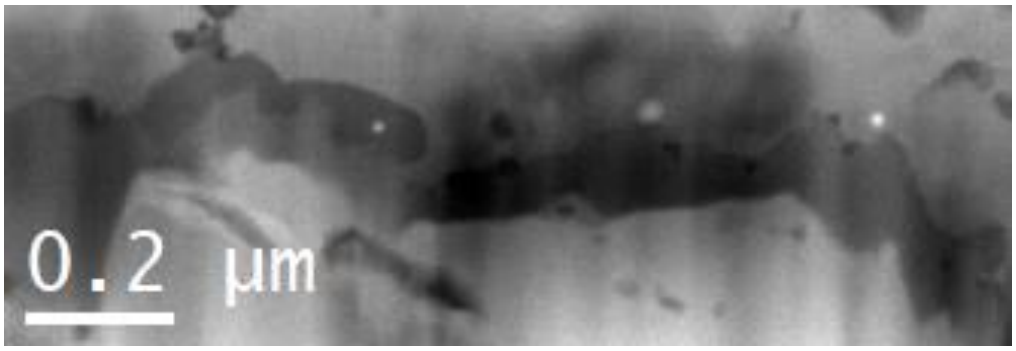

a)

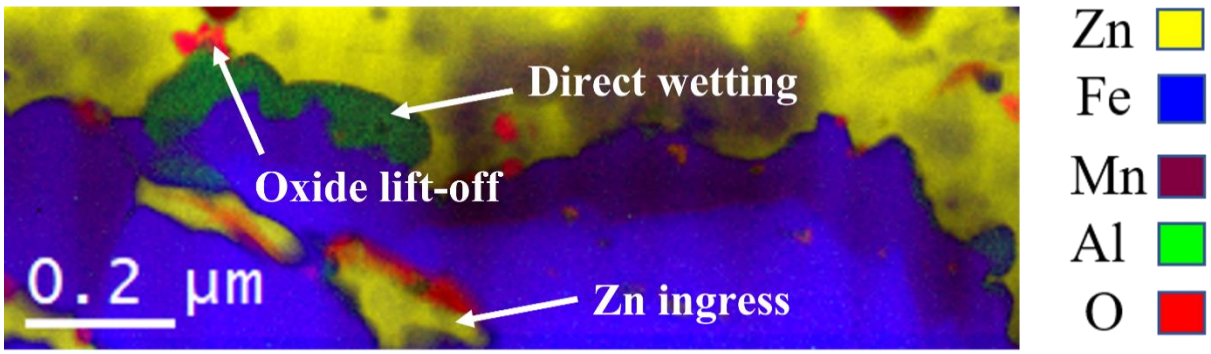

b)

Figure 5.12: a) HAADF image and b) corresponding TEM EELS composite map of steel/coating interface for galvanized M (–30 °C T_{dp})-IA (–10 °C T_{dp}) sample.

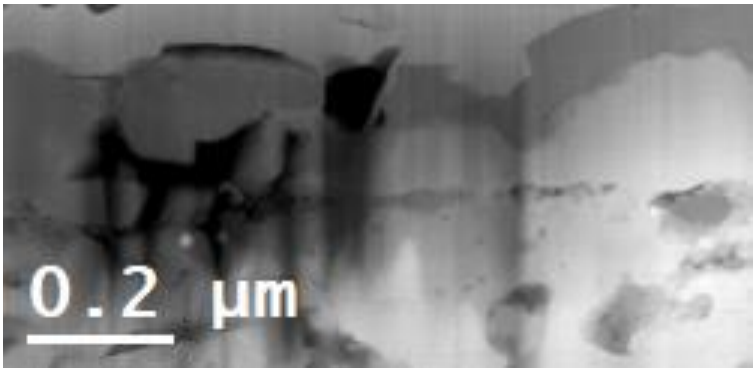

a)

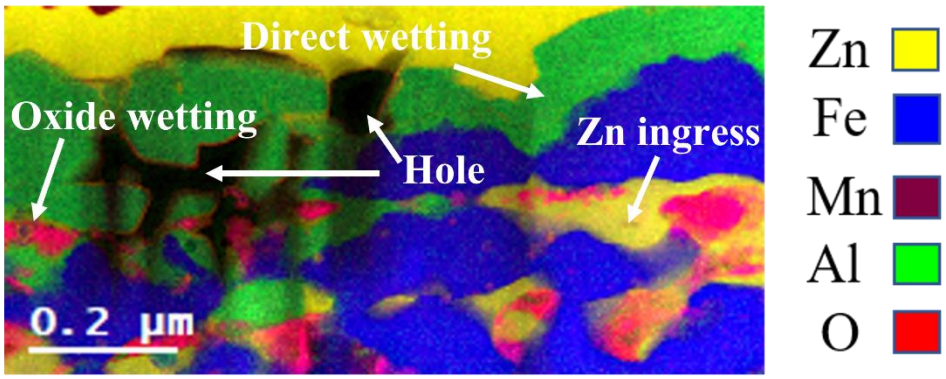

b)

Figure 5.13: a) HAADF image and b) corresponding TEM EELS composite map of steel/coating interface for galvanized M (–30 °C T_{dp})-IA (+5 °C T_{dp}) sample.

5.4.3 Coating Adherence

A customised three-point bend test was used to assess the coating adherence. The same enclosed bend angle (~ 45°) was observed in both the coated and uncoated steel substrates. Furthermore, no cracks or flakes were observed in the zinc layer, as shown in Figure 5.14. The

cross-sections of the bend test samples were analysed with SEM in order to assess any crack formation along the bend radius. The SEM micrographs are shown in Figure 5.15. Although some grain boundary cracks were observed at the outer bend radius of these samples, it can be seen that these cracks did not propagate past the internal oxide network and into the substrate. Furthermore, no cracks were found that went through the coating layer completely (Figure 5.15). This strongly implies that the coating adhesion was good owing to the successful reactive wetting that occurred during the continuous hot-dip galvanizing stage.

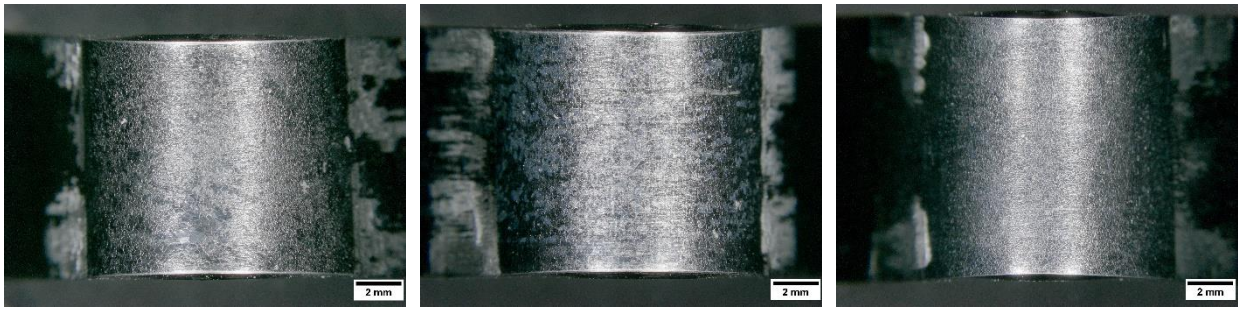

a) b) c)

Figure 5.14: Galvanized a) M (–30 °C T_{dp})-IA (–30 °C T_{dp}), b) M (–30 °C T_{dp})-IA (–10 °C T_{dp}), and c) M (–30 °C T_{dp})-IA (+5 °C T_{dp}) samples after bend test showing no cracking or flaking of the Zn coating.

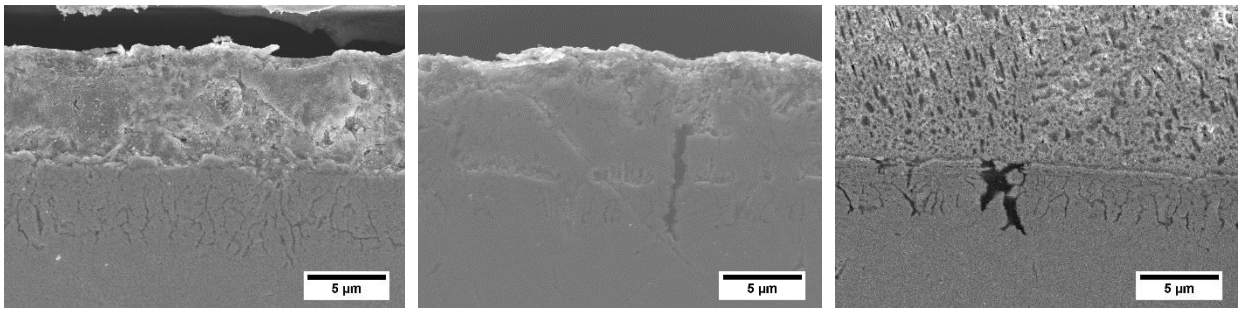

a) b) c)

Figure 5.15: SEM micrographs of galvanized a) M (–30 °C T_{dp})-IA (–30 °C T_{dp}), b) M (–30 °C T_{dp})-IA (–10 °C T_{dp}), and c) M (–30 °C T_{dp})-IA (+5 °C T_{dp}) bend test sample cross-sections.

5.4.4 Tensile Properties of Coated Steels

Uniaxial tensile test was used to determine the tensile properties of the galvanized steels. The resultant engineering stress *vs.* engineering strain curves are shown in Figure 5.16 and the summary of the tensile properties is listed in Table 5.4. A high yield strength (YS) of approximately 900 MPa and ultimate tensile strength (UTS) of approximately 1200 MPa were observed for the galvanized M (–30 °C T_{dp})-IA samples regardless of IA process atmosphere pO_2. However, significantly higher total elongation (TE) was observed for the galvanized M (–30 °C T_{dp})-IA (+5 °C T_{dp}) samples, as shown in Figure 5.16 and Table 5.4. As a result, the highest UTS × TE was observed for the galvanized M (–30 °C T_{dp})-IA (+5 °C T_{dp}) samples. Nevertheless, all three galvanized M (–30 °C T_{dp})-IA samples met the 3G AHSS general target mechanical properties (UTS × TE ≥ 24,000 MPa%) [44] (Table 5.4).

SEM was used to assess the galvanized coating in the gauge length after the uniaxial tensile test to identify possible flaking or crack formation in the coating. The SEM micrographs are shown in Figure 5.17. It should be noted that some stretching of the Zn overlay grain boundaries was observed close to the fracture surface of the galvanized M (–30 °C T_{dp})-IA (–10 °C T_{dp}) samples, marked by arrows in Figure 5.17b). However, no flaking of the coating or intergranular fracture was observed in any of the galvanized M (–30 °C T_{dp})-IA samples (Figure 5.17). This is further proof that good coating adherence was achieved in the galvanized M (–30 °C T_{dp})-IA samples.

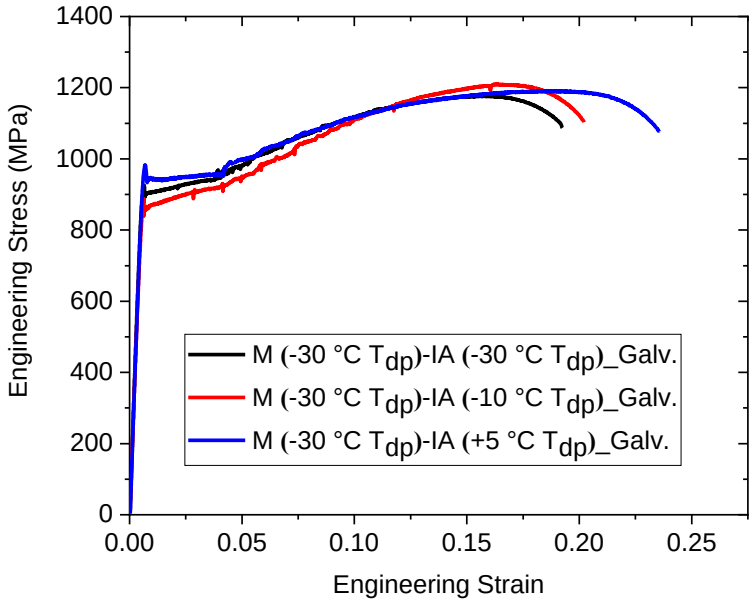

Figure 5.16: Engineering stress *vs.* engineering strain curves for galvanized a) M (–30 °C T_{dp})-IA (–30 °C T_{dp}), b) M (–30 °C T_{dp})-IA (–10 °C T_{dp}), and c) M (–30 °C T_{dp})-IA (+5 °C T_{dp}) samples.

Table 5.4: Summary of Tensile Properties for the Galvanized M (–30 °C T_{dp})-IA Samples.

Steel ID	Yield Strength (YS) MPa	Ultimate Tensile Strength (UTS) MPa	Total Elongation (TE) %	UTS × TE MPa%
M (–30 °C T_{dp})-IA (–30 °C T_{dp})	880 ± 44	1180 ± 59	19.5 ± 1	23,010 ± 1,150
M (–30 °C T_{dp})-IA (–10 °C T_{dp})	865 ± 43	1210 ± 60	20 ± 1	24,200 ± 1,210
M (–30 °C T_{dp})-IA (+5 °C T_{dp})	940 ± 47	1190 ± 59	23.5 ± 1	27,965 ± 1,400

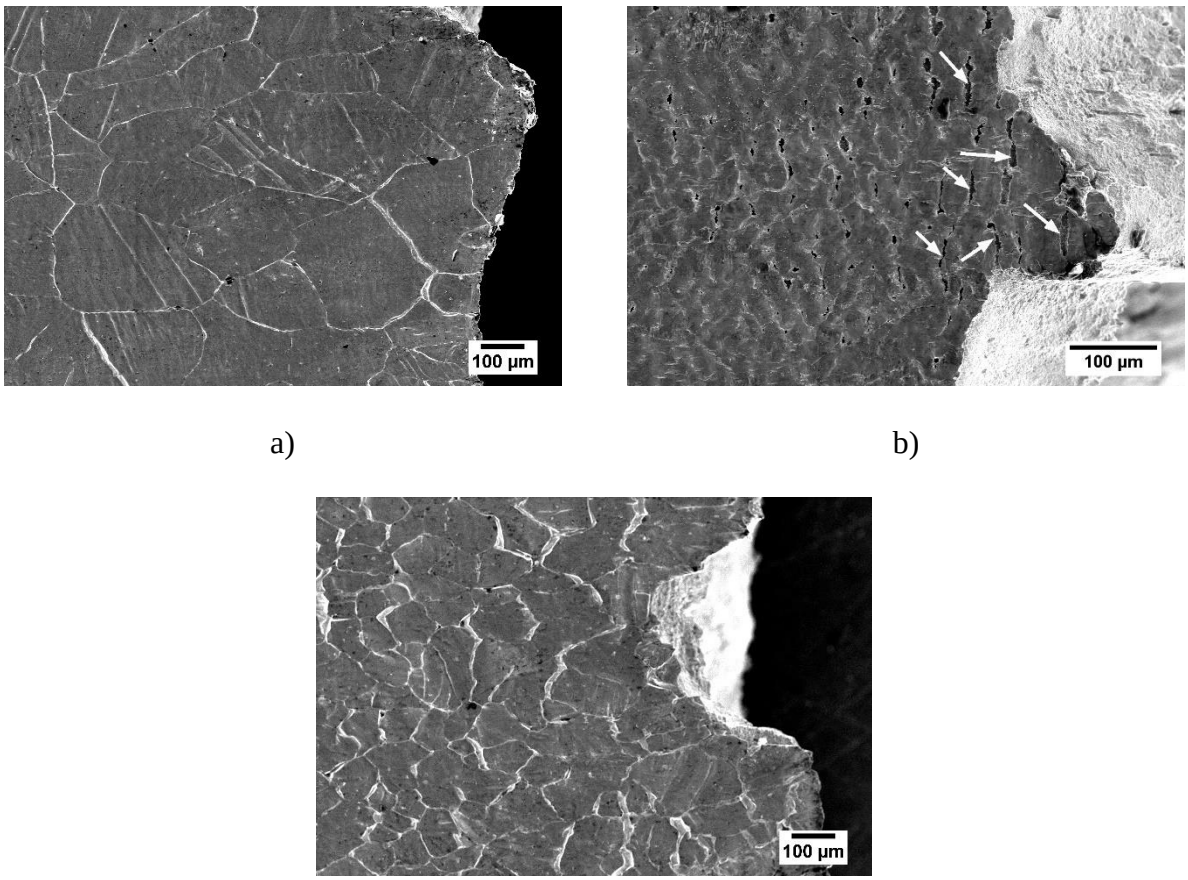

a) b)

c)

Figure 5.17: Zn coating in the gauge length of the galvanized a) M (–30 °C T_{dp})-IA (–30 °C T_{dp}), b) M (–30 °C T_{dp})-IA (–10 °C T_{dp}), and c) M (–30 °C T_{dp})-IA (+5 °C T_{dp}) tensile test samples.

The fracture surfaces of the uniaxial tensile test samples were analysed with SEM in order to determine the critical fracture mode that operated during deformation of the galvanized M (–30 °C T_{dp})-IA samples. Figure 5.18 shows the SEM micrographs of the fracture surfaces. Ductile fracture was observed in these samples as evident from the dimple formation which formed by coalescence of shear voids. Further analysis of the SEM micrographs also revealed grain boundary cracks along with interfacial decohesion and ductile tearing (Figure 5.18). This type of damage mechanism and global fracture mode are consistent with results observed for various med-Mn steels [8,10,11,45].

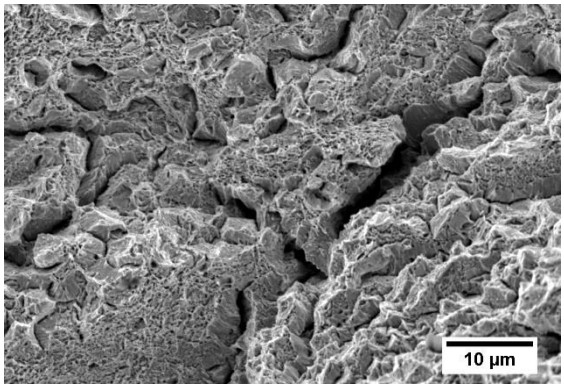

a)

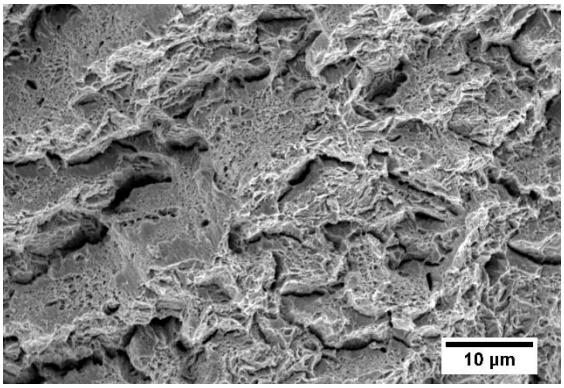

b)

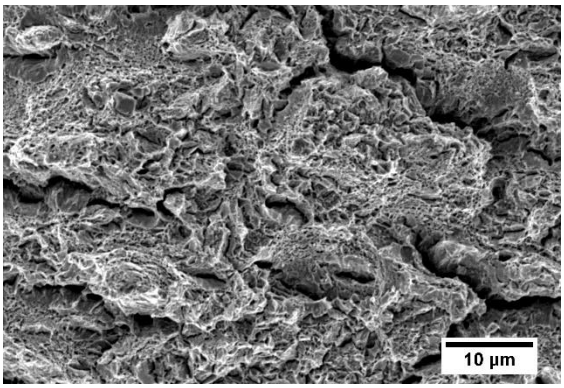

c)

Figure 5.18: SEM micrographs showing the fracture surfaces of the galvanized a) M (–30 °C T_{dp})-IA (–30 °C T_{dp}), b) M (–30 °C T_{dp})-IA (–10 °C T_{dp}), and c) M (–30 °C T_{dp})-IA (+5 °C T_{dp}) tensile test samples.

5.5 Discussion

The austenitizing heat treatment was used to achieve the martensitic starting microstructure in the prototype med-Mn steel. However, the 600 s austenitizing heat treatment at 775 °C under the –30 °C process atmosphere T_{dp} also resulted in Mn-rich nodule-type external oxides which covered the whole surface, as shown in Figure 5.2a) and Figure 5.3. This is consistent with results reported by Pourmajidian and McDermid [24] where external MnO nodules covered the surface of a model med-Mn steel (0.1C-6Mn-2Si wt%) after a 600 s annealing treatment. In this work, a

flash pickling treatment was conducted prior to the CGL-compatible IA treatment in order to dissolve the external oxides. The HCl based flash pickling treatment significantly dissolved the Mn-rich external oxides (Figure 5.2b)) and revealed some extruded Fe nodules that were trapped under the Mn-rich external oxides (Figure 5.4d)). Furthermore, the substrate was exposed in regions where the external oxides were relatively thin prior to the flash pickling treatment. The SAM elemental maps (Figure 5.4) also confirmed flash pickling revealed previously trapped discrete external oxides containing Mn, Cr, Al, and Si. Based on previous research on the selective oxidation of this prototype med-Mn steel [43], these external oxides were identified as $MnCr_2O_4$, $MnAl_2O_4$, $MnSiO_3/Mn_2SiO_4$.

No significant external oxidation was observed during the CGL-compatible IA treatment regardless of the process atmosphere pO_2 employed as evident from the similar SEM micrographs shown in Figure 5.5. This is consistent with the results reported by Pallisco [30] who showed that a partial austenitizing heat treatment at 890 °C for 600 s produced a multi-micron deep solute-depleted layer which was sufficient to prevent solute diffusion from the bulk and inhibit further external oxidation during a 120 s IA treatment. TEM EELS analysis (Figure 5.6) confirmed that the pre-immersion external surface contained discrete Mn and Cr-rich oxides, likely $MnCr_2O_4$, along with extruded Fe nodules and some areas where the Fe substrate was exposed. These features on the intercritically annealed pre-immersion surface were found to be the key factors for producing robust, high-quality galvanized coatings in the M (–30 °C T_{dp})-IA samples regardless of IA process atmosphere pO_2, as shown in Figure 5.7.

Successful reactive wetting was confirmed in all three galvanized M (–30 °C T_{dp})-IA panels as SEM (Figure 5.8 and Figure 5.9), LA-XRD (Figure 5.10), and TEM EELS (Figure 5.11 – Figure 5.13) analysis showed a robust, well-developed $Fe_2Al_5Zn_x$ inhibition layer formed at the

steel/coating interface. Similar robust inhibition layer formation was reported to be essential for high-quality galvanized coating in 1G AHSSs [16,17,20,22,27,29,31,46] and med-Mn steels [24,25,30]. TEM EELS analysis of the galvanized sample cross-sections (Figure 5.11 – Figure 5.13) also revealed that direct wetting was the dominant reactive wetting mechanism that operated during the galvanizing of the M (–30 °C T_{dp})-IA samples. The exposed Fe substrate and extruded Fe nodules on the pre-immersion surface (Figure 5.6) dissolved when the annealed substrate entered the galvanizing bath and came in direct contact with bath dissolved Al to promote the inhibition layer formation at the steel/coating interface. This direct wetting mechanism was also reported by Pallisco [30] for a med-Mn steel that was processed with similar two-stage heat treatment with an intermediate flash pickling step.

It should be noted that a significant amount of ζ-$FeZn_{13}$ intermetallics were detected along with $Fe_2Al_5Zn_x$ at the steel/coating interface albeit using 0.2 wt% (dissolved) Al galvanizing bath [47], as shown in Figure 5.8 and Figure 5.10. This can be indicative of inhibition layer breakdown [48-50] or an indirect confirmation of aluminothermic reduction as suggested by the literature [12,27,29]. However, as shown in Figure 5.11 – Figure 5.13, Cr signal was not detected in the TEM EELS composite maps. This suggests that the Mn and Cr-rich nodule-type oxides observed on the pre-immersion surface (Figure 5.5 and Figure 5.6) were aluminothermically reduced during galvanizing. Hence, it can be concluded that aluminothermic reduction was one of the reactive wetting mechanisms during the continuous hot-dip galvanizing of this prototype med-Mn steel.

Further analysis of Figure 5.11 – Figure 5.13 revealed additional reactive wetting mechanisms that operated during galvanizing. Bath metal (Zn) ingress was identified in all three galvanized M (–30 °C T_{dp})-IA samples (Figure 5.11 – Figure 5.13). The interfacial cracks and voids formed in the oxides during cooling from IAT owing to the coefficient of thermal expansion difference

between the steel substrate and oxide can create routes for Zn infiltration during galvanizing. This oxide cracking and spalling, as suggested by literature [12,17], might be one of the potential ways for bath metal ingress. However, as recently shown by Pallisco [30], partial dissolution of internal oxides, such as MnO, $MnSiO_3$, and Mn_2SiO_4, during the intermediate flash pickling treatment can also be a potential route for Zn infiltration into the steel substrate. This would be consistent with the TEM EELS maps (Figure 5.11 – Figure 5.13) which showed similar Mn and Al-rich internal oxides with significant Zn ingress. Furthermore, oxide wetting was also identified in the galvanized M (–30 °C T_{dp})-IA (+5 °C T_{dp}) sample (Figure 5.13b). The $Fe_2Al_5Zn_x$ intermetallics were in direct contact with Mn, Al-rich oxides as described by Bellhouse and McDermid [31]. Additionally, the oxide lift-off mechanism was also identified in the galvanized M (–30 °C T_{dp})-IA (–10 °C T_{dp}) sample, as shown in Figure 5.12b). These multiple reactive wetting mechanisms operated simultaneously and resulted in the high-quality galvanized coating in the prototype med-Mn steels following CGL-compatible IA treatment.

The coating adhesion and the mechanical properties of the galvanized prototype med-Mn steel were also determined in this research. Good coating adhesion was observed in the galvanized M (–30 °C T_{dp})-IA samples regardless of IA process atmosphere pO_2 with no flaking or cracking of the coating being observed (Figure 5.14). The grain boundary cracks observed by SEM analysis of the bend test sample cross-sections (Figure 5.15) were associated with internal grain boundary oxides which did not propagate into the substrate and more importantly, through the galvanized coating. Moreover, the Zn overlay grains in gauge length of the fractured uniaxial tensile test samples did not deteriorate (i.e., flake off or intergranular fracture) (Figure 5.17). This is additional proof of good coating adhesion in these galvanized samples. Furthermore, uniaxial tensile test results (Figure 5.16 and Table 5.4) confirmed that the galvanized prototype med-Mn steels were

able to meet 3G AHSS general target mechanical properties (24,000 MPa% ≤ UTS × TE ≤ 40,000 MPa%). Based on previous research [11] by the current authors, this high strength and ductility balance would be a result of sustaining a high work hardening rate during deformation owing to successful activation of plasticity enhancing mechanisms (TRIP and TWIP effects).

Overall, it was shown that it is possible to develop a CGL-compatible intercritical annealing treatment and continuous hot-dip galvanizing processing route for a prototype med-Mn steel with martensitic starting microstructure that can result in 3G AHSS general target mechanical properties (24,000 MPa% ≤ UTS × TE ≤ 40,000 MPa%) and high-quality galvanized coating. This is promising in terms of processing med-Mn steels in the existing industrial CGL for 3G AHSS structural applications in automotive industry.

5.6 Conclusions

The effects of austenitizing and intercritical annealing process atmosphere pO_2 on the external oxidation and subsequent continuous hot-dip galvanizing of a prototype 0.2C-6Mn-1.5Si-0.5Al-0.5Cr (wt%) med-Mn steel were determined in this study. Based on the results it can be concluded that:

1) Austenitizing heat treatment resulted in compact external nodule-type Mn-rich oxides on the steel surface. However, flash pickling was successful in dissolving most of these oxides and revealing exposed substrate and extruded Fe nodules on the surface. No significant growth of the external oxide layer was observed after intercritical annealing owing to the multi-micron deep solute-depleted layer that formed during the austenitizing heat treatment.
2) Successful reactive wetting was observed in all three M (–30 °C T_{dp})-IA samples as a well-developed $Fe_2Al_5Zn_x$ inhibition layer formed at the steel/coating interface owing to multiple reactive wetting mechanisms, such as direct wetting, bath metal (Zn) ingress, oxide wetting,

oxide lift-off, and aluminothermic reduction being operational during continuous hot-dip galvanizing.

3) No cracking or flaking of the zinc layer was observed in the bend test samples, confirming good coating adherence for all three galvanized M (–30 °C T_{dp})-IA samples. Furthermore, the galvanized samples met 3G AHSS general target mechanical properties (24,000 MPa% ≤ UTS × TE ≤ 40,000 MPa%).
4) The intercritical annealing and continuous hot-dip galvanizing parameters were compatible with the CGL processing windows.

5.7 Acknowledgements

This research was financially supported by the International Zinc Association Galvanized Autobody Partnership (IZA-GAP) program and the Natural Sciences and Engineering Research Council of Canada (NSERC, grant CRDPJ 522309 – 17). The authors greatly acknowledge U.S. Steel Research for the provision of the steel substrates used in this study. The authors also thank the staff of the Canadian Centre for Electron Microscopy (CCEM), the Brockhouse Institute for Materials Research (BIMR), the McMaster Steel Research Centre (SRC), and the Centre for Automotive Materials and Corrosion (CAMC) for their technical support.

5.8 References

[1] S. Lee, B.C. De Cooman, On the selection of the optimal intercritical annealing temperature for medium Mn TRIP steel, Metall. Mater. Trans. A. 44A (2013) 5018–5024.

[2] W.Q. Cao, C. Wang, J. Shi, M.Q. Wang, W.J. Hui, H. Dong, Microstructure and mechanical properties of Fe–0.2C–5Mn steel processed by ART-annealing, Mater. Sci. Eng. A. 528 (2011) 6661–6666.

[3] P.J. Gibbs, E. De Moor, M.J. Merwin, B. Clausen, J.G. Speer, D.K. Matlock, Austenite stability effects on tensile behavior of manganese-enriched-austenite transformation induced plasticity steel, Metall. Mater. Trans. A. 42A (2011) 3691–3702.

[4] S. Lee, K. Lee, B.C. De Cooman, Observation of the TWIP + TRIP plasticity-enhancement mechanism in Al-added 6 wt pct medium Mn steel, Metall. Mater. Trans. A. 46A (2015) 2356–2363.

[5] A. Arlazarov, M. Gouné, O. Bouaziz, A. Hazotte, G. Petitgand, P. Barges, Evolution of microstructure and mechanical properties of medium Mn steels during double annealing, Mater. Sci. Eng. A. 542 (2012) 31– 39.

[6] J. Shi, X. Sun, M. Wang, W. Hui, H. Dong, W. Cao, Enhanced work-hardening behavior and mechanical properties in ultrafine-grained steels with large-fractioned metastable austenite, Scr. Mater. 63 (2010) 815–818.

[7] K.M.H. Bhadhon, J.R. McDermid, X. Wang, E. McNally, F.E. Goodwin, Fine-scale microstructure characterization and mechanical properties of CGL-compatible heat treated medium-Mn TRIP steel, in: Proc. 11th Conf. Zinc Zinc Alloy Coat. Steel Sheet, Galvatech 2017, ISIJ Int., Tokyo (2017) 493–500.

[8] D.M. Pallisco, J.R. McDermid, Mechanical property development of a 0.15C–6Mn–2Al–1Si third-generation advanced high strength steel using continuous galvanizing heat treatments, Mater. Sci. Eng. A. 778 (2020) 139111, doi: https://doi.org/10.1016/j.msea.2020.139111.

[9] D.M. Pallisco, K.M.H. Bhadhon, V. Patel, M. Pourmajidian, F.E. Goodwin, J.R. McDermid, Galvanizing of medium-Manganese third generation advanced high strength steels, in: Proc. 4th Int. Conf. Mediu. High-Manganese Steels. 9–11 (2019) 375–378.

[10] V. Patel, Microstructure and mechanical properties of medium Mn steel, McMaster University (2019), Hamilton, Canada.

[11] K.M.H. Bhadhon, X. Wang, J.R. McDermid, Effects of CGL-Compatible Thermal Processing, Starting Microstructure, and Sn Micro-alloying on the Mechanical Properties of a Medium-Mn Third Generation Advanced High Strength Steel, Mater. Sci. Eng. A. 833 (2022) 142563.

[12] R. Sagl, A. Jarosik, D. Stifter, G. Angeli, The role of surface oxides on annealed high strength steels in hot-dip galvanizing, Corros. Sci. 70 (2013) 268–275.

[13] J. Mahieu, S. Claessens, B.C. De Cooman, Galvanizability of high-strength steels for automotive applications, Metall. Mater. Trans. A. 32A (2001) 2905–2908.

[14] J. Maki, J. Mahieu, B.C. De Cooman, S. Claessens, Galvanisability of silicon free CMnAl TRIP steels, Mater. Sci. Technol. 19 (2003) 125–131.

[15] M. Blumenau, M. Norden, F. Friedel, K. Peters, Use of pre-oxidation to improve reactive wetting of high manganese alloyed steel during hot-dip galvanizing, Surf. Coat. Technol. 206 (2011) 559–567.

[16] E.M. Bellhouse, J.R. McDermid, Selective Oxidation and Reactive Wetting of 1.0 Pct Si-0.5 Pct Al and 1.5 Pct Si TRIP-Assisted Steels, Metall. Mater. Trans. A. 41A (2010) 1539–1553.

[17] E.M. Bellhouse and J.R. McDermid, Selective Oxidation and Reactive Wetting during Galvanizing of a CMnAl TRIP-Assisted Steel, Metall. Mater. Trans. A. 42 (2011) 2753–2768.

[18] R. Khondker, A. Mertens, J.R. McDermid, Development of the surface structure of TRIP steels prior to hot-dip galvanizing, Mater. Sci. Eng. A. 463 (2007) 157–165.

[19] G.S. Mousavi, J.R. McDermid, Selective oxidation of a C-2Mn-1.3Si (Wt Pct) advanced high-strength steel during continuous galvanizing heat treatments, Metall. Mater. Trans. A. 49 (2018) 5546–5560.

[20] G.S. Mousavi, J.R. McDermid, Effect of dew point on the reactive wetting of a C-2Mn-1.3Si (wt%) advanced high strength steel during continuous galvanizing, Surf. Coat. Technol. 351 (2018) 11–20.

[21] L. Cho, G.S. Jung, B.C. De Cooman, On the Transition of Internal to External Selective Oxidation on CMnSi TRIP Steel, Metall. Mater. Trans. A. 45A (2014) 5158–5172.

[22] L. Cho, M.S. Kim, Y.H. Kim, B.C. De Cooman, Influence of Minor Alloying Elements on Selective Oxidation and Reactive Wetting of CMnSi TRIP Steel during Hot Dip Galvanizing, Metall. Mater. Trans. A. 45A (2014) 4484–4498.

[23] M. Pourmajidian, J.R. McDermid, Selective Oxidation of a 0.1C-6Mn-2Si Third Generation Advanced High-Strength Steel During Dew-Point Controlled Annealing, Metall. Mater. Trans. A. 49 (2018) 1795–1808.

[24] M. Pourmajidian, J.R. McDermid, Effect of Annealing Temperature on the Selective Oxidation and Reactive Wetting of a 0.1C-6Mn-2Si Advanced High Strength Steel During Continuous Galvanizing Heat Treatments, ISIJ Int. 58(9) (2018) 1635–1643.

[25] M. Pourmajidian, J.R. McDermid, On the reactive wetting of a medium-Mn advanced high-strength steel during continuous galvanizing, Surf. Coat. Technol. 357 (2019) 418–426.

[26] Y. Suzuki, T. Yamashita, Y. Sugimoto, S. Fujita, S. Yamaguchi, Thermodynamic Analysis of Selective Oxidation Behavior of Si and Mn-added Steel during Recrystallization Annealing, ISIJ Int. 49(4) (2009) 564–573.

[27] R. Kavitha, J.R. McDermid, On the in-situ aluminothermic reduction of manganese oxides in continuous galvanizing baths, Surf. Coat. Technol. 212 (2012) 152–158.

[28] H. Liu, Y. He, L. Li, Application of thermodynamics and Wagner model on two problems in continuous hot-dip galvanizing, J. Appl. Surf. Sci., 256(5) (2009), 1399–1403.

[29] S. Alibeigi, R. Kavitha, R.J. Meguerian, J.R. McDermid, Reactive wetting of high Mn steels during continuous hot-dip galvanizing, Acta Mater. 59(9) (2011) 3537–3549.

[30] D.M. Pallisco, Mechanical Property Development and Galvanizing of Medium-Mn Third Generation Advanced High Strength Steel, McMaster University (2021), Hamilton, Canada.

[31] E.M. Bellhouse, J.R. McDermid, Selective oxidation and reactive wetting during hot-dip galvanizing of a 1.0 pct Al-0.5 pct Si TRIP-assisted steel, Metall. Mater. Trans. A. 43A (2012) 2426–2441.

[32] N. Birks, G.H. Meier, F.S. Pettit, Introduction to the High-temperature Oxidation of Metals, Cambridge University Press, Cambridge, 2006.

[33] J.R. McDermid, A. Chakraborty, Identification of steel chemistries and galvanizing process design, ZCO-53-1 Project Report, (2012), Hamilton, Canada.

[34] S. Gates-Rector, T. Blanton, The Powder Diffraction File: a quality materials characterization database, Powder Diffr. 34 (2019) 352–360. doi:10.1017/S0885715619000812.

[35] ASTM A 653/A 653M – 05, Standard Specification for Steel Sheet, Zinc-coated (Galvanized) or Zinc-Iron Alloy-coated (Galvannealed) by the Hot-dip Process, (2005).

[36] ASTM E8/E8M-16a: Standard Test Methods for Tension Testing of Metallic Materials, West Conshohocken, PA, USA, 2016.

[37] J.R. Mackert, R.D. Ringle, C.W. Fairhurst, High-temperature Behavior of a Pd-Ag Alloy for Porcelain, J. Dent. Res. 62 (1983) 1229–1235.

[38] S. Guruswamy, S.M. Park, J.P. Hirth, R.A. Rapp, Internal oxidation of Ag-in alloys: Stress relief and the influence of imposed strain, Oxid. Met. 26 (1986) 77–100.

[39] Z.T. Zhang, I.R. Sohn, F.S. Pettit, G.H. Meier, S. Sridhar, Investigation of the Effect of Alloying Elements and Water Vapor Contents on the Oxidation and Decarburization of Transformation-Induced Plasticity Steels, Metall. Mater. Trans. B. 40 (2009) 567–584.

[40] S. Samanta, A.K. Halder, Y. Deo, S. Guha, M. Dutta, Effect of Mn and Cr on the selective oxidation, surface segregation and hot-dip Zn coatability, Surf. Coat. Technol. 377 (2019) 124908.

[41] S. Swaminathan, M. Spiegel, Thermodynamic and kinetic aspects on the selective surface oxidation of binary, ternary and quarternary model alloys, Appl. Surf. Sci. 253 (2007) 4607–4619.

[42] M.S. Kim, J.H. Kwak, J.S. Kim, Y.H. Liu, N. Gao, N.Y. Tang, Galvanizability of advanced high-strength steels 1180TRIP and 1180CP, Metall. Mater. Trans. A. 40A (2009) 1903–1910.

[43] K.M.H. Bhadhon, J.R. McDermid, F.E. Goodwin, Effect of Process Atmosphere Dew point on Selective Oxidation and Reactive Wetting of a Medium-Mn Third Generation Advanced High Strength Steel, 12th Conf. Zinc Zinc Alloy Coat. Steel Sheet, Galvatech 2021, ASMET, Vienna, Austria (2021).

[44] D.K. Matlock, J.G. Speer, Design Considerations for the Next Generation of Advanced High Strength Sheet Steels, in: H.C. Lee (Ed.), Proc. 3rd Int. Conf. Struct. Steels, Seoul, Korea (2006) 774–781.

[45] B. Sun, D. Palanisamy, D. Ponge, B. Gault, F. Fazeli, C. Scott, S. Yue, D. Raabe, Revealing fracture mechanisms of medium manganese steels with and without delta-ferrite, Acta Mater. 164 (2019) 683–696.

[46] R. Sagl, A. Jarosik, G. Angeli, T. Haunschmied, G. Hesser, D. Stifter, Tailoring of oxide morphology and crystallinity on advanced high-strength steel surfaces prior hot-dip galvanizing, Acta Mater. 72 (2014) 192–199.

[47] N.Y. Tang, Thermodynamics and Kinetics of Alloy Formation in Galvanized Coatings, in: F.E. Goodwin (Ed.), Proc. Int'l Symp. Zinc-Based Steel Coat. Syst. Prod. Performance, TMS 1998, TMS, San Antonio, TX, (1998) 3–12.

[48] M. Guttmann, Diffusive Phase Transformations in Hot-Dip Galvanizing, Mater. Sci. Forum. 155–156 (1994) 527–548.

[49] A.R. Marder, The metallurgy of zinc-coated steel, Prog. Mater. Sci. 45 (2000) 191–271.

[50] C.E. Jordan, A.R. Marder, Fe–Zn phase formation in interstitial-free steels hot-dip galvanized at 450 °C Part II 0.20 wt% Al–Zn baths, J. Mater. Sci. 32 (1997) 5603–5610.

6 Global Discussion

The chapter links the key findings from Chapter 3 – Chapter 5 to provide a summative discussion on microstructure and mechanical property development, selective oxidation, and reactive wetting of the prototype med-Mn steel.

6.1 Microstructure and Mechanical Property Development

The effects of starting microstructure, CGL-compatible intercritical annealing (IA) parameters, and Sn micro-alloying on the microstructural evolution and mechanical property development of the prototype med-Mn steel were determined in Chapter 3 of this Ph.D. thesis. It was found that intercritical austenite formation, chemical/mechanical stabilisation, and retained austenite morphology were significantly affected by these experimental variables, which in turn determined the mechanical properties of the heat-treated prototype med-Mn steel.

The retained austenite volume fraction increased with increasing IAT and IA holding time for both starting microstructures, i.e., the as-received cold-rolled (CR) tempered martensite and fully martensitic (M) microstructures. However, the morphology of the retained austenite and, thereby, its chemical and mechanical stability, varied depending on the starting microstructure. Blocky retained austenite was observed in the intercritically annealed med-Mn steel with the CR starting microstructure (Figure 3.4). This type of retained austenite morphology is consistent with that observed in the literature for AHSSs with cold-rolled starting microstructure [1–6]. Carbide evolution analysis (Table 3.3, Figure 3.6) suggested the intercritical austenite nucleated on the carbide particles and grew *via* carbide dissolution during IA of the prototype med-Mn steel without Sn micro-alloying. This suggests the dissolving carbide particles were the main source of C that partitioned into the intercritical austenite and chemically stabilised it. However, it should be noted that the austenite growth kinetics in this process depends on the Mn content of the dissolving

cementite particles [7]. Lai et al. [7] have reported that high Mn content (~ 25 wt%) in cementite changed the austenite growth kinetics from C partitioning controlled to Mn partitioning controlled, thereby resulting in significantly slower growth of the austenite. For the Sn micro-alloyed prototype med-Mn steel, the carbide evolution analysis revealed significant carbide precipitation and coarsening during the IA. However, Sn segregated at the carbide/matrix interface (Figure 3.7) and, similar to its effect on oxidation and decarburization kinetics [8–12], carbide dissolution was inhibited resulting in less C being partitioned into the intercritical austenite. As a result, a lower retained austenite volume fraction was observed in the Sn micro-alloyed med-Mn steel owing to the intercritical austenite being less chemically stable, with significant fractions transforming to martensite during final cooling.

The martensitic (M) starting microstructure, on the other hand, produced a lamellar retained austenite morphology, as shown in Figure 3.5. This lamellar retained austenite is known to be more chemically and mechanically stable compared to its blocky counterpart. As confirmed by various researchers [1,4,5,13–15], the higher chemical stability of lamellar retained austenite is associated with higher C and Mn partitioning from the surrounding martensite phase owing to shorter diffusion distance whereas the higher mechanical stability arises from being mechanically constrained by the surrounding martensite phase. Furthermore, the M starting microstructure also produced a higher volume fraction of retained austenite compared to the CR starting microstructure under the same annealing conditions (Figure 3.8a) *vs.* Figure 3.8b)). This was due to faster austenite reversion transformation (ART) kinetics and rapid C partitioning from the C supersaturated martensite phase. Moreover, the pre-existing interlath austenite that formed during the austenitizing heat treatment was able to grow without any nucleation barrier during the IA treatment. However, similar to the CR starting microstructure, the Sn micro-alloyed med-Mn steel

had a lower retained austenite volume fraction (Figure 3.8b)) owing to the retarding effect of Sn on C diffusion, thereby resulting in less chemically stable intercritical austenite.

Higher IATs (i.e., 710 °C for the CR starting microstructures and 690 °C and 710 °C for the M starting microstructures) resulted in higher volume fraction of retained austenite (Figure 3.8). However, the M_S temperatures and, by inference, the M_S^{σ} temperature, were significantly higher, as shown in Figure 3.9b). This suggests that the retained austenite was not chemically and mechanically stable compared to that formed during the lower IATs (i.e., 675 °C for the CR starting microstructures and 650 °C and 675 °C for the M starting microstructures). This was confirmed by the interrupted tensile test results (Figure 3.13 and Figure 3.16), which showed faster retained austenite to martensite transformation kinetics, exhausting the TRIP effect at lower true strains. As a result, a high work hardening rate was not sustained during deformation, resulting in strength/ductility balances which did not meet 3G AHSS target mechanical properties (24,000 MPa% ≤ UTS × TE ≤ 40,000 MPa% [16]). The cold-rolled prototype med-Mn steel with Sn micro-alloying showed similar TRIP exhaustion at lower true strain for the lower IAT (675 °C) conditions (Figure 3.13) owing to less chemically stable retained austenite, a result of slower C partitioning due to Sn segregation at the carbide/matrix interface. As a result, none of the IA heat treatment produced 3G AHSS target mechanical properties in the cold-rolled med-Mn steel with Sn micro-alloying (Table 3.4).

Contrastingly, the lower IATs (i.e., 675 °C and 690 °C for the CR starting microstructure without Sn micro-alloying and 650 °C and 675 °C for the M starting microstructure, regardless of Sn micro-alloying) produced chemically and mechanically stable retained austenite. The stable retained austenite transformed to martensite gradually, thereby exhausting the TRIP effect at higher true strains (Figure 3.13 and Figure 3.16). Formation of a harder phase (i.e., martensite) and

geometrically necessary dislocations (GNDs) through the activation of the TRIP effect aided in maintaining the desired high work hardening rate (Figure 3.11c), Figure 3.14c), and Figure 3.15c)) and delayed the onset of necking. It should be noted that formation of deformation nano-twins in the retained austenite was also confirmed, as shown in Figure 3.18 – Figure 3.21. This suggests the stacking fault energy (SFE) of the retained austenite was within the range of 15 – 45 mJ/m^2, necessary for activating the TWIP effect [17]. Consequently, a high strength/ductility balance was obtained, meeting 3G AHSS target mechanical properties by carefully balancing the retained austenite SFE, volume fraction, and stability in order to successfully activate both the TRIP and TWIP effects during deformation.

Furthermore, significant post-uniform elongation ($\varepsilon_f \geq 0.40$) was observed for the promising IA conditions that produced target 3G AHSS mechanical properties in the prototype med-Mn steels (Figure 3.11b), Figure 3.14b), and Figure 3.15b)). This is encouraging in terms of having good formability for these med-Mn steels as the literature [18,19] suggests there is a correlation between post-uniform elongation and material formability. However, other mechanical tests, such as uniaxial tensile tests at high strain rates, hole expansion ratio tests, bending etc., should be conducted in the future to fully understand the formability limit of these new generation of AHSSs.

Based on the major findings of this microstructure and mechanical property development study, it was identified that the martensitic starting microstructure had a more robust CGL-compatible processing window that can produce 3G AHSS target mechanical properties. Furthermore, Table 3.4 showed that the A-M 675 °C × 120 s treatment had the highest UTS × TE product. Hence, this thermal processing route, comprising austenitizing and a CGL-compatible IA,

was chosen for further study – i.e., selective oxidation (Chapter 4) and reactive wetting (Chapter 5) of the prototype med-Mn steel.

6.2 Selective Oxidation and Reactive Wetting

The effect of process atmosphere pO_2 (–30 °C, –10 °C, and +5 °C T_{dp}) on external and internal oxidation during the austenitizing and 675 °C × 120 s IA treatments of the prototype med-Mn steel without Sn micro-alloying (i.e., steel A (Table 3.1)) was determined in the selective oxidation study (Chapter 4). FIB trench cut analysis (Figure 4.4) revealed that the austenitizing heat treatment at 775 °C for 600 s produced a relatively thick (~ 200 nm) external oxide regardless of the process atmosphere pO_2 employed. This approximately equal average thickness of the external oxides with increasing process atmosphere pO_2 is likely associated with the external to internal oxidation mode transition for Mn (i.e., $T_{dp} \cong$ –30 °C), as determined by a Wagner model [20] calculation. This is consistent with the SEM micrographs (Figure 4.3a) – Figure 4.3c)) and XPS binding energy analysis (Table 4.4) which revealed nodular MnO on the surfaces of the as-austenitized (M) samples. However, TEM EELS analysis of the M (–30 °C T_{dp}) sample revealed another layer of Mn- and Cr- rich external oxides underneath the MnO layer (Figure 4.6). Although the Wagner model [20] predicts internal oxidation of Cr for all three process atmosphere pO_2, this inconsistency is likely the result of complex $MnCr_2O_4$ formation instead of simple binary oxide of Cr (i.e., Cr_2O_3) assumed by the Wagner formalism. Furthermore, XPS depth profiling (Figure 4.5) and binding energy analysis (Table 4.4) of the M (–10 °C T_{dp}) and M (+5 °C T_{dp}) samples also revealed some $MnAl_2O_4$ with minor $MnSiO_3$/Mn_2SiO_4 on the sample surfaces. Being complex oxides, the Wagner model [20] predictions regarding the formation of these external oxides are also inconsistent. However, similar multi-layered, complex external oxides were reported by

Pallisco [21] for a med-Mn steel (0.15C-6Mn-1.9Al-1Si wt%) that underwent a 890 °C × 600 s martensite-ferrite (MF) heat treatment.

Si and Al were largely internally oxidized, forming thick sub-surface internal oxides, as revealed by the TEM EELS analysis (Figure 4.6). This is consistent with the Wagner model [20] calculation for Al. However, although consistent with –10 °C and +5 °C T_{dp} process atmosphere, the Wagner model [20] predicts external oxidation of Si for the –30 °C T_{dp}. As mentioned above, this disagreement is likely due to the formation of complex $MnSiO_3$/Mn_2SiO_4 external oxides as determined by XPS binding energy analysis (Table 4.4). FIB trench cut analysis (Figure 4.4b)) showed an increase in the internal oxidation layer with increasing process atmosphere pO_2. This was due to higher inward O_2 flux at higher process atmosphere pO_2 which promoted deeper internal oxide formation. These deeper internal oxides were mainly grain boundary oxides which formed a core-shell type structure. Similar core-shell type grain boundary internal oxides have been reported for both 1G AHSS [22] and med-Mn steels [21,23], with the chemistry of the core-shell structure depending on the steel composition. In this case, the core of the internal oxides was enriched with Al whereas the shell was Si-enriched (Figure 4.7). The formation of this type of core-shell structure was further supported by the diffusivity calculations of the alloying element (Table 4.6) and solubility products of the oxides (Table 4.5) in austenite at 775 °C. Furthermore, a multi-micron (~ 2–8 μm) deep solute-depleted layer formed owing to the internal oxidation, as confirmed by the SEM-EDS analysis (Figure 4.8).

Kavitha and McDermid [24] have reported that it is possible to aluminothermically reduce up to approximately 85 nm of MnO within the common CGL dipping time of 4 s for a 0.20 wt% Al (dissolved) bath. Hence, an intermediate flash pickling was carried out which successfully dissolved the Mn and (Mn,Si)-oxides (i.e., MnO and $MnSiO_3$/Mn_2SiO_4) [25–27]. FIB trench cut

analysis (Figure 4.4) showed that the flash pickling dissolved the external oxides to a thickness of approximately 30 nm within 60 s. Furthermore, the flash pickling treatment also revealed additional surface Fe nodules extruded from the substrate owing to the volumetric expansion associated with internal oxidation (Figure 4.7). These extruded nodules were trapped underneath the external oxides prior to flash pickling. The flash pickling also revealed some exposed substrate in regions where the external oxides were relatively thin. This is consistent with the findings reported by Pallisco [21] after flash pickling using the same pickling solution. Furthermore, the author reported that these extruded Fe nodules and exposed substrate were beneficial for direct reactive wetting and the formation of a robust $Fe_2Al_5Zn_x$ inhibition layer.

After the 675 °C × 120 s IA heat treatment, the depth of internal oxidation increased with increasing process atmosphere pO_2 (Figure 4.10b)). TEM EELS analysis (Figure 4.12 and Figure 4.13) revealed that these oxides were grain boundary oxides with core-shell structures. However, the chemistry of this core-shell structure was different compared to those observed after the austenitizing heat treatment. In these cases, the core was enriched with Si whereas the shell was enriched with Mn. This correlates well with the diffusivity calculation shown for the alloying elements in ferrite at 675 °C (Table 4.7). Furthermore, assessment of the solubility product of different oxide species in ferrite at 675 °C (Table 4.5) suggested that the shell oxides would be Mn_2SiO_4. The ferrite phase was considered in both of these calculations owing to the fact that significant de-alloying (Figure 4.8) and decarburization occurred during the 600 s austenitizing heat treatment. The deepest internal oxidation layer was observed in the M (+5 °C T_{dp})-IA (+5 °C T_{dp}) sample. It should be noted that internal oxidation can significantly affect resistance spot welding (RSW), which is a commonly used joining technique in the automotive industry [28,29].

Hence, a future study should focus on the effect of internal oxidation on the RSW process parameters for the med-Mn steels.

External oxides did not form during the IA heat treatment regardless of the process atmosphere pO_2 employed (Figure 4.10a)). This was due to the multi-micron (~ 2–8 µm) solute-depleted layer that formed during the austenitizing heat treatment, where an IA holding time of 120 s was too short for the alloying elements to diffuse from the bulk to the external surface through the solute-depleted layer. The shallowest solute-depleted layer (~ 2 µm) was observed in the M (–30 °C T_{dp}) sample (Figure 4.4b)). This is significantly thicker versus the distance that solutes, such as Mn, Si, Cr, and Al, can diffuse in ferrite at 675 °C for 120 s, as shown in Appendix D in Chapter 4. As a result, the substrate surface after the IA treatment was similar to that observed after the flash pickling treatment.

The features identified on the intercritically annealed pre-immersion surface were found to be the key factors which facilitated successful reactive wetting and produced robust, high-quality galvanized coatings, as reported in Chapter 5. A well-developed $Fe_2Al_5Zn_x$ inhibition layer, evidence of successful reactive wetting, was confirmed for the M (–30 °C T_{dp}) samples intercritically annealed at 675 °C × 120 s under –30 °C, –10 °C, and +5 °C T_{dp} process atmosphere and subsequently galvanized in a 0.2 wt% (dissolved) Al galvanizing (GI) bath (Figure 5.8 – Figure 5.13). Multiple reactive wetting mechanisms were identified which resulted in high-quality galvanized coatings in this med-Mn steel. Direct wetting was the main reactive wetting mechanism in all three galvanized M (–30 °C T_{dp})-IA samples. The exposed substrate and extruded Fe nodules dissolved upon immersion of the steel substrate, reacted with the galvanizing bath Al, and promoted the formation of $Fe_2Al_5Zn_x$ at the steel/coating interface. This is consistent with the

literature [21,30,31], which also reported direct wetting mechanism in AHSSs owing to extruded Fe nodule dissolution and presence of exposed substrate in the pre-immersion surface.

TEM EELS analysis of the steel/coating interface (Figure 5.11 – Figure 5.13) revealed several secondary reactive wetting mechanisms that operated alongside direct wetting. Bath metal ingress was observed in the galvanized M (–30 °C T_{dp})-IA samples. A combination of oxide cracking and spalling [30], and partial dissolution of internal oxides during the intermediate flash pickling treatment [21] facilitated Zn infiltration into the steel substrate. Furthermore, oxide wetting (Figure 5.13b)) – where the $Fe_2Al_5Zn_x$ intermetallics were in direct contact with (Mn, Al)-rich oxides – and oxide lift-off mechanisms (Figure 5.12b)) were also identified. Aluminothermic reduction also operated during galvanizing of the steel substrate. An indirect confirmation of aluminothermic reduction, as suggested by the literature [24,32,33], was the ζ-$FeZn_{13}$ intermetallics observed along with $Fe_2Al_5Zn_x$ at the steel/coating interface (Figure 5.8 and Figure 5.10) despite using a 0.2 wt% (dissolved) Al GI bath [34]. However, Cr was not detected in the TEM EELS analysis (Figure 5.11 – Figure 5.13), suggesting that the Cr-rich oxides observed on the pre-immersion surface (Figure 5.5 and Figure 5.6) were aluminothermically reduced during galvanizing. These reactive wetting mechanisms were successful in producing high-quality robust galvanized coatings as determined by the three-point bend test (Figure 5.14) and analysis of the cross-section of the bend radius (Figure 5.15) and gauge length of the tensile test samples (Figure 5.17) with SEM. Although some grain boundary cracks were observed at the outer bend radius of the bend test samples (Figure 5.15), these cracks did not propagate to either bulk of the substrate or the coating layer and it was concluded that these were associated with grain boundary internal oxides. Furthermore, uniaxial tensile tests (Figure 5.16 and Table 5.4) confirmed that the galvanized prototype med-Mn steels met 3G AHSS target mechanical properties.

Overall, based on the findings from Chapter 3 – Chapter 5, it can be concluded that it is possible to employ a two-stage heat treatment – comprising austenitizing and CGL-compatible intercritical annealing – with an intermediate flash pickling step to produce 3G AHSS target mechanical properties and a pre-immersion surface that can be galvanized *via* successful reactive wetting. Figure 6.1 presents a summative schematic showing the bulk microstructure and surface structure evolution during this processing cycle. This is promising in terms of developing med-Mn 3G AHSS that can be utilised in future automotive applications.

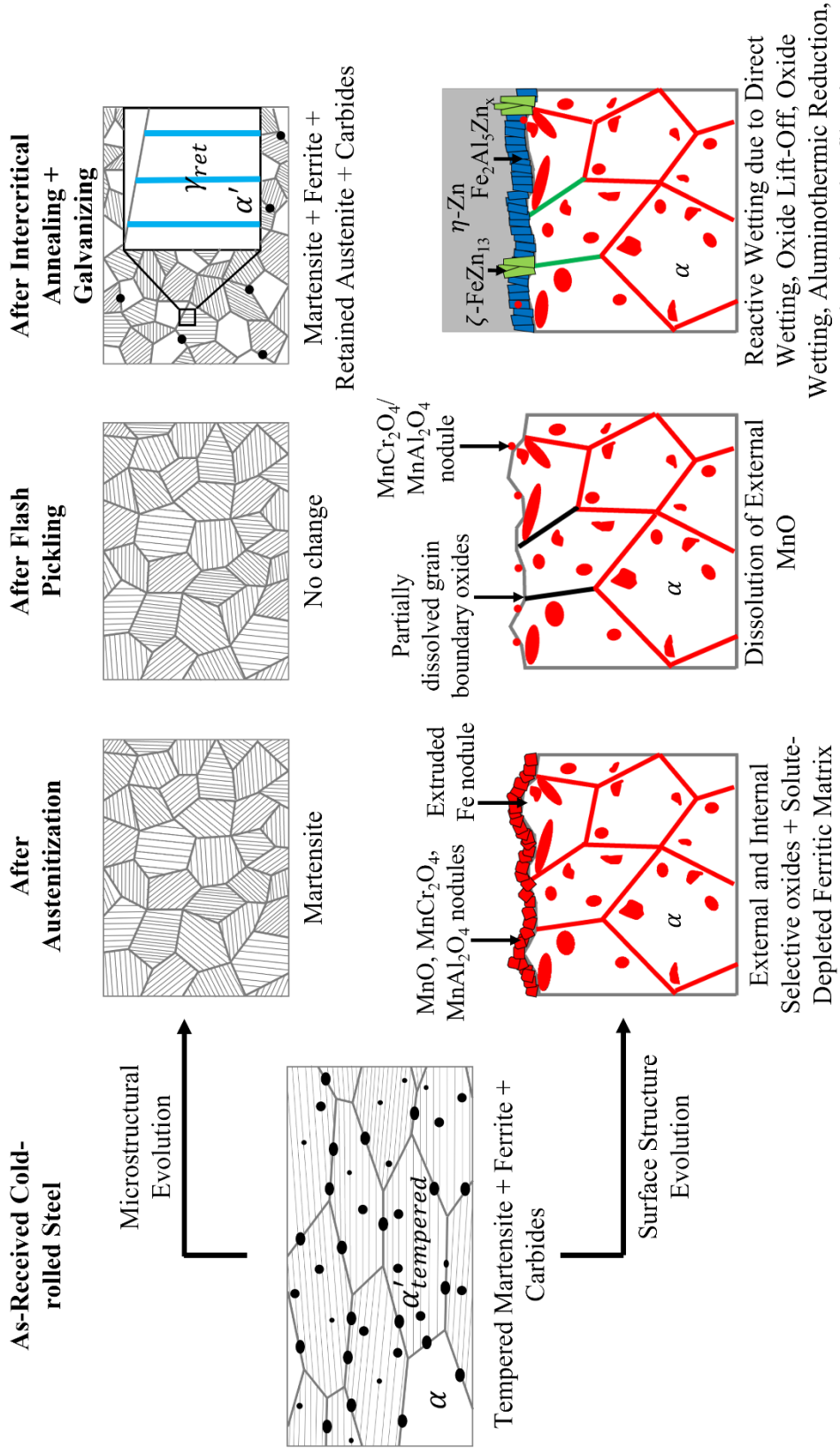

Figure 6.1: Summative schematic showing the microstructure and surface structure evolution during each stage of the processing cycle which resulted in the desired final bulk microstructure and successful galvanizing of the prototype med-Mn steel; the bulk internal grain boundary oxides formed a core-shell type structure (Figure 4.7, Figure 4.12, and Figure 4.13).

6.3 References

[1] H. Luo, H. Dong, New ultrahigh-strength Mn-alloyed TRIP steels with improved formability manufactured by intercritical annealing, Mater. Sci. Eng. A. 626 (2015) 207–212.

[2] A. Arlazarov, A. Hazotte, O. Bouaziz, M. Goune, F. Kegel, Characterization of microstructure formation and mechanical behavior of an advanced medium Mn steel, in: Proc. MS&T 2012, Pittsburgh, PA, (2012) 1124–1131.

[3] J.I. Kim, J.H. Ryu, S.W. Lee, K. Lee, Y.-U. Heo, D.-W. Suh, Influence of the initial microstructure on the reverse transformation kinetics and microstructural evolution in transformation-induced plasticity – assisted steel, Metall. Mater. Trans. A. 47 (2016) 5352–5361.

[4] D.M. Pallisco, J.R. McDermid, Mechanical property development of a 0.15C–6Mn–2Al–1Si third-generation advanced high strength steel using continuous galvanizing heat treatments, Mater. Sci. Eng. A. 778 (2020) 139111.

[5] V. Patel, Microstructure and Mechanical Properties of Medium Mn Steel, McMaster University (2019), Hamilton, Canada.

[6] J. Han, S.-J. Lee, J.-G. Jung, Y.-K. Lee, The effects of the initial martensite microstructure on the microstructure and tensile properties of intercritically annealed Fe–9Mn–0.05C steel, Acta Mater. 78 (2014) 369–377.

[7] Q. Lai, M. Gouné, A. Perlade, T. Pardoen, P. Jacques, O. Bouaziz, Y. Bréchet, Mechanism of Austenite Formation from Spheroidized Microstructure in an Intermediate Fe-0.1C-3.5Mn Steel, Metall. Mater. Trans. A. 47A (2016) 3375–3386.

[8] E.D. Hondros, M.P. Seah, Segregation to interfaces, Int. Met. Rev. 22 (1977) 262–301.

[9] M. Seah, Quantitative prediction of surface segregation, J. Catal. 57 (1979) 450–457.

[10] L. Cho, E.J. Seo, G.S. Jung, D.W. Suh, B.C. De Cooman, Surface selective oxidation of Sn-added CMnSi TRIP steel, Metall. Mater. Trans. A. 47 (4) (2016) 1705–1719.

[11] G. Seyed Mousavi, B. Langelier, J.R. McDermid, Effect of Sn Addition, Process Atmosphere pO2, and Annealing Time on the Selective Oxidation of a C-2Mn-1.7Si (Wt Pct) Advanced High-Strength Steel During Continuous Galvanizing, Metall. Mater. Trans. A. 50 (2019) 2898–2911.

[12] M. Pourmajidian, B. Langelier, J.R. McDermid, Effect of process atmosphere dew point and Tin addition on oxide morphology and growth for a medium-Mn third generation advanced steel during intercritical annealing, Metall. Mater Trans. A. 49 (2018) 5561–5573.

[13] J.R. McDermid, H.S. Zurob, Y. Bian, Stability of Retained Austenite in High-Al, Low-Si TRIP-Assisted Steels Processed via Continuous Galvanizing Heat Treatments, Metall. Mater. Trans. A. 42 (2011) 3627–3637.

[14] P.J. Jacques, F. Delannay, J. Ladrière, On the influence of interactions between phases on the mechanical stability of retained austenite in transformation-induced plasticity multiphase steels, Metall. Mater. Trans. A. 32 (2001) 2759–2768.

[15] F.G. Caballero, C. Garcia-Mateo, J. Chao, M.J. Santofimia, C. Capdevila, C.G. de Andres, Effects of Morphology and Stability of Retained Austenite on the Ductility of TRIP-aided Bainitic Steels, ISIJ Int. 48 (9) (2008) 1256–1262.

[16] D.K. Matlock, J.G. Speer, Design Considerations for the Next Generation of Advanced High Strength Sheet Steels, in: H.C. Lee (Ed.), Proc. 3rd Int. Conf. Struct. Steels, Seoul, Korea (2006) 774–781.

[17] B.C. De Cooman, Y. Estrin, S.K. Kim, Twinning-induced plasticity (TWIP) steels, Acta Mater. 142 (2018) 283–362.

[18] J. Sarkar, T.R.G. Kutty, D.S. Wilkinson, J.D. Embury, D.J. Lloyd, Tensile properties and bendability of T4 treated AA6111 aluminum alloys, Mater. Sci. Eng. A. 369 (2004) 258–266.

[19] P. Larour, J. Freudenthaler, T. Weissböck, Reduction of cross section area at fracture in tensile test: Measurement and applications for flat sheet steels, J. Phys. Conf. Ser. 896 (2017).

[20] C. Wagner, Reaktionstypen bei der Oxydation von Legierungen, Zeitschrift für Elektrochemie. 63 (7) (1959) 772–782.

[21] D.M. Pallisco, Mechanical Property Development and Galvanizing of Medium-Mn Third Generation Advanced High Strength Steel, McMaster University (2021), Hamilton, Canada.

[22] G.S. Mousavi, J.R. McDermid, Selective oxidation of a C-2Mn-1.3 Si (Wt Pct) advanced high-strength steel during continuous galvanizing heat treatments, Metall. Mater. Trans. A. 49 (2018) 5546–5560.

[23] M. Pourmajidian, J.R. McDermid, Selective Oxidation of a 0.1C-6Mn-2Si Third Generation Advanced High-Strength Steel During Dew-Point Controlled Annealing, Metall. Mater. Trans. A. 49 (2018) 1795–1808.

[24] R. Kavitha, J.R. McDermid, On the in-situ aluminothermic reduction of manganese oxides in continuous galvanizing baths, Surf. Coat. Technol. 212 (2012) 152–158.

[25] C.F. Jones, R.S.C. Smart, P.S. Turner, Dissolution kinetics of manganese oxides. Effects of preparation conditions, pH and oxidation/reduction from solution, J. Chem. Soc. Faraday Trans. 86 (1990) 947–953.

[26] W.H. Casey, M.F. Hochella, H.R. Westrich, The surface chemistry of manganiferous silicate minerals as inferred from experiments on tephroite (Mn2SiO4), Geochim. Cosmochim. Acta. 57 (1993) 785–793.

[27] J.F. Banfield, G.G. Ferruzzi, W.H. Casey, H.R. Westrich, HRTEM study comparing naturally and experimentally weathered pyroxenoids, Geochemica Cosm. Acta. 59 (1995) 19–31.

[28] X. Han, C. DiGiovanni, J.R. McDermid, E. Biro, N.Y. Zhou, Effect of internal oxidation on the weldability of CMnSi steels, Weld. World. 63 (2019) 1633–1639.

[29] N.T. Williams, J.D. Parker, Review of resistance spot welding of steel sheets: Part 1 - Modelling and control of weld nugget formation, Int. Mater. Rev. 49 (2004) 45–75.

[30] E.M. Bellhouse, J.R. McDermid, Selective Oxidation and Reactive Wetting during Galvanizing of a CMnAl TRIP-Assisted Steel, Metall. Mater. Trans. A. 42 (2011) 2753-2768.

[31] E.M. Bellhouse, Galvanizing of Al-Si TRIP-Assisted Steels, McMaster University (2010), Hamilton, Canada.

[32] R. Sagl, A. Jarosik, D. Stifter, G. Angeli, The role of surface oxides on annealed high strength steels in hot-dip galvanizing, Corros. Sci. 70 (2013) 268–275.

[33] S. Alibeigi, R. Kavitha, R.J. Meguerian, J.R. McDermid, Reactive wetting of high Mn steels during continuous hot-dip galvanizing, Acta Mater. 59 (9) (2011) 3537–3549.

[34] N.Y. Tang, Thermodynamics and Kinetics of Alloy Formation in Galvanized Coatings, in: F.E. Goodwin (Ed.), Proc. Int'l Symp. Zinc-Based Steel Coat. Syst. Prod. Performance, TMS 1998, TMS, San Antonio, TX, (1998) 3–12.

7 Conclusions and Future Directions

7.1 Conclusions

The main objective of this Ph.D. was to develop a CGL-compatible thermal processing route for a prototype 0.2C-6Mn-1.5Si-0.5Al-0.5Cr-xSn (wt%) (x = 0 and 0.05 wt%) med-Mn steel that would meet 3G AHSS target mechanical properties and be successfully galvanized *via* enhanced reactive wetting. In that regard, Chapter 3 of this thesis determined the effects of starting microstructure, CGL-compatible intercritical annealing parameters, and Sn micro-alloying on the microstructure and mechanical property development of the above prototype med-Mn steel. The results outlined in Chapter 3 identified the most promising starting microstructures and heat treatment parameters for use in the selective oxidation (Chapter 4) and reactive wetting studies (Chapter 5). In these Chapters, the effects of three process atmosphere pO_2 (i.e., –30 °C, –10 °C and +5 °C T_{dp} N_2–5vol%H_2) on both selective oxidation and reactive wetting were determined to develop a CGL-compatible thermal processing route that produced a high-quality galvanized med-Mn steel with 3G AHSS target mechanical properties.

The major findings of these studies are summarised as follows:

1) A martensitic starting microstructure was more robust in achieving 3G AHSS general target mechanical properties of 24,000 MPa% ≤ UTS × TE ≤ 40,000 MPa%. Lower IATs (650 and 675 °C) and short holding times (60 and 120 s), compatible with CGL processing windows, produced chemically and mechanically stable retained austenite owing to faster austenite reversion transformation (ART) kinetics and relatively rapid C partitioning from the surrounding C supersaturated martensite. A gradual transformation of the retained austenite to martensite (TRIP effect) and formation of deformation-induced nano-twins in the retained austenite (TWIP effect) aided in sustaining high work hardening rate during deformation. As

a result, the onset of necking was delayed and a high strength/ductility balance, meeting 3G AHSS target mechanical properties, was achieved.

2) Sn micro-alloying had more profound effect on the carbide evolution and, in turn, retained austenite stability and mechanical properties for the as-received cold-rolled med-Mn steel. Sn segregation at the carbide/matrix interface inhibited C dissolution and partitioning to the intercritical austenite, resulting in poor retained austenite stability. Consequently, the Sn-containing cold-rolled med-Mn steels failed to meet 3G AHSS general target mechanical properties.
3) The austenitizing heat treatment at 775 °C for 600 s (used to produce the martensitic starting microstructure) produced a thick (~ 200 nm) external oxide layer regardless of the process atmosphere pO_2 (i.e., –30, –10, or +5 °C T_{dp}) employed. However, intermediate flash pickling was successful in dissolving the external oxides to an average thickness of 30 nm as well as revealing trapped extruded Fe nodules that formed owing to the volume expansion associated with internal oxidation. Flash pickling also exposed the substrate in regions where the external oxides were relatively thin.
4) A multi-micron (~ 2–8 µm) deep solute-depleted layer formed during the austenitizing heat treatment, where the depth of the solute-depleted layer increased with increasing process atmosphere pO_2 owing to a higher inward O_2 flux which promoted internal oxidation deeper into the substrate.
5) No significant growth of the external oxides remaining after flash pickling occurred during intercritical annealing at 675 °C × 120 s regardless of the process atmosphere pO_2. The multi-micron solute-depleted layer, formed during the austenitizing heat treatment, prevented solute diffusion from the bulk substrate within the 120 s annealing time.

6) The discrete external oxide distribution along with extruded Fe nodules and exposed substrate on the pre-immersion surface facilitated successful reactive wetting of the prototype med-Mn steel using a conventional 0.2 wt% (dissolved) Al Zn(Al,Fe) galvanizing bath with a well-developed $Fe_2Al_5Zn_x$ inhibition layer forming at the steel/coating interface. This resulted in a high-quality galvanized coating with good coating adherence, as shown by the three-point bend test results.
7) Direct wetting was the main reactive wetting mechanism, where the exposed substrate and extruded Fe nodules dissolved readily upon immersion in the galvanizing bath and reacted with the bath dissolved Al to form the requisite $Fe_2Al_5Zn_x$ interfacial layer. Detailed analysis of the steel/coating interface revealed that oxide lift-off, oxide wetting, bath metal ingress, and aluminothermic reduction were the secondary reactive wetting mechanisms.
8) The galvanized prototype med-Mn steels met 3G AHSS general target mechanical properties, confirming that CGL-compatible thermal processing can be successfully employed to produce target 3G AHSS mechanical properties and high-quality galvanized coating in med-Mn steels.

7.2 Future Directions

Based on the findings of this Ph.D., some future research projects can be recommended. These following research projects will help develop this emerging 3G AHSS further and promote accelerated adoption of galvanized med-Mn steels by the automotive industry.

1) High strain rate mechanical property and fatigue tests: Additional mechanical tests, such as tensile tests at high strain rates, need to be performed to assess the strain rate sensitivity of these new generations of AHSSs. Furthermore, fatigue tests should be conducted to evaluate the response of these med-Mn steels during repeated loading.

2) *Effect of micro-alloying elements (V, Ti, Nb) on the mechanical properties:* Micro-alloying elements, such as V, Ti, and Nb, can further increase the strength of med-Mn steels *via* grain refinement and precipitation strengthening mechanisms. Nevertheless, it should be noted that formation of carbides, nitrides or carbonitrides of the micro-alloying elements can lead to less C being available for chemically stabilising the retained austenite, which can affect the TRIP kinetics and in turn, the mechanical properties. However, the literature on low-alloy TRIP steels [1-6] reported contradicting results regarding this. Hence, the effect of V/Ti/Nb micro-alloying on both the mechanical properties and retained austenite stability should be extensively studied for these med-Mn steels.
3) *Delayed hydrogen cracking analysis:* AHSSs with retained austenite are known to be susceptible to delayed hydrogen cracking [7,8]. Hydrogen has a higher solubility in austenite compared to martensite. As a result, the TRIP effect can produce hydrogen-rich martensite during any type of deformation process and, thereby, increase the risk for delayed hydrogen cracking. In that regard, deep-drawing cup test should be conducted for the galvanized med-Mn steels to evaluate delayed hydrogen cracking susceptibility.
4) *Different galvanizing bath compositions:* The galvanizibility of med-Mn steels in Zn-Al-Mg galvanizing baths should be investigated.
5) *Weldability of the galvanized steel substrates:* Resistance spot welding (RSW) is the most commonly used joining technique in assembling automotive body parts. However, the galvanized coating and internal oxidation of AHSSs can significantly affect RSW process parameters [9–11]. Hence, weldability studies need to be carried out for successful integration of med-Mn steels into the automotive industry.

7.3 References

[1] D. Krizan, B.C. De Cooman, J. Antonissen, Retained Austenite Stability in Cold Rolled CMnAlSiP Microalloyed TRIP Steels, in: Proc. Int. Conf. Adv. High Strength Sheet Steels Automot. Appl., AIST, Winter Park, USA (2004) 205–216.

[2] I.B. Timokhina, P.D. Hodgson, E.V. Pereloma, Effect of microstructure on the stability of retained austenite in TRIP steels, Metall. Mater. Trans. A. 35 (2004) 2331–2340.

[3] S. Traint, A. Pichler, M. Blaimschein, B. Röthler, C. Krempaszky, E. Werner, Alloy design, processing and properties of TRIP steels: A critical comparison, in: Proc. Int. Conf. Adv. High Strength Sheet Steels Automot. Appl., AIST, Winter Park, USA (2004) 79–98.

[4] W. Bleck, A. Frehn, J. Ohlert, Niobium in dual phase and TRIP steels, in: Proc. Int. Symp. Niobium, TMS, Orlando, USA (2001) 727–752.

[5] A.Z. Hanzaki, S. Yue, P.D. Hodgson, The Influence of Bainite on Retained Austenite Characteristics in Si-Mn TRIP Steels, ISIJ Int. 35 (1995) 79–85.

[6] K. Sugimoto, M. Mukherjee, TRIP aided and complex phase steels, in: R. Rana, S.B. Singh (Eds.), Automot. Steels Des. Metall. Process. Appl., Woodhead Publishing (2017) 217–257.

[7] R.A. McCoy, W.W. Gerberich, Hydrogen Embrittlement Studies of a TRIP Steel, Metall. Trans. 4 (1973) 539–547.

[8] J. Li, W. Wang, Y. Zhou, S. Liu, H. Fu, Z. Wang, B. Kan, A Review of Research Status of Hydrogen Embrittlement for Automotive Advanced High-Strength Steels, Acta Metall. Sin. 56 (4) (2020) 444–458.

[9] X. Han, C. DiGiovanni, J.R. McDermid, E. Biro, N.Y. Zhou, Effect of internal oxidation on the weldability of CMnSi steels, Weld. World. 63 (2019) 1633–1639.

[10] S.A. Gedeon, Resistance Spot Welding of Galvanized Sheet Steel, Massachusetts Institute of Technology, 1984.

[11] N.T. Williams, J.D. Parker, Review of resistance spot welding of steel sheets: Part 1 - Modelling and control of weld nugget formation, Int. Mater. Rev. 49 (2004) 45–75.